Reliable detection of rotor electrical faults in induction motors using frequency extraction of stator current and stray magnetic flux signals

Panagiotou, Panagiotis

Award date:
2020

Awarding institution:
Coventry University

Reliable Detection of Rotor Electrical Faults in Induction Motors Using Frequency Extraction of Stator Current and Stray Magnetic Flux Signals

by

Panagiotis A. Panagiotou

Ph.D Dissertation

June 2020

Faculty of Engineering, Environment and Computing

School of Computing, Electronics & Mathematics

Content removed on data protection grounds

Certificate of Ethical Approval

Applicant:

Panagiotis Panagiotou

Project Title:

Reliable Detection of Rotor Electrical Faults in Induction Motors Using Frequency Extraction

This is to certify that the above named applicant has completed the Coventry University Ethical Approval process and their project has been confirmed and approved as Low Risk

Date of approval:

26 November 2019

Project Reference Number:

P93718

Content removed on data protection grounds

Dedicated to my family.

Acknowledgements

I would like to thank the following people, who all to some extent contributed to the success of this endeavour:

My supervisory team, Dr. Konstantinos Gyftakis, Dr. Neophytos Lophitis, and Dr. Ioannis Arvanitakis for their guidance and trust throughout the PhD journey. In particular, I want to thank my advisor, Dr. Arvanitakis, for his time, patience, insight and knowledge imparted to me over the last three years.

I am also eternally thankful to my family; my parents, Achilles and Evangelia, for their unconditional love and support, as well as my brother, Orestis, for his advice and help through my career. I would also like to thank Ioanna Vassi for her caring love and support over the last five years, and Awina Kaur for always praying for me and trying to boost my motivation. My cousin, Zoe Giora, for her love, for being there and for supporting me in my every decision. Thank you all for always believing in me. Your presence and moves have taught me that courage is not the absence of fear or despair, but the strength to conquer them.

Special thanks also go to Dr. Ioannis Lagkas, Mr. Nikolas Koumpis, and Mr. Nikolas Lamprianidis for sharing their mathematical expertise and wisdom, as well as for emphasizing the significance of rigour in research. My friend and colleague, Samuel Joseph Perkins, for his company and help in the Power & Energy Lab during our parallel PhD paths. Thank you all for being there. Our exchange of ideas and intellectual interaction has taught me that, even in the darkest times, it is not pointless to hope for light.

Many thanks to Mr. Jon Weston, technician of Coventry University's Electrical Engineering Faculty, for his assistance during the experimental measurements in the Power & Energy Lab. I would also like to acknowledge Professor Jose-Alfonso Antonino-Daviu from the Universitat Polytechnica de Valencia, Spain, for sharing his data with me and for his useful consulting during all our collaborations.

Finally, I would like to thank my wonderful friends, Mr. Kostas Dimitriou and Mr. George Marougas, for their support and for the faith they always had in me, as well as for the extraordinary times we spent together over the last eight years.

Abstract

A recent and continuously developing trend in Fault Diagnostics (FD) of Induction Motors (IM) is the measurement of electromagnetic fields attenuated in the vicinity of the machine for diagnostic purposes. This type of analysis is referred to as Stray Flux Signature Analysis (SFSA) and has proven at least as valuable as the traditionally applied Motor Current Signature Analysis (MCSA). The stray fields are captured with magnetic field sensors or with the use of search coils as induced voltage, which is the final signal of interest to apply Digital Signal Processing (DSP) and FD.

To this direction, the presented thesis has contributed in the field by proposing a diagnostic solution for a specific type of faults, rotor faults. The method is referred to as frequency extraction, as it is based on the extraction of frequency information with advanced DSP, and takes advantage of the fault related speed ripple effect during the steady-state operation. Initially, it is successfully applied on stray magnetic flux measurements, a purpose for which special sensor coils were also designed and constructed. Afterwards, the method is demonstrated on measurements of stator currents as the most traditional measurement in FD. The validation of the method regarding both stray flux and stator currents is done with Finite Element (FE) simulations and experimental measurements.

Table of contents

List of figures

List of tables

List of Abbreviations

ATCSA	Advanced Transient Current Signature Analysis
CM	Condition Monitoring
CTFT	Continuous-Time Fourier Transform
CWT	Continuous Wavelet Transform
DFT	Discrete Fourier Transform
DWT	Discrete Wavelet Transform
DSP	Digital Signal Processing
EMD	Empirical Mode Decomposition
EPVA	Extended Park Vector Approach
EMF (or emf)	Electromotive force
FD	Fault Diagnostics
FE	Finite Element
FEM/FEA	Finite Element Methods/Analysis
FEPVA	Filtered-Extended Park Vector Approach
FFT	Fast Fourier Transform
FPVA	Filtered Park Vector Approach
FT	Fourier Transform
HT	Hilbert Transform
IM	Induction Motor
MCSA	Motor Current Signature Analysis
MEC	Magnetic Equivalent Circuit
MMF (or mmf)	Magneto-motive force
MUSIC	Multiple Signal Classification
MWFA	Modified Winding Function Approach
NVH	Noise, Vibration & Harshness
PCA	Principal Component Analysis
PSH	Principal Slot Harmonics
PVA	Park Vector Approach
RF	Radio Frequency
SFSA	Stray Flux Signature Analysis
STFT	Short Time Fourier Transform
TCSA	Transient Current Signature Analysis
WFA	Winding Function Approach
WT	Wavelet Transform
WVD	Wigner-Ville Distribution

ZFFT	Zoom-FFT
ZSC	Zero-Sequence Current
ZSF	Zero-Sequence Flux

List of Symbols

Chapter 2

Subsection 2.1.1

m	Number of phases
N	Number of slots
p	Number of pole pairs
q	Characteristic number of induction motors (slots per pole per phase)
τ_p	Pole pitch
D	Inner stator diameter
t	Variable in the time domain
n_s	Synchronous rotational speed
n_r (or n_{slip})	Rotor rotational (slip) speed
n_m (or n)	Rotational mechanical speed of the rotor body
ω_s	Synchronous angular speed
ω_r (or ω_{slip})	Rotor angular (slip) speed
ω_m (or ω)	Angular speed of the rotor body (mechanical)
s	slip(%)
f_s	Synchronous frequency (supply)
f_r (or f)	Rotor frequency
f_m	Mechanical frequency of the rotor body
B	Stator's rotating magnetic field
B_{max}	Magnitude of the rotating magnetic field
x	Peripheral distance on the circle defined by the inner stator radius
α	Angular coordinate corresponding to x
δ''	Air-gap length adjusted by Karter's coefficient
μ_0	Magnetic permeability of free space
w	Number of turns per phase
ξ	Winding factor
S	Coil span
m_r	Number of phases in rotor
N_r	Number of rotor bars

Subsection 2.1.2

R_1	Stator per-phase resistance
X_1	Stator per-phase reactance
I_1	Stator line current
V_{ph}	Phase voltage
R_r	Rotor actual resistance
L_r	Rotor actual inductance
X_r	Rotor reactance
X_{r0}	Rotor reactance at standstill
V_r	Rotor voltage
V_{r0}	Rotor voltage at standstill
I_r	Rotor current
R_2	Referred rotor resistance
X_2	Referred rotor reactance
I_2	Rotor line current
R_c	Resistance expressing core losses
X_m	Leakage inductance
P_{in}	Input power
P_{out}	Output power
P_{ag}	Air-gap power
P_C	Core losses
P_{sCL}	Stator copper losses
P_{rCL}	Rotor copper losses
P_{mech}	Converted mechanical power
P_{fr}	Friction losses
P_{stray}	Stray losses
τ_{ind}	Induced torque
τ_{load}	Load torque
J	Moment of inertia
ω (or ω_r)	Rotational mechanical speed of the rotor
Z_{tot}	Total equivalent impedance
V_{Th}	Equivalent Thevenin voltage
R_{Th}	Equivalent Thevenin resistance
X_{Th}	Equivalent Thevenin reactance
Z_{Th}	Equivalent Thevenin impedance

Subsection 2.1.3

t	Variable in the time domain
ω	Mechanical angular frequency
$\omega_r^{'}$	Electrical angular frequency of rotor quantities
N	Number of slots
N_s	Number of stator slots
N_r	Number of rotor slots
p	Number of pole pairs
$\kappa \in \mathbb{N}$	Integer
$\nu \in \mathbb{N}$	Order of stator slot harmonics
$\text{ł} \in \mathbb{N}$	Integer
α	Angular coordinate
α_ν	Angular coordinate for a harmonic of $\nu - th$ order
F_s	Stator mmf
F_r	Rotor mmf
F_m	Amplitude of mmf wave
$F_{m,\nu}$	Amplitude of the $\nu - th$ harmonic order mmf wave
$F_{m,\mu}$	Amplitude of the $\mu - th$ harmonic order mmf wave
φ	Angular phase shift
ξ_ν	Winding factor
$\mathrm{B_s}$	Magnetic flux density of the stator magnetic field
$\mathrm{B_r}$	Magnetic flux density of the rotor magnetic field
$\mathrm{B_{sat}}$	Magnetic flux density of the saturation magnetic field
$\mathrm{B_{tot}}$	Magnetic flux density of the total magnetic field
Λ_g	Relative permeance of the air-gap
Λ_{g0}	Amplitude term (constant) of the relative permeance of the air-gap Λ_g
$\lambda_{g,s}$	Relative permeance of the air-gap due to slotting of the stator
$\lambda_{g,r}$	Relative permeance of the air-gap due to slotting of the rotor
Λ_{sat}	Permeance due to saturation
μ_0	Magnetic permeability of free space
A_0	Amplitude term (constant)
k_C	Carter's coefficient
A_k	Amplitude term for stator slot related permeance
A_l	Amplitude term for rotor slot related permeance
g	Air-gap length

φ_{μ}	Angular phase shift of rotor-related quantities
φ_{sat}	Angular phase shift of saturation-related quantities

Subsection 2.2.1

t	Variable in the time domain
f	Variable in the frequency domain
ω	Angular frequency corresponding to f
$x(t)$	Time domain representation of a signal x
$X(f)$	Frequency domain representation of a signal x
j	Imaginary unit
$e^{(.)}$	Exponential map
F_s	Sampling frequency
k	Variable in the discrete time domain
n	Variable in the discrete frequency domain
$x[k]$	Discrete signal corresponding to the continuous time representation $x(t)$
$X[n]$	Discrete Fourier transform of the discrete time signal $x[k]$
N	Number of discrete samples
T_F	Time duration of a continuous time signal
Δf	Frequency resolution of the FFT

Subsection 2.2.4

t	Variable in the time domain
f	Variable in the frequency domain
$t-f$	Time-frequency
$X(t,f)$	Time-frequency domain representation of $x(t)$
$w(t)$	Window function
$S(t,f)$	Squared norm of the STFT (spectrogram) of $x(t)$
$\Delta\tau$	Time resolution of the STFT
Δf	Frequency resolution of the STFT
f_{sc}	Characteristic frequency for short circuit harmonic signature
k	Time-harmonic order of the short-circuited faulty part of the winding
n	Space-harmonic order of the short-circuited faulty part of the winding
s	Motor slip
f_s	Fundamental supply frequency

ν	Time-harmonic order
N_R	Number of rotor bars
γ	Coefficient within the set of the natural numbers $\mathbb{N}$
$j_{rot,sat}$	Coefficients within the set of Integers $\mathbb{Z}$
$i_{rot,sat}$	Coefficients within the set of Integers $\mathbb{Z}$

Subsection 2.3.3

f_{brb}	Characteristic frequency for the broken bar harmonic signature
$f_{sideband}$	Sideband frequencies of the broken bar fault
O_r	Center of the rotor
O_s	Center of the stator
f_{ecc}	Characteristic frequency for the mixed eccentricity harmonic signature
f_r	Frequency of the rotor electrical quantities
f_s	Frequency of the stator quantities (supply)

Section 2.4

$\vec{A}$	Magnetic vector potential
μ	Magnetic permeability
$\vec{J}$	Current density
$\vec{E}$	Electric field intensity
$\vec{B}$	Magnetic field intensity
J_0	Current density of the applied stator currents
$\frac{\partial \vec{A}}{\partial t}$	Induced currents (eddy currents)
σ	Conductivity

Chapter 3

t	Variable in the time domain
f	Variable in the frequency domain
$t-f$	Time-frequency
s	slip $(\%)$

f_s	Fundamental supply frequency
f_{mech}	Rotational mechanical frequency for the rotor
f_{brb}	Characteristic frequency for broken bar harmonic signature
$f_{sideband}$	Sideband frequencies of the broken bar fault
f_r	Rotor electrical frequency

Chapter 4, 5 & 6

t	Variable in the time domain
f	Variable in the frequency domain
$t-f$	Time-frequency
f_s	Fundamental supply frequency
s	slip $(\%)$
$X[t_k, f]$	Discrete STFT of a discrete signal $x[n]$
F_s	Sampling frequency
L_w	Window sequence length
β	Local equivalent noise bandwidth
$S(t, f)$	Power spectral density (spectrogram) over the $t-f$ plane
f_a	Central harmonic of $a-$th order
f_i	The $i-$th sideband around the central harmonic of an examined signal
$S(t, f_{\alpha,i})$	Power spectral density over time for the $i-$th sideband of the $a-$th harmonic

Chapter 1

Introduction

Induction machines are the most widely used devices for electromechanical energy conversion [1, 7–9]. Since their invention in the late 1890's, they have been used in various applications including power generation and conversion [7, 8], mobility and transport applications [7, 9], as well as a lot of industrial-based applications like pumping, drilling, oil & gas, hydroelectric, petrochemical, power plants, etc, [10–16]. Their widespread use due to their facile handle, efficiency, robustness, and reliability makes them a vital part of the modern industry. The same reasons give growth to the field of induction machines condition monitoring and fault diagnostics [7–10]. This chapter briefly introduces the field of research subject and the contribution of this thesis.

1.1 The Induction Motor

The induction motor (IM) consists from two basic components: the stationary part which is called the *stator* and the rotating one which is called the *rotor*, both designed and constructed with slots and separated from each other by a thin layer of air referred to as the *air-gap* [1, 17]. The stator of a 3-phase induction machine consists of a 3-phase winding configured with 120° angle difference in space. There are two types of induction machines, depending on the rotor construction: the *wound rotor* and the *cage rotor* induction machines. A wound rotor is constructed from coils, placed inside the rotor slots in a similar manner as the 3-phase winding's wires of conductors are slotted in the stator. A cage rotor consists of a series of conducting bars incised at the rotor slots, close to the face of the rotor and shorted at either end by large shorting rings [1, 17]. Both types of motors are shown in Figure 1.1. To avoid high losses (e.g. eddy-currents and cross-currents [1, 7]), both the stator and rotor iron cores are manufactured from laminated material which is compressed to form the final body.

Fig. 1.1 A cage rotor (left) and a wound rotor (right) [1, 3]

The stator winding is placed inside the stator slots in such a way that, when the stator winding is symmetrically supplied, magnetic regions are formed in which a specific number of slots is included and current of the same direction is flowing. These are the machine's poles depending on the winding's configuration, distribution, and placement, while the distance between two consecutive poles is called the *pole pitch* [1, 17]. The pole pitch can also be defined as "the half period of the machine's rotating magnetic field" [1, 17]. The interaction of the stator and rotor magnetic fields results in the production of electromagnetic torque, which is desired to be smooth and sinusoidal to avoid higher harmonics and their consequences [1, 7, 8, 17]. In order to create magnetic fields that are morphologically as close as possible to sinusoidal, the winding distribution is ideally a sinusoidal one. However, this is not feasible in real life applications and this is the main reason -along with the slotting- for the existence of higher space harmonics in the electromagnetic quantities of all AC machines [1, 2, 7, 17].

Regarding the rotor construction, a wound rotor consists of a 3-phase coil placed inside the rotor slots usually in star (Y) configuration [1]. The winding terminals are connected to the slip rings, which are connected through brushes to an external circuit (e.g. a 3-phase resistor bank). A cage rotor consists, as described, of a series of conducting bars made of either copper or aluminium. These conductors are put together to form a cage, which is enclosed inside the rotor iron core slots either by casting (*die-cast rotors*) or by manual placement of manufactured bars. A rotor can also be unslotted, consisting only from solid material. These are special types of rotors called *solid rotors* and are used in high-speed applications due to their high endurance in harsh conditions and centrifugal forces [1, 2].

1.2 Induction Motor Faults & Fault Diagnostics

A fault in electrical machines is an undesired situation or damage, which can directly affect the machine's normal operation or progressively lead to machine failure. Many reasons can constitute the cause of fault existence: inherent manufacturing defects, machinery long overdue life-time, operation in harsh environments, frequent start-ups and so on [7–9]. Incipient faults might not always evidently affect the machine operation, however their progression can evolve undetected and thus endanger both safety of users/equipment/facility and money lost from downtimes or invested in maintenance. Therefore, it is a matter of uttermost urgency to detect faults in early stages and prevent as much as possible potential risk emerging from faults [7, 8, 10, 12].

A list of the most frequently occurring faults in an IM that are also continuously investigated by the research community is the following [7–10]:

1. Stator faults originating from core lamination damage or open-circuits
2. Stator faults due short-circuits
3. broken bars and/or broken end-rings (for cage rotors)
4. rotor winding short-circuits (for wound rotors)
5. bended shaft
6. eccentricity faults
7. bearing faults

Considering the above list, faults in induction machines are essentially categorised in three main types of faults: stator faults, rotor faults and mechanical faults [7–9]. The main stator fault being of prior interest to the research community is the inter-turn short-circuit and is usually caused due to insulation failure [7, 8]. Rotor faults include primarily the broken bar and broken end-ring fault [7, 8]. Although rotor faults are mainly considered as electrical faults, due to their origin and aftermath they might sometimes be categorised as partial electrical and partial mechanical faults [12]. Mechanical faults refer to a bended shaft, the static, the dynamic and the mixed eccentricity, as well as the bearing faults [7–9]. An overview of faults, their origin and their symptoms is given in the theoretical background of Chapter 2, along with the Digital Signal Processing (DSP) techniques used for purposes of Fault Diagnostics (FD).

The repercussions of the aforementioned faults are symptoms that can be generally summarised as below [7–9]:

1. asymmetries in the phase currents or voltages
2. increased torque and speed ripples
3. reduction of useful electromagnetic torque
4. excessive vibrations and noise
5. unbalancing or stalling of heavy loads
6. reduction of the efficiency
7. impairment of the power factor ($\cos\phi$)
8. overheating and excessive fumes or smells

Condition monitoring and fault diagnostics of IM handle the task of detecting a fault on time and prevent all its risky -or even fatal- consequences [7–10]. This is done through the monitoring -by measurement means- of a vital parameter or a set of vital parameters, that are of major importance in terms of information comprised in their time waveform, harmonic content or any other type of signal representation and analysis [7, 8]. The following list is a summary of such parameters and consequently of the diagnostic methods they have prospered in the field [7–9]:

1. Vibration, noise & harshness analysis (NVH)
2. Current measurements
3. Torque and speed measurements (usually by consequent ripples)
4. Active & reactive power measurements
5. Electromagnetic fields analysis (air-gap flux, stray flux, etc)
6. Temperature and thermal analysis
7. RF emission analysis
8. Chemical analysis (for insulation and windings)

Apparently a condition monitoring and fault detection procedure ideally consists of multiple choices from this list, since additional measurements of any kind are always useful to cross-validate with the main measurements or to provide extra information [16, 18].

However, this is not always feasible; hence, one or a couple of them are chosen and usually prove enough to guarantee a successful diagnosis [16, 18–20]. In this thesis, a successful rotor fault detection method is proposed and demonstrated on measurements of stator current and stray flux signals, encapsulating the originality of a novel DSP approach during the steady-state of the machine operation.

1.3 Aims & Objectives

The motivation for this research springs from the problem of rotor electrical faults and their unpredictable dynamic nature during the machine operation. Such a case in induction motors is the problem of broken rotor bars and broken rotor end-rings. These issues are being extensively studied in academia for more than five decades. In particular, when these faults occur in multiple locations of the rotor, diagnostic engineers face the problem of adjacent and non-adjacent cracks and breakages on the rotor body. Along with other complex phenomena like the magnetic saturation, the proximity and the skin effect, phenomena of thermal nature, etc., these faults make up very challenging diagnostic cases. Due to all these factors, it is frequently the case for motors installed in industry to encounter incidents of false-positive or false-negative diagnosis. Therefore, an aim of this research is to fill this diagnostic gap and solve the problem of non-adjacent breakages.

Another issue in applications of rotor fault diagnostics is the parameter setting during digital signal processing with regards to the parameters of the induction motor, the duration of the signal measurements, and the boundaries within which a diagnostic method can be applied. Consequently, this research investigates such questions and aims to set the boundaries required for the reliable tracking of rotor fault related frequencies. The proper tracking and evaluation of these frequencies require to account for certain inherent system parameters, as these relate to the speed ripple effect which is continuously altered and modulated at the presence of rotor faults and in turn affects the motor's magnetic fields distribution.

Finally, regarding the stray magnetic field measurements, commercially available sensors are usually very expensive and sometimes not very user-friendly or facile to install. It is well known amongst researchers that such sensors require extensive additional research regarding their suitability, placement, properties, etc., which means additional time and effort that can be sometimes be costly. Therefore, this research aims for the proposal of a low-cost monitoring device to measure stray magnetic fields in the vicinity of the motor. The device can be constructed in a laboratory environment with low-cost materials and be embedded on induction motors of various sizes.

1.4 Key Achievements & Contribution

The key achievements of the present research are both of diagnostic and technical value. Regarding diagnostics of induction motors, a new diagnostic technique is proposed for rotor faults which solves the problem of adjacent and non-adjacent broken rotor bars. This problem has been studied extensively over the past decades in academia, as it is continuously reported to be a vice in the industry. This work successfully confronts the problem and resolves it by reliably tracking the fault-related speed ripple effect and by taking advantage of the spectral components it generates. The proposed method was validated on various induction motors experimentally and computationally for the electromagnetic variables of stator current and stray magnetic flux. Moreover, a subset of harmonics which is adequate to reveal frequencies related to rotor electrical faults was ushered in these signals, using the frequency extraction process formulated in the methodology. This is of additional diagnostic value, as such frequency subsets can be extracted and investigated in the future for measurements of other signals like electromagnetic torque, acoustic noise, zero-sequence currents or voltages, and many others.

Regarding the key achievements of technical nature, a search coil sensor was designed and manufactured to acquire stray magnetic flux measurements for diagnostic purposes. This monitoring device was tested in laboratory level and in some selected industry applications like large industrial motors embedded in hydroelectric power plant installations [16]. It provides a low-cost solution for diagnostic purposes and can be easily implemented on machines of different sizes and power rating. Another contribution of this research is in the DSP domain, as the proposed methodology formulates the boundaries for the apt parameter tuning regarding applications of rotor fault detection. Finally, the latter contribution leads to the aspect of the time-varying nature and non-linearities in the behaviour of induction motors at the presence faults, which are studied extensively by research works of the latest years presented in the literature. These can be respected with assumptions and fine tuning that consider inherent parameters on system level, like the induction motor slip or the sampling frequency during measurements. Such aspects are discussed in the methodology chapter and taken into account during the application of the proposed method.

The original contribution of this thesis can be found in publications [6, 21–24]. In [6] the proposed approach is introduced in an investigative manner, while [21] finalises its pre-setting and fine-tuning to define the limits within which the method can be applied for the detection of rotor faults. In [22] the preliminary results of the proposed method are applied on stray magnetic flux data acquired from FEM simulations, while the work is extended in [23] validating the method with experimental measurements. Finally, the method is applied

on stator current measurements in [24] to confirm its validity with the most traditional and commonly used measurement in FD.

1.5 Thesis Outline

The dissertation consists of seven chapters in total. Excluding the current chapter, the rest of the thesis is structured as follows:

Chapter 2, providing the basic theoretical background regarding induction motors, digital signal processing, and fault diagnostics.

Chapter 3, which performs a review on the state of the art diagnostic techniques for rotor fault detection using stator current and stray magnetic field measurements.

Chapter4, where the proposed methodology is formulated. Afterwards, the chapter describes the induction motor models used for the FEA simulations, their design, their parameter setting, and their simulation process. The chapter concludes with the two experimental set-ups, where data were acquired on various induction motors for the analysis and experimental validation.

Chapter 5, presenting the results from FEA simulations on three motors: two $4-pole$ induction motors of 4 kW power with different rotor slot number, and one large $6-pole$ industrial 1.1 MW induction motor. Each motor was extensively studied under five different scenarios, namely the healthy model and the models suffering from broken bar faults. The chapter concludes with a brief discussion on the results of each examined model.

Chapter 6, presenting the results from experimental measurements on two different motors: a $4-pole$ induction motor of 4 kW power, and a 1.1 kW, $4-pole$ induction motor, while the faulty motors regard multiple cases of adjacent and non-adjacent breakages in the rotors. The chapter finishes with some conclusive remarks on the experimental results for each motor and the corresponding motors with broken rotor bars.

Chapter 7, where the overall conclusion is presented with the contribution of this research to existing knowledge. The chapter concludes with the limitations and the suggestions for future work, that spring from obstacles faced during the current study.

Chapter 2

Theoretical Background

This chapter provides the main theoretical background of the thesis regarding the induction motor (IM), Digital Signal Processing (DSP) and Fault Diagnostics (FD). As the scope of the chapter is to apprehend basic concepts used throughout the thesis for literature (Chapter 3), presentation of methodology (Chapter 4) and presentation of results (Chapter 5 & 6), the theory is described here briefly.

2.1 The Induction Motor

2.1.1 Basic Theory & Fundamental Principles of Operation

The stator winding of an induction machine can come in various configurations, in either single-layer or double-layer coiling. Considering m the number of phases, N the number of slots and p the number of pole pairs, an important parameter to know is the characteristic number q defining the number of slots per pole and per phase [1, 3, 17]:

$$q = \frac{N}{2\mathrm{p}m} \tag{2.1}$$

There are windings with q integer and windings with q fractional, providing a full-pitched or fractional-pitched configuration respectively. Fractional-pitched windings are mainly used in large industrial induction machines for avoidance of higher harmonics in the stator core, which is extremely expensive to maintain or repair in such scales [1, 3, 17]. The pole pitch, which is defined either as the distance between two consecutive poles or as the half period of the rotating magnetic field's wave, electrically covers 180° and is measured in meters [17]:

$$\tau_{\mathrm{p}} = \frac{\pi D}{2\mathrm{p}}, \tag{2.2}$$

where D is the inner stator diameter.

Now, when the stator winding is supplied from a symmetrical 3-phase source of frequency f_s, a rotating magnetic field is created in each phase of the stator. Their speed of rotation in rpm is called the *synchronous speed* [1, 3]:

$$n_s = 60\frac{f_s}{\mathrm{p}} \tag{2.3}$$

These rotating magnetic fields are practically stationary waves. The superposition of the three stationary waves results in a rotating magnetic field which is a travelling wave, being a function of both time and space, and whose general form is given from the following equation [3, 4]:

$$B(x,t) = B_{\max}\sin\left(\omega_s t + \pi\frac{x}{\tau_{\mathrm{p}}}\right)\left(\tag{2.4}$$

where t is the time, x the peripheral distance on the circle defined by the inner stator radius (space dependence), $B_{\max}$ the magnitude of the magnetic field, $\omega_s = 2\pi f_s$ and τ_{p} the pole pitch. Relationship (2.4) describes the magnetic field of the machine under the influence of the fundamental harmonic and it denotes the existence of harmonics in a machine's electromagnetic quantities with either spatial origin (space harmonics), or with time origin (time harmonics). In all related equations and formulas, it is more convenient to use the angular coordinate α, which is defined as [25]:

$$\alpha = \frac{1}{\mathrm{p}}\frac{\pi}{\tau_{\mathrm{p}}}x \tag{2.5}$$

To account for adjustment of the air-gap variation by the stator and rotor teeth with a constantly adjusted air-gap δ'', the Carter coefficient is use [3, 4, 17, 26]. The final form of the magnetic field's fundamental harmonic accounting for Carter's theorem is given by [3, 4]:

$$\mathrm{B}(\alpha,\mathrm{t}) = \mu_0 \cdot \frac{3\mathrm{w}\xi I\sqrt{2}}{\pi\mathrm{p}\delta''} \cdot \cos(p\alpha - \omega_{\mathrm{s}}\mathrm{t} - \varphi) \ . \tag{2.6}$$

where μ_0 is the magnetic permeability of free space, w the number of turns per phase with $2w$ being the number of conductors, ξ a geometrical parameter called winding factor defined as $\xi = \frac{\sin\beta}{\beta}$ and $\beta = \frac{S}{\tau_p}\cdot\frac{\pi}{2}$, with S being the winding's width (coil span) in radians [1, 3, 4, 26]. Similarly with the characteristic number q given by (2.1), ξ is also defined for the rotor. In the case of a wound rotor, where the number of phases is $m_r = 3$, it is defined in the same

way as for the stator. In the case of a cage rotor, it is considered that the number of phases m_r is equal to the number of rotor bars N_r, the winding factor is $\xi_r = 1$ and one accounts for $w_r = 1/2$ turns per phase since there is $w_r = 1$ conductor (bar) per phase [1, 3, 4, 26].

The field of (2.6) induces currents in the rotor cage, which in turn create a rotating magnetic field in the rotor. The interaction of the two fields results in the production of electromagnetic torque on the rotor cage, which turns the rotor in the same direction as the fields' direction of rotatio [1, 3]. It is due to the nature of this mechanism that these machines are called induction machines, since the continuous induction is caused by the relative motion of the rotor with respect to the rotating magnetic field and this is what produces electromagnetic torque. In other words, the rotor of the machine rotates asynchronously at its own speed which is slightly smaller than n_s, continuously trying to catch up with the speed of rotation of the magnetic field that slips away [1, 3, 4, 26]. The mechanical speed of the rotor body in rpm is usually indexed as n_m or simply n, while its angular velocity in rad/sec is symbolised with ω_m or simply ω. The difference of the synchronous speed and the rotor speed is called the *slip speed* and is symbolised as n_r or n_{slip} [1]:

$$n_{slip} = n_r = n_s - n_m \quad , \tag{2.7}$$

which in rad/sec can be expressed as:

$$\omega_{slip} = \omega_r = \omega_s - \omega \tag{2.8}$$

The motor's slip, symbolised with s, is consequently defined as [1]:

$$s = \frac{n_s - n}{n_s} = \frac{n_r}{n_s} = \frac{\omega_s - \omega}{\omega_s} \tag{2.9}$$

It is obvious from (2.9) that the slip s relates the slip speed n_r with the synchronous speed n_s via the relationship:

$$n_r = s \cdot n_s \quad , \tag{2.10}$$

while the rotor electromagnetic quantities carry the frequency:

$$f_r = p \cdot n_r = s \cdot f_s \tag{2.11}$$

From all the above and accounting for (2.7)-(2.11), the following relations are valid relating the frequencies of stator and rotor quantities as well as their rotational speeds [1, 3, 4, 26]:

$$n_m = (1 - s) \cdot n_s, \quad \omega_m = (1 - s) \cdot \omega_s \tag{2.12}$$

$$n_s = n_r + n_m \ , \quad f_s = f_r + pn \ , \quad s = \frac{f_r}{f_s} \tag{2.13}$$

Practically, the slip s is used to express the percentage of the rotor's speed relative to the synchronous speed. At standstill $s = 1$ since $n = 0$ and the machine behaves as an ideal transformer (locked rotor) [1, 26]. On the other hand, close to the synchronous speed n_s we have $s \to 0$ and for any point in between the two extremes $f_r = s \cdot f_s$.

2.1.2 Per-Phase Equivalent Circuit & Development of Torque

As mentioned, the induction machine behaves as a rotating transformer with the stator being the primary part and the rotor being the secondary, while the only difference from an ideal transformer is that the secondary operates at a slightly different frequency [1, 3, 4, 27]. Hence, from the classical theory of electrical machines, a useful tool for the representation of the IM during steady-state operation is the per-phase equivalent circuit. This refers to the per-phase equivalent shown in Figure 2.1, for which: R_1 the stator per-phase resistance, X_1 the stator per-phase reactance, R_2 the referred rotor resistance, X_2 the referred rotor reactance, X_m the leakage inductance, R_c the core losses resistance, V_{ph} the phase voltage, I_1 the stator line current, I_2 the rotor line current [1, 3, 4, 27].

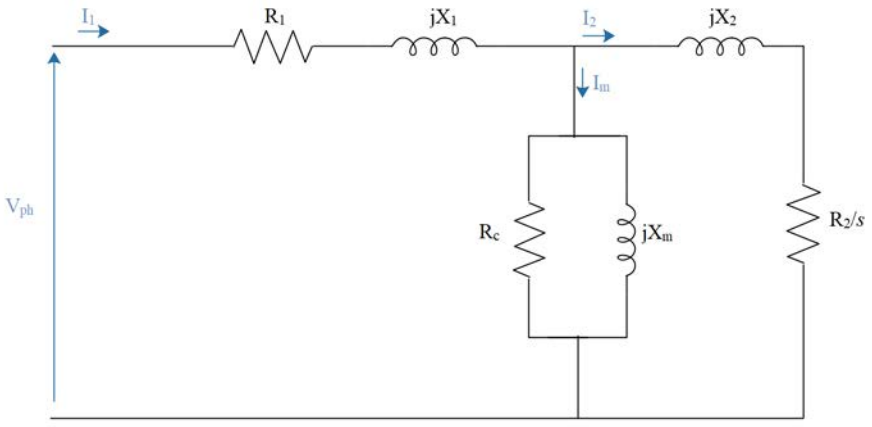

Fig. 2.1 Equivalent Circuit of the IM assuming ideal transformer model [1, 2]

The resistance R_1 expresses the per-phase stator resistive losses, while the reactance X_1 expresses the per-phase inductance of the winding [1, 3, 27]. Considering R_r and L_r the actual rotor resistance and inductance respectively, V_r the rotor voltage, I_r the rotor current and that all the rotor quantities operate at frequency f_r:

$$V_r = sV_{r0} \quad , \quad \text{and} \tag{2.14}$$

$$X_r = \omega_r L_r = 2\pi f_r L_r = 2\pi s f_s L_r = sX_{r0} \quad , \tag{2.15}$$

where V_{r0} and X_{r0} the rotor voltage and reactance respectively when the rotor is at standstill ($s = 1$). Now, isolating the rotor side in the circuit of Figure 2.1 and accounting for (2.14)-(2.15), the rotor current I_r can be obtained as [1]:

$$I_r = \frac{V_r}{jX_r + R_r} = \frac{V_r}{R_r + jsX_{r0}} = \frac{V_{r0}}{\frac{R_r}{s} + jX_{r0}} \tag{2.16}$$

Considering the induction machine as an ideal transformer with ratio ζ, the rotor referred resistance and referred reactance can be defined as $R_2 = \zeta^2 R_r$ and $X_2 = \zeta^2 X_{r0}$ respectively [1, 27]. In a real life application and especially in the case of cage rotors, the ratio ζ, the actual rotor resistance R_r and the standstill rotor reactance X_{r0} are very difficult or even impossible to measure, while R_2 and X_2 can be directly measured at the terminals [1, 3, 27]. Hence, it is commonly established to use the refered values R_2 and X_2 when it regards the modelling of induction motors with the per-phase or MEC [1, 3, 4, 27]. To relate Eq. (2.16) with the production of torque, two factors are required: a clear idea of the power flow in the induction motor and, secondly, the equivalent Thevenin circuit from the terminals coupling magnetically the primary (stator) with the secondary (rotor). For the circuit of Figure 2.1, the total equivalent impedance of the circuit is easily calculated as follows [1, 4]:

$$Z_{\text{tot}} = R_1 + jX_1 + \frac{1}{G_C - jB_M + \frac{1}{R_2/s + jX_2}} \quad , \tag{2.17}$$

In references [1, 3, 4, 7, 8, 27, 28] the steps for the derivation of the Thevenin equivalent are in detail described with analytical formulation, from which one can derive the current I_2 as [1]:

$$I_2 = \frac{V_{th}}{Z_{th} + Z_2} = \frac{V_{th}}{\sqrt{(R_{th} + \frac{R_2}{s})^2 + (X_{th} + X_2)^2}} \quad , \tag{2.18}$$

where V_{th} the Thevenin voltage, Z_{th} the equivalent Thevenin impedance, Z_2 the referred rotor impedance of the circuit in Figure 2.1, which are given by [1]:

$$V_{th} \approx V_{ph} \frac{X_m}{X_1 + jX_m} \quad , \quad R_{th} \approx R_1 (\frac{X_m}{X_1 + X_m})^2 \quad , \quad \text{and} \quad X_{th} \approx X_1 \tag{2.19}$$

The power flow diagram of an induction motor is shown in Figure 2.2 and it provides a mapping of the induction machine power distribution from input to output. The depicted components are: $P_{s_{CL}}$ the stator copper losses, P_C the core losses, P_{ag} the air gap power, $P_{r_{CL}}$ the rotor copper losses, P_{mech} the converted mechanical power, P_{fr} the friction losses, P_{SL} the stray losses [1, 27]. From Eq. (2.17) and Fig. 2.2 it is seen that, in the rotor side, "only the resistance R_2/s consumes power during conversion of the air-gap power P_{ag} to the mechanical power P_m" [1, 27]. Regarding the stator copper losses and the core losses, they are given from [1, 27]:

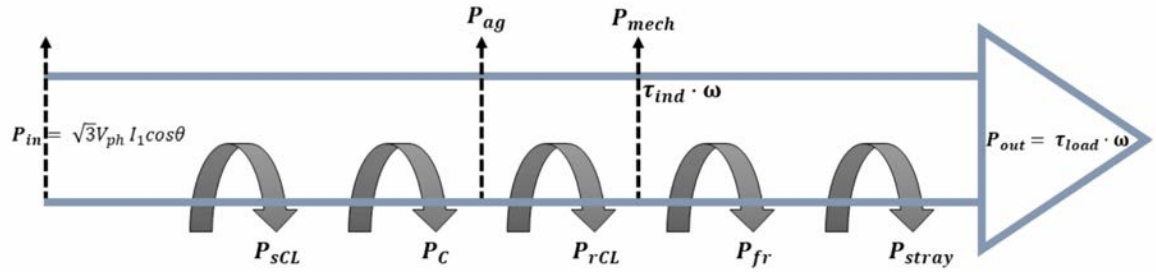

Fig. 2.2 Power flow diagram of an induction motor [1–4]

$$P_{s_{CL}} = 3I_1^2 R_1, \quad \text{and} \quad P_c = 3V_1^2 G_c \ , \tag{2.20}$$

and since only R_2/s consumes power:

$$P_{ag} = 3I_2^2 R_2/s, \quad and \quad P_{r_{CL}} = 3I_r^2 Rr = 3I_2^2 R_2 \ , \tag{2.21}$$

since the power is considered not to change in an ideal transformer [1, 27]. From the latter relationship it can be seen that $P_{r_{CL}} = s \cdot P_{ag}$, hence the converted mechanical power is given by [1]:

$$P_{mech} = P_{ag} - P_{r_{CL}} = 3I_2^2 R_2/s - 3I_2^2 R_2 = 3I_2^2 R_2(\frac{1}{s} - 1) = 3I_2^2 R_2(\frac{1-s}{s}) \ , \tag{2.22}$$

$$\text{or by} \quad P_{mech} = P_{ag} - P_{rCL} = P_{ag} - sP_{ag} \Longrightarrow P_{mech} = (1-s)P_{ag} \ . \tag{2.23}$$

The latter two relationships practically show that, from the IM equivalent circuit standpoint, the resistor R_2/s quantifies the resistance on which the air-gap power P_{ag} in an induction motor would be consumed, the resistor R_2 quantifies the resistance on which the

rotor copper losses $P_{r_{CL}}$ would be consumed, while their difference $P_{ag} - P_{r_{CL}}$ would be consumed on a resistor $R_{mech} = R_2(\frac{1-s}{s})$ [1, 27, 28]. Hence the resistance R_2/s of the circuit is encountered as $R_2\frac{1-s}{s}$, when it is desired to separate the rotor copper losses from the converted mechanical power P_{mech} in a problem that is dealt with by the per-phase or MEC approach [1, 3, 4, 27, 28].

The induced torque on the shaft of the machine will be [1]:

$$\tau_{ind} = \frac{P_{mech}}{\omega_m} = \frac{(1-s)P_{ag}}{(1-s)\omega_s} = \frac{P_{ag}}{\omega_s} \tag{2.24}$$

Finally, using Eq. (2.18) and (2.21)-(2.24), the induced torque can be quantified electrically by the circuit parameters as [1]:

$$\tau_{ind} = \frac{3 \cdot V_{th}^2 \cdot R_2/s}{\omega_s \left[(R_{th} + R_2/s)^2 + (X_{th} + X_2)^2\right]} \tag{2.25}$$

The characteristic curve of the induced torque versus speed (or versus slip) of an induction motor compared with its load curve is shown in Figure 2.3. By [1, 3, 4], the critical point between instability and stability is the point where the maximum torque occurs, which is called the pull-out torque. The machine motion of equation holds during every time-instant by the torque equilibrium given from [1, 3, 4]:

$$\tau_{\text{ind}} = \tau_{\text{load}} + J\frac{d\omega}{dt} \quad , \tag{2.26}$$

where τ_{load} the load torque, J the moment of inertia and $J\frac{d\omega}{dt}$ the acceleration torque. To be in the stability area, from (2.26) the following condition must hold:

$$\frac{\partial \tau_{load}}{\partial n} \geq \frac{\partial \tau_{ind}}{\partial n} \quad , \tag{2.27}$$

n being the speed in rpm.

Induction motors are known to have low starting torque and high starting currents, which affects not only the efficiency via the losses but also the the ability to start the motor with loaded shaft. The problem of low starting torque is compensated by the use of external resistances in wound rotors. Variation of these resistances provides the ability to transit the torque-speed curve to the left, hence increasing the starting torque while also drawing lower starting currents. This is more detailed described in [1, 3, 4, 27, 28]. In cage rotors, a similar concept is applied aiming to take advantage of the skin effect by the use of different designs, meaning the shape and depth of the rotor bars [1, 3, 17]. Hence, depending on the application, motors of different rotor cage design might be required. These are specified

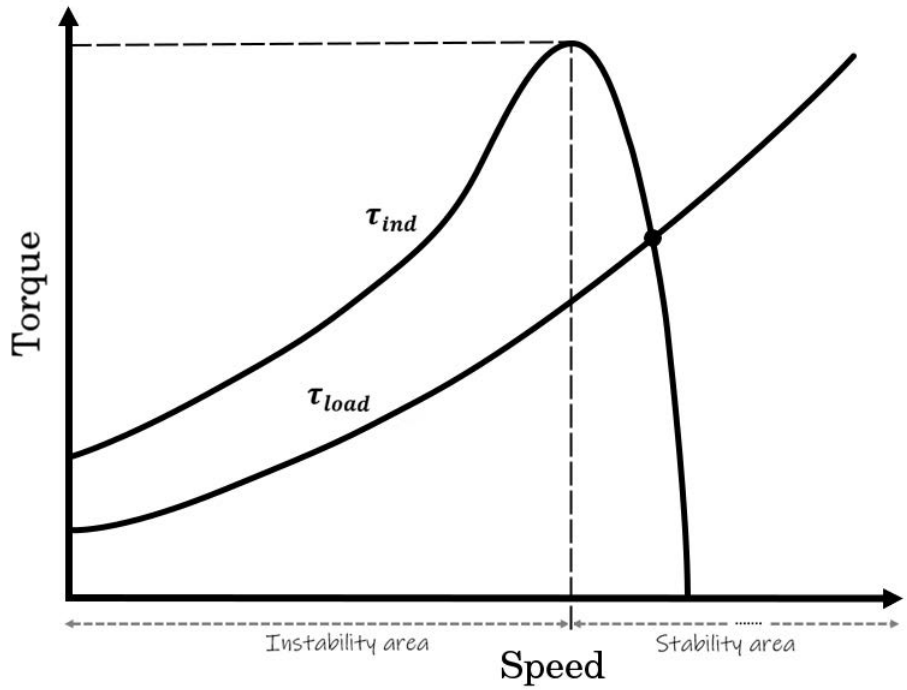

Fig. 2.3 Torque-Speed Characteristic of an Induction Motor [1, 3]

according to the specifications of NEMA [1], and the rules of Richter [17]. More information on the torque-speed characteristics, how motor designs are classified by NEMA and Richter and how these can affect the per-phase and MEC approach and its parameters can be found in [1, 3, 4, 7, 17, 26].

In practice, the spatial variation of the air-gap by the stator and rotor teeth as well as the slotted stator winding's non-sinusoidal distribution cause a non-sinusoidal distribution of the magnetic fields of the rotor and the stator, which is due to the non-sinusoidal distribution of the initial current-sheet and mmf [17, 25, 26]. This results in the presence of higher harmonics and since the induced torque is the result from the interaction of these two magnetic fields, this causes also higher harmonic content in the torque of the machine known as higher synchronous and higher asynchronous torques [3, 25, 26].

The problem of higher space and time dependent harmonic content in the electromagnetic variables of induction machines as well as the materials' non-linearities make the MEC approach to hold some disadvantages: a relatively satisfying accuracy only during the steady-state [1, 3]; a characterisation of the IM from a static analysis point of view [1, 3]; assumptions not satisfying for geometries with curvatures and corners [1, 7, 8]; results within a small percent of accuracy and increased errors, especially during transient operation [1, 7]. Despite its disadvantages, the MEC approach is the most fundamental one. It has rendered

valuable results and is very frequently used by engineers on the field in practical applications for quick evaluation of induction motor parameters [29–32].

2.1.3 Space Harmonics of the Induction Motor Magnetic Field

In subsection 2.1.1, the fundamental harmonic of the rotating magnetic field in an induction motor were described. The current section aims to describe the higher space harmonic content of the air-gap magnetic flux density in an induction motor, as well as how it is derived by the MMF and magnetic permeance variation using fundamental laws. The effect of slotting and saturation is included, as well as the mutual effects from stator to rotor and vice-versa.

By [25] and [26], the stator slot higher harmonic content is of the order:

$$\nu = \kappa\frac{N_s}{\mathrm{p}} \pm 1 \quad , \quad \kappa \in \mathbb{N} \tag{2.28}$$

while the order of the rotor slot harmonics is:

$$\mu = \kappa\frac{N_r}{\mathrm{p}} \pm 1 \quad , \quad \kappa \in \mathbb{N} \tag{2.29}$$

The negative sign (-) represents the rotating waves with clockwise direction, considered as the positive direction of rotation (forward). The positive sign (+) represents the waves rotating counter-clockwise (backwards), considered as the negative direction of rotation [25]. For any higher harmonic of order ν, the angular coordinate α must be accounted for as [26]:

$$\alpha_\nu = \nu\alpha = \nu\mathrm{p}\frac{2\pi}{N} \quad . \tag{2.30}$$

By Fourier series expansion, the mmf of the stator winding carries harmonics of the order $\nu = 6\kappa \pm 1$ with $\kappa \in \mathbb{N}$ ($\nu = 5, 7, 11, 17, 19...$), and its general form is thus given from [25, 26]:

$$F_s(\alpha,t) = \sum_{\nu=6\kappa\pm1}^{\infty} F_{m,\nu}\cos(\nu\mathrm{p}\alpha \mp \omega_s t) \quad , \tag{2.31}$$

while the mmf of the rotor cage is given from [25, 26]:

$$F_r(\alpha,t) = \sum_{\mu=1}^{\infty} F_{m,\mu}\cos(\mu\mathrm{p}\alpha \mp \omega_\mu t - \varphi_\mu) \quad , \tag{2.32}$$

where α the angular distance from the origin of the coordinate frame, φ_μ the angle between the vectors of the stator and rotor harmonics of equal order, ν and μ the order of space

harmonics at the stator and rotor respectively and $\omega = 2\pi f$. The amplitude peaks $F_{m,\nu}$ and $F_{m,\mu}$ are given from the following two formulas respectively [25, 26, 33]:

$$F_{m,\nu} = \frac{2\sqrt{2} I_1 \xi_\nu N_s}{\pi \nu \mathrm{p}} \quad , \quad F_{m,\mu} = \frac{\sqrt{2} I_1 N_r}{\pi \mu \mathrm{p}} \tag{2.33}$$

The magnetic flux density in the air-gap results from the mmf and the relative permeance of the air-gap as [25, 26, 34]:

$$\mathrm{B}(\alpha,t) = F(\alpha,t)\Lambda_g(\alpha,t) \quad , \quad \text{with} \quad \mathrm{B_{tot}} = \mathrm{B_s}(\alpha,t) + \mathrm{B_r}(\alpha,t) + \mathrm{B_{sat}}(\alpha,t) \quad , \tag{2.34}$$

$\mathrm{B_{sat}}$ being the magnetic flux density due to magnetic saturation, $\mathrm{B_s}$ and $\mathrm{B_r}$ the stator and rotor magnetic flux density respectively and $\Lambda_g(\alpha,t)$ the relative permeance (or magnetic conductance of the air-gap), whose general form is given from [25, 26, 35]:

$$\Lambda_g(\alpha,t) = \Lambda_{g0}\lambda_{g,s}(\alpha)\lambda_{g,r}(\alpha,t) \tag{2.35}$$

In the air-gap permeance given by Eq. (2.35), the term $\lambda_{g,s}(\alpha)$ expresses the relative permeance of the air-gap due to the slotting of the stator, which -as originating from the spatial geometry of the stationary part, the stator- is only space dependent by the angular coordinate α. The term $\lambda_{g,r}(\alpha,t)$ expresses the relative permeance of the air-gap originating from the effect of slotting in the rotor, which is at any case time *and* space dependent due to the difference in angular speed between the rotor body and the rotating magnetic field. The amplitude term Λ_{g0} is given from [25, 33]:

$$\Lambda_{g0} = \frac{A_0}{2} = \frac{\mu_0}{k_c g} \tag{2.36}$$

The air-gap permeance variation $\lambda_{g,s}(\alpha)$ including the effect of stator slots is given from [25, 34]:

$$\lambda_{g,s}(\alpha) = 1 + \sum_{k=1}^{\infty} A_k \cos\left(k N_s \alpha\right) \quad \forall \quad k \in \mathbb{N} \ . \tag{2.37}$$

The air-gap permeance variation $\lambda_{gr}(\alpha,t)$ including the effect of rotor slots is given from [25, 34]:

$$\lambda_{g,r}(\alpha,t) = 1 + \sum_{l=1}^{\infty} A_l \cos\left[l N_r \left(\alpha - \omega_r' t\right)\right] \quad \forall \quad l \in \mathbb{N} \ , \tag{2.38}$$

where $\omega_r' = \mathrm{p}\omega_m$ the electrical frequency of the rotor quantities with $\omega_m = (1-s)\omega_s$ the mechanical. In Eq. (2.37) and (2.38), A_k and A_l are the peak amplitude values of the $k-th$ and $l-th$ harmonic respectively at stator and rotor.

By setting $\lambda_{g,s}(\alpha)\lambda_{g,r}(\alpha,t) = \lambda_g(\alpha,t)$, the air-gap relative permeance becomes $\Lambda_g(\alpha,t) = \Lambda_{g0}\lambda_g(\alpha,t)$ and by substitution of (2.37) and (2.38) we get for λ_g:

$$\lambda_g(\alpha,t) = 1 + \sum_{k=1}^{\infty} A_k \cos(kN_s\alpha) + \sum_{l=1}^{\infty} A_l \cos\left[lN_r\left(\alpha - \omega_r' t\right)\right] +$$
$$+\frac{1}{2}\sum_{k=1}^{\infty}\sum_{l=1}^{\infty} A_k A_l \left\{\cos\left[\left(lN_r + kN_s\right)\alpha - lN_r\omega_r' t\right] + \cos\left[\left(lN_r - kN_s\right)\alpha - lN_r\omega_r' t\right]\right. \quad (2.39)$$

It is quite vital to refer to each one of the components in (2.39) seperately, since they constitute the fundamental source of higher space harmonics in any induction motor [25, 26, 33–35]. First, the unitary term expresses the permeance of the equivalent uniform air-gap as accounted for by Carter's theorem [25, 26, 33]. The second and third terms express the permeance of stator and rotor respectively accounting also for the effect of slotting [25, 34, 35]. The final term, including the two summations in multiplication, expresses the stator and rotor mutual permeance due to their electromagnetic coupling and continuous interaction by induction and reflection of quantities from one to another and vice-versa [25, 26, 33]. In the classical theory of induction machines, this is sometimes referred to as "reciprocal effect" [25]. In practical terms, a continuous injection of harmonics is taking place in the electromagnetic quantities of each motor part acting as a filtering of frequencies from one entity to the other.

Multiplying the latter equation by Λ_{g0} provides the air-gap relative permeance $\Lambda_g(\alpha,t)$ and by Eq. (2.34) one can obtain how the total magnetic flux density of the air-gap is formulated:

$$\mathrm{B}_{tot}(\alpha,t) = \mathrm{B}_s(\alpha,t) + \mathrm{B}_r(\alpha,t) + \mathrm{B}_{sat}(\alpha,t) =$$

$$= F_s(\alpha,t)\Lambda_g(\alpha,t) + F_r(\alpha,t)\Lambda_g(\alpha,t) + (F_s(\alpha,t) + F_r(\alpha,t))\Lambda_{sat} =$$

$$= \left[F_s(\alpha,t) + F_r(\alpha,t)\right]\left[\Lambda_g(\alpha,t) + \Lambda_{sat}(\alpha,t)\right] \quad , \quad (2.40)$$

$\Lambda_{sat}(\alpha,t)$ being the saturation related variation of permeance which is accounted for by its fundamental harmonic ($\nu = 1$) given from [33–35]:

$$\Lambda_{sat}(\alpha,t) = -\Lambda_{sat}\cos(2\mathrm{p}\alpha - 2\omega_s t - 2\varphi_{sat}) \quad . \quad (2.41)$$

The final form of Eq. (2.40) represents the basis formulation of a cage rotor induction machine's harmonic content by means of the fundamental quantities, thus being the stator and rotor mmf and air-gap permeance variation having accounted for the slotting and saturation effects [33–35]. However, what is of main interest is the initial form of (2.40), since the harmonic content of the air-gap magnetic field will be directly reflected in quantities of practical interest in fault diagnostics like the machine's stator current, electromagnetic torque, stray flux etc. For perspicuity, the three fields $B_s(\alpha,t)$, $B_r(\alpha,t)$ and $B_{sat}(\alpha,t)$ of the initial form of (2.40) will be separately discussed to conclude on the final harmonics included by the contribution of each component.

By [33–35], the air-gap magnetic flux density component related to the stator quantities is given from:

$$\mathrm{B}_s(\alpha,t) = F_s(\alpha,t)\Lambda_g(\alpha,t) = \Lambda_{g0}\cdot\left[\sum_{\nu=6\pm1}^{\infty} F_{m,\nu}\cos(\nu p\alpha \mp \omega_s t)\right]\Bigg($$

$$\cdot\left[\begin{array}{l} 1+\sum_{k=1}^{\infty} A_k\cos\left(kN_s\alpha\right)+\sum_{l=1}^{\infty} A_l\cos\left[lN_r\left(\alpha-\omega_r' t\right)\right]+ \\ +\frac{1}{2}\sum_{k=1}^{\infty}\sum_{l=1}^{\infty} A_k A_l\left\{\cos\left[\left(lN_r+kN_s\right)\alpha - lN_r\omega_r' t\right]+\cos\left[\left(lN_r-kN_s\right)\alpha - lN_r\omega_r' t\right]\right\} \end{array}\right]\Bigg($$

$$= \left[\Bigg(\Lambda_{g0}\sum_{\nu=6\pm1}^{\infty} F_{m,\nu}\cos(\nu p\alpha \mp \omega_s t)\right] + \left[\Bigg(\Lambda_{g0}\sum_{\nu=6\pm1}^{\infty} F_{m,\nu}\cos(\nu p\alpha \mp \omega_s t)\right]\cdot\left[\sum_{k=1}^{\infty} A_k\cos\left(kN_s\alpha\right)\right]\Bigg($$

$$+\left[\Bigg(\Lambda_{g0}\sum_{\nu=6\pm1}^{\infty} F_{m,\nu}\cos(\nu p\alpha \mp \omega_s t)\right]\cdot\left[\sum_{l=1}^{\infty} A_l\cos\left[lN_r\left(\alpha-\omega_r' t\right)\right]\right] + \left[\Bigg(\Lambda_{g0}\sum_{\nu=6\pm1}^{\infty} F_{m,\nu}\cos(\nu p\alpha \mp \omega_s t)\right]\Bigg($$

$$\cdot\left[\frac{1}{2}\sum_{k=1}^{\infty}\sum_{l=1}^{\infty} A_k A_l\left\{\cos\left[\Big(lN_r+kN_s\right)\alpha - lN_r\omega_r' t\right]+\cos\left[\Big(lN_r-kN_s\right)\alpha - lN_r\omega_r' t\right]\right\}\right]\Bigg(\quad (2.42)$$

The air-gap magnetic flux density component related to the rotor quantities is given from [33–35]:

$$\mathrm{B}_r(\alpha,t) = F_r(\alpha,t)\Lambda_g(\alpha,t) = \Lambda_{g0}\cdot\left[\sum_{\mu=1}^{\infty} F_{m,\mu}\cos(\mu \mathrm{p}\alpha \mp \omega_\mu t - \varphi_\mu)\right]\Bigg($$

$$\cdot\left[\begin{array}{l} 1+\sum_{k=1}^{\infty} A_k\cos\left(kN_s\alpha\right)+\sum_{l=1}^{\infty} A_l\cos\left[lN_r\left(\alpha-\omega_r' t\right)\right]+ \\ +\frac{1}{2}\sum_{k=1}^{\infty}\sum_{l=1}^{\infty} A_k A_l\left\{\cos\left[\left(lN_r+kN_s\right)\alpha - lN_r\omega_r' t\right]+\cos\left[\left(lN_r-kN_s\right)\alpha - lN_r\omega_r' t\right]\right\} \end{array}\right]\Bigg($$

$$= \left[\left(\Lambda_{g0} \sum_{\mu=1}^{\infty} F_{m,\mu} \cos(\mu \mathrm{p}\alpha \mp \omega_\mu t - \varphi_\mu) \right] + \left[\left(\Lambda_{g0} \sum_{\mu=1}^{\infty} F_{m,\mu} \cos(\mu \mathrm{p}\alpha \mp \omega_\mu t - \varphi_\mu) \right] \cdot \left[\sum_{k=1}^{\infty} A_k \cos(kN_s\alpha) \right] \right(+$$

$$\left[\left(\Lambda_{g0} \sum_{\mu=1}^{\infty} F_{m,\mu} \cos(\mu \mathrm{p}\alpha \mp \omega_\mu t - \varphi_\mu) \right] \cdot \left[\sum_{l=1}^{\infty} A_l \cos\left[lN_r \left(\alpha - \omega_r' t \right) \right] \right] \right(+$$

$$+ \left[\Lambda_{g0} \sum_{\mu=1}^{\infty} F_{m,\mu} \cos(\mu \mathrm{p}\alpha \mp \omega_\mu t - \varphi_\mu) \right] \left(\right.$$

$$\cdot \left[\frac{1}{2} \sum_{k=1,2,3}^{\infty} \sum_{l=1}^{\infty} A_k A_l \left\{ \cos\left[\left(lN_r + kN_s \right) \alpha - lN_r \omega_r' t \right] + \cos\left[\left(lN_r - kN_s \right) \alpha - lN_r \omega_r' t \right] \right] \right(\tag{2.43}$$

By (2.42) and (2.43), it is evident how the final sets of higher harmonics are formed by mulitplication of the mmf in each case with the permeance. In order to finalise the calculation of the total magnetic field given from (2.40), the saturation space harmonics are needed which are evident via the saturation magnetic field that is derived from development of the last term in (2.40):

$$\mathrm{B}_{sat}(\alpha,t) = (F_s + F_r)\Lambda_{sat}(\alpha,t) = -\Lambda_{sat} \cdot \cos(2\mathrm{p}\alpha - 2\omega_s t - 2\varphi_{sat}) \cdot \left[\begin{array}{l} \sum_{\nu=6\pm1}^{\infty} F_{m,\nu} \cos(\nu \mathrm{p}\alpha \mp \omega_s t) \quad + \\ \sum_{\mu=1}^{\infty} F_{m,\mu} \cos(\mu \mathrm{p}\alpha \mp \omega_\mu t - \varphi_\mu) \end{array} \right] \left(=$$

$$= -\Lambda_{sat} \cdot \left[\begin{array}{l} \cos(2\mathrm{p}\alpha - 2\omega_s t - 2\varphi_{sat}) \cdot \sum_{\nu=6\pm1}^{\infty} F_{m,\nu} \cos(\nu \mathrm{p}\alpha \mp \omega_s t) \quad + \\ \cos(2\mathrm{p}\alpha - 2\omega_s t - 2\varphi_{sat}) \cdot \sum_{\mu=1}^{\infty} F_{m,\mu} \cos(\mu \mathrm{p}\alpha \mp \omega_\mu t - \varphi_\mu) \end{array} \right] \left(=$$

$$= -\Lambda_{sat} \cdot \frac{1}{2} \cdot \left\{ \begin{array}{l} \sum_{\nu=6\pm1}^{\infty} F_{m,\nu} \left[\begin{array}{l} \cos(\nu \mathrm{p}\alpha \mp \omega_s t + 2\mathrm{p}\alpha - 2\omega_s t - 2\varphi_{sat}) + \ldots \\ \ldots + \cos(\nu \mathrm{p}\alpha \mp \omega_s t - 2\mathrm{p}\alpha + 2\omega_s t + 2\varphi_{sat}) \end{array} \right] + \\ \sum_{\mu=1}^{\infty} F_{m,\mu} \left[\begin{array}{l} \cos(\mu \mathrm{p}\alpha \mp \omega_\mu t - \varphi_\mu + 2\mathrm{p}\alpha - 2\omega_s t - \varphi_{sat}) + \ldots \\ \ldots + \cos(\mu \mathrm{p}\alpha \mp \omega_\mu t - \varphi_\mu - 2\mathrm{p}\alpha + 2\omega_s t + 2\varphi_{sat}) \end{array} \right] \end{array} \right\} \left(=$$

$$= -\Lambda_{sat} \cdot \frac{1}{2} \cdot \left\{ \left(\begin{array}{l} \sum_{\nu=6\pm1}^{\infty} F_{m,\nu} \left\{ \begin{array}{l} \cos\left[(\nu+2)\mathrm{p}\alpha - (2\omega_s \pm \omega_s)t - 2\varphi_{sat}\right] + \\ \cos\left[(\nu-2)\mathrm{p}\alpha + (2\omega_s \mp \omega_s)t + 2\varphi_{sat}\right] \end{array} \right\} + \ldots \\ \ldots + \sum_{\mu=1}^{\infty} F_{m,\mu} \left\{ \begin{array}{l} \cos\left[(\mu+2)\mathrm{p}\alpha - (2\omega_s \pm \omega_\mu)t - (\varphi + 2\varphi_{sat})\right] + \\ \cos\left[(\mu-2)\mathrm{p}\alpha + (2\omega_s \mp \omega_\mu)t - (\varphi - 2\varphi_{sat})\right] \end{array} \right\} \end{array} \right) \right\} = \tag{2.44}$$

The summation of (2.42), (2.43) and (2.44) provides the total magnetic field in the induction machine. Hence, the order of the harmonics carried in each flux density wave will be equal to the summation of each of its individual component's harmonics and the final set of harmonics carried in $\mathrm{B_{tot}}$ will be of the harmonic sets from $\mathrm{B_s}$, $\mathrm{B_r}$ and $\mathrm{B_{sat}}$. More precise, by (2.42)-(2.43), the stator, rotor and saturation related magnetic fields respectively include harmonics of the order [33–35]:

$$\left\{ \left(\begin{array}{c} \nu\mathrm{p} \\ \nu\mathrm{p} \pm kN_s \\ \nu\mathrm{p} \pm lN_r \\ \nu\mathrm{p} \pm kN_s \pm lN_r \end{array} \right), \left\{ \left(\begin{array}{c} \mu\mathrm{p} \\ \mu\mathrm{p} \pm kN_s \\ \mu\mathrm{p} \pm lN_r \\ \mu\mathrm{p} \pm kN_s \pm lN_r \end{array} \right), \left\{ \begin{array}{c} (\nu \pm 2)\mathrm{p} \\ (\mu \pm 2)\mathrm{p} \end{array} \right\} \right. \right. , \tag{2.45}$$

with $\nu = 6\kappa \pm 1$, and $\mu, \kappa, k, l \in \mathbb{N}$.

Accounting for the electrical angle $a_{el} = \mathrm{p}\alpha$, one can reform (2.45) and refer all the harmonics in each set with respect to the fundamental harmonic. This is more convenient for comparison reasons during any spectrum representation etc. The harmonic orders described by (2.45) then come in their final form as [33–35]:

$$\left\{ \left(\begin{array}{c} \nu \\ \nu \pm kN_s/\mathrm{p} \\ \nu \pm lN_r/p \\ \nu \pm kN_s/\mathrm{p} \pm lN_r/\mathrm{p} \end{array} \right), \left\{ \left(\begin{array}{c} \mu \\ \mu \pm kN_s/\mathrm{p} \\ \mu \pm lN_r/\mathrm{p} \\ \mu \pm kN_s/\mathrm{p} \pm lN_r/\mathrm{p} \end{array} \right), \left\{ \begin{array}{c} (\nu \pm 2) \\ (\mu \pm 2) \end{array} \right\} \right. \right. , \tag{2.46}$$

with $\nu = 6\kappa \pm 1$, and $\mu, \kappa, k, l \in \mathbb{N}$.

Equation (2.46) fully describes the sets of space harmonics existing fundamentally in any cage induction motor during normal operation, thus providing an analytical mapping of all harmonics carried in the total magnetic field of the machine. Some of these will be also carried in the electromagnetic quantities of the motor, providing sometimes significant diagnostic value during fault conditions.

2.2 Digital Signal Processing

To facilitate a better understanding of how harmonics such those described in previous section are visualised, assessed and interpreted in practical applications of condition monitoring & FD, this section introduces the basic fundamental theory of DSP as to how it is used in FD.

2.2.1 Signals in Time Domain

A signal in time $x(t)$ is usually acquired by a simulation dataset or by raw measurement on a system, i.e. the induction machine, and defines the waveform of the measured quantity over time (Fig. 2.4). Such signals in induction machines usually have a form like that of Eq. (2.6) including also higher harmonics. Although from the raw time representation of a signal not much information can be provided, early works in the field of electrical machine diagnosis investigated how fault conditions can be detected from anomalies in the time waveform of a signal [36–39]. The time domain representations have also proved useful for modelling purposes during fault conditions, e.g. fault-related pulsations creating harmonics of diagnostic value in the signal [8], ripples in quantities like the speed and torque [40–42] etc.

In the last decade, time-domain representations are mainly used for monitoring and fault diagnostics when the application includes aspects of the power system [7, 9]. In the latest years, some newly introduced techniques for induction machine fault diagnostics have been proposed taking advantage of tools provided during the ongoing evolution and developments in machine learning, computational algorithms, feature extraction tools, etc [43–48]. Some of these methods are based in the time domain representation of a signal for their feature extraction or metrics definition, diagnostic indices etc [46, 49], while some other indirectly consider the time-domain representation of a signal to initiate the steps of their algorithm [50, 51], or define the initial parameters for means of pattern recognition [52], spectral subtraction and estimation [53–56], frequency extraction [23] and so on.

Finally, some recently published works suggest approaches and methods that redefine and reconfide the assumptions made for stationary and non-stationary conditions during faulty operation of electrical machines or their modelling during faults [57–61]. Some works like [58] investigate the non-stationary approach during faults and propose the modulation/demodulation pattern. Other works like [62] and [63] propose approaches via analysis of the envelope of the time-waveform because it sometimes helps to better extract information about the instantaneous frequencies if the process is executed properly. Such methods are more extensively discussed in Chapter 3 with the literature review of advanced DSP used in fault diagnostics.

However, information only by a raw signal's time domain representation has the disadvantage of limitations in handling and in revealing global information about harmonics and their origin. Apart from that, the input and output signals of an induction machine system are mainly composed from sinusoids or sinusoidal-like waveforms and, for condition monitoring, their time-dependent harmonic content needs to be evaluated. Hence, the use of frequency domain and time-frequency domain representations and transformations like the ones following have been established in the field.

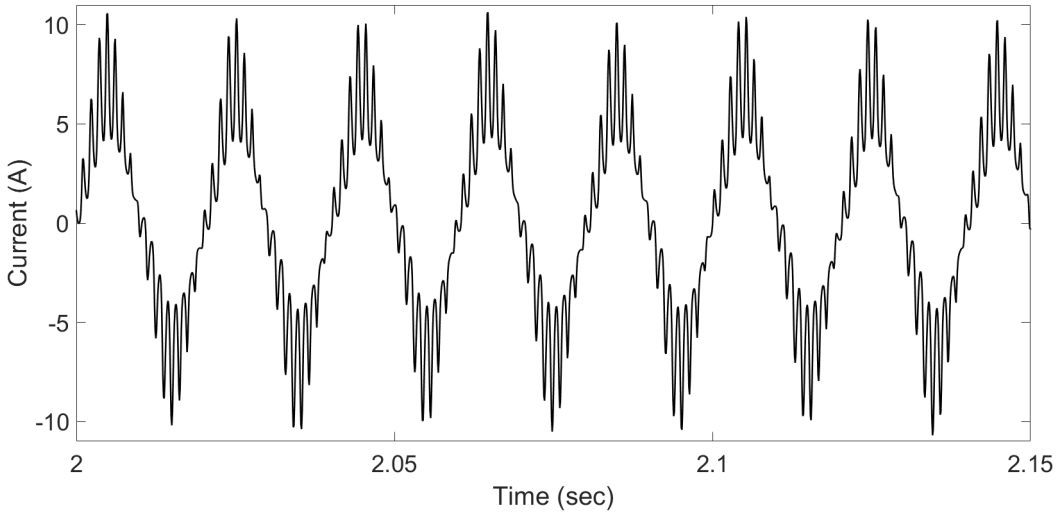

Fig. 2.4 Stator line current waveform over time

2.2.2 Signals in Frequency Domain & Fast Fourier Transform

The harmonics included in the air-gap magnetic flux density as described in Section 2.1.3 will also be carried in the signals of current and stray magnetic flux, as these are directly related with the total rotating magnetic field. In addition, these signals will be carrying time harmonics as their morphology in time is never a pure sinusoid due to the effect of space by the stator and rotor slots, number of phases and rotor bars, winding distribution etc. These harmonics are visualised and examined over frequency by means of the Fourier Transform (FT), yielding a representation of the signal in the frequency domain [7, 8]. An example of such a visualisation is given in Fig. 2.5. In other words, the Fourier transform decomposes the signal into a weighted summation of sine and cosine functions. The continuous-time Fourier Transform (CTFT) of a signal $x(t)$ is defined as [64–67]:

$$X(f) = \int_{t=-\infty}^{\infty} x(t) e^{-j2\pi ft} dt \quad , \quad f = \frac{\omega}{2\pi}. \tag{2.47}$$

In system level and practical DSP applications it is most commonly the case that sampled and discretised signals are handled, i.e. a simulation data-set or an experimentally acquired discrete sample of a signal's measurements with a sampling frequency F_s. Moreover, since the analysis of the signals in frequency domain are handled in a discrete manner, the Discrete Fourier Transform (DFT) [64–67] is utilised. Let $x[k],\ k = 0,1,\ldots,N$ be a discrete signal of N samples, acquired from a continuous signal of finite duration T_F with a sampling frequency F_s. The Discrete Fourier Transform can be defined as:

$$X[n] = \frac{1}{N}\sum_{k=0}^{N-1} x[k]e^{-j2\pi\frac{nk}{N}},\ n = 0,1,\ldots,N. \tag{2.48}$$

A natural approach to understand the DFT is that if the Fourier Transform is applied to a discrete signal and the resulting $X(f)$ is sampled every $\Delta f = \frac{F_s}{N}$, then we get equation (2.48). From this it is apparent that the quantity

$$\Delta f = \frac{1}{\Delta T} = \frac{F_s}{N}\ , \tag{2.49}$$

is defined as the frequency resolution [64–66] in the frequency domain, which expresses the localisation of the discrete frequency components in terms of accuracy for frequency separation [7, 8, 67]. From relation (2.49), it is apparent that the sampling frequency is an important system parameter for acquired signals. As an inner product transformation [64–67], practically the DFT is computed over a number of samples N by multiplication of the signal with a $N \times N$ matrix containing the primitive $n-$ th root of the unity vector matrix $e^{\frac{-j2\pi}{N}}$. This allows to unfold the frequency components over the frequency spectra and reveal information about the average spectral energy by means of amplitude spikes, usually measured in dB and normalised to the fundamental harmonic of the system (supply frequency f_s). The computational complexity of the DFT is $O(N^2)$ [68, 69], derived from the summation of operations required to produce the final transformation result. The transformation of Eq. (2.48) is derived using tools like the Fast Fourier Transform (FFT) in commercially available software packages like MatLab from Mathworks. These enhance algorithms for recursively computed DFTs in signals of smaller chunks, reducing the number of samples to the half in each repetition and hence reducing the computational complexity to $O(NlogN)$ [68, 69].

The DFT and its applications like the FFT have provided valuable results for condition monitoring and fault diagnostics since the early 90's. Its application in the stator line current has provided the traditional technique of Motor Current Signature Analysis for the detection of various types of faults [10, 11]. Also, the FFT is used for diagnostic purposes by application on stray magnetic flux signals and has yielded the topic of Stray Flux Signature

Analysis (SFSA) since the late 90's [70]. However, frequency domain transformations hold some disadvantages regarding not only frequency resolution, but also lack of competence when the application implies time-varying conditions like variable load, fault existence, variable frequency content or/and variable amplitudes, changing spectral characteristics, etc [60]. Some optimisations of the FFT and windowing functions to this direction will be discussed in later chapter. Apart from that, such transformations assume that the system's frequencies are time invariant; thus, they are limiting the application only during the steady-state time regime, where the system's frequencies have been stabilised and cannot include the transient response part [7, 69].

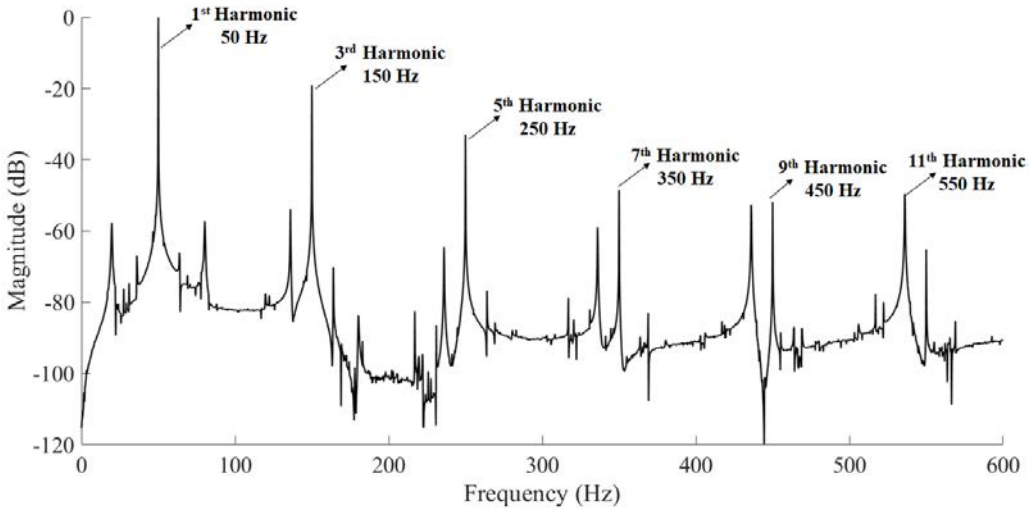

Fig. 2.5 FFT spectrum of the stator line current in an induction machine [5]

2.2.3 Time-Frequency Representations

Time-frequency ($t-f$) representations constitute an advanced signal processing approach, in terms of providing globally information about the signals spectral characteristics. These transformations expand the signal on a joint time-frequency plane, thus providing the advantage to examine the spectral energy density of a signal [59, 69, 71]. This allows the inspection of the time-varying information comprised in a signal and a global response overview. This way the transient response part of a signal -where frequency content is of a variable nature- can be included in the transformation and the harmonics are visualised as trajectories or orbits, which are drawn according to the pattern that a specific harmonic's spectral energy follows. The magnitude of each harmonic is expressed by the intensity of its energy and is usually color-coded on the plane via an intensity contour plot [59, 69, 71].

Characteristic $t-f$ representations applied in the field of induction machines condition monitoring for the detection of various types of faults include: the Short-Time Fourier Transform (STFT) [21, 72], the Wigner-Ville Distribution (WVD) [73, 74], the Wavelet Transform (WT) [75, 76], the Hilbert Transform (HT) [62, 77, 78], Multiple Signal Classification (MUSIC) [79, 80] etc. As expected, their success of application depends on the nature of the problem, i.e. the type of fault, on the frequency area aiming to provide diagnostic information (specific band of frequencies indicative for a fault), on inherent system parameters like the sampling frequency or the induction motor slip, etc. Nevertheless, they all constitute tools which in one case or the other have proved reliable and useful in CM and FD over the years. Using $t-f$ analyses, diagnostic procedures have advanced from every manner: from MCSA the field has expanded to TCSA (Transient Current Signature Analysis) [14, 81, 82]; similar approaches have been introduced and established for other types of measurements like transient responses of vibration [83, 84], stray magnetic flux [85, 86], etc. The field still advances rapidly during recent years, with methods being continuously optimised and adapted to new findings and with algorithms continuously suggested for improvement of diagnostic procedures.

Despite their facile application and sophisticated visualisation of results, $t-f$ representations are not a panacea. In other words, there might be cases where the use of $t-f$ analysis is not required, or its application yields nothing but already known results just acquired with increased computational complexity and resources. Also, a very vital part of a $t-f$ analysis is the definition of parameters, the initiation of the process and what boundaries within it can be applied, as well as how these can be optimised when something like a fault condition affects globally the set of parameters that relate with the $t-f$ process. This gap in the existing literature is discussed more extensively in Chapter 4, where the formulation of the proposed methodology is presented.

2.2.4 Short-Time Fourier Transform

The STFT is one of the basic time-frequency representations and is derived by the FFT over a sliding window, shifted in time to create overlapping chunks. The continuous-time STFT for a signal with time representation $x(t)$ is given from [71]:

$$X(t,f) = \iint_{-\infty}^{+\infty} x(\tau)w(\tau-t)\mathrm{e}^{-\mathrm{j}2\pi f\tau}\mathrm{d}\tau \quad , \tag{2.50}$$

where $w(t)$ the window function used during the transformation and $X(t,f)$ the transformed representation in the time-frequency domain. The windowing function $w(t)$ must be of unit energy to provide a unitary and adjoint vector-space for the transformation to be scattered on

its Gabor frame [71] and hence the frequency resolution (and time resolution) of the STFT are kept constant over the $t-f$ plane for windows such that:

$$\iint_{-\infty}^{\infty} |w(t)|^2 dt = 1 \tag{2.51}$$

In practice, the spectral energy density is used to visualise harmonics and evaluate them by means of the spectrogram which is defined as the squared magnitude of the signal [71, 23]:

$$S(t,f) = |X(t,f)|^2 \tag{2.52}$$

An example of spectrogram derived using the STFT analysis is shown in Fig. 2.6 for the stray flux of an induction machine used in the results chapter. As in the case of the FFT, the amplitude of the trajectories is expressed in dB or dBm and is normalised to the fundamental harmonic for comparison purposes.

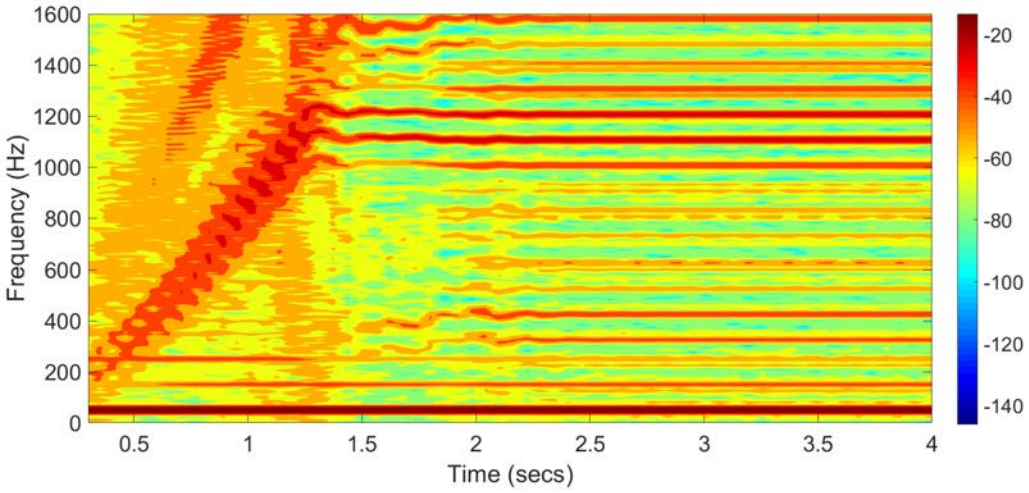

Fig. 2.6 STFT spectrogram of the stray magnetic flux in an induction machine acquired with external flux sensor [6]

As in all $t-f$ representations, the time resolution of the STFT is defined as [87]:

$$\Delta\tau = \left(\frac{\int_{-\infty}^{\infty} (\tau - \overline{\tau})^2 |w(t)|^2 d\tau}{\int_{-\infty}^{\infty} |w(t)|^2 d\tau} \right)^{\frac{1}{2}}, \tag{2.53}$$

while the frequency resolution is defined as [87]:

$$\Delta f = \left(\frac{\int_{-\infty}^{\infty} (f - \overline{f})^2 |W(f)|^2 df}{c \int_{-\infty}^{\infty} |W(f)|^2 df} \right)^{\frac{1}{2}} \tag{2.54}$$

The time and frequency resolution of the STFT are analytically discussed in Chapter 4, where its pre-setting and fine-tuning are described extensively during the initiation of the proposed methodology. This also includes a discussion on the effect of windowing regarding frequency separation during slip dependent faults.

2.3 Overview of Induction Motor Faults & Fault Diagnostics

This section provides an overview of the most frequently encountered faults in induction motors. Main focus is given on rotor faults, as the scope of the thesis is to build a diagnostic method for their reliable detection. However, for completion of the theoretical background, all other types of faults are described sententiously.

2.3.1 Stator Faults: Insulation Failures & Short-Circuits

Origin & Symptoms

Stator faults account for $30\% - 40\%$ of faults, the primary fault being short-circuits which are discerned in the following types: turn-to-turn (interturn), phase-to-phase (interphase), turn-to-ground, phase-to-ground and they occur mainly due to insulation failures [7, 8, 88]. The reasons causing insulation to fail may be of various origin: thermal stresses due to non-uniform temperature distribution, frequency variations, copper and stray losses, etc [7–9]; electrical stresses due to voltage spikes, arcs, partial discharges and others [7–9, 89]; ambient stresses due to inherent manufacturing imbalances, harsh environmental conditions, etc [7–9, 89]; mechanical stresses due to vibrations, spread forces or expansion forces caused by overheating [7–9, 89]. All these mechanisms are known as TEAM stresses (Thermal-Electrical-Ambient-Mechanical), causing insulation to degrade much faster than expected and eventually to fail [7–9, 89].

The event of a short-circuit comes with multiple consequences and symptoms. One of them is local overheating and progressive degradation of winding and insulation, which consequently leads to higher voltage stresses on the machine [7, 89]. Other repercussions are: additional harmonics in the induction machine, or globally in the system where it is connected; poor power quality; reduction of the line voltage over the power system with asymmetries in the currents and voltages; extra harmonics pulsation to the load side. If not detected, a short-circuit can lead to total destruction of the motor within a very narrow time

frame and its fatal nature makes even more challenging the detection at early stages, which is still an open question to the research community [7–9, 89].

Diagnosis

At very low levels of short-circuit between turns (within $1\% - 4\%$) the fault is very difficult to detect [7, 8]. Higher than that, due to its static nature as it exists on the stator, the short-circuit fault is usually detected using frequency domain analysis [90, 91]. The fault designates characteristic frequencies as harmonic (or spectral) signatures on the frequency spectra (or the $t - f$ plane) regardless the measurement. In the axial magnetic flux the characteristic frequency indicating the fault was originally given in [92, 93] and [94]. With the axial flux being zero in a healthy and normally operating motor, the asymmetry caused by a short-circuit is large enough to produce the signature [7]:

$$f_{sc} = \left(k \pm n \frac{1-s}{p} \right) f_s \quad , \tag{2.55}$$

k being the time-harmonic order, n the space-harmonic order of the short-circuited faulty part of the winding, s the motor slip, p the number of pole pairs and f_s the fundamental supply frequency.

Regarding the use of external flux sensors, frequency components that might alarm about the short-circuit fault arise from the following signature [7, 94]:

$$f_{sc} = \left(\gamma N_R \frac{1-s}{p} \pm \nu \right) f_s \quad , \tag{2.56}$$

ν being the time-harmonic order, N_R the number of rotor bars, $\gamma \in \mathbb{N}$. The harmonic signature carried in the stator current indicative to denote the fault existence is [7, 95]:

$$f_{sc} = \left(j_{rot} R \frac{1-s}{p} \pm 2 j_{sat} \pm i_{st} \right) f_s \quad , \tag{2.57}$$

where j_{rot}, j_{sat}, i_{rot}, i_{sat}, $k \in \mathbb{Z}$, while the subscripts st, rot, sat denote the relevance with stator, rotor or saturation respectively [7, 95]. During the steady-state all these frequencies can be looked for either with a frequency domain or $t - f$ approach. During the transient of the start-up, a frequency domain analysis is not applicable and hence patterns of the frequency trajectories are looked for using $t - f$ analysis [7, 8, 69].

2.3.2 Rotor Faults: Broken Bars & Broken End-Rings

Origin & Symptoms

Rotor faults account for a percentage of faults between 7% and 12% and usually emanate from a cracked point on the cage [7, 8, 88]. The primary reason for this fault are weak connections (joints) between the bars of the cage and its end-rings [7, 8, 69] which become even more weak during machine operation due to excessive overheating and thermal stresses. Another reason for rotor cage deficiencies are manufacturing defects like material impurities, existence of porosity (air-bubbles), the laminations' magnetic anisotropy or imperfections [96–100]. In the long term operation, all the above factors become more tangible at the presence of magnetic stresses due to magnetic forces, variable frequency content or additional harmonics (and consequent effects of magnetic saturation), local maxima of the magnetic fields at sharp edges and corners, uneven distribution of eddy-currents, etc [7, 8, 97–100]. Ambient conditions play an important role, since the rotor of a machine can develop fatigue and corrosion when exposed to harsh environments like humidity, dust, high pressures, toxic fumes etc [7, 8, 96, 97].

It is highly likely that a rotor fault will lead to direct failure of the machine as it comes with long-term consequences, that affect both the general motor's health as well as the financial costs of overall repercussions [7, 8, 69, 88, 100]. For example, a motor with one or two broken bars might seem to operate normally and not provide indications for the fault immediately; nevertheless the power factor, and consequently the power quality, will diminish [101, 102]. This will not constitute a direct safety or accident risk, but it will affect the power consumption in terms of quality, higher harmonics and losses and therefore will have a financial impact on the whole system [101–104]. The asymmetry induced by the bar breakage affects the distribution of magnetic fields, as it is interpreted by the rotor flux as an open circuit -or partial open circuit if it is cracked instead of broken. These distorted rotor fields will contribute in the production of electromagnetic torque, so essentially the torque and speed will undergo more intense ripples and eventually more noise and vibration will be present on the motor [7, 8, 69, 88, 100]. The breakages will also have an impact on the lamination material at the points where they occur. As the material undergoes thermal, mechanical and magnetic stresses, it will continue to weaken with the possibility to locally delaminate [7, 8, 96, 97]. The latter leads to the possibility of the closest bar to break, although some works reviewed in Chapter 3 have shown differently. Delaminating spots also endanger to harm the stator at extreme centrifugal forces causing dispersion of metallic powder fibres, or from small bended lamination parts that can scratch the stator teeth and winding during the rotor's rotation [10, 11, 96, 97].

Diagnosis

One of the mentioned symptoms of the broken bar or/with broken end-ring condition has proven an advocate ally and been extensively taken advantage of in fault diagnostics. The stator and rotor magnetic fields are the only two fields contributing to the production of torque and they are intercorrelated by the slip (so practically the speed). As the two fields interact, the mentioned non-uniformity and distortion of rotor flux palpitates ripples in the stator magnetic field that are consequently forced into the stator current [7, 8, 42, 88]. These will be translated as additional harmonics and will be also injected in the axial flux and the stray magnetic flux of the machine. The continuous induction between stator-rotor and the reflection of electromagnetic quantities under the broken bar fault can be considered as a reciprocal modulation/demodulation pattern [7, 8, 42, 88]. In other words, fault-related frequencies are continuously filtered from one entity to the other and, due to the nature of the pulsating ripples, frequencies arise in the current from [7, 8, 42, 69, 88]:

$$f_{brb} = \left[\frac{k}{p}(1-s) \pm s\right] f_s \quad , \quad k = 6\nu \pm 1 \quad \text{with} \quad \nu \in \mathbb{N} \tag{2.58}$$

where f_s the fundamental frequency of supply, p the number of pole pairs, s the slip and in practice all the odd harmonics are investigated except for the saturation triplets, since $k = 1,5,7,11,13...$ with $\nu \in \mathbb{N}$. The same signature is used in the parameter of the stray magnetic flux, while its harmonic content is usually acquired for diagnostic purposes by means of induced voltage captured with external or internal search coils. The mechanism of the fault frequencies genesis and their chain reaction are extensively discussed in the literature review of Chapter 3 and the methodology of Chapter 4, alongside the effect of speed-ripple and the appearance of sideband frequencies indicative for the fault given from [7, 8, 42]:

$$f_{sideband} = (1 \pm 2ms) f_s \quad , \quad m \in \mathbb{N}. \tag{2.59}$$

Over the past two decades, research on the diagnosis of rotor -as well as other- faults using external search coils has been extensively undertaken [7, 8, 69]. In parallel with the stator current, stray flux analysis has also been investigated with $t-f$ analysis over the transient [69, 85, 86, 105]. A commonly discussed pattern of rotor fault signature that a $t-f$ analysis usually aims for is the the "V-shape trajectory" written by a frequency component over the transient response of a motor's start-up [75, 106–109]. Other proposed frequency components for detection of the fault are debriefed in the literature review with the method of stray flux analysis and different ways to achieve it.

2.3.3 Bearing Faults

Origin & Symptoms

The percentage of bearing faults is 70% in low voltage machines, somewhat bigger than 40% in medium voltage machines and around 10% in high voltage machines, as the bearings are components permanently absorbing forces and vibration -sometimes even violently- during machine operation [7–9, 110]. Bearings are enhanced to assure stability, proper support and rotation of the shaft, the most established type in use being the ball bearings [110, 111]. They consist of a number of metallic spheres within a metal cage that is made of two concentric cylinders and upon which two race-ways are curved, the inner and the outer [110–112]. The main origin of bearing faults consist in magnetic and TEAM stresses, rough ambient conditions and excessive use under operation that is not always ideal [84, 110–112].

Symptoms are not evident incipiently as the fault starts from the balls or cage, where most of the forces and stresses are exerted [110, 113–115]. Consequently the material will undergo changes in its mechanical/magnetic properties and eventually the fault will propagate affecting the races [84, 112, 113, 115]. When the fault reaches a considerable severity level, inspection reveals corrosion, fatigue, cut slots of roughness or rubbing in bearing balls, cage and races. Sometimes excessive lubrication negatively affects the bearing itself and can speed up the development of the fault [72, 84, 112, 113, 115].

Diagnosis

Bearing faults are mainly detected using vibration analysis, sometimes advanced by additional noise analysis, as they are a mechanical fault with mainly mechanical aftermath [7, 8]. The mapped frequencies for bearing fault detection by vibration analysis regard a specific component of the whole bearing structure, hence there is a specific formula which will classify them either as a ball defect, cage defect, inner race or outer race fault. For specific types of bearings, approximation formulas are used. References [7, 8, 84, 110–115] discuss these aspects in deep detail.

2.3.4 Eccentricity Fault: Static & Dynamic

Origin & Symptoms

The eccentricity fault is a condition at which the rotor and stator geometrical centres have come out of their normal and concentric alignment, causing an unsymmetrical air-gap [7–9, 33, 114]. The fault mainly originates from manufacturing anomalies, and bearing faults in extreme severity. Other reasons are excessive mechanical stresses with possible partial damage during transportation or installation, from a bended shaft, from improper reinstalling after a routine maintenance or from improper coupling of the shaft with other machines and loads [7, 8, 85, 114]. There are three types of eccentricity faults namely the static, the dynamic and the mixed eccentricity [7].

Assuming the geometrical centres of stator and rotor are O_s and O_r respectively, in a healthy machine they coincide ($O_r \equiv O_s$). In the static eccentricity the axes through the centres of stator and rotor have been slightly misaligned and the rotor steadily rotates around a new point $O'_r \not\equiv O_s$. Consequently the air-gap's non-uniformity is not changing over time and the machine operates normally, hence at low levels of severity it will not be very harmful and directly evident [7, 8, 33]. Dynamic eccentricity is present when the rotor rotates around a centre O'_r changing position over time, so the air-gap non-uniformity will vary with time [7, 8, 114]. At the presence of both static and dynamic, the type of eccentricity is referred to as mixed eccentricity [7, 8]. Although it doesn't account for a large percent of faults (between 5%-7%), at extreme levels of dynamic and mixed eccentricity one risks the possibility of scratching the stator, which is harmful for the stator winding and laminations and might even destroy it irreparably. At that stage, the already eccentric rotor will also undergo further harm [7–9, 33, 85, 114].

Diagnosis

Multiple works have been published on the diagnosis of the three eccentricity types. The analysis of eccentricity related frequencies -and the tools for its diagnosis at any of its three types- require further discussion on the modelling of the equivalent air-gap magnetic resistance under different assumptions for each type. However this is considered out of scope, since the eccentricity fault is not investigated throughout this thesis. By fundamental works like [7–9, 33, 85, 114] one of the original frequencies to detect the mixed eccentricity fault is:

$$f_{ecc} = f_s \pm k f_r \quad , \quad k \in \mathbb{N} \quad \text{and} \quad f_r = \frac{1-s}{p} f_s \ . \tag{2.60}$$

2.4 Finite Element Method (FEM)

As already mentioned, the MEC approach is an efficient model of the IM during the steady state. Approaches like the analytical model, the dynamic model with Park's transformation [8], the WFA and MWFA [7] etc can include the transient response part in their analysis with satisfying results, but not always followed from accuracy [1, 7]. This is because the assumptions made in these approaches will essentially require direct simplifications or further subsequent simplification assumptions, about phenomena whose existence -regardless if directly evident or not- affects directly the operation of the IM [7]. Furthermore, a number of reasons like the geometry of the induction machine meaning the stator and rotor slot shape, edges, depth etc, the air-gap non-uniform nature and its adjustment by Carter's coefficient, the stator winding and the rotor bars spatial distribution, possible internal core material magnetic anisotropy, the internal distribution of electromagnetic fields, and many others make the induction machine a very complex device regarding analytical methods to approach a "realistic solution" [7, 8, 116–118].

Such a problem is resolved in real-life applications with numerical methods, which divide the real space in a set of finite elements and recursively solve a fundamental set of electromagnetic and motion equations, using a specific algorithm that approaches the solution under time-stepping [7, 8, 119]. That is how the FEM approach works, in addition with the fact that it provides the ability of coupling the FEA and the mechanical aspects of the problem with the electrical circuits designed by the user. It is the most popular, effective and reliable tool for modelling electrical machines in either healthy or faulty condition, providing the ability to model and simulate the operation of a machine either in 3D or 2D [7, 8]. In either case, geometrical characteristics like a non-uniform air-gap and the winding spatial distribution, electrical characteristics like the feeding supply and resistances, mechanical load coupling and material non-linearities can be accounted for [7, 8, 119].

Although the solver of a commercially available FEA software usually provides several types of analyses (Static, Time-Harmonic, Transient or Transient with Motion, etc), usually the time-stepping transient with motion is utilised for simulations regarding fault diagnostics applications and investigations [7, 8]. This type of analysis can be run in either 2D or 3D mode, however 2D is usually chosen since it provides accurate solutions and can account for some of the 3D aspects by appropriate modifications in the model. Another reason is that 3D is much more complex in design, meshing and boundary conditions; FEM is also characterised by increased computational burden both in resources and time required for 3D simulations to run [7, 8, 119].

After specifying the machine geometry, a design of the motor is made and the material characteristics are assigned for each component of the geometrical model (Fig. 2.7 a & b).

Then the electrical components are specified and all input entries for sources, resistances, coil windings etc are given in the software (Fig. 2.8). Final step before simulation is the mesh generation and the definition of mesh and re-mesh components for decimation of the space - usually in triangles (Fig. 2.7 c). This is done by a set of generic rules for the meshing according to the area of the machine and its material [7, 8, 119]. Most commonly used materials provided in a FEM software package are: copper for windings and coils, silicon steels, aluminium, air or virtual air, stainless steel and paper [7, 8]. After setting the mechanical parameters like load, torque etc, the solver then aims to approach a numerical solution for the electromagnetic problem by solving the equations in time-step for every node and loop created from the mesh. The time-stepping and the mesh are two aspects that play the most important role in the accuracy of solutions [7, 8, 119].

A series of numerical methods can be deployed to recursively solve such a problem (Euler, Range-Kutta, Gauss-Seidel, Euler-La Grange, Newotn-Raphson, etc). The most established one is the Newton-Raphson due to its fast convergence and relatively satisfying accuracy [7, 8, 119]. The solver uses the concept of the magnetic vector potential $\vec{A}$, which is calculated from the following equation as [7, 8]:

$$\nabla^2 \vec{A} = -\mu \vec{J} \quad , \quad \vec{J} = \sigma \vec{E} \tag{2.61}$$

where μ the magnetic permeability, σ the conductivity, $\vec{J}$ the current density of the input currents and $\vec{E}$ the electric field intensity. Considering Maxwell's equations, the magnetic vector potential is used to calculate the magnetic field intensity $\vec{B}$ from [7, 8]:

$$\vec{B} = \nabla \times \vec{A} \tag{2.62}$$

The general form of the final equation to be solved iteratively by the solver for the electromagnetic problem is [7, 8]:

$$\nabla \times \left(\frac{1}{\mu} \nabla \times \vec{A} \right) = J_0 - \sigma \frac{\partial \vec{A}}{\partial t} \quad , \tag{2.63}$$

where J_0 the current density of the applied stator currents and $\frac{\partial \vec{A}}{\partial t}$ the induced currents (eddy-currents). For a 2D problem, where the z axis direction of the magnetic vector potential is considered to be known, the last equation is simplified to [7, 8]:

$$-\nabla \cdot \frac{1}{\mu} \nabla A_z = J_0 - \sigma \frac{\partial A_z}{\partial t} = \frac{1}{\mu} \frac{\partial^2 A_z}{\partial x^2} + \frac{1}{\mu} \frac{\partial^2 A_z}{\partial y^2} = -J_0 + j\omega\sigma A \tag{2.64}$$

As expected, such a problem is followed by losses from the thermal and the electromagnetic point of view. It is known that these are directly related with the $B-H$ characteristic

curve, which is is in turn frequency dependent. To include such aspects in a FEM model and acquire a more accurate data set after solution of the model, FEM software packages compensate the issue with the use of Steinmetz equation [8]. This is a model which accounts by its coefficients for variable $B-H$ curve points in different frequencies to include an approximation of the aforementioned phenomena as accurately as possible in the losses calculation. Assiduous in-depth analysis regarding the implementation of numerical methods and FEM can be found in [7, 119], alongside with modelling rules for meshing and circuit modelling. More general information on FEM and how it is used to model faults can be found in [7, 8] and some of these aspects will be discussed in later chapter, where the FEM models used in this thesis will be presented. An example of a 2D FEM model pre and post simulation is shown in the following figures, where an example of the coupled MEC, the mesh generation and magnetic field spatial distribution is also shown (Fig. 2.7 d).

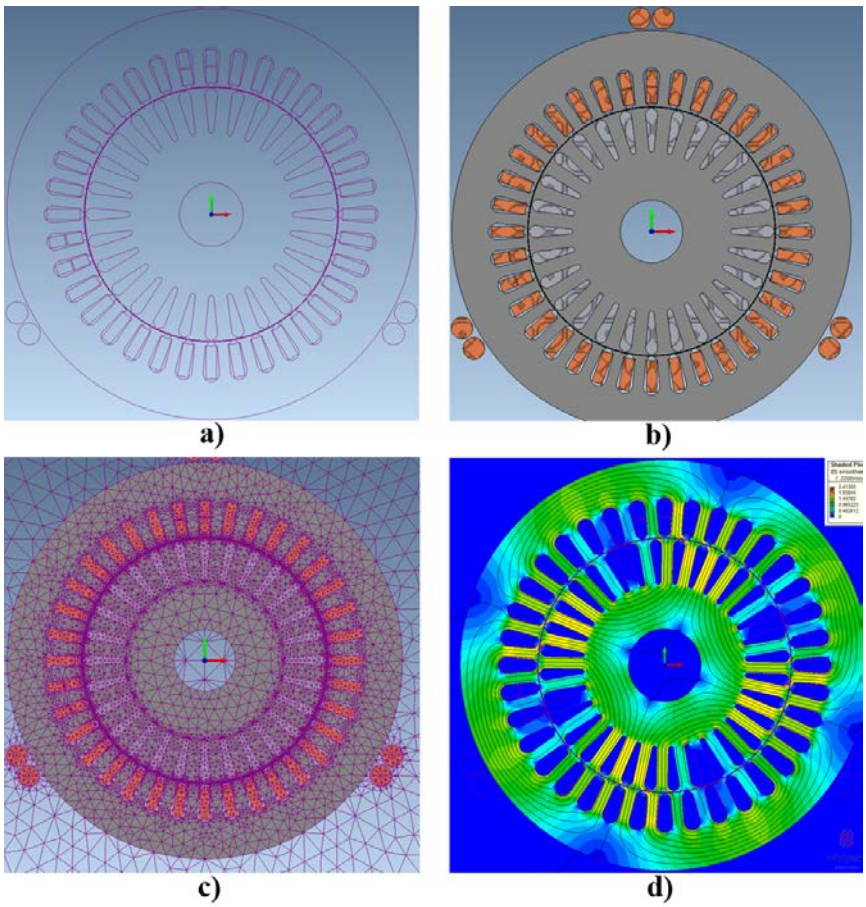

Fig. 2.7 FEM model at different stages of design and simulation

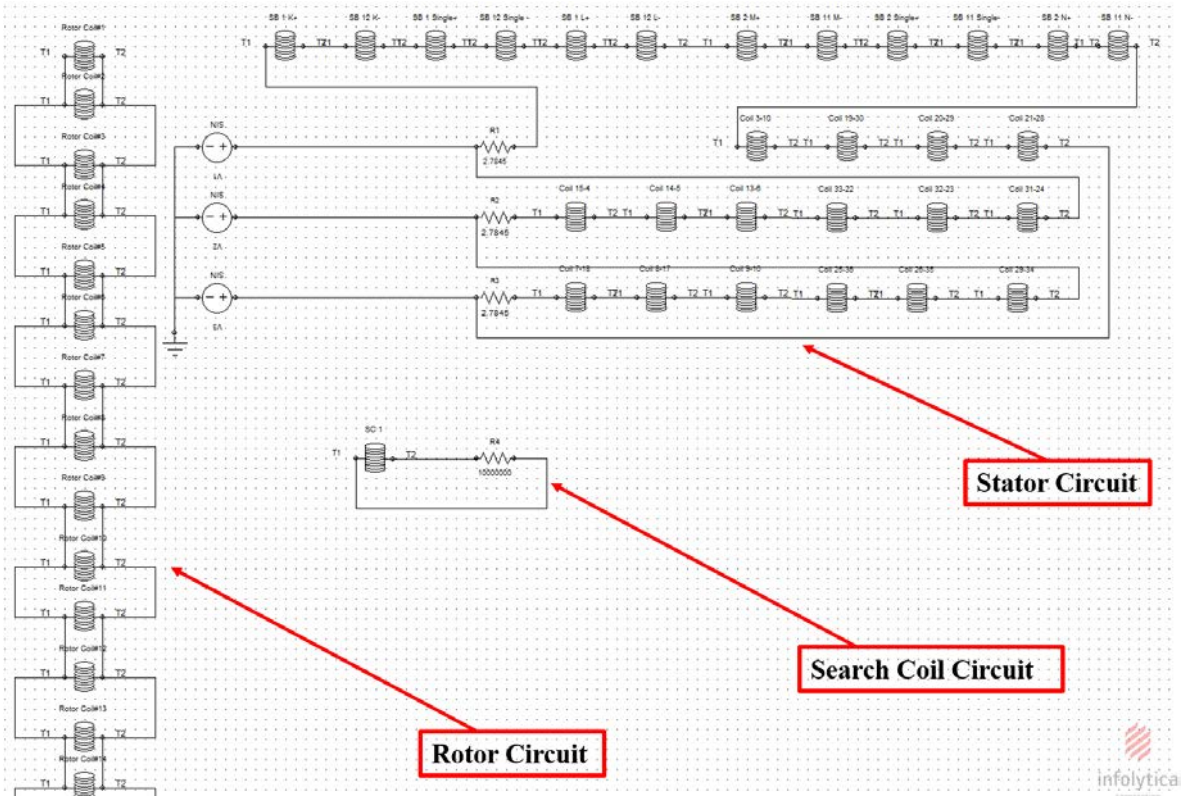

Fig. 2.8 MEC of the FEM model and its components

Chapter 3

State of The Art in Rotor Fault Detection

3.1 Applied DSP and Fault Diagnostics

Applied digital signal processing has been deployed in electrical machines condition monitoring and fault diagnosis since the 80's. During that period, the earliest and most fundamental works in the field are reported [37, 120–123]. With the means and resources provided at that time, DSP was still in its primitive form. Hence, only a steady state analysis would be included in investigations of faults and it would regard aspects of the machine performance [121], torque with power and efficiency over the steady-state speed [122], modelling and formulation approaches for current distribution and inter-bar impedance drops [123], or simply analysis of anomalies in the time-domain representation [36]. Signal anomalies over the time waveform were detected and evaluated by decimation of the time axis in small windows and by analysis of the patterns regarding maxima or spikes, harmonic distortion (THD), periodical disturbances, over-voltages or over-currents, etc.

One of the earliest works using stator current successfully for detection of bearing damage is reference [110]. Contributive works for broken bar detection using stator current monitoring are: reference [124] providing a very good explanation of the broken bar mechanisms and how they affect the inter-bar currents by means of harmonics; reference [39] explaining the effect of broken bars and broken end-rings on speed as well as torque (cogging and crawling) by time-domain analysis; and reference [41] also by time-domain analysis and by the use of a numerical model for the motor parameters. The latter two ([39], [41]) along with [40] are considered two of the most important studies in the field regarding rotor faults and detection of relevant defects by means of torque monitoring.

Characteristic works of the same era for fault detection, including also measurements of magnetic fields with the use of search coils (externally by leakage fields or internally), are found in [37, 38, 93, 125]. Apart from the fact that these works use magnetic field

measurements, except for current and torque, they also consist the first works applying frequency domain analysis with the use of the FFT alongside the time-waveform analysis. As a result, the decade of the 90's is a period during which the field of CM and FD reports significant advances by a series of works [42, 126–130]. A time-based model using magnetic coupled circuits theory and the $d-q$ transformation of the stator current is delivered by [127] with a numerical modelling approach for the equivalent motor parameters. By results from simulation datasets, abrupt changes in the mutual inductance of the examined models and small fractioned transients of the torque and speed are evaluated for diagnostic purposes on a 5 hp, 4-$pole$ IM.

Another important contribution of that early era was published in 1987 for the detection of electrical failures on three-phase induction motors by the use of Park's Vector [131, 132]. The Park's Vector Approach (PVA) was then implemented in [133], aiming for on-line diagnostics of current source inverter-fed induction machines, and in [134] for the on-line detection of air-gap eccentricities. A few years later, in 1995 and 1996, the PVA was validated successfully for rotor cage failures in induction motors [135] and for semi-converter faults in DC motor drives [136] respectively. Regarding its application for targeted rotor fault detection, it was also successfully performed in [137]. As a result, the PVA formed historically a significant tool for fault diagnostics, which is why it was proposed in 1997 as a general tool for diagnostics of general purpose, namely in electrical machines, power electronics and adjustable speed drives [138]. In 1999 and 2000, the discussed method was extended and applied for rotor cage fault diagnosis in grid-fed [139] and in voltage source inverter-fed induction motors [140], providing the Extended Park Vector Approach (EPVA). Advances in fault diagnostics regarding methods deploying the PVA and its derivatives are extensively discussed in [141].

At the same time, a very important contribution in the knowledge of rotor fault detection is formed from [42, 126, 128]. The chain reaction of harmonic signatures over the frequency spectra due to the counter rotating fields at the event of a breakage and the genesis of fault related speed-ripple effect sidebands, is analytically formulated and described in [42]. In the same work the authors define a fault severity indicator by means of a currents difference ratio during quasi steady-state operation. Then, it is shown how the fault related frequencies included in the current -and propagated by the torque and speed ripple effect- affect this ratio. The approach is then further validated in [128] experimentally on a 1.5 kW, 4-$pole$ IM, where the authors demonstrate the same method under different profiles of constant load torques. The broken bar frequencies in the terminal voltage over the low frequencies range are examined in [126] during supply disconnection, for datasets acquired both from simulation models and experimental set-up on 3 hp IM identical with the simulation model.

Moreover, a similar approach to the latter one for the detection of rotor bar and end-ring faults in adjustable speed drives is delivered by [129, 130] using FEM. These are two papers published in that period with a severe contribution in FEM for fault diagnostics, since they included ohmic and core losses in a successful model analysis with satisfying accuracy during fault conditions. They also provided a competent comparison for the method between the conditions of broken bar faults and eccentricities in IM of low power applications ($1\ hp\ -\ 2\ hp$). Finally, two important reviews which also summarise the evolution of the field for that decade can be found in [142] and [143]. The first one reviews and compares aspects of vibration and stator current monitoring by a demonstration on experimental data; the second one reviews and compares signal analysis methods deploying frequency-domain and $t-f$ spectral approaches for eccentricities, broken bars and bearing faults including load effects.

During the decade of 1999-2009, a series of publications were made available for fault diagnostics using power spectrum analysis. The instantaneous power spectral analysis was initially proposed in [144] for rotor cage fault diagnostics. A few years later, approaches in a similar context were performed for rotor cage fault diagnostics using the instantaneous non-active power signature analysis [145] and the instantaneous reactive power approach [146] for induction motor drives. The authors of the latter two works presented a similar analysis in 2007/2008 providing studies for the reliable detection of rotor cage faults by the use of the instantaneous phase-angle signature analysis [147], the instantaneous power factor approach [**?**], as well as the instantaneous-reactive-power signature analysis. Approximately half a decade later, in the years 2014 and 2016, the power spectrum analysis methods were expanded to more advanced approaches; this provided the publication of [148] which deploys the discrete wavelet transform (DWT) of the instantaneous reactive power signal for a spectral analysis under time-varying load conditions, and the publication of [149] -which uses the active and reactive power analysis- performing a spectra-based detection of rotor faults and their separation from low-frequency load torque oscillations.

There is also a plethora of research works published from the late 90's until almost the latest years in the decade of $2000-2009$, which have given rise to new approaches, have redefined assumptions on stationary/non-stationary conditions and the so called quasi-steady-state, or have even ushered new frequency bands for IM's fault detection. These approaches have paved the road for the field to advance from the year 2010 and on by integrating new hardware technologies and novel updates in DSP, regardless the acquired measurement or the fault type. They mainly include $t-f$ representations deployed for FD applications and have acted as a connecting bridge that linked the premature decade of the 90's with the millennium and made the field to what it currently is. The majority of these works is reviewed either in

the section discussing applied FD with advanced DSP, or in Chapter 4 with the formulation of the proposed methodology.

There is also a conceivable population of novel works providing successful methods for reliable diagnostics without using $t-f$ analysis. These works are not devalued by $t-f$, as they have equipped researchers with knowledge on how to proceed to further expansion of traditionally applied methods into $t-f$. Now, traditionally applied CM usually employs measurements of vibrations/noise, torque, stator current, stray magnetic flux, or a combination of these with some additional measurement as an extra prophylactic measure (e.g. thermography or infrared [20]). The scope of the work presented in this thesis is the reliable detection of rotor faults by measurements of stator currents and stray magnetic flux.

On this basis, the current section reviews the most valuable works in the field regarding the techniques of Motor Current Signature Analysis (MCSA) and Stray Flux Signature Analysis (SFSA) over the past two decades. In parallel, some works that have contributed to the expansion of the two methods using $t-f$ analysis during transients (and/or steady state) will be referred to, due to the need to cover all the recent advances and state of the art in the field. Another portion of the literature from these two decades is used thereafter to present the proposed methodology and justify its own contribution.

3.1.1 Motor Current Signature Analysis (MCSA)

There are several advantages of the stator current that have established its use in CM and FD: it can be acquired safely from a distance, as usually it is measured anyway for control and stabilisation reasons [10, 110]; unless the installation or its application is very complex, the stator current provides a non-intrusive option with relatively low complexity in interpretation [10–12]; it can be applied on-line, so the process that the machine serves can remain uninterrupted [10–13]; apart from non-intrusiveness, it is a reliable and low-cost solution [10, 13, 110]; the stator current is an electromagnetic variable of the induction motor that carries a lot of useful information for diagnostics, in terms that it relates directly with the magnetising flux of the machine and hence will reflect the reciprocal effect of the continuous stator-rotor magnetic fields interaction [88].

In the year 2001 the authors of [128] update their work of the year 2000 with further simulations and experimental measurements [150], providing some additional information on their modelling approach for the fault indicator. A similar approach is shown for discrimination of electric and magnetic asymmetries in [13], which is a work demonstrating diagnostics by means of the stator current with laboratory tests and actual on-field experiences to evaluate the effectiveness of MCSA. The study includes diagnosis on a special type of rotors referred to as "spider-structured rotors". Some deficiencies of MCSA were reported at this

point, occurring due to the special structure of some rotors like spider type rotor structures, rotors with axial cooling air-ducts etc. Such special rotor structures sometimes -or always- relinquish the diagnostic ability of MCSA, alarming for a rotor fault when the machine is healthy or masking the fault when it exists. The latter two cases are known as false-positive and false-negative MCSA respectively, hence induction motors with the discussed structures run the danger of being misdiagnosed. This fact alone was enough to form an area of research by itself, where diagnostic engineers started looking for a reliable modelling solution back in the years [151–154]. In applied fault diagnostics it is an open issue being investigated still to this day, with mainly experimental works being published from 2012 until today, using measurements mainly of current, torque or stray flux [155–161].

Meanwhile, reported cases from applications in industry are continuously published during the discussed era. The authors of [12] demonstrate the reliable detection of mechanical faults with MCSA and torque disturbances analysis in the low frequencies range for a 6 kV, 550 kW, 6-$pole$ IM used in coal mills. The authors of [11] demonstrate MCSA and propose an instrumentation for industrial applications, to reliably diagnose symptoms of eccentricity and air-gap disturbances as well as: broken rotor bar faults in a 11 kV, 1950 kW, 4-$pole$ IM used to drive the compressor for cement plant applications, where the excessive broken bar failure damaged also the stator winding due to centrifugal forces; broken bars in a cage IM (440 V, 134 kW, 4-$pole$) driving an offshore gas compressor; rotor winding failures in a wound rotor IM (575 V, 74.6 kW, 8-$pole$) driving the fan in a cement plant; and the effect of gearboxes in a 575 V, 223.8 kW, 8-$pole$ IM driving a coal crusher. Another published work with case histories from industrial environments is [10], which includes various types of applications (pumping, oil & gas, low voltage applications) for motors being diagnosed with broken bars, eccentricity and stator shorted turns. Finally, a work for diagnostics of rotor cage defects during the mentioned years is [162], which includes the effect of higher mmf harmonics during the broken bar fault in a 4-$pole$, 1.1 kW IM. The latter work is proven rather insightful, as some years later it gave birth to a very instructive publication by the same authors [163], questioning the diagnostic competence of the stator current sidebands for broken rotor bar detection at some specific locations of the fault.

To perceive and comprehend the actual need for research emerging from the aforementioned works and other relevant publications in the field, it is considered essential to hold a discussion on the broken bar fault itself. When the induction motor is healthy and under normal operation, only two magnetic fields exist fundamentally in the machine: the stator magnetic field rotating at the supply frequency f_s (fundamental) and the rotor magnetic field rotating at frequency sf_s, with s denoting the motor slip [37, 122, 124]. Now, at the event of a severe cracking in the rotor or at bar breakage, the bar is electrically discon-

nected from the rest of the cage and the point of previous connection is replaced by an open-circuit [37, 42, 122, 124]. Due to the asymmetry caused by this open-circuit at the point of breakage, the magnetic field -and consequently the stator current and the magnetic flux- will return with distorted waveforms over time [37, 122, 124]. Eventually, these distortions will be reflected in the frequency spectra (or $t-f$ spectral content) of the measured signals. Apart from that, three rotating magnetic fields exist during the fault and these come at frequencies: f_s at the stator and $\pm sf_s$ at the rotor [42, 88, 128, 164]. A simplified illustration of the magnetic fields' direction of rotation is depicted for healthy and faulty condition in Fig. 3.1 and Fig. 3.2 respectively, while Fig. 3.3 shows the distortion of the magnetic fields' spatial distribution during the fault by a FEM simulation.

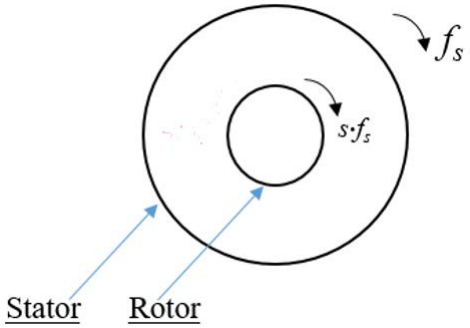

Fig. 3.1 Magnetic fields and their direction of rotation in a healthy IM

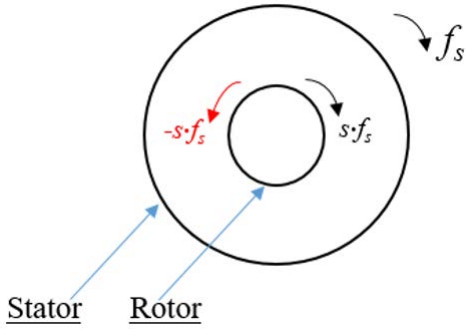

Fig. 3.2 Magnetic fields and their direction of rotation in rotor fault condition

The chain reaction of harmonic signatures over the frequency spectra due to the counter rotating field at $-sf_s$ and the genesis of fault related speed-ripple effect sidebands, is thoroughly described in [42, 88, 150, 164–166] and [167, 168]. At any case, the rotational frequency of the rotor (mechanical) is $f_{mech} = (1-s)f_s$. During a breakage the $\pm sf_s$ frequencies interact with the mechanical frequency f_{mech}, injecting the $(1-2s)f_s$ frequency in the current; this is expressed in the stator current or magnetic field spectra with a sideband component known as the left sideaband of the fundamental. Due to the speed-ripple, an additional sideband component is created at $+2sfs$ in the EMF and injected back in the magnetic field, which feeds it back in the stator current; this is known as the right sideband of the fundamental. Regarding a higher harmonic, i.e. the 5-th: the $\pm sf_s$ frequencies interact with the mechanical frequency $(5-5s)f_s$ causing two sidebands at $(5-4s)f_s$ and $(5-6s)f_s$, referred to as upper and lower respectively, and so on for every higher harmonic.

As already discussed in Chapter 2, Subsection 2.3.2, the general equation for tracking the frequency signatures induced by the broken bar fault is [167, 169–171]:

$$f_{brb} = [k(1-s) \pm s]f_s \ , \ k = 6\nu \pm 1 \quad \text{with} \quad \nu \in \mathbb{N} \ , \tag{3.1}$$

and essentially the spectrum will contain neighbouring frequencies (sidebands) which usually spike at twice the supply frequency times the slip:

$$f_{sideband} = (1 \pm 2ms) f_s \ , \ m \in \mathbb{N}. \tag{3.2}$$

Such components are detected practically near all the odd frequencies, except for the triplet harmonics which usually belong to considerations regarding saturation and some times the effect of loading. So, at the presence of rotor electrical faults like broken bars and rotor ring failures, potential frequency components preserving diagnostic information are the following: the $f_s \pm 2sf_s$, the $5f_s - 4sf_s$ & $5f_s - 6sf_s$, the $7f_s - 6sf_s$ & the $7f_s - 8sf_s$ and so on [88, 164–167, 169, 170]. The side-effects and repercussions of the fundamental harmonic's sideband at $+2sf_s$ is extensively discussed later in this chapter and is taken advantage of in the formulated methodology of Chapter 4.

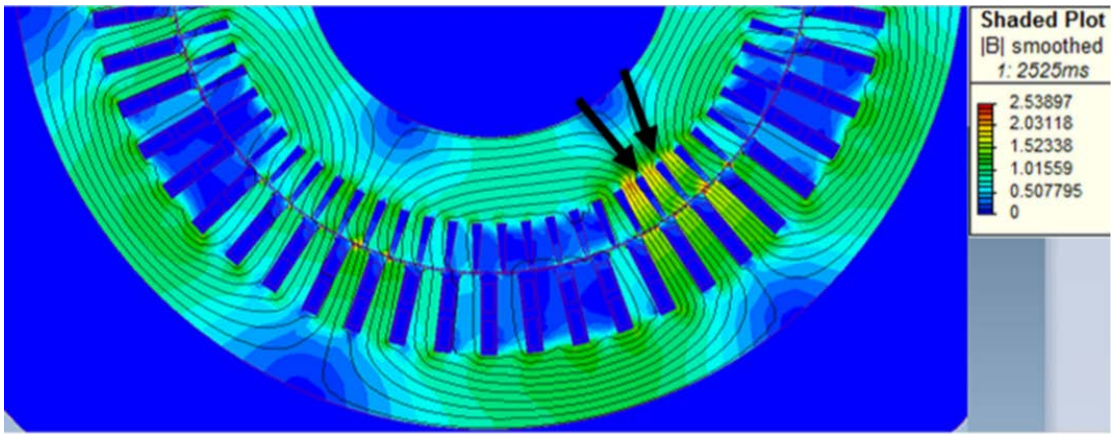

Fig. 3.3 Magnetic field local asymmetry during the broken bar fault

In the majority of works mentioned so far, traditionally applied MCSA inspects those signatures over the frequency spectra to evaluate their amplitudes. This is done under the assumption that the motor is operating at the late steady-state being healthy or at a "quasi-steady-state" mode, a term used to refer to the condition where a machine is operating steadily but its operational state is periodically disrupted by the fault-induced disturbances [42, 88, 150]. The most significant contributions in MCSA and its application for rotor fault diagnostics are seen in the following publications: the work presented in [172] validating the theoretical and experimental frequency content -by MMF with winding function approach and laboratory tests respectively- for the stator and rotor space harmonics under healthy condition, one, two, and three broken bars, examining the diagnostic potential of broken bar sidebands in the stator current up to the 7-th harmonic (3 kW, 4-$pole$ IM); with multiple experimental measurements, the work presented in [173] examines the effect of different

inertia values and torque disturbances on the current spectra and specifically the sidebands of the the fundamental frequency f_s; the publication presenting rotor condition assessment by a multi measurement approach (stator current, stray flux and vibration analysis) [18], demonstrating apart from the fundamental's f_s also the diagnostic potential of the rotor speed frequency f_r and its own sidebands for the detection of rotor faults; a device proposed for on-line MCSA monitoring using the two aforementioned frequencies sidebands is presented in [174], contributing also to the knowledge regarding eccentricity and bearing faults; the work presented by [175], which -although not using MCSA- is considered a very notable work providing a semantic global index for the broken bar fault by the instantaneous power spectrum in a 3 kW, 4-$pole$ IM.

At the early decade of 2000-2009, some very important works make their manifest regarding DSP and its application in FD, not only for IM but for fault diagnostics of all electromechanical machinery. From the DSP point of view, the works presented by [176–181] provide significant new knowledge on the analysis of non-stationary signals and exploit by what means signals during fault conditions can be approached in such a manner. The work of [181] also relates with the inclusion and use of envelope analysis as an approach in fault diagnostics. This method will later provide valuable results by [182], using the Hilbert transform and Park's transform for stator condition assessment and by the authors of [183], who provide a novel approach for monitoring the sidebands' behaviour combining the classical FFT method with phase analysis via the Hilbert Transform for broken bars. Concise works summarising the impact of this period's integration are found in [171] and [184], which provide condensed reviews with comparison of spectral methods for different faults with different measurement techniques. Likewise, the authors of [185] contribute to the detection of broken bars with a method referred to as "frequency tracking maximum covariance method", which uses the covariance to statistically calculate a windowed DFT using the rotor slot frequencies for the slip estimation (1.5 kW, 4-$pole$ IM).

As a matter of fact, the evolution mentioned by the imprint of these works justifies questions in the field as put by [163, 171] and [184] for the need of improved diagnostics by new diagnostic approaches. So the field witnesses the emergence of new diagnostic tools at these years [186–188]. Cracked beams in electromechanical devices diagnosed by the phase spectrogram is demonstrated in [186] under steady frequency and frequency excitation by sweeps. Recalling the $t-f$ transformations discussed in Chapter 2, Section 2.2, the spectrogram of the STFT as diagnostic tool is also utilised in [189] for an application regarding sensorless speed estimation by analysis of space vector amplitudes fluctuation. As will be seen in later section of this Chapter, due its low computational complexity from other $t-f$ transformations and due to the optimisation it has been applied to over the

past few years [190], the STFT spectrogram is being deployed -at least for slip dependent faults- as a useful diagnostic tool providing valuable results for rotor fault detection still to this day [22, 191, 192]. Moreover, the authors of [187] present an approach for improved monitoring by deploying the "maximum covariance frequency method" and the algorithm of the "zoom-FFT (ZFFT)" for higher resolution in selected frequency bands.

The main role of advanced DSP was to model and analyse signals of variable frequency content. Given the fact that a rotor fault signature is propagated as a modulation through the $(1-s)f_s$ fault component, the transient response regime of the motor's start-up seemed more promising as the effects of faults are more likely to be evident due to high currents, strong magnetic fields and saturation effect, torque-speed transient, etc [7–9, 193]. Compelling candidates to achieve the aims of such an analysis by modulation/demodulation patterns for a signal's frequencies classification were two types of analysis: the HT [106, 194] and the DWT [106, 188, 195]. The latter three works practically compare the two methods and their application for rotor fault detection in datasets from: experimental measurements for one partial broken bar until its total disconnection in a 4-$pole$, 2.2 kW [188]; one and two broken bars in a 4-$pole$, 1.1 kW IM [106]; for a 5.5 hp IM with one broken bar [195], where also a probability density function calculation of windowing parameters during the envelope analysis is used. The idea of HT application is also attempted for broken bar detection by analysis of the neutral voltage in [196] for broken bar detection in two low power motors, a 4-$pole$, 0.25 kW IM and a 2-$pole$, 3 kW IM.

Nevertheless, the calculation of the instantaneous frequencies required for the HT is not always an easy task to achieve in DSP, as the use of the analytic signal and derivation of the phase might affect unknown frequency content with its amplitudes and hence affect the result of the process [197, 198]. Apart from that, the concept of a signal's phase itself and the information it carries are not always veritably convenient to facilitate a deterministic and conclusive interpretation [199, 200]. For these reasons the HT was outrun by the DWT, as the DWT promises a definitive higher resolution in the frequency bands that it resolves [75, 201, 202]. Within the end of the discussed decade, the very first primitive approaches of the MUSIC algorithm are also approached for detection of rotor faults in low power IM's: by [203] using the terminal voltage's harmonics (5th, 7th, 11th, 13th, 17th, 19th) for one and two broken bars, while the same is done in a year's earlier work using stator currents by [204]. Two significant works cannot be excluded from the literature which -although don't handle rotor faults- provide useful information during this period for $t-f$ analysis using the WVD: the work of [205] for discrimination of load oscillations from eccentricity related frequency components and the work of [73] for an attempt to reliably diagnose stator winding short-circuits.

Finally, this decade finishes with a credible amount of works on which the final decade of FD (2010-2019) will be grounded on. These are considered to be condensed in the following: the work presented in [206] delivering a study of the spectral signatures in the vibration pattern and air-gap MMF distribution, by a numerical model (FEM) and by experimental measurements on a 35 kW, 4-$pole$ IM with three broken bars; the one presented in [207], which provides a pattern of study for the fundamental harmonic's left and right sidebands induced by the broken bar fault using time-stepping FEM simulations; the publication presented in [19], which uses the triple-variable measurement of currents, stray fluxes, and vibrations and -regarding MCSA and flux monitoring- it analyses sidebands around the frequency f_s, for a diagnostic strategy to detect one and two broken bars of a 1.5 kW, 4-$pole$ IM; the work of the authors in [107], which provides an insightful analysis of the modulation/demodulation mechanisms during rotor faults under time-varying condition assumptions for a 7 kW, 4-$pole$ IM validated by FEM simulations and experiments.

Reviews of the decade providing a synopsis of its main contribution up until the year of their publication are found in [88, 169] and [170], the latter two addressing the confrontation of multiple faults with MCSA and other newly introduced methods. Regarding stator current analysis from the year 2010 and on, the rest of the published works in the field are discussed in the advanced DSP approach for FD (Section 3.2.1). What is noteworthy from the comparison of methods presented in [170] and [208] is that -except for some first preliminary attempts during the 90's discussed in the beginning of this Chapter- stray flux monitoring methods are applied until the year 2009 mainly for stator faults with the frequency-domain approach, while they are not very popular for rotor faults.

3.1.2 Stray Flux Signature Analysis (SFSA)

In the very beginning of this chapter, some early research works regarding approaches from the first decades of FD (late 70's-1999) using measurements of the stray flux approach were mentioned [37, 38, 93, 125]. Being the first ones in the field, they define the basis of the SFSA methods, as mentioned however DSP was primarily developed during those years. Apart from that, the modelling of attenuated magnetic fields in the vicinity of a motor and the formulation of its harmonic signatures was also premature at that point, something also explained in [209]. As mentioned in one of the first important works of the decade, up unto that time "a model was not available and the procedure on spectral analysis was more qualitative than quantitative" [70].

Another reason for its delay in development is that stray flux monitoring required a complete exploitation and robust finalisation of the possibilities provided by the stator current; not only because the current and stray flux would provide the same harmonics [210],

but also because measurement of currents was much more simple and stabilised back then, whereas the measurement of externally radiated magnetic fields is something still being researched today. So, the main advance in IM fault diagnostics by SFSA is noted from the year 2003 and on. Due to the needs of industry however and the short background compared to the variable of stator current, the method was edged out by MCSA until almost 2010 and the published research works are not of the same population. For this reason, the time-line of SFSA is divided in two main periods: the first decade ($2003-2013$), and the works published in the last five years 2014-2019 including practically the advanced DSP for stray flux analysis.

To begin with, the basis of frequencies included in the stray flux calculated by the mmf and main air-gap fluxes was formulated in [70, 165] and [211]. In [70] the authors explain how the quantity of flux relates to the current and specifically, what frequencies are the stator and rotor currents injecting in the magnetic field that is eventually measured around the motor's periphery with a search coil by means of induced voltage. In [165] the authors propose a model which provides a 3D version of the MEC to account for the effect of axial fluxes disturbance and inter-bar currents during faults; the results of the proposed model validate experiments on a 2 hp, 6-$pole$ IM acquired with internal search coils. The formulated approach is verified experimentally up until the 19-th harmonic and then the study demonstrates the potential of SFSA for the detection of stator winding short circuits in a 11 kW, 4-$pole$ IM.

At the years 2003 and 2006, two research works are published in the field with major contribution in SFSA. They can be considered to mark the beginning of the completely non-intrusive monitoring trends by stray flux measurements, which characterise the era we are currently going through. The first one (2003) is presented in [212] and regards an experimental work validating non-intrusive monitoring with axial leakage flux measurements. The study handles mainly stator winding short-circuit faults, while diagnosis using the fundamental harmonic are studied to some extend for broken rotor bars. Also, a review of the stator and rotor induced frequencies during the named faults in the stray magnetic flux is provided. Apart from its value in stray flux diagnostics, the work delivers a review of the most commonly used types of sensors and the measurement principles for magnetic fields. The sensor deployed in the study is an "air-core flux sensor" commonly referred to as "coil-type flux sensor" [212], connected with a digitisation and amplifying system, while the SFSA is demonstrated in low and high frequencies range using FFT analysers. The work concludes that coil-type sensors are practically convenient for non-intrusive monitoring and that more reliable results are acquired with compact sensors, meaning search coils with reduced slot surface and increased number of turns. This is coherent with other works from

the same years, most of them confirming that these types of sensors render compelling results "if sized much less than the machine's height" [94], within a reel or race of small surface in order to "totally cover an area of several stator slots" [94]. At the same time, the coil must have as many turns as possible in order to amplify the magnitude of its induced voltage, without affecting high order components during the flux derivation [18, 94, 115].

The second work (2006) is presented in [213]. It explains the role of the stator winding and how -by being the stationary part- it practically acts as a search coil for the rotor-induced frequencies by asymmetries in the cage. The same principle makes the stray magnetic flux carry the same frequencies with the stator current, as the flux sensor is placed on the stator periphery and captures asymmetries in a stationary manner, similarly with the stator current carrying winding. The discussed work also includes an in-depth study using FEM and experimental set-up for various types of faults, first by classical MCSA and then by SFSA under three different measurement types. Regarding SFSA, intrusive and non intrusive measurements are acquired. The intrusive ones regard a search coil mounted around one stator tooth and then mounted around serial stator teeth, so that the mounting includes two pole pitches. The non-intrusive ones regard search coils of the air core type as described in the work of [212], placed coaxially with the machine's shaft or at the fan-drive end. Despite using the similar coaxial technique with [212], conclusions of this study regarding rotor faults summarise in the observation that the latter two techniques did not render promising results for rotor faults detection. Expectedly the vicinity points chosen for the axial leakage flux monitoring run such risks due to excessive noise and vibrations at these points, something that can affect the resonance frequencies of the sensor and interfere with additional or counter-cancelling harmonic content [18, 115, 212]. This can be further complicated if the measurement is taken in industrial environments; e.g.: in a production line with series of motors coupled, the shaft sides are not of easy access; or in power plant applications using large IM in vertical alignment and orientation, where neither of these points are accessible. However, rotor faults provide promising results with the intrusive techniques in the mentioned work, especially for the search coil mounted around a single stator tooth. This comes again in agreement with the observations from the other works of the decade regarding the coil sensor dimensionality.

In a nutshell, there are two possible positions to allocate a sensor for a stray flux measurement, the frontal and the lateral. At the frontal position the coil senses axial flux only and can measure it in two ways: the air-coil is placed coaxially to the machine shaft or around it, the latter case usually including multiple sensors placed symmetrically in quartiles. In the lateral position, the sensor accounts for pure radial or mixed axial/radial flux quantities. The first one is achieved by placement of the coil peripherally, so that its surface lies in the

machine's precinct side; the second one is measured with the sensing coil placed vertically to the machine cross-section. All the possible sensor orientations regarding radial stray flux are shown in Figure 3.4. Although in the mixed axial/radial flux measurement more signatures unfold in the spectra, either pure axial or pure radial is chosen as the frequencies have been discriminated from the works discussed in the previous and current section.

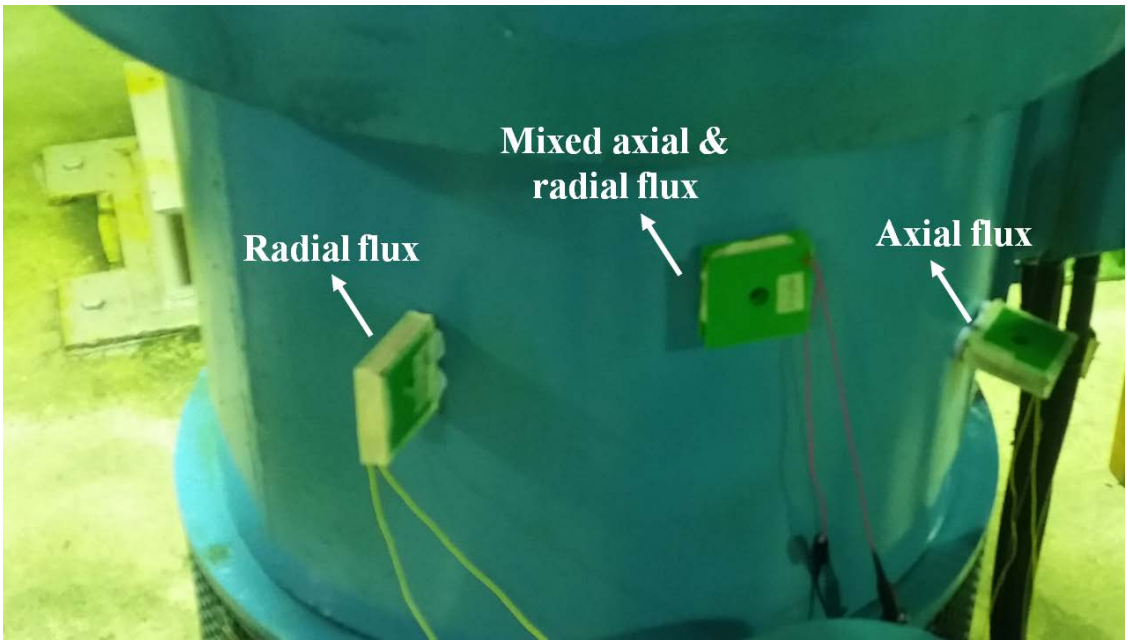

Fig. 3.4 Orientation of stray flux sensing coils

Moreover, a very important contribution in SFSA is found in [211], which is the main modelling basis of the magnetic fields radiated externally from a physical point of view. The work validates the approach experimentally and includes analysis of the rotor current distribution and rotor mmf for a 3 kW, 4-$pole$ IM; the studied faults are one broken bar and one inter-turn short-circuit. Stator short-circuit faults are also investigated in [94, 214] and [215] on the same 11 kW, 4-$pole$ IM, while the same fault and its detection are examined by internal flux sensors in [216]. The correspondence of the sidebands around the supply frequency in the spectrum of stray flux under rotor faults is researched in [217]; with only experimental approach, three different machines are tested in healthy and faulty conditions: two squirrel-cage IM (18.5 kW, 4-$pole$ and $1.1/1.8$ kW, $6/4$-$pole$) and one wound rotor IM (0.09 kW, 4-$pole$). The pair of healthy versus broken bar motor apparatus of the 18.5 kW, 4-$pole$ IM is also used in [218] for trajectory identification in signals of stray flux during supply disconnection at the medium frequency band. Lastly, SFSA is used in [219] to study the impact of gearing in an electromechanical system by monitoring two IM's it enhances,

one 4 kW, 4-$pole$ IM and one 5.5 kW, 8-$pole$ IM, and a comparison between MCSA and SFSA as media to detect rotor faults is delivered by [220].

In the years 2010-2013 there are ten works with main contribution in SFSA, handling mainly short-circuits and mechanical faults with more focus on eccentricity, while roughly five works are handling rotor faults. In 2010 a universal model framework for the theoretical calculation of the healthy magnetic field captured externally in AC machines is given, with focus in stator short-circuits for the stator of a low power IM and a synchronous generator [221]. The same authors explained in [164] the use of the rotor frequency harmonic f_r (or f_{mech}) in stray flux, when captured from the different peripheral positions by numerical simulations under eccentricity and one broken bars -the latter followed by an experiment. A similar approach but for the area of the fundamental f_s is deployed by other authors of [222] for eccentricity faults without really satisfying results; however the method is later improved in [114] with an experimental investigation of the frequency $f_s \pm f_r$ and further improvement takes place in [223], with addition in the investigation of the 5-th harmonic and the PSH. Three interesting works of those years regarding bearing fault detection with SFSA are presented in [113] and in [224] from a statistical perspective, which was later extended in [115]. Conclusive works on stator faults with frequency domain analysis of stray flux for this decade are summarised in [90, 91, 225] and [226].

With regards to rotor condition assessment, in [227] a flux-based monitoring method is proposed using a threshold for zero-crossings detection, in the flux sensed by a search-coil sensor planted internally on the stator periphery. The method is demonstrated on a 11 kW, 4-$pole$ IM with three broken bars. The rotor frequencies in the low frequency range of the flux spectrum are investigated for a broken bar fault in [166], with a study of axial and radial fluxes measured externally in different positions around the machine; the investigation includes two 4-$pole$ machines: a 4 kW and a 7.5 kW. A similar study in a more quantitative attempt for the pure radial flux is given in [228] for a 11 kW, 4-$pole$ IM and a 4 kW, 4-$pole$ IM under the effect of short-circuits and one broken bar respectively, by a quantification of the radial field's components through the air-gap permeance and mmf. Using a hall sensor planted on the stator teeth of a 42 kW, 4-$pole$ IM, the authors of [229] examine experimentally the effect of one, two, four and six broken bars -analysing the diagnostic dependence in the low frequencies range to the windowing and spectral leakage. The year of 2014 ends under two works with significance regarding air-gap flux -from the space harmonics perspective- for broken rotor bar detection, with an intrusive method for the stator and rotor fluxes [230, 231]. In [230] the applicability of the space harmonics amplitudes for the detection of eccentricity and broken bars is evaluated on a simulated 11 kW, 4-$pole$ IM; in [231] their time-dependent harmonic content is examined for eccentricity by simulation

and experimental results. All works from the year 2014 and on are discussed in the next section.

3.2 Advanced DSP and Fault Diagnostics

3.2.1 Diagnostics Using Stator Current Measurements

As already discussed in Subsection 3.1.1, some works between 2001 and 2012 had contributed in establishing advanced DSP approaches both in frequency domain and $t-f$ analysis. This section discusses the most dominant approaches of the last decade using stator current for rotor fault detection. A few works that do not handle rotor faults will only be mentioned when necessary, due to their significance regarding advanced DSP or contribution in FD. Mixed diagnosis of broken bars and eccentricity is performed in [232]. By time-stepping FEM simulations and experimental measurements regarding a 3 hp IM, the 5-th and 7-th harmonics' sidebands are evaluated after the fundamental's, alongside an examination of the PSH. The lower sideband harmonic of the stator current, and the trajectory it orbits during the transient start-up, are examined with Gabor analysis and proposed in [108] for rotor faults mixed with eccentricity in a 1.1 kW, 4-$pole$ IM. The work also explains the effect of leakage and windowing selection and the repercussions during transients of short duration. A high resolution analysis for the lower sideband by $t-f$ representation with a short-time MUSIC algorithm is presented for broken bars in [233], using spectral power density estimators.

Semantic part of the advanced approaches in the years 2011-2014 is the Hilbert Transform, although its use by now was limited to very few works. The mixed fault of broken bar and eccentricity in a 1.1 kW, 4-$pole$ IM is attempted by the Hilbert-Huang analysis in [234] with some vagueness in results. A similar approach suggesting a frequency classification criterion is provided in [235], comparing broken bar diagnosis in line-start and inverter-fed IM. The HT is used also for bearing faults during those years, with two main significant contributions in the field: the work of [236] examining the line current with the HT on two 3 kW IM, one 4-$pole$ and one 8-$pole$; the work of [237] providing one of the most novel approaches of the last years, deploying the HT and Park Vector's modulus and using a neural network for fault feature and classification, to successfully discriminate between eccentricity and bearing failures.

Other advances on mechanical faults and rotor faults detection with stator current measurements are publications [238] and [239], both works considering inverter-fed IM. The first one examines the application of the Chirplet Transform during rotor faults for scattering

on a Gabor frame the spectral content of components located in close frequency bands, while the second examined eccentricity faults with the use of an adaptive slope $t-f$ representation. Moreover, a reconfigurable monitoring device with embedded FPGA for industrial equipment diagnosis is proposed in [240] for analysis via the STFT and DWT. A similar strategy regarding the STFT and DWT is applied by the authors of [241] for a load monitoring application. The STFT spectrogram is also successfully used for detection of bearing faults and excessive lubrication forces in [72], while latest works with the Wavelet Transform for rotor fault conditions are given by [242] for a 1.1 kW, 4-$pole$ IM in operation with soft starter and in [243] for a 1 hp, 4-$pole$ IM.

During the years 2013-2018, analysis of the Zero-Sequence Current (ZSC) proved a useful complementary tool in MCSA for Δ-connected motors [244]. An experimental investigation is demonstrated in [245] for one and two broken bars, comparing the mean amplitude fluctuations for a fault severity evaluation between MCSA and ZSC. In [246] a similar comparative investigation is delivered, where the authors examine the fault severity with respect to the broken bar location, pointing out diagnostic issues arising from the non-adjacency in breakages of a 1.1 kW, 4-$pole$ IM. The ZSC is used reliably to detect rotor failures in [80] by a $t-f$ analysis using the MUSIC algorithm on a laboratory 1.1 kW, 4-$pole$ IM and on a a 1.1 MW, 6-$pole$ IM FEM model.

Another tool of complementary use for MCSA is vibration analysis as used in [247], with improved power spectral density by a high resolution buffer to acquire the vibration and current spectra. A work proving useful for transient operations is the publication of [248], formulating a diagnostic index by space vector theory under changing operating conditions in speed for wound rotors. A space vector extracted index is also formulated in [168] to discern rotor faults from torque-load oscillations. In a similar concept, a generalised scheme for quantification of the rotor fault mechanisms by an index is presented in [249] for various IM sizes aiming for improved diagnostics. The t-f representations of the STFT, DWT and WVD are applied in [109] to demonstrate the detectability of the fault imprint in the trajectory pattern using the different $t-f$ representations. Advanced DSP on the transient current using the STFT is shown in [192] for coupling imbalances and misalignment, while the recently published work in [24] demonstrates the frequency extraction process on the stator current.

In the prospect of the ongoing evolution in machine learning and data analysis techniques, intelligent tools have been deployed in the attempt to integrate diagnostics. Also, DSP tools and algorithms are being continuously optimised for a wide range of applications, including condition monitoring and FD. On this agenda, apart from the approaches mentioned so far regarding neural networks and classification algorithms, some works presenting promising results in the latest years are the following: rotor asymmetries detection by a scale invariant

$t-f$ framework using a 2-D correlation coefficient for feature extraction and wavelet analysis [250] ; a piecewise aggregate approximation algorithm with the use of the STFT and Principal Component Analysis (PCA) for definition of the healthy/faulty class and classification of the studied IM [251]; in a similar concept with the latter, the classification is performed in [252] by Empirical Mode Decomposition (EMD); PCA classification combined with intelligent icon algorithms is also examined in [253] for classification of motors from different applications; the accuracy in classification by different classification algorithms is compared in [254] for rotor faults in inverted-fed IM; fault-indicative harmonic features extracted using Pearson's correlation coefficient are used in [255] to train machine learning classifiers for inverter-fed IM; wavelet analysis regarding the frequency content and statistical means regarding quality control charts are deployed in [256], which compares robust and non-robust tools applied within a threshold of tolerance to examine fault alarm levels for broken bars, bearing and eccentricity faults, while the method's validity is confirmed via the application on IM fed from different inverter sources .

Finally, some industrial case histories reported over the last five years are presented in [14, 15] and [16]. The first one applies current analysis ("Advanced Transient Current Signature Analysis - ATCSA") using DWT decomposition for IM used in petrochemical plants by an amplitude indicator [14]. For similar applications, the second one performs ATCSA with the STFT analyses and frequency domain approach [15]. The last one presents the monitoring of 6.6 kV IM used for pumping applications in a hydro-electric power plant and investigates the diagnostic potential of the $f_s \pm f_r$ frequency in the stator current and stray flux, concluding that combination of MCSA and SFSA equips a user with robust diagnostic means, as potential sensitive frequencies in the one variable might be immune in the other. Reviews denoting -up unto their publication year- the works with the most marginal contribution and a comparison of MCSA with t-f during transient can be found in references [208, 257] and [258], which provide a complete state of the art in the field for the era.

3.2.2 Diagnostics Using Stray Flux Measurements

As described, by the year 2018 stator current analysis had been exploited by all means to a determinant maxima. By that time, deficiencies of the technique had been as well documented and reported from all perspectives: false/negative and false/positive outcomes, special rotor designs, combination of rotor faults leading to more complex problems for challenging diagnostics, non-stationary conditions, manufacturing defects amplifying all these problems, and so on. As a result, stator current monitoring was saturated from the FD point of view, so research works started diminishing and most comprehensive diagnostics

related to stator current would regard methods using advanced DSP or machine learning tools.

At the same time, the stray flux methods were -and still are- rendering valuable results, either on their own or as an additive technique to cases of MCSA weaknesses and failures. There are several advantages of stray flux monitoring that have made it a favourable diagnostic tool for electrical machines: the non-intrusive nature, the fact that it is independent from the number of poles, it provides a mapping of same or similar frequencies with the stator current, it constitutes a low-cost monitoring solution with relatively facile implementation, etc. Among some fundamental works comparing stator current analysis and stray flux analysis for FD it is elaborated that: "the stator current gives information about power supply and rotor cage structure and the rotor current gives information about stator coils" [70], however "a search coil located outside the IM gives information about all IM electrical phenomena" [70]; although current measurement is to some extend also non-intrusive, sometimes "in the real world the measurement of the current in one phase of the stator and its transformation in the frequency domain is not always possible, since often the winding of one phase cannot be accessible" [90]; whereas "stray flux analysis is expected to convey the same information that can be obtained by conventional current analysis" [90].

The above facts have brought stray flux monitoring to the epicenter of FD over the past five years [259]. In [260] it is applied with vibration analysis to detect stator winding faults, while short-circuit detection at different load levels is also evaluated in [261] by an improved diagnostic system embedding Emerson flux coils in a 1.5 kW, 4-$pole$ IM. An IM of the same power rating and pole pairs is used in [262] for a comprehensive review of the short-circuit detection frequencies in axial flux; and a similar analysis is delivered in [263] for the radial flux in a 1 hp, 4-$pole$ IM. A publication examining stator faults at the levels of 5% and 10% with the stray flux by advanced diagnostic means is presented in [264]. The work uses wavelet analysis in inverter-fed IM and compares the results acquired with an Emerson coil and a custom in-house built search coil. An advanced framework for improved diagnostics of stator inter-turn faults is also provided by the authors of [265] with internal flux measurement, studying the impact of coil pitching in the space distribution of the air-gap magnetic flux for large induction motors. Finally, a novel work studying inter-turn short-circuits by stray flux monitoring was recently published in [266] for induction motors and synchronous machines. The novelty lays within the use of correlation analysis between harmonics of the stray flux acquired from two individual sensors, placed diametrically on the machine periphery.

The comparison between Emerson coils and custom flux coils is also demonstrated in [267] for rolling bearing element faults in a 2.2 kW, 2-$pole$ IM. The eccentricity mechanical fault is studied in [268] via the space and time harmonics in the main air-gap flux,

acquired with an internal sensor in a 11 kW, 4-$pole$ IM by simulations and experiments. Other publications regarding mechanical faults are [269] and [270]. The first one evaluates the 1st, 5th and 7th harmonics, as well as the 1st and 2nd PSH for an experimental study of the eccentricity fault in inverter-fed IM, comparing MCSA and SFSA in a specific type of machines. The latter presents an experimental investigation for the same fault in a 1 kW, 4-$pole$ IM. Mechanical aspects by a model-based approach including both simulations and experiments are studied in [271]. The work applies classical control theory and transfer function concepts combined with $t-f$ analysis for monitoring the condition of loading and its effects on the acquired stray flux signals.

A series of works handling stray flux analysis have been published over the last four years with an added value to FD and rotor faults. To begin with, electromagnetic fields are resolved in a generalised framework using demodulation analysis for the detection of dynamic eccentricity and shaft oscillations in [272]. Intrusive monitoring using a growler apparatus and magnetic films for detection of rotor damages is applied in [273]. Other research works with intrusive monitoring are presented in [167, 265] and [274]. Advanced diagnostics aiming for rotor fault detection are applied in [265] using the space harmonics of a 11 kW, 4-$pole$ IM with one broken bar at different load levels. The work is expanded by the same authors two years later in 2018, with the use of the differential air-gap flux between two poles and a spreading of its frequency content on a $t-f$ frame. With the same method of differential flux, experimental validation for eccentricity, broken bars and short-circuits is performed in [167] to evaluate the dependencies of space and time harmonics and their diagnostic capability. Classical SFSA is compared with MCSA by FEM and experimental work in [275] for one broken bar and for two different double bar breakage scenarios, adjacent and opposite located.

Despite the fact that internal flux sensors provide robust results for the main air-gap flux, as they are planted inside the machine and very close to the air-gap, intrusive methods demand to disassemble the IM and place the sensors internally or mount them around a stator area. Not really a convenient case, for it is a time consuming process and users always run the possibility to grant the motor with inherent defects during the process of reassembling. Therefore, non-intrusive monitoring of stray flux has been established as a dominant approach during the past three years. The known chain reaction of the speed ripple frequency components induced by bar breakages are elaborated on by FEM and experimental measurements in [276], where a fluxgate sensor is used on a 2.2 kW, 4-$pole$ IM. The same authors demonstrate their method in [277] for the same experiment apparatus and simulation model but with the fluxgate sensor at two different positions on the machine frame, to separate the low frequency load oscillations from the broken bar induced low

frequency components. Two different sensor positions are also examined in [85] to evaluate the detectability of high eccentricity level and two broken bars in a 1.1 kW, 4-$pole$ IM, using STFT analysis and wavelet decomposition with a wavelet indicator for determination of the fault severity. The same analysis for detectability of rotor faults during transient is performed in [105] for a 1.1 kW, 4-$pole$ IM, examining the impact of adjacent and non-adjacent broken bars on the severity indicator. A mixed case of electromechanical faults are examined on the same basis under three different sensor positions in [86] using the STFT and DWT analyses. Extraction of the amplitude information in a two-stage manner with application of the STFT analyses and then the classical FFT is implemented in [22]. A combination of adjacent and non-adjacent broken bars is assessed using radial stray flux signals from FEM simulations, to evaluate the detectability of the fault in a 1.1 MW, 6-$pole$ IM. The method is further validated with experimental measurements in [23], where the successful detection of non-adjacent broken bars is achieved in the same FEM motor and a laboratory scale IM (1.1 kW, 4-$pole$ IM). Finally, a work presenting a novel approach using stray flux was published very recently in [278], proposing the detection of rotor electrical faults with the use of the Zero Sequence Flux (ZSF). The novelty of the method lays within the use of three individual sensors, capturing stray fluxes at 120° angle difference to acquire by post processing the Zero-Sequence Flux signal for harmonic analysis.

3.3 The Problem of Adjacent and Non-Adjacent Broken Rotor Bars

The extensive research undertaken for broken rotor bars over the past twenty years shows that although the problem does not account for a large percentage amongst faults, its incipient state does not necessarily create large asymmetries and is therefore rarely spotted [246, 279]. As a result, the fault and its undesired physical mechanisms evolve undetected and propagate to a terminal stage, whereas the machine indicates a seemingly normal operation. At that stage, damages in the rotor are extended and very hard to repair in maintenance [96, 279]. Hence, the rotor service or replacement will amount to costs that equate with extreme financial losses affecting the supplier, the distribution network and the end users [96, 279].

On the other hand, there is a series of factors with vital, and sometimes dominant role, regarding how this specific type of fault will evolve: the rotor design and constructional aspects [13, 155, 156]; general manufacturing asymmetries [97, 129], or porosity (air-bubbles) in the rotor core [98]; material defects like magnetic anisotropy [99] and/or inherent local deformations [100]; partial discharges and/or TEAM stresses [89]; and so on. All

the mentioned aspects however cannot be predicted and modelled, except from created case-scenarios in order to study the effects of such phenomena on the hypothetical basis that some of them -or a combination- will exist. One way or the other, all these factors will determine the fault evolution and the flow sequence of the breakages.

What usually happens is that the open-circuit induced by a bar breakage will directly affect the two neighbouring bars, for the flow of inter-bar and eddy-currents will distribute in the closest paths available [280]. Consequently, additional electrical and thermal stresses will be exerted on those bars diminishing the robustness of their material properties; hence, they are expected to crack and break [280]. For this reason, works of major contribution to the effect of the broken bars population has been undertaken with FEM for multiple breakage scenarios randomly distributed in [281], with multi-variable measurement techniques (current, speed & torque) for multiple consecutive breakages [280], with advanced techniques for frequency and amplitude tracking [282], and so on. Nevertheless, it has been shown in various works that it is not always the case for the cage bars to break in a sequential mode [246, 279, 283–285]. For a series of known and unknown reasons, frequent cases have been reported where bars do not break in a consecutive pattern [246, 279, 283]. This happens mainly in large industrial machines, but manufacturing defects that "spread randomly" [246, 286] can be the motif for such a mechanism to arise in smaller scale IM as well [279]. This designates an even more challenging problem in FD, the detection of non-adjacent broken bars. As mentioned in one of the works published in 2016, "the reliable diagnostic of non-adjacent bar breakages in induction motors is still an unsolved industrial problem" [286]. Such cases make up a diagnostic challenge, as the location of such non-consecutive breakages might deflect the asymmetries and the anomalies that can reveal the indication of the fault.

A practical example by visual demonstration of the problem is shown in Figure 3.5. The graph depicts a comparative FFT of the stray flux in different broken bar scenarios, adjacent and non-adjacent, from one of the FEM models used in later chapters for simulation purposes. The broken bar sideband frequencies used for the detection of the fault at the quasi-steady-state mode are not always of resolute ability to reveal the fault. More specifically, the spectrum signatures around the area of the fundamental harmonic behave in a somehow random and unpredicted pattern: at the $-4sf_s$ and $+2sf_s$ sidebands, the adjacent broken bar scenario shows a signature of highest amplitude (red spectrum) compared to all the other cases, because the fault is intensively localised at a point of double breakage over the rotor surface, arising from two consecutive breaking points -and hence the magnetic field local asymmetry radiated from the rotor magnetic field through the air gap to the stator and then further to stray fields out of the frame will be larger; the first non-adjacent broken bar scenario (black line spectrum) regards two broken bars at half pole-pitch distance and the examined

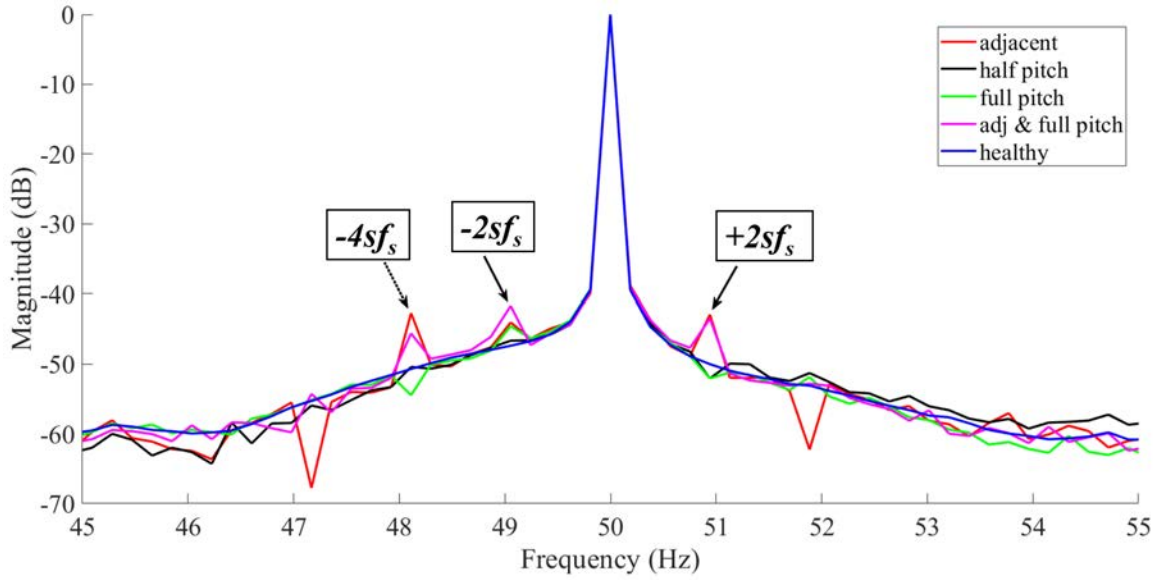

Fig. 3.5 Comparative FFT spectrum of different broken bar scenarios

sidebands significantly drop at every frequency, indicating a healthy spectrum (danger of false-negative misdiagnosis), whilst this issue could deflect and mask the asymmetry even further if the problem of spectral leakage would be present at the FFT extraction; the second non-adjacent scenario -at one complete pole-pitch distance (green)- rises slightly lower than the amplitudes risen by the two adjacent broken bars regarding the $-2sf_s$ sideband, however it behaves similarly with the half-pitch scenario regarding the other two sidebands endangering false-negative diagnosis; the third broken bar case, combining a mixed fault scenario of adjacent and non-adjacent breakages, is getting masked indicating an adjacent scenario (purple-dashed).

An example of the magnetic field local asymmetry at specific time instants during the simulation are shown in Figure 3.6; the adjacent broken bar scenario (left) presents a tangible local asymmetry, while the half-pitch breakage distance (middle) and the full-pitch one (right) express a weak local asymmetry in the magnetic field distribution. There can be time instants where the rotating fields will not mask their asymmetry and will locally spike or be visually seen, when screened through a simulation software; however, whether this asymmetry will be reflected or not on a stationary flux sensor, or superimposed with other asymmetries, or attenuated through the air gap to the stator winding (that acts for stator current measurements in a similar manner with a stationary field sensor), is unknown. And so is the evolution of the fault progression, especially if a real world application is considered. The described problem becomes even more complex for large industrial motors, for rotors where bars are manually placed and not melted in by casting, for rotors of special construction like spider or ducted

rotors, for rotors being recursively maintained and replaced back in the stator as the whole process might introduce inherent imbalances, for rotor operating in harsh conditions, for frequent start-ups, and so on.

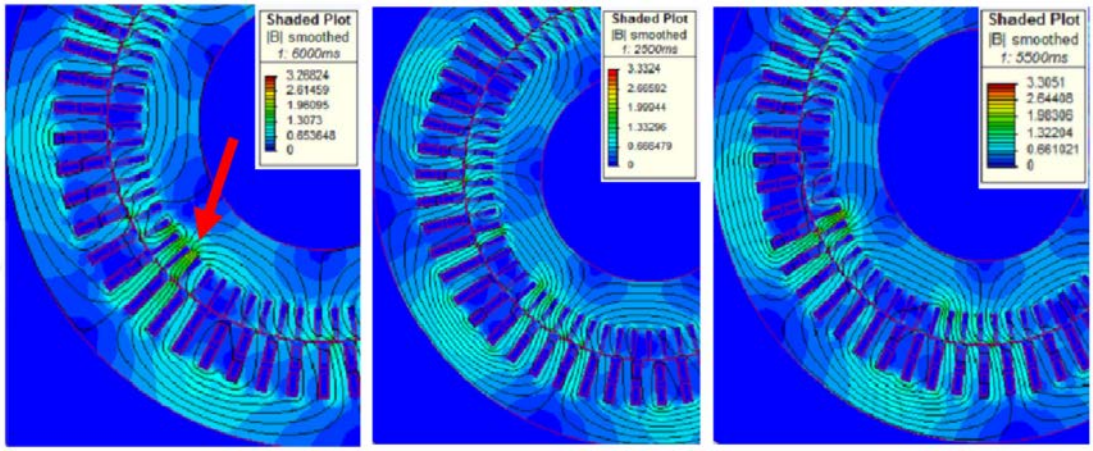

Fig. 3.6 Magnetic field spatial distribution at the presence of adjacent and non-adjacent broken bars

A small population of research works have conducted investigations on the influence of all these phenomena regarding fault diagnostics. The majority of this literature was published after 2006/2007, which is when the issue was put under the scope for two reasons: it was no frequently encountered and hence not often reported until that time, considering reported case-studies from industrial on-site experiences, except for some rotors with special structure [13, 155, 156]; however, more recent studies and experimental cases from on-sites more and more frequently report such cases, as explained in works like [246, 279, 283, 286]; another reason is the lack of knowledge regarding the actual formulation and modelling of the mechanisms during non-adjacency and its propagation, something that was for the first time given during 2007-2009 from works like [284] and [285] experimentally; and from works like [100] on a theoretical framework, the latter leading to the later publication of [283] in 2009 using a simplified 8-bar-rotor model and a MEC representation. The research question was firstly put in [163], a work examining the problem of non-adjacent broken bars at various locations, proving the monitoring of the fundamental's sidebands via MCSA not reliable for the majority of the studied cases.

Considering the distribution of the already discussed literature, the main research on the matter has been undertaken using stator current measurements. In the recent years, current analysis using advanced DSP has been applied to some extent, while some promising results are very lately given from stray flux analysis. In particular, the work presented in [284] approaches the problem with a multiple coupled MEC accounting for the motion equation at steady state; then experimentally, the changes awaited in the calculated model parameters

are verified on a 1.1 kW, 2-$pole$ IM with broken bars spaced at different angles inside the pitch, and the fundamental harmonic lower and upper sidebands are examined in the stator current by the classical FFT. The work shows that, depending on the examined angle between breakages, both the left and the right sideband behaviours alter in amplitude without a distinct pattern or monotony. The same theoretical model of analysis and experimental rig are used in [285] for a simultaneous study of the breakages location and the effect of load, whose pulsations obscured the complex phenomena and their impact on the spectra even more. One, two, three and pairs of adjacent broken bars planted non-adjacently from each other and spread randomly around the cage are examined by multiple FEM models in [281], which examined the $1 \pm 2sf_s$ and $1 \pm 4sf_s$ components in the stator line current for a 4-$pole$, 3 hp IM model.

A fundamental research work dealing with the problem in an abstract way comes in [283], which denotes the deficiencies of classical methods like MCSA [246] and the Vienna monitoring method [287] to detect non-adjacent breakages. With a simplified model of a 8-bar cage and a MEC representation, the authors explain how the asymmetries -that spring from dislocation of the symmetry axes in current sheet and mmf- can mask the fault. Then, they distinguish the locations of breakages that are endangering the diagnosis: the diagnosis could state the machine as healthy at half pole pitch breakage distance ($\pi/2$ electrical radians), something that was also explained in [171] theoretically and shown in [246] experimentally for 1.1 kW, 4-$pole$ IM rotors. At a full pitch spatial separation (π electrical radians) the fault frequencies rise back indicating a case of adjacent broken bars or a single breakage, something that runs an additive danger of being overlapped and obscured by the fundamental harmonic through spectral leakage overlap if the machine is characterised from high inertia or very low value of slip ($s\%$) [22, 280, 283]. However, even if the examined fault frequency remains intact in the latter case, the theoretical model used to explain these mechanisms in [100] and [283] regards a cage with 8 bars (or 16 bars like the ones in [284] and [285]). In actual cases reported from industry like [13, 14] and [156] -where special construction rotors or rotors used in harsh environments were examined- it has been seen and proved otherwise, as the visual inspection of rotors revealed breakages at such locations, whilst the frequency spectra indicated no fault. The work of [283] compares the classical MCSA with an alternative method called "Magnetic Field Pendulous Oscillation (MFPO)", which was proposed in [288] and [289] and was applied in [290] successfully for broken bars and some levels of inter-turn faults. The advantage of the method compared to MCSA is the extraction of information about the angle swing between the original symmetry axes of the magnetic field space vectors and the shifted ones during a fault condition. Examination of the $1 \pm 2sf_s$ and $1 \pm 4sf_s$ components allows the authors to take advantage of some additional "secondary

saturation effects" [283] for diagnosis. However, deficiencies during multiple breakages like three broken bars, each at distance half pitch from the other, still remained and the problem is still pointed out both from FEM approaches [291] and from experimental [246, 286], or from industrial experiences [14, 15].

The influence of non-consecutive broken bars has also been examined with FEM in [291] for one, two and three broken bars distributed randomly over the rotor cage. The work studies seven different FEM models with broken bars to examine the $1 \pm 2sf_s$ frequencies and their amplitudes' unexpected behaviours for a 1.1 kW, 4-$pole$ IM. The phenomenon of non-adjacency is then studied in [96] for different supply conditions for a 1.1 kW, 4-$pole$ IM spaced at half pole pitch. An experimental investigation comparing MCSA and ZSC methods at 1.1 kW, 4-$pole$ IM for the problem is given in [246], while the work is expanded in [286] to provide a reliable indicator for some adjacent cases with the use of the "Filtered Park Vector Approach (FPVA)" [132, 135] and the "Filtered Extended Park Vector Approach (FEPVA)" [139, 292]. Over the past two years (2017-2019), the problem of non-adjacent broken bars is being looked into with stray flux methods. The works of [85] and [105] described in the literature of advanced SFSA (Section 3.2.2) are characteristic works examining the problem with DWT and STFT analyses. Also, the work presented in [86] which applies extraction of the amplitude information for mixed rotor faults and eccentricities. Finally, the discussed problem is confronted with a reliable solution presented in [22] by FEM for a large industrial 1.1 MW, 6-$pole$ IM; the work is extended later in [23] to validate the method experimentally for 1.1 kW, 4-$pole$ IM, where the method is proved immune to inherent manufacturing defects and asymmetries. A demonstration of the DSP implementation of the frequency extraction method shown in the latter work by FEM and experimental approach, is then presented in [24] using stator current measurements on a 4 kW, 4-$pole$ IM.

3.4 The Problem of Parameter Setting for FD Applications

By the theoretical background of Chapter 2 and the literature presented so far, it is seen that various DSP approaches have been implemented in FD throughout the decades. The main reasons are the advances in DSP over the past two decades, as well as the fact that -regardless the diagnostic technique and measurement- with every different DSP approach a different outcome might be provided [21, 69, 185]. The use of $t-f$ approaches like the STFT and the Wavelet analyses have provided the field of FD with a significant advantage: the ability to properly monitor transient phenomena, meaning time-varying and/or non-stationary conditions of operation, or changing frequency content at steady-state due to faults

existence [21, 107, 208, 293]. Indeed the application of $t-f$ analyses during the transient start-up of IM has utterly contributed to model some fault aspects, like the commonly known "pattern of V-shape" which denotes the orbit of a frequency trajectory at the presence of a broken bar fault [75, 106–109]. However, during the problem of multiple adjacent or non-adjacent broken bars multiple V-shaped trajectories are curved on the $t-f$ plane, from each broken bar induced spatial asymmetry locally in the IM magnetic fields [6, 14, 15]. In such cases, the trajectory patterns might overlap in time and frequency step and spread obscurity on the $t-f$ plane, depending on the frequency resolution used and on the motor's slip s, that is practically an inherent system parameter [6, 21, 75, 107, 280].

The fact that the inherent system parameter of slip affects a diagnostic process for rotor faults, has raised questions on whether one specific $t-f$ analysis is enough to represent and map all investigated aspects of a fault [21, 171]. On the one hand, targeted $t-f$ analysis of high resolution provides satisfactory results under specific frequency areas and, if tuned by the appropriate parameters, it can conveniently detect the fault induced oscillating frequencies of that area given a reasonably long transient response to acquire samples; on the other hand, if the transient response is of short duration, the $t-f$ analysis might not be advocate enough due to the samples limitation and impairment of the frequency resolution [21, 69, 171]. The apt tuning of parameters for an advocate $t-f$ analysis is somewhat arbitrary and is usually chosen by the user's experience or by trial and error [21, 69, 171, 294]. Especially when an FD application like rotor faults is considered, the trial and error option is sometimes the only one as the pre-setting and fine tuning will definitely depend on the slip and hence potentially on the inherent imbalances and defects, that can indirectly affect the rotor parameters and consequently the slip [21, 69, 108, 109].

Issues like the discussed have given birth to publications that handle the optimality of $t-f$ analysis from the DSP point of view, accounting for such aspects and for implementation in various applications. Early works in DSP like [295, 296] have studied the effect of windows on Fourier-based transformations. A similar individual work for the behaviour of the local bandwidth and optimal windowing functions for the STFT is found in [297]. In the most recent years modern research works examine approaches for: setting of parameters in deployed $t-f$ analysis and their fine tuning [87, 294]; optimal windowing for robust $t-f$ analysis [298–300]; improvement of resolution [190, 301, 302]; adaptivity of transformations [50, 239, 302]; and other abstract approaches for applications oriented from engineering [303–305] to economics [87, 306] and from geological applications [307] to biomedical and health sciences [308–310].

Regarding FD targeted to rotor fault detection, in the majority of the existing literature $t-f$ analysis is applied over the transient response [75, 85, 108, 192, 200]. The main reasons

are the dynamic nature of the transient start-up interning variable frequency content, and the distinctive patterns that can be marked upon the $t-f$ plane to indicate a fault. Nevertheless, despite the fact that FD during the transient start-up is novel and has provided reliable results, the setting of parameters becomes even more challenging and vague [21, 69, 87, 108]. Besides, it is usually the steady-state response where condition monitoring is applied in practice. Except for applications with frequent start-ups (drilling, mining, mobility, etc), induction motors in industrial processes with major production lines, power generation and conversion, or stable transportation, are mainly operating at fixed speed and being monitored in the steady state [21, 311, 312]. The advantage of monitoring signals of the IM in the steady state comes in the stabilisation of the frequency content and relaxation of slip transitions after the transient, something that allows the apt monitoring of the speed-ripple effect [10, 11, 21, 23, 42]. Recalling the literature of Sections 3.1 and 3.2, the healthy steady-state mode and smooth spectral characteristics of monitored signals under a fault condition practically transit to a quasi-steady-state mode, which embeds non-stationary characteristics and frequency content of time-varying nature [42, 107, 128, 293]. The latter two observations are also the reasons why implementation of approaches over the steady state response is frequently encountered in works over the past few years providing promising results, for $t-f$ analysis [21, 23] and other sophisticated or automated smart approaches [313, 314].

On this agenda, a limitation of the windowing function used to derive the STFT analysis is proposed from the DSP point of view in Chapter 4. The proposed windowing limit ensures the apt setting of parameters to separate rotor related frequency components under potential broken bar conditions. Then, it is used as the first step initiating the frequency extraction process, proposed to reliably detect rotor faults. The method is implemented over the steady-state regime, something that allows to properly take advantage of the speed-ripple effect. In the final step, the method proceeds with a two-stage analysis to provide an advocate signal representation for global monitoring.

Chapter 4

Methodology and Research Approach

Within the literature review, some problem statements were structured regarding non-adjacent broken bars, FD with advanced DSP and performance of DSP applications in induction machines. This chapter describes the theory and formulation of the proposed methodology regarding the frequency extraction method, which is used to reliably detect rotor faults. Also, the research approach is shown by the description of the designed FEM models and simulations; this is followed by the experimental procedure of designing and constructing the stray flux sensors (search coils), as well as the motors and test-rig used for measurements.

4.1 Formulation of the Frequency Extraction Process

The proposed methodology uses the STFT of a measurement to visualise its spectral content, with focus on the steady-state. Apart from the reasons mentioned in Section 3.4 regarding application of a method over the steady-state regime, another reason is the next step of the method. This is the extraction of the spectral content, regarding frequency bands of interest to detect the fault. The referred bands are the frequency areas around the $5-th$ and $7-th$ harmonic, which are examined for fault related sidebands in order to extract their own spectral content by the classical FFT. In order to apply the method reliably and extract accurate frequency information, some limitations must be set regarding the windowing functions which results to the system-oriented parameter setting of the STFT.

As explained in [21], the discussed approach practically deploys a two-stage $t-f$ analysis for rotor fault detection. The first stage includes the advanced analysis of the acquired signals executed with the STFT under two different window sequence lengths. The first one is the long-term window to localise the sidebands in frequency so as to provide a first indication

of a fault existence, while the second is a short-term one which is limited by a lower bound. This is to ensure frequency separation in the examined frequency zone, meaning that the trajectories examined by frequency tracking will belong in different frequency bins or chunks, therefore spectral leakage overlap and spectral energy diffusion between closely positioned components on the spectrogram is avoided [21, 24]. The second stage includes the extraction of a desired frequency trajectory from the spectrogram and its processing to evaluate it over time, as well as the classical FFT analysis of the extracted result. In practice, the quasi-steady state is approached with tools of $t-f$ analysis and, since localised over the steady-state, the post processing of the $t-f$ analysis results is done with the FFT. An example of the spectral information representation with the STFT analysis is shown in Figure 4.1, where the ripples of spectral components extracted are circled in dashed. The depicted spectrogram regards the 4 kW motor with one broken bar, used for experimental measurements.

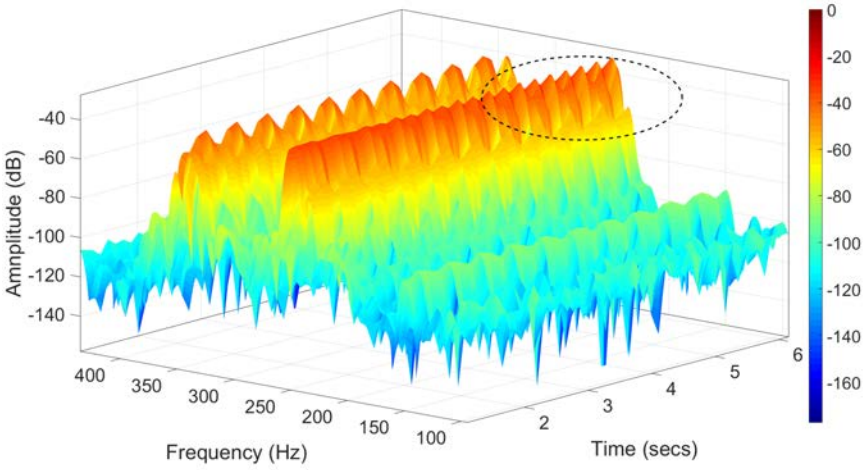

Fig. 4.1 STFT ridges of spectral components to be extracted

A flowchart of the proposed methodology is shown in Figure 4.2 and can be summarised in the following steps: the initialisation step, where the window of interest is chosen and the lower bound limit of the data sequence length is defined according to the slip (rated or estimated); the analysis steps under improved frequency and then improved time resolution, where the speed ripple effect is evaluated from the trajectories visualised with the STFT analysis; the implementation step, where the spectral density information $S(t, f_i)$ is extracted for any frequency f_i detected in the analysis step; the diagnosis step, where the extracted spectral content $S(t, f_i)$ is treated as a periodical function of time and analysed with the classical FFT to detect subcomponents related to rotor faults.

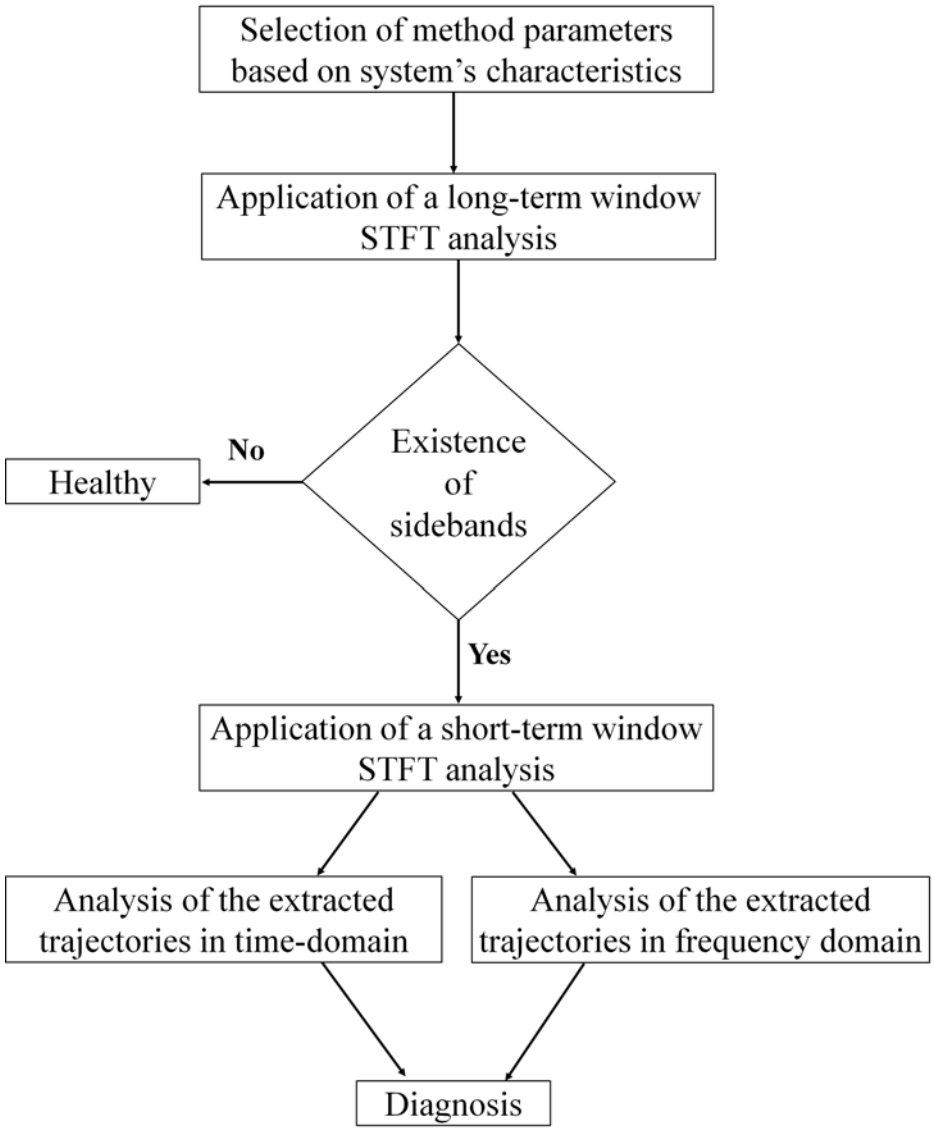

Fig. 4.2 Flowchart of the proposed methodology

4.1.1 Parameter Setting for Frequency Separation

In order to apply the frequency extraction reliably, the spectral components examined with frequency tracking must be separated. This means that the frequencies examined will belong in different bins or frequency chunks, not to be overlapped or diffused. The theoretical framework for extraction of spectral information is discussed in works like [49, 51] and [176, 177]. The implementation of methods like extraction or decomposition analysis springs from the nature of slip dependent faults like rotor faults to generate modulating/demodulating frequency patterns. This makes AM-FM analysis appropriate for the measured signals, which are in their general form multicomponent non-stationary signals in the quasi-steady-state [50, 181, 315, 316].

As mentioned in Chapter 2, the discrete-time STFT is given from [302]:

$$X[t_k, f] = \sum_{n=t_k-L/2}^{t_k+L/2} [x_n \cdot w_{n-t_k}] \cdot \mathrm{e}^{-\mathrm{j}2\pi f n t_k} \quad , \tag{4.1}$$

and requires the selection of a window that is apt to capture the event of a frequency, or the time instants at which the examined frequency exceeds transitions in time. This commonly establishes the time resolution seen in Chapter 2, that is calculated in practice from the window sequence length L_w and the sampling period $1/F_s$ as [280, 300]:

$$\Delta t = L_w T_s \tag{4.2}$$

Improved resolution in time is given by a window of short length in time; this provides adequate knowledge of the frequencies' instants at the cost of poor frequency resolution. What is usually aimed for in $t-f$ analysis is a compelling frequency resolution, which similarly to the time resolution (4.2) can be practically calculated from [294, 296, 300]:

$$\Delta f = \beta \frac{F_s}{L_w} \quad , \tag{4.3}$$

with β the local equivalent noise bandwidth, as defined and used in [295–297, 301]. Improved frequency resolution is acquired with a long window in time, localising the position of the frequency trajectory. Equations (4.2)-(4.3) show the inverse relationship between time and frequency resolution. This inverse relationship is in general terms referred to as the Heisenberg uncertainty principle [87, 317] and was introduced in $t-f$ analysis by Gabor [318, 319]. It practically states that, when examining harmonics of a signal, it is not possible to calculate simultaneously -and with the maximum precision- the frequency and time of that harmonic. In $t-f$ analysis the uncertainty principle is expressed as [87, 318]:

$$\Delta t \cdot \Delta f \geq \frac{1}{4\pi} \tag{4.4}$$

and shows that there is always a trade-off between frequency and time resolution. In the majority of $t-f$ analysis tools a user is called to choose between either an advocate time or an advocate frequency resolution, and usually the corresponding parameters like the window length and overlap are chosen with a trial and error method.

By [21, 319] and [320], in order to obtain reliable results by an unambiguous analysis before drawing cogent conclusions on a signal, a $t-f$ analysis imposes to be held under three types of windows. A short-term window will reveal the time information and modulation patterns comprised in the signal (AM/FM law); a long-term window that will localise the frequency posistions and allow amplitude inspection at very specific frequency points; an intermediate state window within the two extremes to validate the observations by the short-term and long-term window. The concept of such an analysis is deployed in the proposed approach for two main reasons. Firstly, this analysis provides global information of the quasi-steady-state response during a rotor fault condition, where modulating frequencies are inducing time-varying oscillations in amplitudes due to the magnetic field asymmetries over the rotation of the rotor body. The second reason is that approaches like the frequency extraction require improved time resolution, hence a short-term window. The question is how short can the length of the window be in order to avoid undesired phenomena like the spectral leakage and diffusion and, most of all, at no cost of information loss regarding the signal's frequency content.

The answer to this question is frequency separation, since obscurity of the spectral content will be the result of diffused energy between sidebands and main harmonic, or generally from closely positioned components. Considering f_i a central frequency like the fundamental or the 5th harmonic, frequency separation is fortified when the frequency resolution Δf is at least equal to the distance of f_i from its corresponding sidebands [21]. Therefore, when applying $t-f$ -or even simply frequency- analysis, the resolution is also dependent on the slip s. This is also discussed in [21] and [280], explaining how the window sequence length and consequently the frequency resolution are indirectly bounded by the slip. However, the frequencies investigated in FD using applied or advanced DSP are of discrete nature. Hence, it is possible to calculate the minimum window length required to reliably perform the step of the discussed two-stage approach regarding short-term windows.

Let $f_i \in \mathbb{R}$ be the $i-$th harmonic of the examined signal. The STFT effectively quantises this frequency with the quantisation step of Eq. (4.3) into frequency bins $f_i^q = n_i \Delta f$, $n_i \in \mathbb{Z}$. The actual frequency relates to the quantised one via [21]:

$$f_i = f_i^q + \xi_i \Delta f = n_i \Delta f + \xi_i \Delta f \quad , \quad \xi_i \in [0,1) \tag{4.5}$$

Considering f_1 a central frequency of interest and f_2 its lower sideband, the two frequencies can be written due to (4.5) as follows:

$$\begin{aligned} f_1 &= n_1 \Delta f + \xi_1 \Delta f \\ f_2 &= n_2 \Delta f + \xi_2 \Delta f \end{aligned} \tag{4.6}$$

and since $f_1 > f_2$, the following relation is valid:

$$n_1 = n_2 + m \ , \ m \in \mathbb{Z}^+ \tag{4.7}$$

By substituting (4.7) into (4.6) we obtain:

$$\begin{aligned} f_1 &= (n_2 + m)\Delta f + \xi_1 \Delta f \\ f_2 &= n_2 \Delta f + \xi_2 \Delta f \end{aligned} \tag{4.8}$$

By subtracting Eq. (4.8) we obtain

$$f_1 - f_2 = m\Delta f + \xi \Delta f \quad , \quad \text{where } \ \xi = \xi_1 - \xi_2 \in (-1,1) \tag{4.9}$$

By substituting Δf from (4.3) into (4.9) and solving for L_w, the lower limit of the window sequence length is obtained by the equality:

$$L_w = \frac{\beta F_s}{f_1 - f_2}(\xi + m) \tag{4.10}$$

Since $m \in \mathbb{Z}^+$ defines the distance between the quantised frequencies, the minimum value of m for which they are separated is $m = 1$. As described in Chapter 3, the rotor fault related sideband tones are distanced from a main harmonic at even multiples of the factor sf_s. Therefore, without loss of generality, the difference $f_1 - f_2$ can be set as $f_1 - f_2 = 2\rho sfs$, where $\rho \in \mathbb{N}$ and Eq. (4.10) thereof becomes:

$$L_w \geq \frac{\beta F_s}{2\rho s f_s}(\xi + 1) \tag{4.11}$$

Inequality (4.11) provides the minimum lower bound of the window length for separation of the examined quantised frequencies. It should be noted that this bound depends to the

windowing function w through parameter β. Selection of the windowing function is an important step in the proposed method. Intuitively the windowing function can be considered as a filter in the information that is carried within the signal under investigation and will be revealed by the STFT analysis. Proper selection of this function will optimise the amount of spectral information to be extracted. Therefore, the Gaussian and the Kaiser-Bessel windows were chosen for implementation of the method in the following chapters, obeying to the limitation of inequality (4.11). The main reason is their ability to properly analyse short transients and frequency components located close to each other (sideband tones). Another fact that makes these windows apt is that they provide an optimal main-lobe-to-side-lobe energy ratio, a property desired in electrical machine diagnosis, where faults leave their print as sideband tones carrying the information of spectral distortion.

In practical terms, the limitation provided by (4.11) is the lower extreme where extraction is applicable without information loss regarding spectral characteristics. This allows to evaluate components designated by the speed ripple effect over time and carried in the spectral energy density amplitude of the spectrogram. The stages of analysis by short-term and long-term windows is shown in Figures 4.3 and 4.4, for a healthy motor and a motor with broken bars respectively, around the frequency zones of the $5-th$ and $7-th$ harmonics. As explained in [21], $\xi \in (-1,1)$ is an inherent system parameter that can not be controlled, in terms that it inherently depends on characteristics like the slip, the effective equivalent noise bandwidth, the sampling, the quantisation step, the length of the dataset, etc. Therefore the most convenient way to select an appropriate value is by an exhaustive search algorithm within $(-1,1)$ until convergence is achieved [321], cross-validating that it returns resolutions obeying to inequality of (4.4) and a frequency resolution twice the distance between an examined sideband and the main harmonic it belongs to (central frequency) [21].

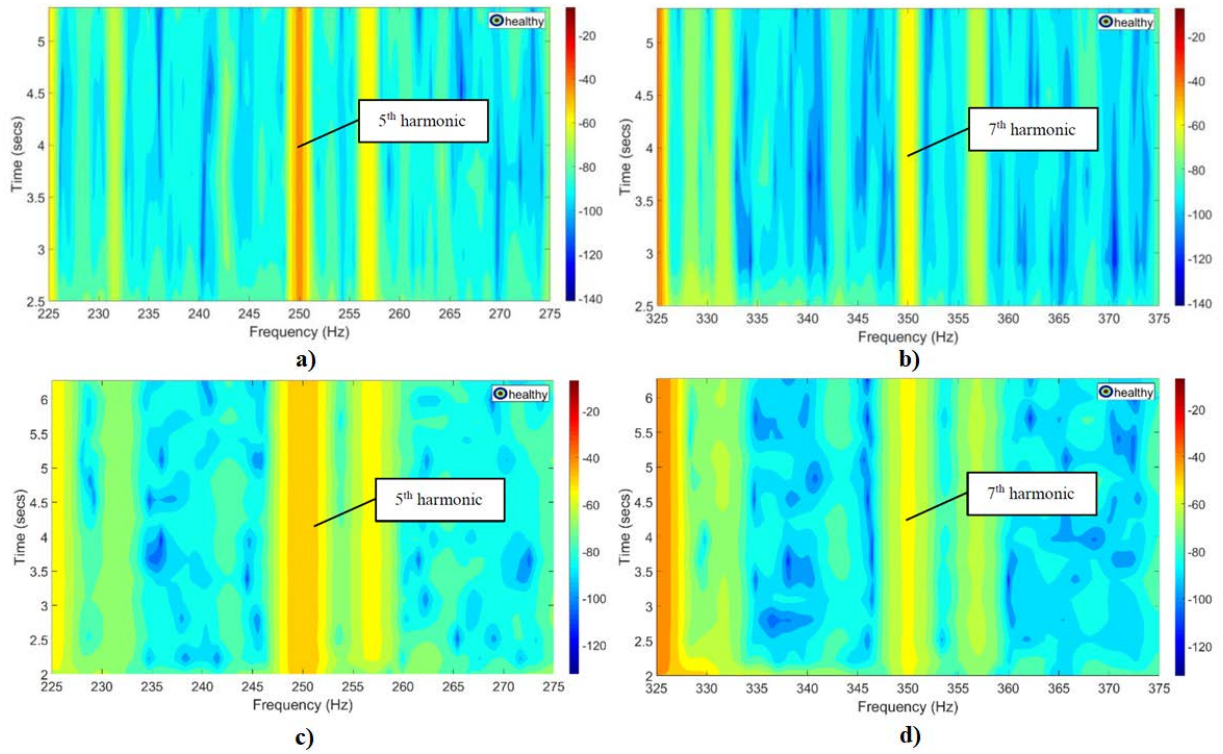

Fig. 4.3 Stages of analysis: localisation in frequency (a & b) & localisation in time (c & d) for a healthy motor

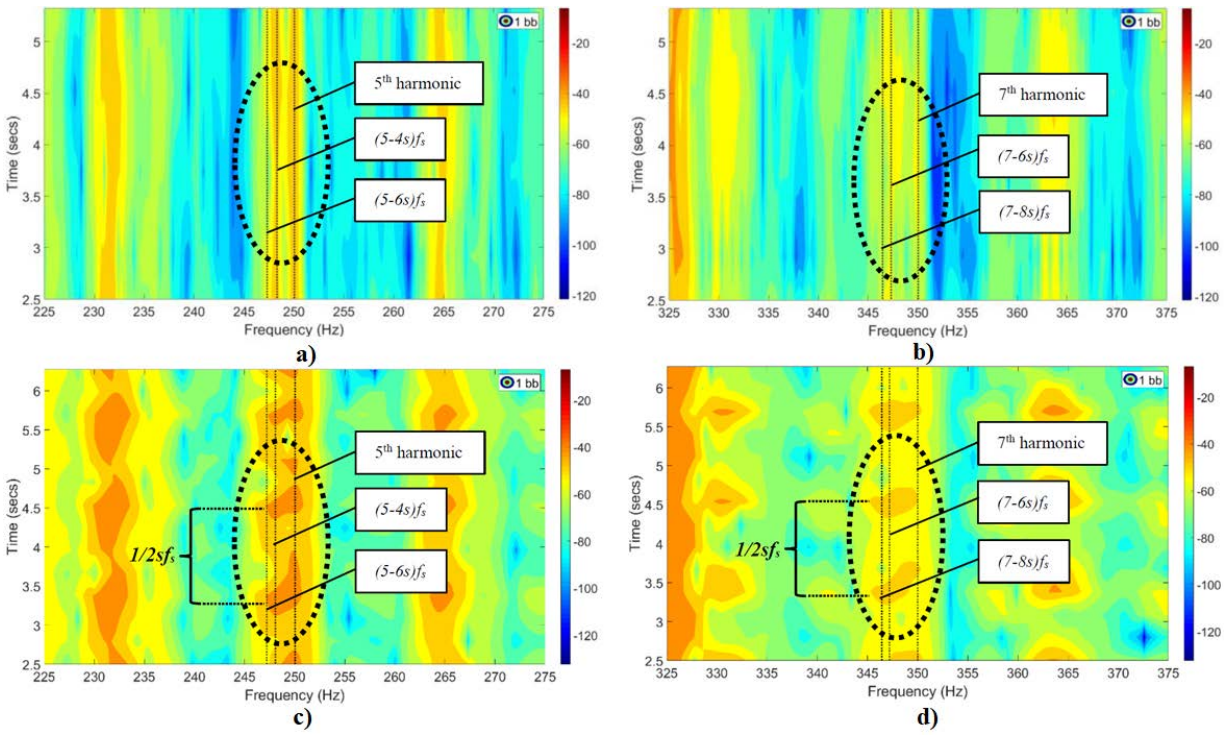

Fig. 4.4 Stages of analysis: localisation in frequency (a & b) & localisation in time (c & d) for a faulty motor

4.1.2 Extraction of the Separated Frequencies

As soon as seperability of the spectral components is assured by the described limitation, the result of the spectrogram is used to isolate the amplitude information over time at a desired frequency. The component is extracted on the chosen fixed frequency f_i and the trajectory of $S(t, f_i)$ is plotted over time. An example of the extracted trajectory for the $5-th$ harmonic's upper sideband is shown in Figure 4.5, blue color representing the healthy motor and red the faulty motor. The final diagnosis stage is the time waveform evaluation of the trajectory and examination of its signatures with the FFT; this is depicted in Figure 4.6 for the lower sideband of the $7-th$ harmonic. The circled frequencies show bands of interest in the low frequency range for frequency tracking of fault related components.

The t-f representation of the STFT is calculated for the examined signals over the whole duration of the measurement (or simulation dataset), using Gaussian windows and Kaiser-Bessel windows. The Kaiser parameter and its overlap are chosen by ad-hoc selection, always setting the window's frequency response to be with the smoothest ripple around the unit, smoothing the cut-off from the rectangular shape [23, 24, 201]. This way spectral diffusion on the boundaries of the window and the Gibbs phenomenon are avoided. As discussed in Chapter 3, DSP issues or deficiencies can potentially arise when analysing the fundamental 50 Hz harmonic and its sidebands [22, 23, 75]. Therefore the diagnostic method with extraction focuses on analysis of sidebands at the higher harmonics of the $5-th$ and $7-th$ harmonic. The discussed harmonics are chosen in a variety of works as they are free from load and saturation effects [75, 201], hence more likely to be immune to false negative or misinterpreted diagnosis from secondary effects [100, 283]. Considering f_a the $a-th$ central harmonic under investigation, and i the index equal to 1 or 2 for the first or second sideband respectively, then $S(t, f_{a,i})$ is the magnitude of the spectral density over the spectrogram's $t-f$ plane [22–24]. Fixing a frame around a frequency zone by means of overlapping windows, a chosen frequency f_a or $f_{a,i}$ in that frequency band curves on the spectrogram a distinct ripple over time.

The STFT output at short-term windows maps the modulation of these ripples and examines denoted periodicities at each band with focus in the steady-state. The $t-f$ analysis is paused at this point and its outputs are evaluated at the chosen f_a or $f_{a,i}$ over time. The classical FFT of the stator current and stray flux signals is examined to track the rotor frequency f_r and calculate the slip. Regarding FEM datasets, the motor speed over time is always acquired in transient time-stepping simulations. Hence, the only unknown time-varying quantity is the slip and it can be used in the process either in its mean value or modelled over time $s(t)$, the latter being more accurate in the frequency localisation. An example of extracted trajectories is shown in Fig. 4.5 comparing healthy with single breakage

case, for the spectral information of some of the components shown in Figures 4.3 and 4.4 (bottom); Fig. 4.6 shows the trajectories' comparative FFT at the final diagnosis stage. The results regard the 4 kW motor used in the experimental validation.

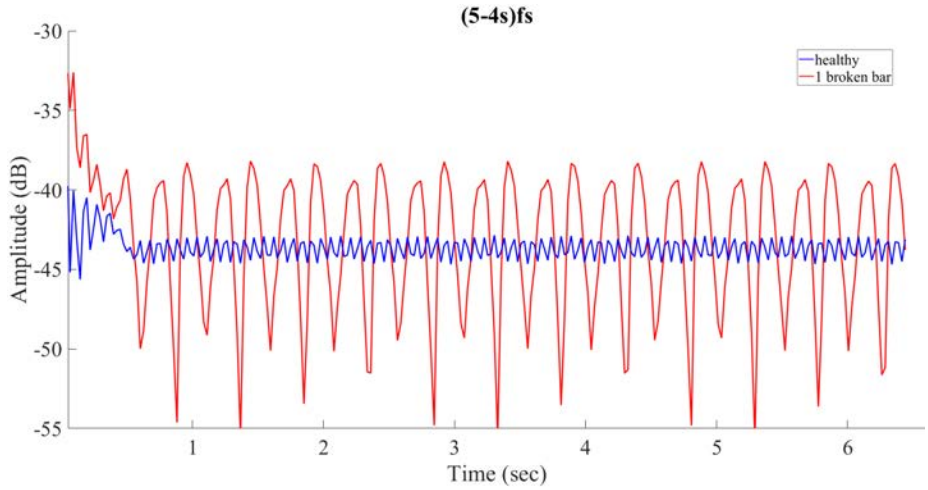

Fig. 4.5 Extracted trajectory over time of a healthy motor (blue) and motor with one broken bar (red)

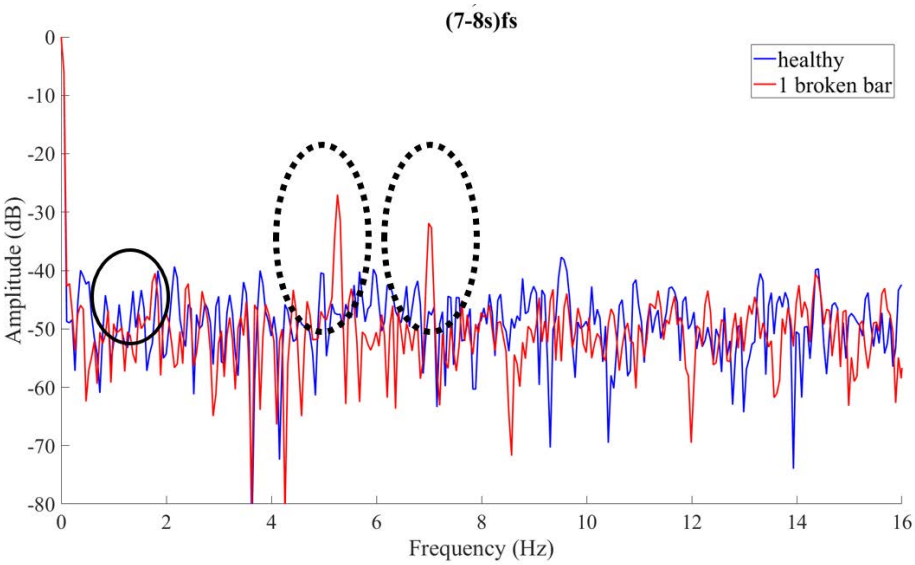

Fig. 4.6 Final diagnosis stage: FFT analysis of extracted trajectories

4.2 FEM models & simulations

The models used for the FEM validation were designed and simulated in MagNet, a FEM software provided by Mentor/Infologic [5]. The models are run under 2-D transient time-stepping analysis with rotary load-driven motion, which is a type of simulation accounting for the machine's motion equation and the moment of inertia [5, 22]. Initially, three models of induction motors were designed, two 4 kW motors with four poles and a 1.1 MW motor with six poles. The first 4 kW model (Model #1) fully corresponds to the motor used for experimental validation [24]; the second 4 kW model (Model #2) is used for further data collection and validation of the method on the same machine, embedding a rotor with different number of bars; the third model (Model #3) regards a large industrial 1.1 MW motor, so that the method is generalised by demonstration on a machine of different size, design/geometry and number of pole pairs [21, 23].

For each motor, five different models were simulated and studied: the healthy, the model with one broken bar, two adjacent broken bars, two broken bars at half pole-pitch and two bars at full pole-pitch distance. Consequently, 15 different FEM models were used for the data collection. The software provides the ability of modelling the multiple coupled equivalent circuit of the machine, where each component is modelled by material and equivalent circuit components. The air-gap is divided in three layers to create mesh and re-mesh components during transient time-stepping motion (Figure 4.7), for accurate calculation of the air-gap torque. One air-gap layer corresponds to the stator, one to the rotor and the in between re-mesh layer that changes in every time instant. The numerical method used by the solver is the Newton-Rapshon method by conversion of the conjugate gradient [322, 323].

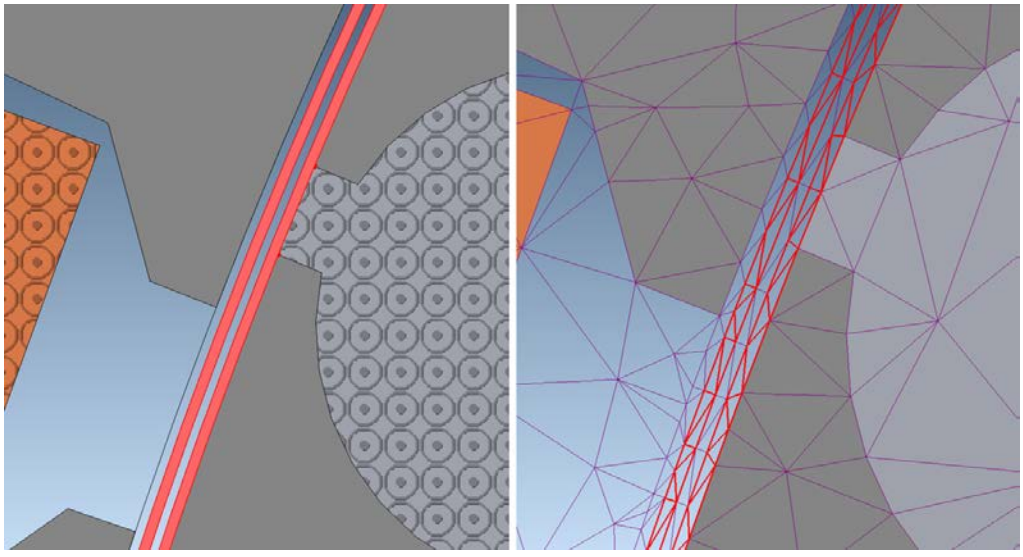

Fig. 4.7 Air-gap with mesh and re-mesh components

Apparently 2D FEM does not account for friction and end effects. However, lumped resistances in the equivalent circuit compensate the ohmic losses, while the MEC components' ohmic losses are calculated from the current density in each component. For the iron core losses, the solver uses a penalty function to compensate their calculation with the use of the Steinmetz coefficients and the Jiles-Atherton model [322, 323]. More specifically, current driven stranded coils are used for the stator winding modelled with material "Copper 100 % IACS" [322, 323]. The MEC components for the rotor bars are chosen as solid coils with fill 100% factor and unit winding factor. Both the stator and rotor iron cores are modelled with laminated steel material, given in the model description from the manufacturer. In the geometrical parameterised model, rotor bars are modelled with material "Aluminum 50 % IACS" for the low power induction motors and with "Copper 100 % IACS" for the large industrial motor.

4.2.1 Model #1: 400 V, 4 kW, 4-pole IM (36/32)

The characteristics of Model #1 are presented in Table 4.1. The discussed motor is a Delta-connected 400 V, 4 kW, 4-$pole$, 50 Hz IM, designed with 36 stator slots and 32 rotor bars and fully corresponds to the laboratory motor used for experiments [5]. The schematics of the basic motor geometry were provided by the manufacturer in a DXF file, which was imported in the FEM software for further components design, definition, expansion, material assignment, etc. The stator is designed with round slots, where the stator winding is placed. The winding configuration includes six coils per phase, with 49 turns per coil (98 conductors) and a 2.785 Ω per-phase resistance. The rotor is also designed with round bars, slots and shaft, included in the motion component through the defined reference paths. The flux sensor is a stranded search coil of 1000 turns, placed on the external periphery of the motor to capture stray fields of radial flux in the vicinity of the machine [5]. To model the open-circuit condition of the voltage meter, a large value resistance (1 $M\Omega$) is connected in series with the coil. The stator equivalent circuit is shown in Figure 4.9, while the air-gap of the motor with the mesh and re-mesh components highlighted is shown in Figure 4.7. A full geometrical view of the model is shown in Figure 4.8, along with the spatial distribution of the magnetic field at a single bar breakage. The stator and rotor iron cores are modelled with laminated material "M800-50A", while the rotor bars are modelled with "Aluminum 50 % IACS".

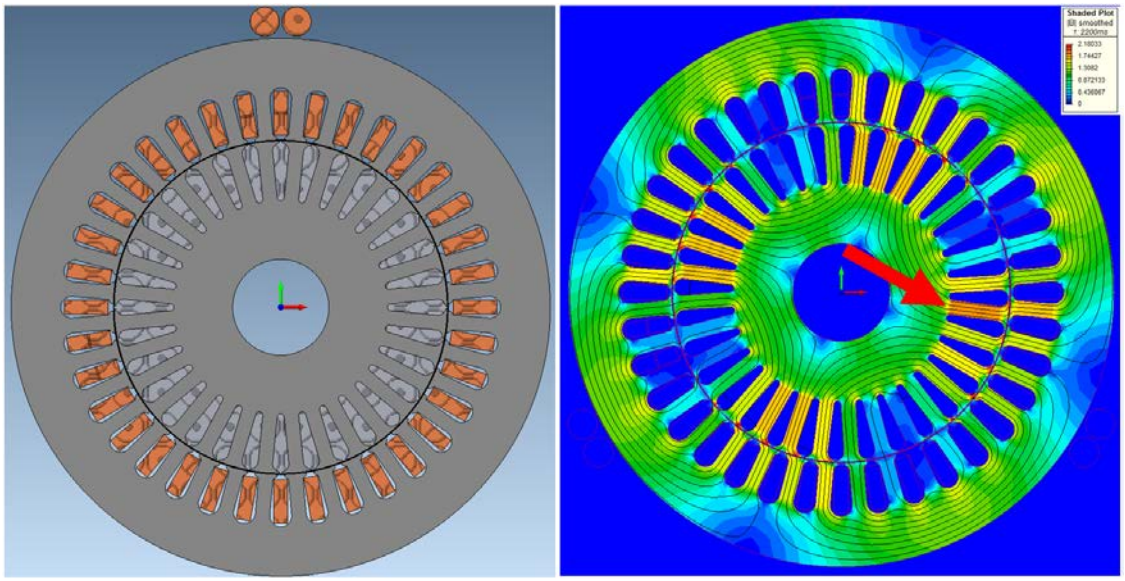

Fig. 4.8 FEM model of 4 kW motor with 32 rotor bars (Model #1)

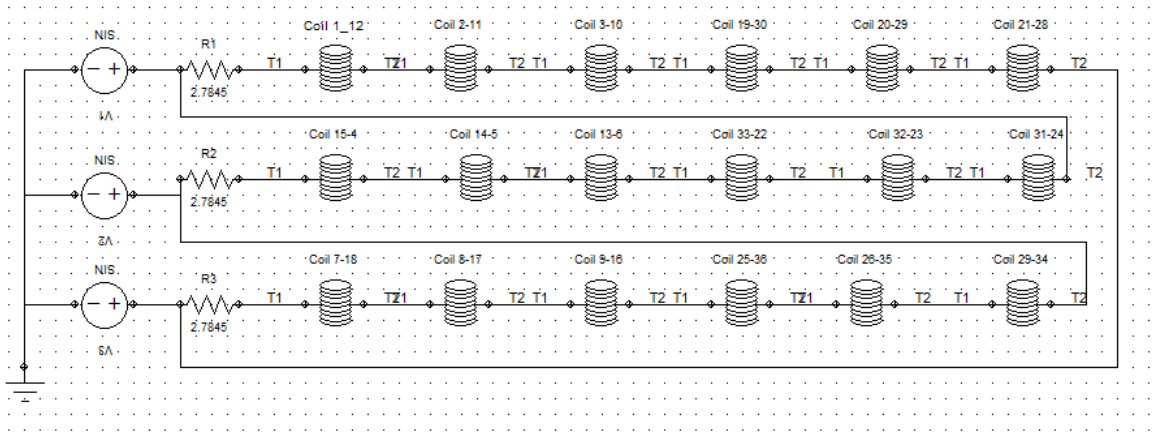

Fig. 4.9 Stator MEC of Model #1 & Model #2

Table 4.1
Characteristics of Model # 1

Characteristics	**Model # 1**
Supply Frequency f_s	50 Hz
Stator Connection	△
Output Power	4 kW
Rated Voltage	400 V
Rated Current	10 A
Number of Poles	4
Rated Speed	1416 rpm
Number of stator slots	36
Number of rotor bars	32

4.2.2 Model #2: 400 V, 4 kW, 4-pole IM (36/28)

The second motor (Model #2) has an identical stator with Model #1 and different rotor design. The rotor of Model #2 is designed with 28 rotor bars and it is chosen to examine the effectiveness of the proposed method on a motor of the same power rating but with different rotor construction [24]. The geometrical view of the model is shown in Figure 4.10 (left), which also presents the magnetic field spatial distribution during a single breakage. The arrow points the asymmetry in the rotating magnetic field caused by the bar breakage. Figure 4.11 depicts the stator slot and rotor bar geometry, which is the same for Model #1 and Model #2, while the characteristics of the motor are listed in Table 4.2.

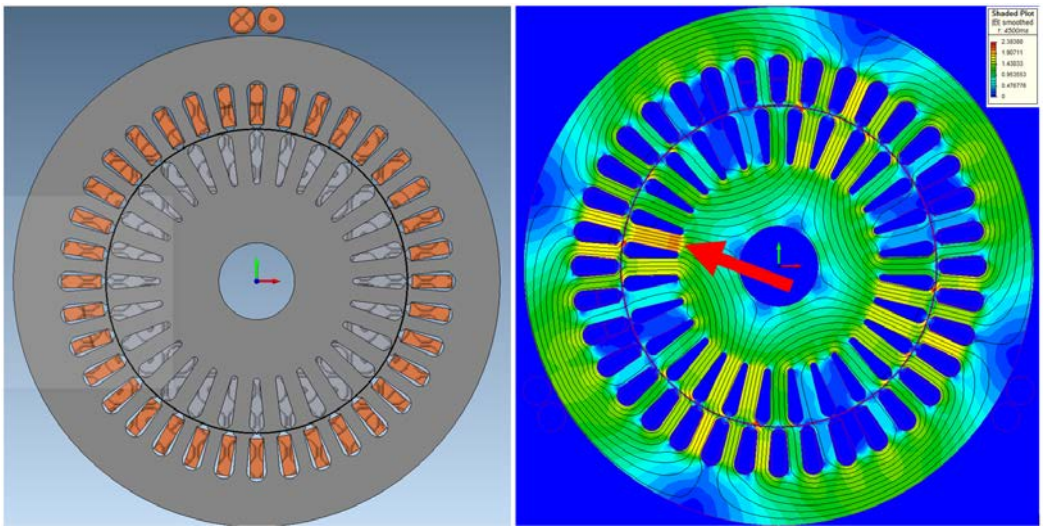

Fig. 4.10 FEM model of 4 kW motor with 28 rotor bars

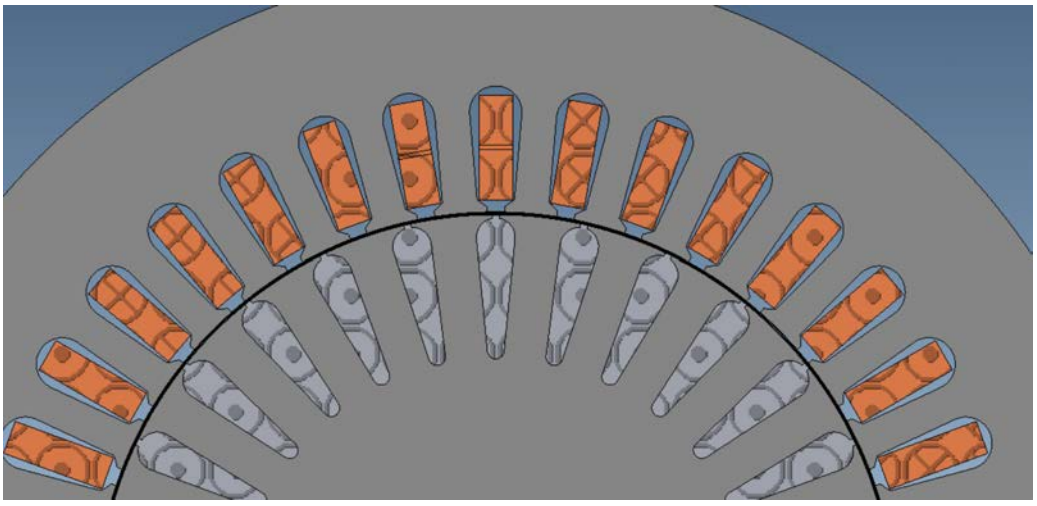

Fig. 4.11 Geometry of stator and rotor slots for Model #1 & Model #2

Table 4.2
Characteristics of Model # 2

Characteristics	**Model # 3**
Supply Frequency f_s	50 Hz
Stator Connection	$\triangle$
Output Power	4 kW
Rated Voltage	400 V
Rated Current	10 A
Number of Poles	4
Rated Speed	1416 rpm
Number of stator slots	36
Number of rotor bars	28

4.2.3 Model #3: 6.6 kV, 1.1 MW, 6-pole IM (54/70)

The motor referred to as Model #3 is a large industrial 6.6 kV, 1.1 MW, 6-$pole$ motor with the schematics provided by the manufacturer and its characteristics as given on the nameplate are listed in Table 4.3. The rotor consists of 70 copper bars and the stator of 54 slots, where a fractional-pitched 1-9 double layer winding is placed after modelled with "Copper 100 % IACS". The stator circuit includes 18 stranded coils per phase, with 24 turns per coil (48 conductors) and a 0.99 Ω stator per-phase resistance [6, 21, 22]. The stator and rotor back iron are modelled with laminated material "M-19 29 Ga", while the rotor bars of this motor are modelled with "Copper 100 % IACS" as solid coils in a similar manner with Model #1 & Model #2. The slot and bar geometry is depicted in Figure 4.13, where also the double layer winding is shown with the slot coil and its coil mate. A full geometrical view is shown in Figure 4.12 with the magnetic field distribution under the single breakage fault. The flux sensor is designed with 1000-turns on a stranded copper coil, placed on the periphery of the stator back iron [6, 21, 22].

Table 4.3
Characteristics of Model # 3

Characteristics	Model # 3
Supply Frequency f_s	50 Hz
Stator Connection	⅄
Output Power	1.1 MW
Rated Voltage	6.6 kV
Rated Current	170 A
Number of Poles	3
Rated Speed	990 rpm
Number of stator slots	54
Number of rotor bars	70

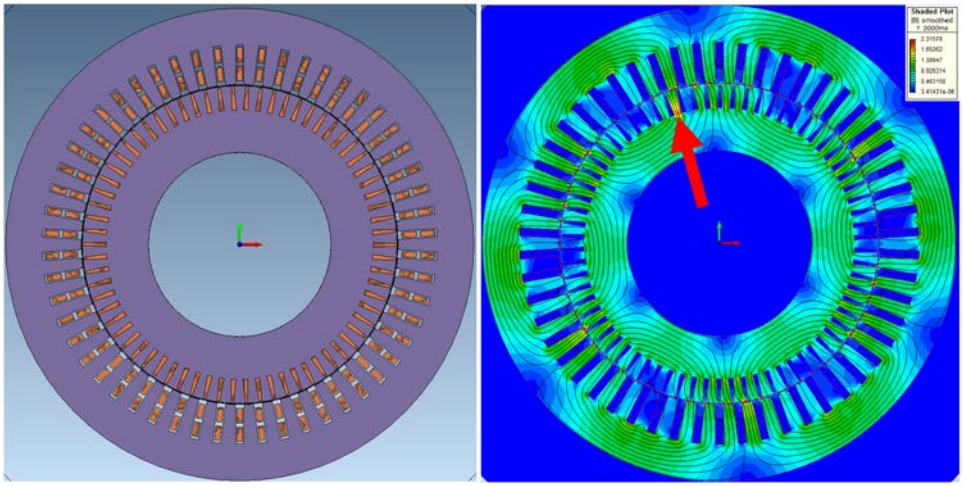

Fig. 4.12 FEM model of 1.1 MW motor (Model #3)

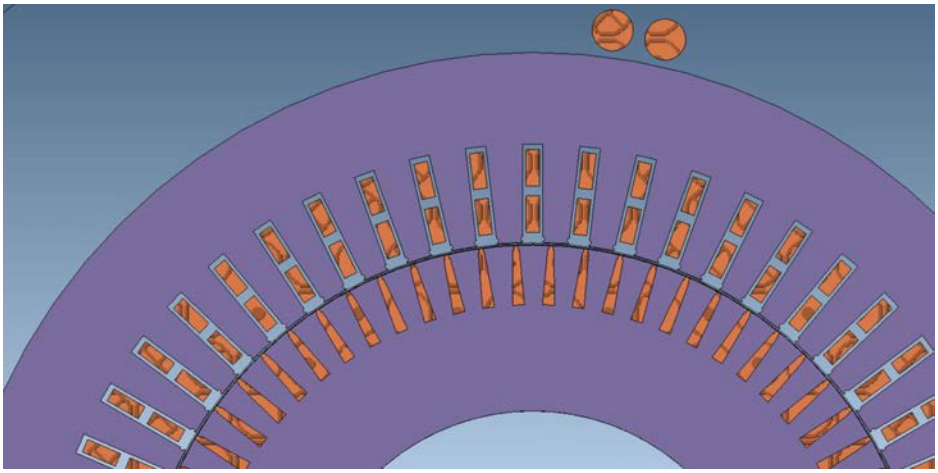

Fig. 4.13 Geometry of stator and rotor slots for Model #3

4.3 Experimental Procedure

4.3.1 Motors & Monitoring Equipment

The laboratory test-rig was provided from the company AE Electromagnetics BV, Netherlands. It consists of a supply fed 4 *kW* induction motor driven by the load, which is a permanent magnet generator, via the IPC of an industrial safety cabinet [24]. The custom pre-installed monitoring software displays the rms value of the 3-phase current and voltages, the instantaneous value of torque, the input/output power and the efficiency. The permanent magnet generator's output are connected to a variable three phase load, connected in Star connection. The end user side of the monitoring display is shown in Figure 4.14, along with the variable load topology. The test-rig with the embedded induction motor and permanent magnet generator is shown in Figure 4.15, which also shows the rotor drilled to emulate the broken bar faults and the additional current sensors used to acquire the datasets of the stator current waveforms [24, 324].

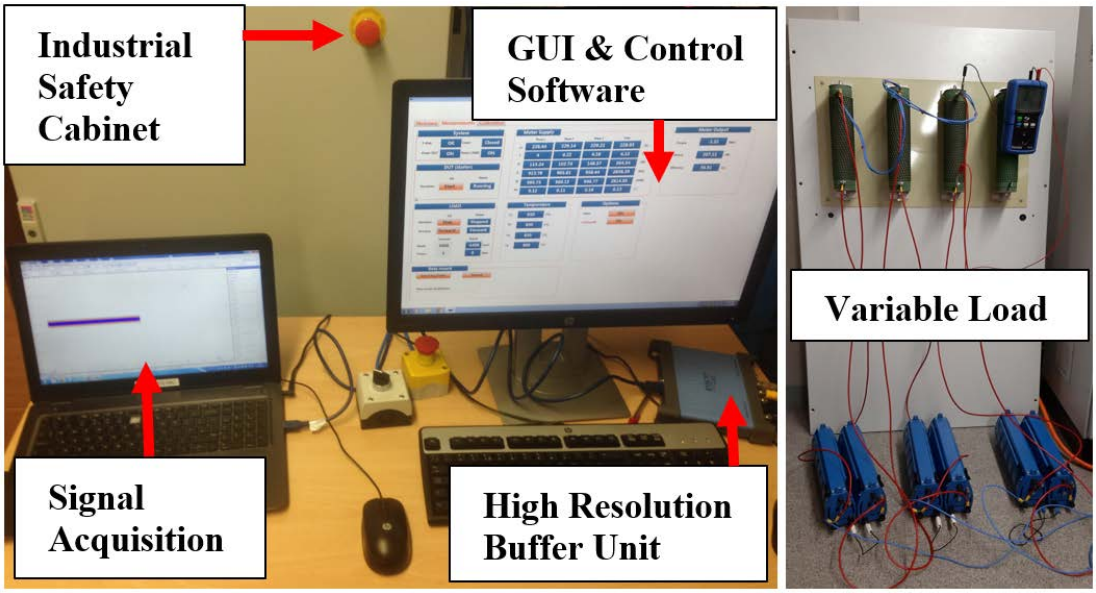

Fig. 4.14 End user side of monitoring equipment (left) and variable load topology (right)

The multi-variable measurements of the stator current and the stray flux signals are acquired with a high resolution, deep memory, 8-channel board, which is the 4824 Series PicoScope operating as a portable multifunctional oscilloscope [24, 324]. Offering a 12-bit resolution and serial bus decoding with 256 MS buffer memory and a 20 MHz bandwidth, each signal waveform was captured within 12 frames of $10-15$ *sec* each, providing the ability to gather extended waveforms over the steady state of the motors, for reliable signal representation in both the time and frequency domain. For the current measurements, three

picoThech TA 167 current probes are used for monitoring the line current of each phase. The current probe has a sensitivity of 10 mV/A and an accuracy of $\pm 1\%$ of reading at $\pm 100/\pm 500$ mA, so the stator currents of each motor were captured with a set of three identical current probes. Providing a safety BNC connector, this measurement was at later stage logged onto the digital high resolution buffer memory unit of the 4824 Series PicoScope used for acquisition of signal waveforms and data [24, 324].

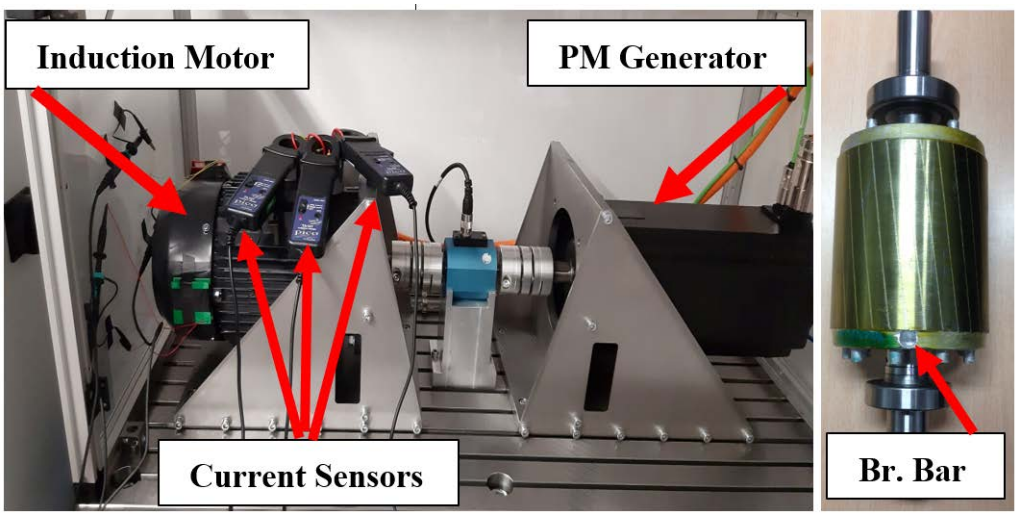

Fig. 4.15 Experimental rig and monitoring equipment (left), drilled rotor to emulate the broken bar fault (right)

To emulate the broken bar fault, the rotor cage was drilled at the connection point of the bar with the end-ring. After the acquisition of all datasets in the three conditions of load, the rotor was removed and drilled to a second connection point to emulate the non-adjacent broken bar fault at the distance of half pole pitch. This way, the studied faulty cases of one broken bar and two non-adjacent broken bars at half pole-pitch are in full correspondence with Model #1. Additional experimental validation of the proposed methodology has been demonstrated on stray flux data from a 230 V, 1.1 kW, 4-$pole$, 50 Hz IM with 28 rotor bars and 36 stator slots, performing its diagnostic validity for adjacent and non-adjacent broken bars at half pole-pitch and one full pole-pitch at the full load condition. These measurements were taken in collaboration with the University of Valencia, where the discussed test-rig belongs, and the results are also shown in the next chapters, corresponding to cases like two adjacent, the half and full pole-pitch breakages of the low power FEM models. The test-rig and sensor topology of the Δ-connected 1.1 kW IM, shown in Figure 4.16, are described in [21] and [23], while the rotors emulating the broken bar fault were drilled with a similar process, breaking the connection between rotor bar and end-ring. The characteristics of both experimental motors are given in Table 4.4.

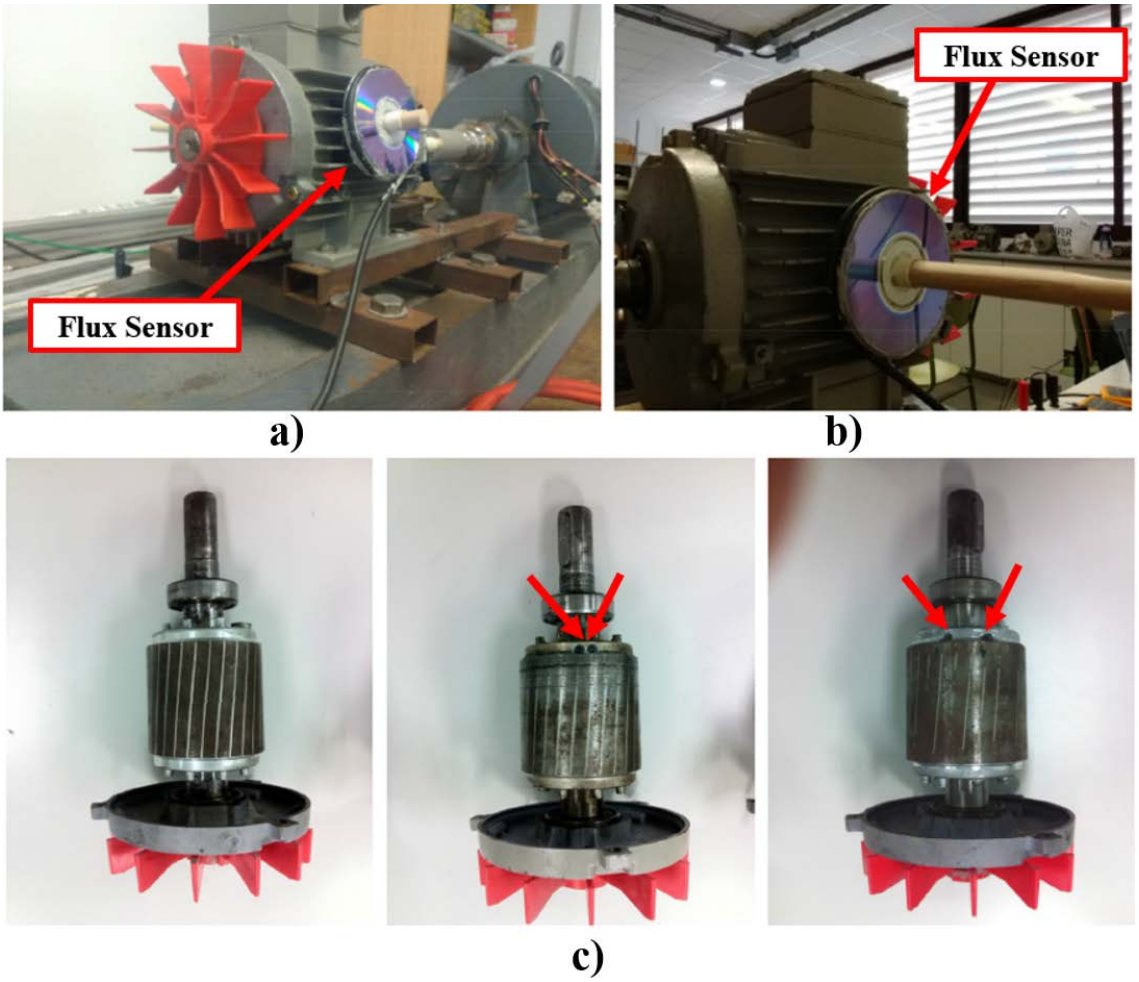

Fig. 4.16 a) Experimental rig of 1.1 *kW* & flux sensors b) flux sensor in position to capture radial flux c) healthy rotor (left) and drilled rotors for the adjacent broken bar fault (middle) and non-adjacent broken bar fault (right)

Table 4.4
Characteristics of experimental motors

Characteristics	**Motor # 1**	**Motor # 2**
Supply Frequency f_s	50 Hz	50 Hz
Stator Connection	△	△
Output Power	4 kW	1.1 kW
Rated Voltage	400 V	230 V
Rated Current	10 A	4.5 A
Number of Poles	4	4
Rated Speed	1416 rpm	1410 rpm
Number of stator slots	36	36
Number of rotor bars	32	28

4.3.2 Flux Coils: Design & Construction

The flux coils used to acquire experimental measurements of the stray flux are in-house built search coils, designed and constructed in the PowerLab of Coventry University. The software CATIA V5 was used for the design of the coil reel in the environment for parts and components. The reel was then 3D printed and coiled under the same identical construction and winding process with a custom self-constructed winder, by a simple topology of a DC motor and a breadboard with a controller and a digital counter circuit -for exact number of turns in each coil slot- regulated by a voltage and frequency regulator. A 3D view of the designed sensor prototype is depicted in Figure 4.17, while the internal and external dimensions of the sensor core are given in Figures 4.18 and 4.19 respectively.

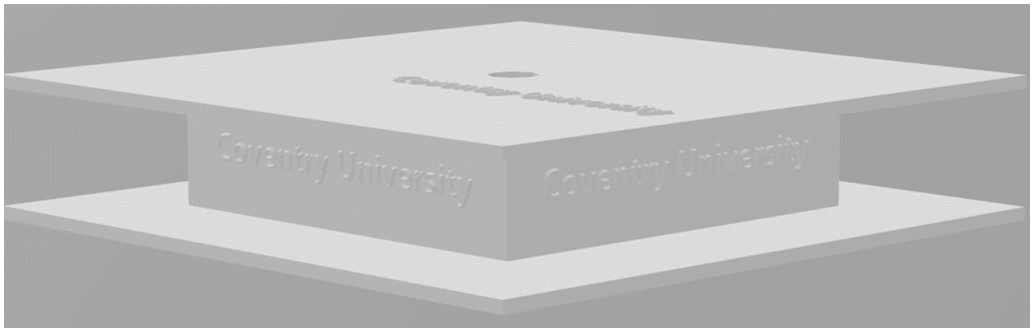

Fig. 4.17 Sensor 3D side view

Each of the rigid search coils consists of several number of turns wounded on a square-body reel of dimensions $40x40\ mm^2$ for the main body and $55x55\ mm^2$ for the salient edges at each top and bottom end of the reel, while the 8 *mm* slot height of the reel is fully filled with a 0.1 *mm* diameter distributed copper winding of resistance 3.4 Ω/m. For capturing the waveform of the voltage induced on the search coil, a voltage probe was installed so as to clamp one of the two ending connectors of the sensor, while the other end of the sensor was grounded. The voltage probe was connected to the BNC input of the Picoscope to log the data of the induced voltage time waveforms.

Several coils were 3D printed and wounded by different number of turns. Different groups of sensors were tested, consisting from 1500, 2000, 3000 and 3500 turns. The testing proved more efficient for the sensors of 2000 turns for laboratory motors of low power rating like the ones used in the experimental test-rig. The main reason is the distortion in stray flux waveforms, as it originates from the derivative of the induced voltage on the sensor, which is affected by the number of turns due to the amplification of high-order components [5, 18, 19, 274]. For larger machines, sensors with 3000 and 3500 turns proved more reliable as the number of turns attenuates the stray fields around the motor frame. The

process of winding the coils is shown in Figure 4.20, while Figure 4.21 shows the testing of the different sensors. Figure 4.22 shows all the tested sensors and the data acquisition unit (Picoscope), with the current probes used to measure the induced voltage on the search coils.

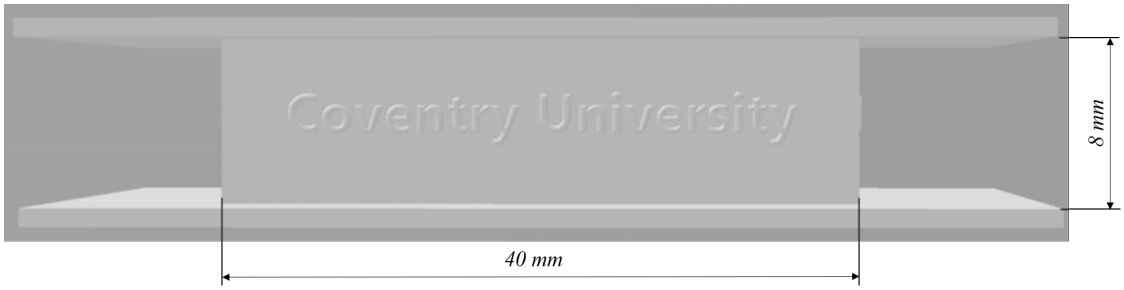

Fig. 4.18 Flux sensor inner dimensions (coil slot and core length)

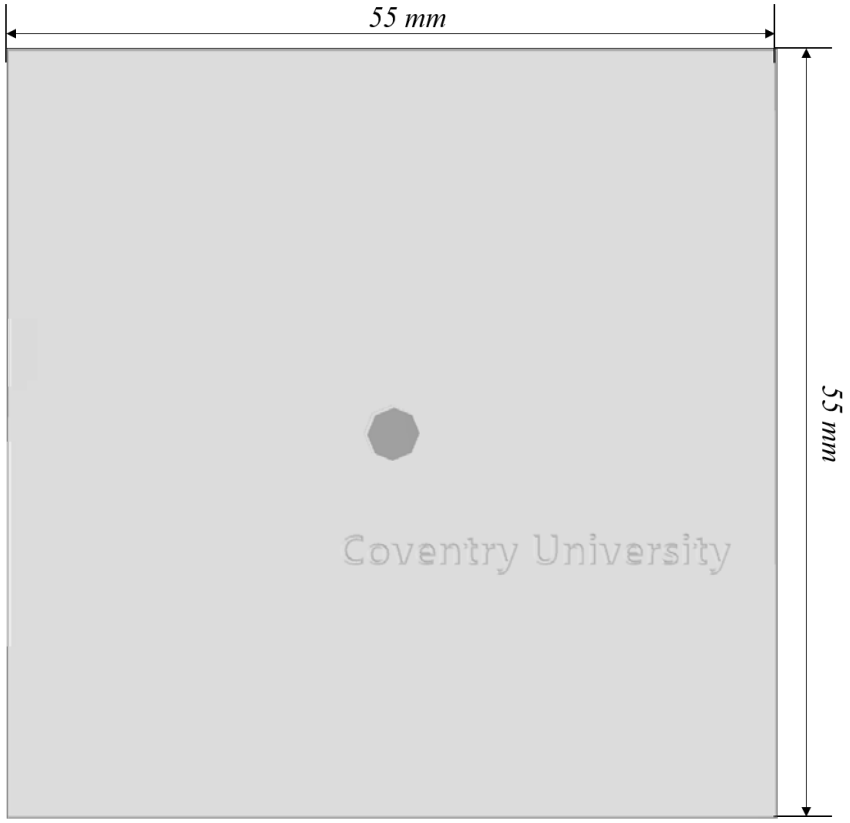

Fig. 4.19 Flux sensor outer dimensions (coil reel)

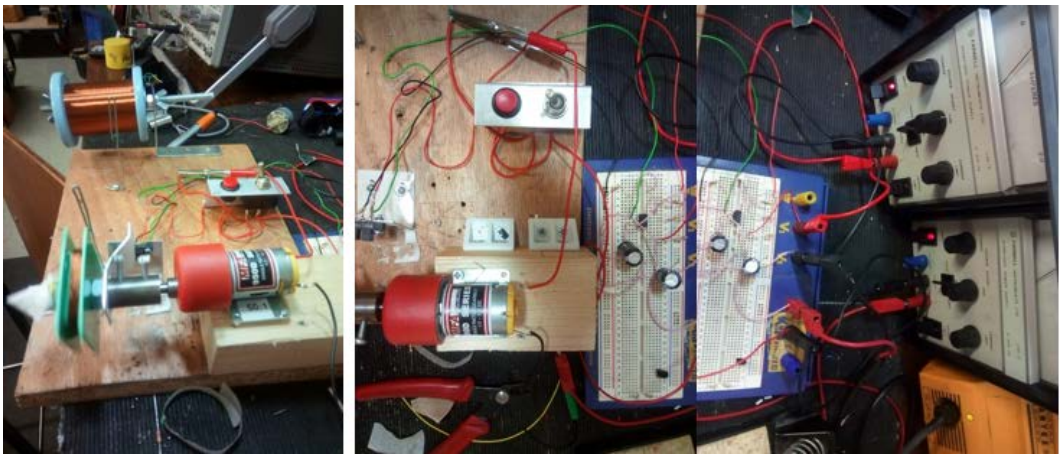

Fig. 4.20 Coil winder device used to wind the 3D printed coil reels

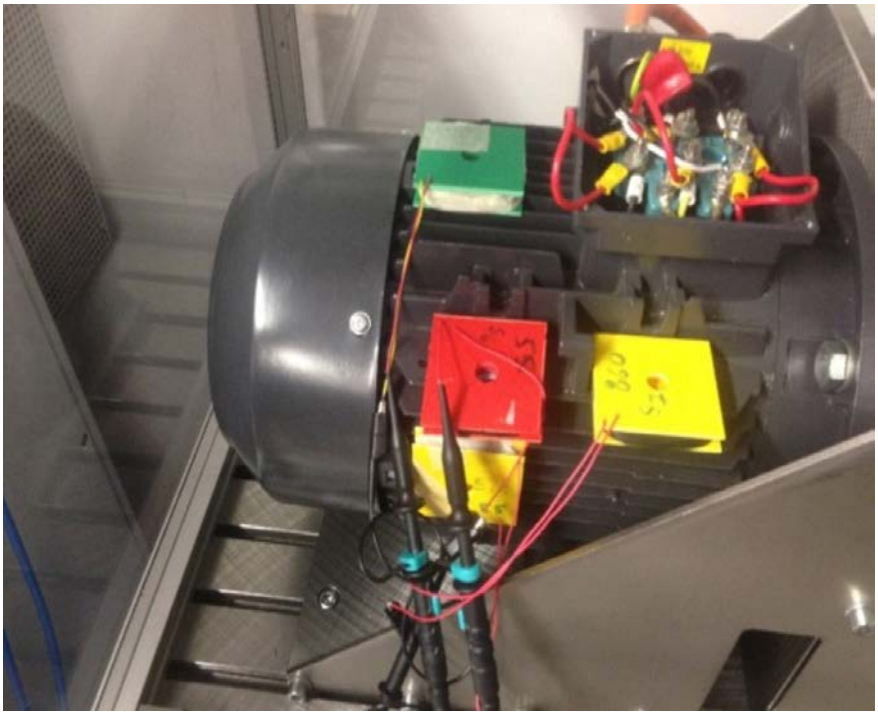

Fig. 4.21 Coil sensor testing in different orientations

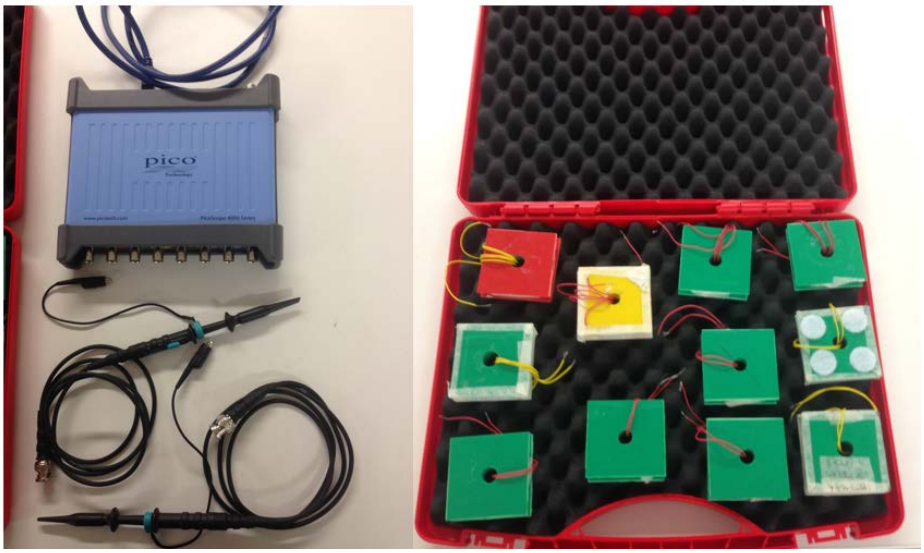

Fig. 4.22 All the coil sensors used with different number of turns

Chapter 5

Results from FEM simulations

This chapter presents the results from all simulated FEM models. To aid the reader, all cases examined with FEM are labelled for convenience in the same way for each model: Case #1 is always the healthy model; Case #2 regards the single bar breakage, while Case #3 the scenario of two adjacent broken bars; Case #4 and Case #5 represent the scenarios of two non-adjacent broken bars, at half pitch and full pitch distance respectively. All cases are summarised in Table 5.1. Initially the frequency extraction method is applied on stator current signals, then on radial stray flux signals. The spectral components of interest examined with the proposed method in all models are listed in Table 5.2. The analysis of long-term windows versus short-term windows is shown only for the $5-th$ and $7-th$ harmonics in the stator current and stray flux of Model #1, to demonstrate the concept of the extracted spectral components analysis as time-signals; since the process is identical, for the rest of the models the extraction method is applied directly, with a presentation and discussion of the derived windowing limits per model. Each of the five cases created to investigate and compare the fault detection method provides a separate model by itself and are consequently handled as 15 different motors. Due to the time consuming nature of the FEM simulations, the 15 models are simulated at the full-load condition. However, in the next chapter the method is validated experimentally by results which regard also a lower level of load (half the rated load).

Table 5.1
Summary of cases for every model

Case	Breakage Location
Case #1	healthy
Case #2	single breakage
Case #3	2 adjacent bars
Case #4	2 bars at half pitch
Case #5	2 bars at full pitch

Table 5.2
Spectral components used in the method

Examined Sidebands	Spectral component
$(5-4s)f_s$	$S(t, f_{5,1})$
$(5-6s)f_s$	$S(t, f_{5,2})$
$(7-6s)f_s$	$S(t, f_{7,1})$
$(7-8s)f_s$	$S(t, f_{7,2})$

5.1 Model #1

Reliable Limit for Extraction

The instant measurement of speed is available in every dataset from the FEM simulations, hence the value of slip s is easily acquired. All components at twice the slip frequency ($\simeq 2ksf_s$ components) are calculated for each model's case and are given with the values of slip in Table 5.3. Each presented value expresses the distance of an examined component from the central harmonic and is accounted for when deriving the lower bound of the window sequence length. The minimum window is derived by the parameter ξ, converging in values where the accrued resolutions capture such neighbouring components, without obscuring any information of the spectral content. The latter distances are calculated for the healthy motor as well, on the assumption of unawareness whether they are comprised in the examined signal and, if existent, they would have required a resolution at least equal to this distance. The FEM model for this motor is shown in Fig. 5.1.

Table 5.3 Slip values & distances of the $2ksf_s$ components in Hz for all cases of Model #1

Component	Case #1	Case #2	Case #3	Case #4	Case #5
	$s_1 \simeq 0.0174$	$s_2 \simeq 0.018$	$s_3 \simeq 0.0189$	$s_4 \simeq 0.0187$	$s_5 \simeq 0.0207$
$2sf_s$	1.7397	1.803	1.8853	1.8737	2.0688
$4sf_s$	3.4793	3.6061	3.7705	3.7473	4.1376
$6sf_s$	5.219	5.4091	5.6558	5.621	6.2064
$8sf_s$	6.9586	7.2122	7.5411	7.4946	8.2752

The minimum required window sequence lengths, calculated as described in Chapter 4, are presented in Table 5.4, with the value used for the parameter ξ derived from exhaustive search. Each value in the table provides a window length capable to separate and capture the the sideband given in the first column. Any of these values will separate the component from the main harmonic and will allow to apply the frequency extraction reliably. However, the largest of each column is chosen to assure seperability of frequencies distanced at least $2sf_s$ from each other; this way each sideband -if existent- will be localised on the spectrogram in a different frequency chunk, without being diffused or obscured by spectral leakage, and will be separated both from its neighbouring sideband and the main harmonic.

Table 5.4 Window sequence lower bounds for Model #1

$\xi = -0.29$	Case #1	Case #2	Case #3	Case #4	Case #5
$2sf_s$	4369	4215	4031	4056	3674
$4sf_s$	2184	2107	2016	2028	1837
$6sf_s$	1456	1405	1344	1352	1225
$8sf_s$	1092	1054	1008	1014	918

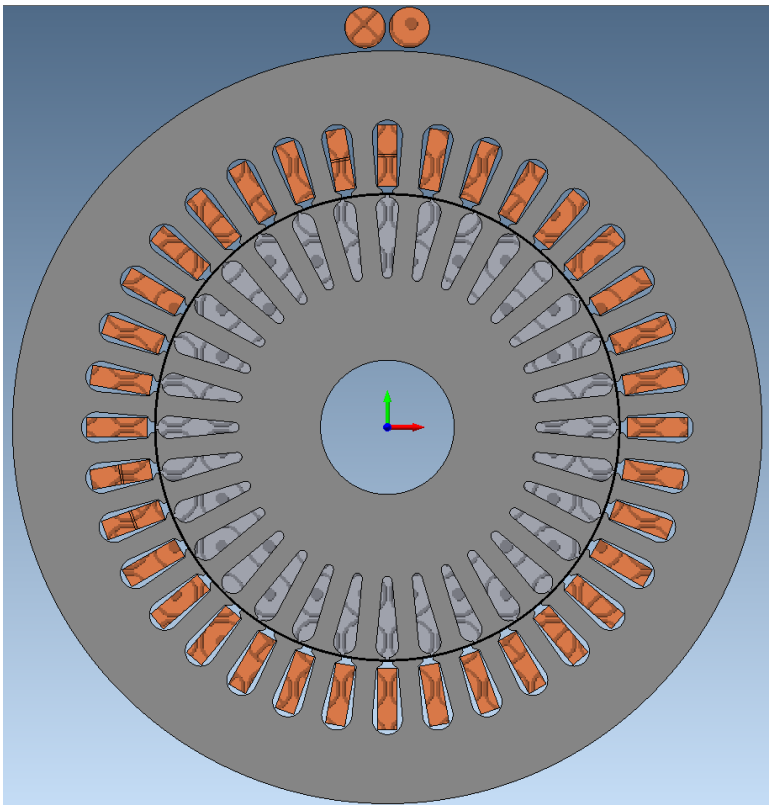

Fig. 5.1 FEM model of Model #1

5.1.1 Stator Phase Current Analysis

Long-Term vs Short-Term Windows Analysis

The two-stage analysis at the two windows of different sizes is shown in Figures 5.2 - 5.6 for every case. In each of these figures, the subfigures a & b depict the analysis under the long-term window, while the subfigures c & d the analysis under short-term windows. Starting with the first one (Fig. 5.2), by examination of the spectrogram in both stages -either with improved localisation in time or in frequency- one can easily conclude on the same observation, thus being the non-existence of sideband frequencies. Neither the $(5-4s)f_s$ and $(5-6s)f_s$, nor the $(7-6s)f_s$ and $(7-8s)f_s$ trajectories are present in the motor of Case #1. Apart from the absence of such components, the discussed spectrograms clearly denote that for a healthy machine, the spectral signatures' trajectories are of flat morphology and without undergoing any modulations at all during the steady-state regime. So, using the long-term window (Fig. 5.2 a & b), improved localisation in frequency shows that the spectrogram is clear around the area of the 5th and 7th harmonic; on the other hand, improved localisation in time confirms the assumption of a healthy motor, since the trajectories of each central harmonic are smooth and straight over time with no fluctuation of the amplitude components (Fig. 5.2 c & bd). These spectrograms are to be used as a baseline for the rest of the cases.

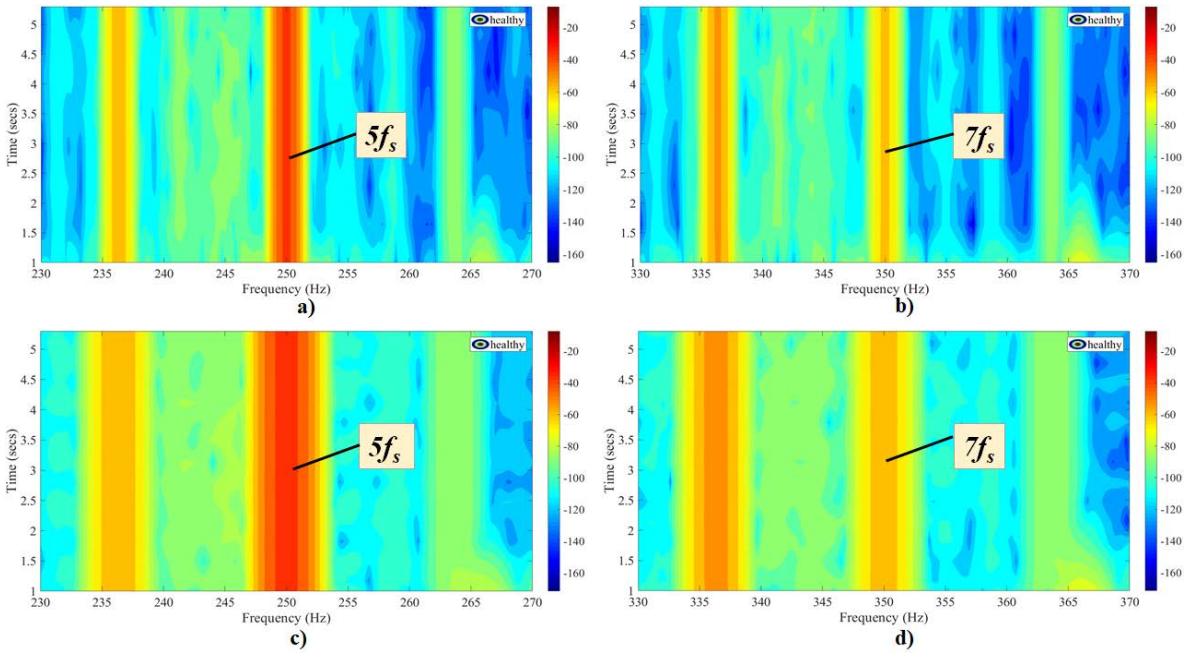

Fig. 5.2 Stages of analysis: localisation in frequency (a & b) & localisation in time (c & d) for Case #1

Nevertheless, a machine operating under the existence of a fault is practically operating in time-varying conditions. The periodicity introduced on a signal representation by the

fault's non-linearity during such time-varying conditions, is designated according to the periodicity of the fault appearance over the rotation of the rotor and the continuous induction of electromagnetic quantities from the stator to the rotor and vice-versa. The latter modulation is occurring with the $(1-2s)f_s$ as a modulating carrier, and superimposed with the even multiples $2ksf_s$ generated by the $2sf_s$ speed ripple component. Such periodicities are not always easy to track through the frequency spectra, as the assumption of quasi-state diminishes their effect during the calculation of the average spectral characteristics; therefore a time-frequency representation -where they are translated on a spectrogram as modulations- provides more definite indications for the fault condition on the pipeline for a diagnostic decision, in cases where using the classical FFT as in traditional MCSA might fail to do so due to loss of diagnostic information.

In Fig. 5.3 a & b, the spectrograms under improved frequency resolution are shown for the single bar breakage (Case #2) for the $5-th$ and $7-th$ harmonic respectively. The bins created by the rolling windows are shown upon the area of interest, marking the location of each harmonic component observed. As sidebands are clearly detected around the areas of interest, improved frequency resolution confirms they should be separated at least $2sf_s$ to allow examination for potential rotor faults and tracking of their frequency components. The components captured at the current stage are analysed at the second stage with a short-time window (Fig. 5.3 c & d). Although each selected window resolves the modulation sufficiently enough to observe its characteristics, the sideband tones might not be visually discriminated easily. However, due to the predetermined lower bound, the frequency spread has been bounded to be such that for the aim of the analysis, any existing amplitude oscillations are also discriminated. To extract such information reliably, the windows from Table 5.4 are used, providing the depicted frequency bins.

In contrast with Fig. 5.2, analysing Fig. 5.3 allows to spot the characteristics of a signal carrying information of rotor faults: a multicomponent FM signal with non-stationary characteristics is spotted by the energy transitions, which are expressed via the designated ripples; these ripples obey the modulation (FM law) with a period of $\simeq 1/2ksf_s$ and with the carrier getting strongly modulated continuously over the whole steady-state. Similar observations are valid for the adjacent double breakage scenario (Case #3). The spectrograms of Fig. 5.4 admit a multi-tone FM signal with more stationary characteristics over time which encloses a modulated carrier with modulated components, having dominant periods ranging between $\simeq 1/2sf_s$ and $\simeq 1/4sf_s$, evident in the marked areas of both the $5-th$ and the $7-th$ harmonic.

Furthermore, Fig. 5.5 and Fig. 5.6 present the spectrograms under the two analysis stages around the $5-th$ and $7-th$ harmonics frequency zones respectively. What is interesting

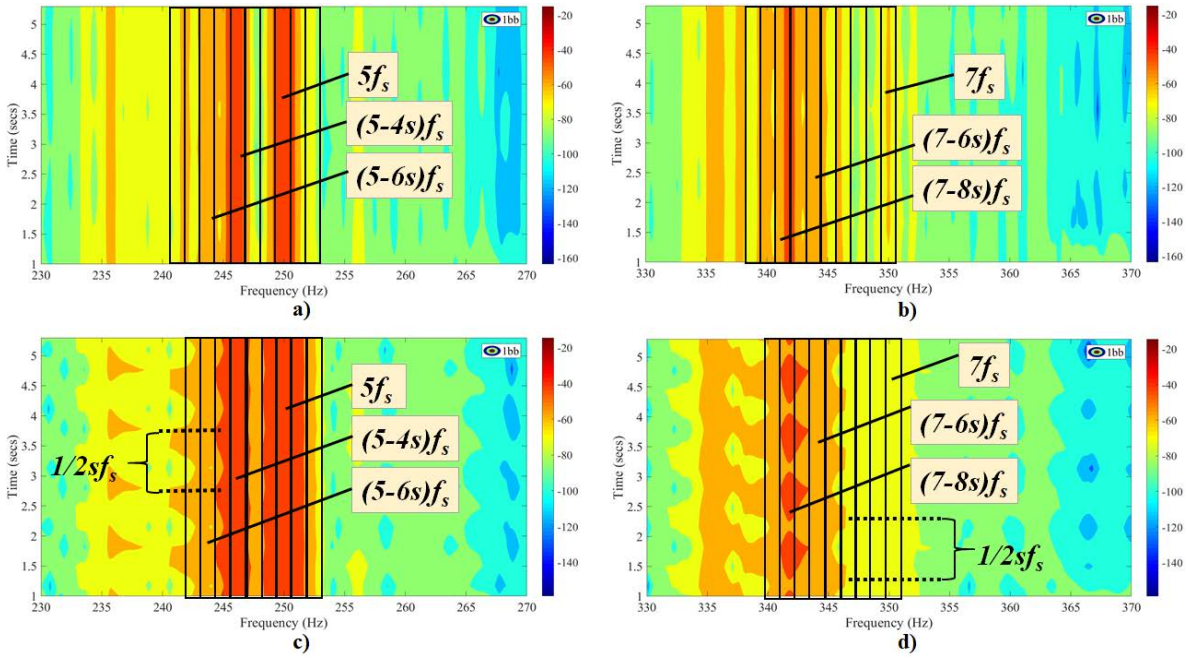

Fig. 5.3 Stages of analysis: localisation in frequency (a & b) & localisation in time (c & d) for Case #2

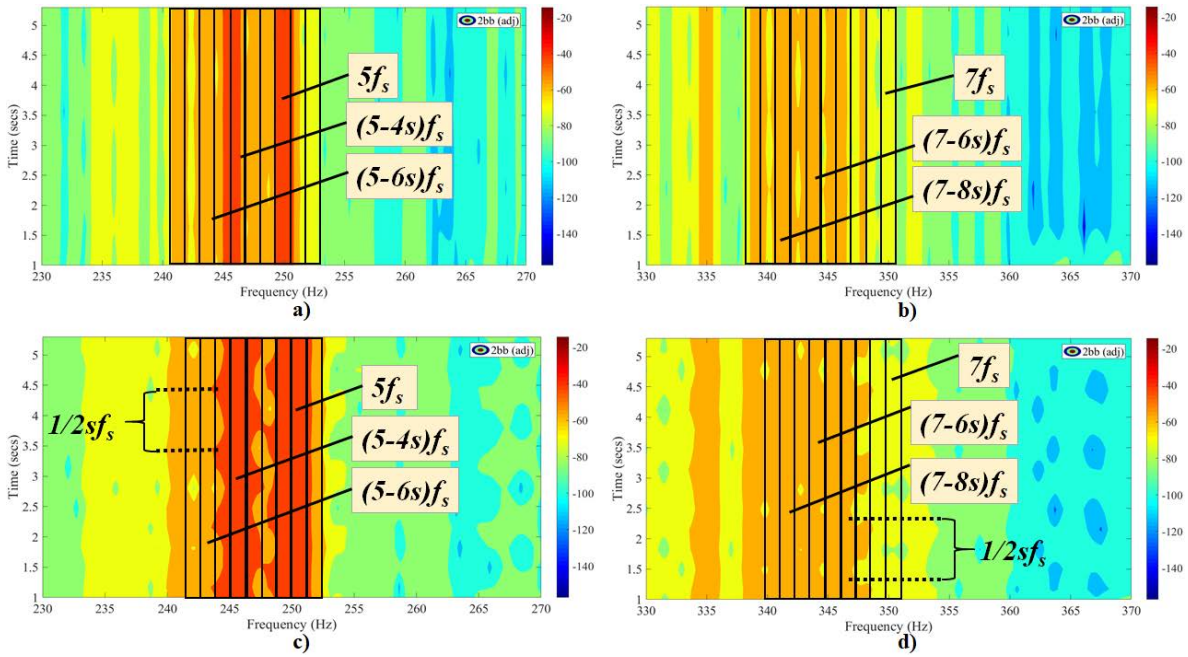

Fig. 5.4 Stages of analysis: localisation in frequency (a & b) & localisation in time (c & d) for Case #3

in both figures, is the clear presence of ripples over the whole steady-state, which are designated by the relative position of the broken bars during the rotor rotation with the stator-current winding sensing the relative position difference with the rotor mechanical frequency. This the reason that the fault modulated trajectories appear as multicomponent signals being dominantly non-stationary, whereas the single and double breakage and the double breakage are sensed once per rotor revolution due to their localisation in one point of the rotor only. This fact makes the method advantageous for the challenging cases of non-consecutive breakages at half and full pole pitch distance, as it tracks such modulations over the spectrograms before to extract the final subcomponents and represent them with the FFT.

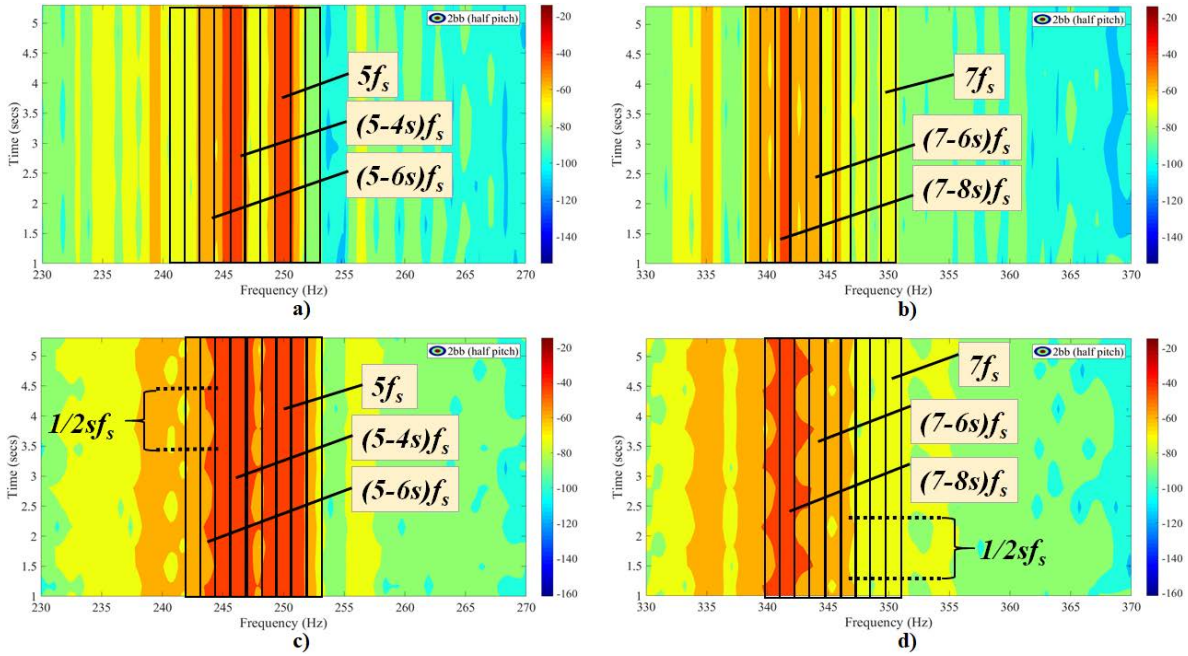

Fig. 5.5 Stages of analysis: localisation in frequency (a & b) & localisation in time (c & d) for Case #4

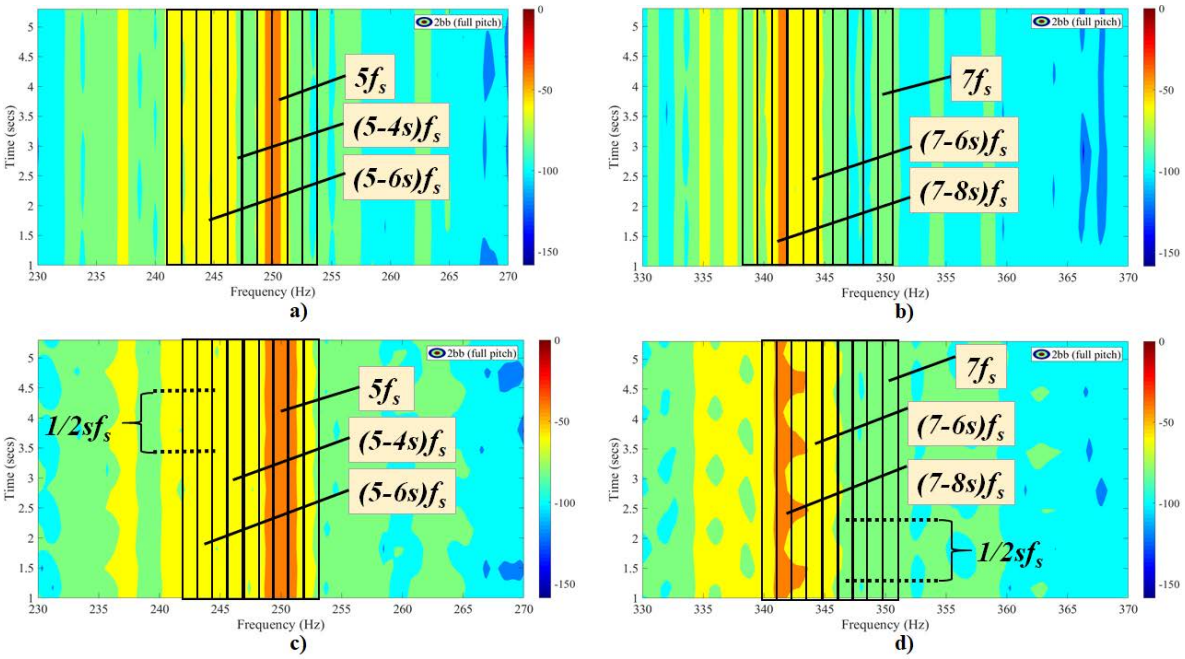

Fig. 5.6 Stages of analysis: localisation in frequency (a & b) & localisation in time (c & d) for Case #5

Frequency Extraction

After resolving the examined signals with the discussed two-stage analysis, the spectral content $S(t, f)$ is extracted. During the STFT computation with the short-term windows, three variables of the set of results are isolated from the algorithm: the time and frequency vectors and the density of the spectral energy. These are logged on a one-to-one correspondence with each other and they fully embed within the time-frame of the initial measured raw signal. Such a correspondence provides the ability to represent the spectral density $S(t, f_{a,i})$ designated over time within a specific frequency bin $f_a \pm sf_s$, hence providing a trajectory as a unique time-signal representation. An example of such a representation is shown in Fig. 5.7 & Fig. 5.8 for the upper and lower sideband components of the $5-th$ harmonic respectively.

Some of the modulations equal to $2sf_s$ and $4sf_s$ in both figures, that can be easily located visually, are labelled on the depicted waveforms. The extracted trajectory is in turn handled as a periodical time-signal, which expectedly has itself a transient response and a steady-state regime. Regarding the analysis part, the discussed approach allows to handle these signals with the FFT, as soon as the transient has elapsed and stationarity supervenes over the steady-state. The discussed signals represent the amplitude information derived from the STFT of the first stage and express how their fluctuations are correlated with the oscillations analysed on the previous spectrogram examples. The waveforms admit signals that can be characterised as stationary and mono-component, as fixing them over a frequency frame will

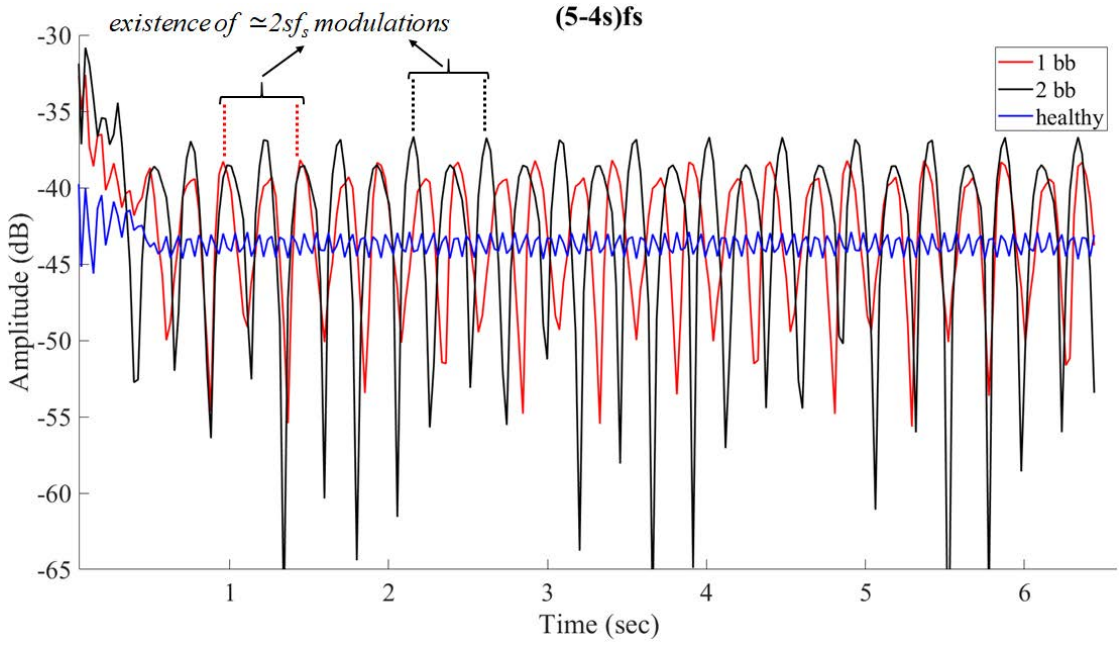

Fig. 5.7 Representation of the $S(t, f_{5,1})$ trajectories for Cases #1, #2 & #3

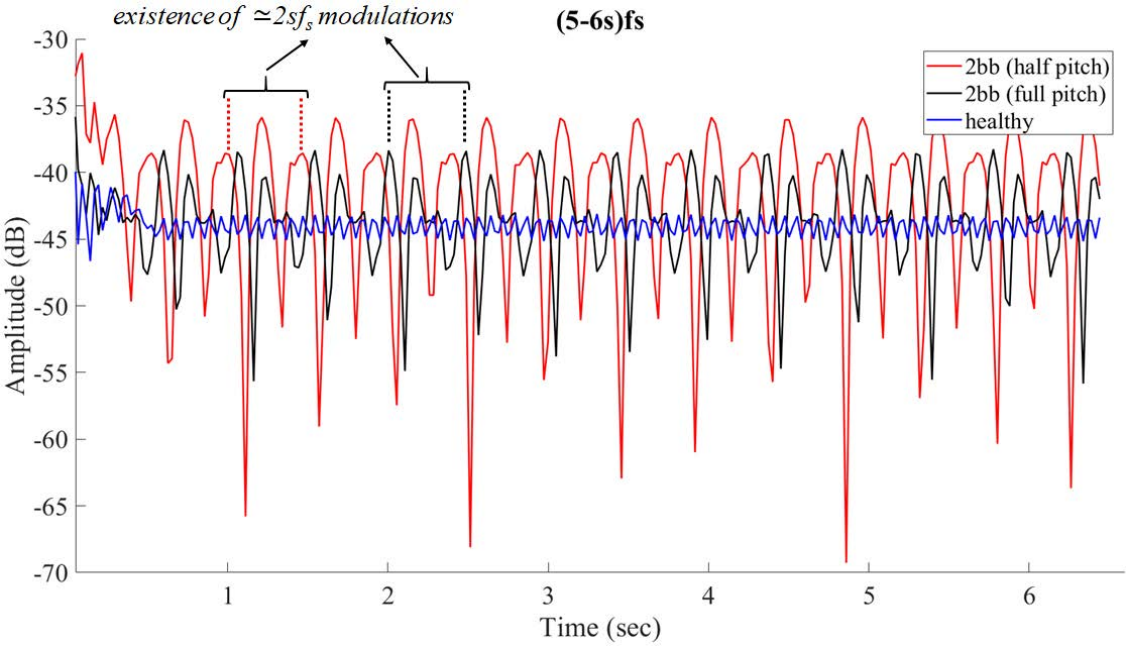

Fig. 5.8 Representation of the $S(t, f_{5,2})$ trajectories for Cases #1, #2 & #3

represent how they evolve in time, therefore the FFT is reliable to reveal their frequency content over the whole duration of the steady-state.

5-th Harmonic

Regarding the area of the $5-th$ harmonic, the results provided by the frequency extraction method are shown in Figures 5.9 & 5.10 and the amplitudes of the extracted frequency components in each harmonic are given in Table 5.5. In all FFT representations of these trajectories, even multiples of the sf_s are present, as data acquired from 2-D FEM regard a theoretically ideal model where the fault and its propagation will be tangible throughout the signals responses and transferred throughout the frequencies of stator current or stray flux during continuous induction. However, it has been shown in various works like the ones discussed in Chapter 3, and will be evident in the results of the next chapter, that in real life experimental measurements the 3-D nature of the stray magnetic fields, the inherent manufacturing imbalances, the cancellation of harmonics due to absolute symmetry and other similar factors will not reveal all of these harmonics. What is worth examining in all models at any case is the speed ripple component at $2sf_s$ and then, as each trajectory acts as a carrier, the corresponding sidebands tones. A characterisation of all these amplitudes is given at this point discussing analysing them in the $S(t, f_{5,1})$ and $S(t, f_{5,2})$ trajectories, while a comparative table for the $2sf_s$ components is discussed at the end of each analysis section for all cases in all extracted trajectories.

Considering the values presented in Table 5.5, it can be seen from Figure 5.9 that a healthy motor's extracted trajectory is of a totally different morphology than a faulty motor's, meaning that no spikes arise in any speed ripple related subcomponents and the value of the spectrum can be considered as almost a constant line. At the point where the line is drawn over a frequency bin's length, the healthy motor's (Case #1) spectrum at the $4sf_s$ and $6sf_s$ locations yields amplitudes at $-75.67\ dB$ and $-78.31\ dB$ respectively for the $S(t, f_{5,1})$ trajectory. During the single breakage (Fig. 5.9a), the same components spike at $-26.63\ dB$ and $-35.11\ dB$ respectively for Case #2. Expectedly, at the double breakage (Case #3), the discussed amplitudes are tangibly present at the level of $-22.92\ dB$ and $-30.71\ dB$ respectively (Fig. 5.9b). Interestingly, the analysed frequencies spike at a close level for the brekage at the half-pitch scenario (Case #4), thus being at $-23.76\ dB$ and $-29.28\ dB$ (Fig. 5.9c). From Fig. 5.9d, Case #5 reveals the $4sf_s$ subcomponent at $-27.67\ dB$ and the $6sf_s$ at $-38.36\ dB$. These initial results provide an indication that the method helps to track subcomponents in the post-extracted spectra, even for the challenging case of non-adjacent breakages located at half-pitch and full-pitch distance. The $2sf_s$ component presents the

values of $-70.58\ dB$, $-44.74\ dB$, $-36.02\ dB$, $-40.17\ dB$ and $-34.52\ dB$ from Case#1 - Case #5 respectively (Table 5.7).

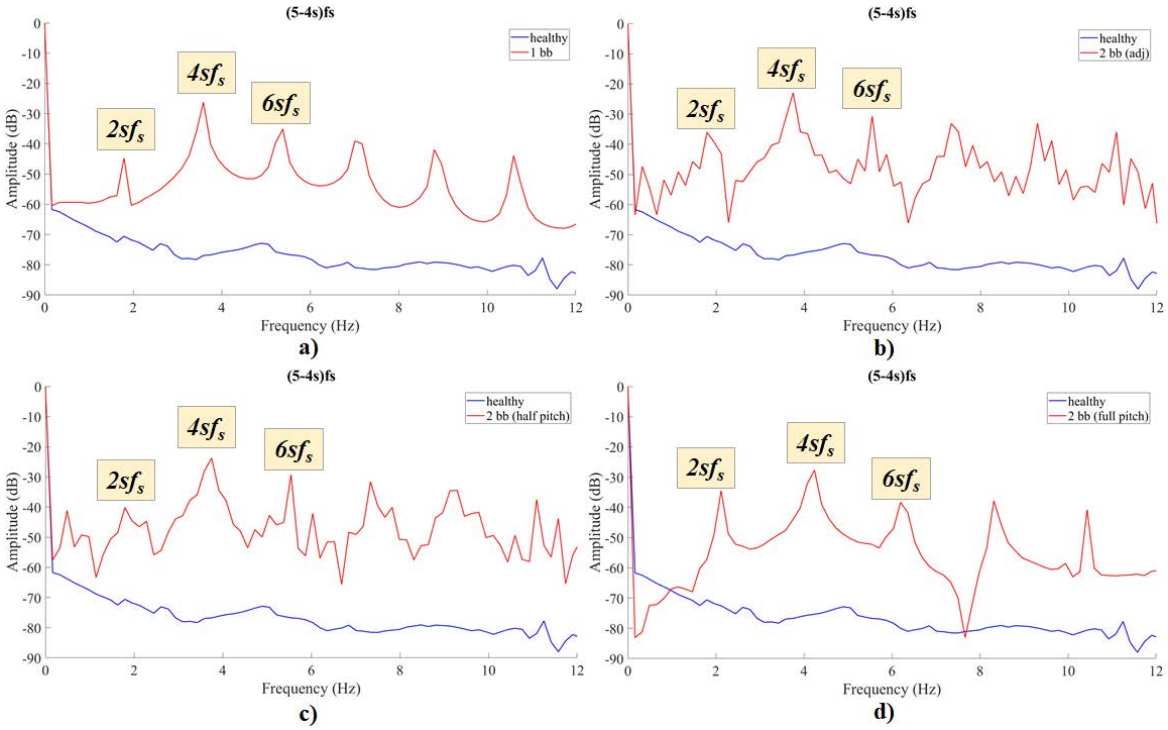

Fig. 5.9 Comparative spectra of extracted trajectories in the stator phase current for the $S(t, f_{5,1})$ spectral component: a) Case #1 vs Case #2 b) Case #1 vs Case #3 c) Case #1 vs Case #4 d) Case #1 vs Case #5

Regarding the $S(t, f_{5,2})$ trajectory, Case #1 holds an amplitude of $-76.72\ dB$ and $-78.17\ dB$ at the points of $4sf_s$ and $6sf_s$ respectively, while the same observations apply for its spectrum morphology and distribution (Fig. 5.10). These components hold the amplitude values of -25.91 and -34.62 respectively for the one broken bar of Case #2 (Fig. 5.10a). The two adjacent broken bars fault of Case #3 (Fig. 5.10b) elevates the discussed components at -23.09 and -31.38 respectively, as expected to be due to the larger asymmetry caused in the rotating magnetic field by the extended broken bar area. For the half pitch scenario of Case #4 (Fig. 5.10c), the subcomponent at $4sf_s$ elevates at $-23.74\ dB$ and the $6sf_s$ one at $-28.95\ dB$. Finally, from Fig. 5.10d, the examined components spike at $-27.74\ dB$ and $-38.26\ dB$ respectively for Case #5. Again, the latter two FEM cases are identified as rotor faults, both by the lower and upper sidebands's subcomponents at $4sf_s$ and $6sf_s$ and by the presence of the fault-related speed-ripple effect subcomponent at $2sf_s$. The latter one presents from Case #1 - Case #5 the values of $-70.59\ dB$, $-44.48\ dB$, $-34.38\ dB$, $-43.23\ dB$, $-32.93\ dB$ respectively (Table 5.7).

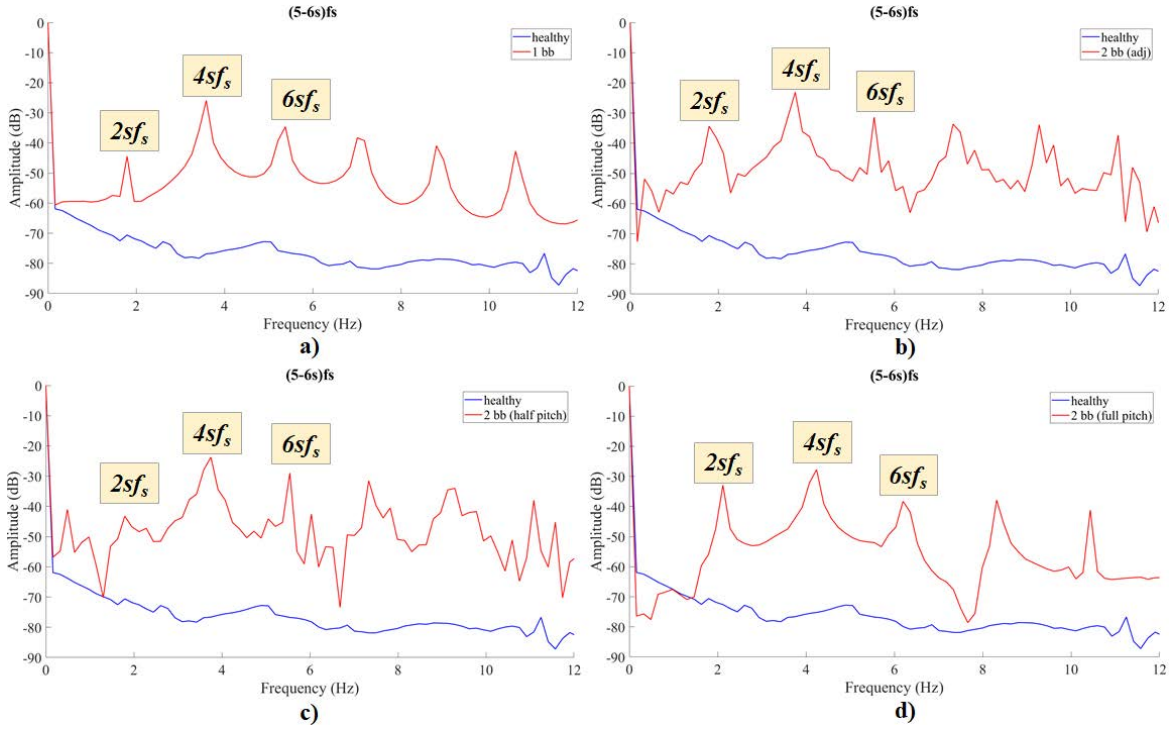

Fig. 5.10 Comparative spectra of extracted trajectories in the stator phase current for the $S(t, f_{5,2})$ spectral component: a) Case #1 vs Case #2 b) Case #1 vs Case #3 c) Case #1 vs Case #4 d) Case #1 vs Case #5

Table 5.5 FFT Amplitudes (dB) of $S(t, f_{5,i})$ for all cases of Model #1 (Stator Current)

Case	$5f_s - 4sf_s$		$5f_s - 6sf_s$	
	$4sf_s$	$6sf_s$	$4sf_s$	$6sf_s$
Case #1	-75.67	-78.31	-76.62	-78.17
Case #2	-26.23	-35.11	-25.91	-34.62
Case #3	-22.92	-30.71	-23.09	-31.38
Case #4	-23.76	-29.28	-23.74	-28.95
Case #5	-27.67	-38.36	-27.74	-38.26

7-th Harmonic

In the area of the $7-th$ harmonic, the results provided by the frequency extraction method are shown in Figures 5.11 & 5.12 and the investigated components' amplitudes are given in Tbale 5.6. The subcomponents examined in the $S(t, f_{7,i})$ carrier are the $6sf_s$ and $8sf_s$, along with the $2sf_s$ subcomponent. For the $S(t, f_{7,1})$, the healthy motor (Case #1) performs values of $-63.38\ dB$ at $6sf_s$ and $-69.67\ dB$ at $8sfs_s$. Comparing this as a baseline with Case #2, the $6sf_s$ signature rises with a difference of $27.88\ dB$ at $-41.79\ dB$, while the $8sf_s$ one performs an increase of $37\ dB$ reaching at $-32.67\ dB$. In a very similar manner with the $5-th$ harmonic, in the signatures of Case #3 the amplitudes spike at $-33.47\ dB$ and

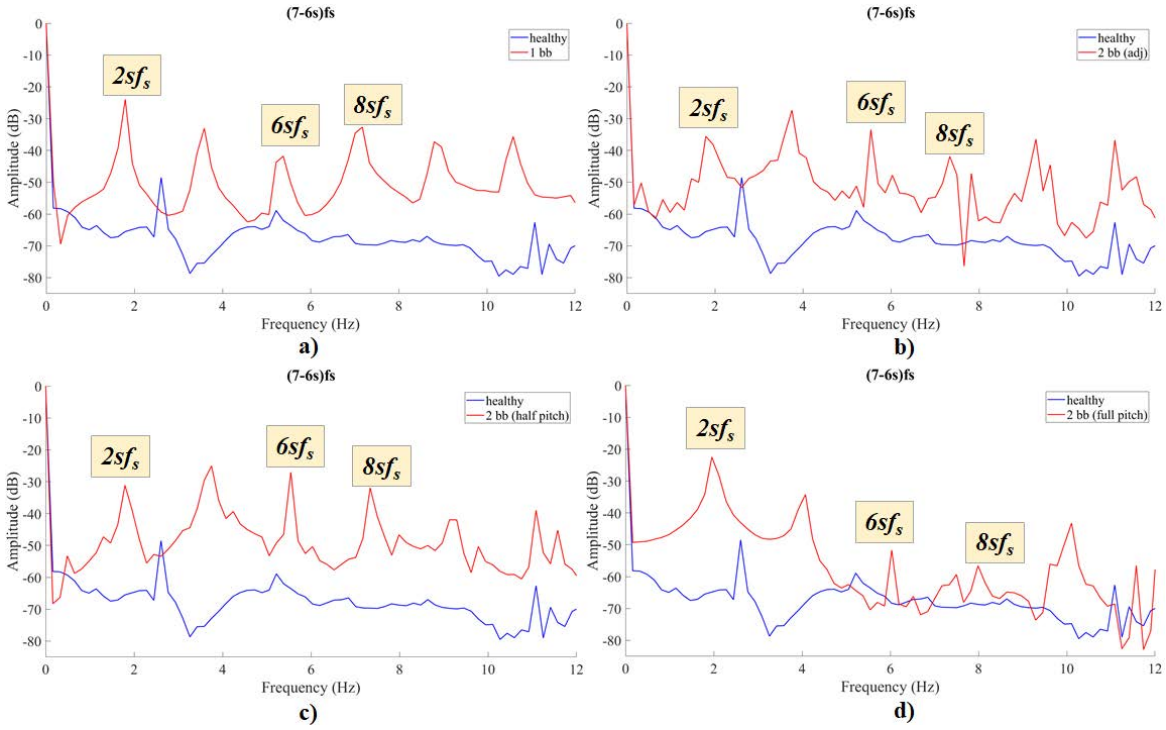

Fig. 5.11 Comparative spectra of extracted trajectories in the stator phase current for the $S(t, f_{7,1})$ spectral component: a) Case #1 vs Case #2 b) Case #1 vs Case #3 c) Case #1 vs Case #4 d) Case #1 vs Case #5

$-41.89\ dB$ for the $6sf_s$ and $8sf_s$ respectively, showing a corresponding increase of $29.91\ dB$ and $27.87\ dB$ with respect to the healthy motor (Fig. 5.11b). Compelling amplitude values to detect the fault are yielded for the challenging half-pitch breakage of Case #4, which present an increase of $36.36\ dB$ with respect to healthy motor at $6sf_s$, while the $8sf_S$ signature spikes $-31.91\ dB$ performing an increase of $37.76\ dB$ (Fig. 5.11c). In the full-pitch located breakages case (Case #5) the subcomponent of the $6sf_s$ and $8sf_s$ are not competent enough in terms of increase, however still present and tangible enough to indicate a rotor fault condition; the first one rises $11.65\ dB$ at $-51.73\ dB$, while the latter one rises $13.08\ dB$ at $-56.59\ dB$

with respect to Case #1 (Fig. 5.11d). The speed-ripple subcomponent signature at $2sf_s$ holds for thus specific trajectory the values of $-64.18\ dB$, $-23.95\ dB$, $-35.58\ dB$, $-31.15\ dB$ and $-22.51\ dB$ for Case #1 - Case #5 respectively (Table 5.7).

Table 5.6 FFT Amplitudes (dB) of $S(t, f_{7,i})$ for all cases of Model #1 (Stator Current)

Case	$7f_s - 6sf_s$		$7f_s - 8sf_s$	
	$6sf_s$	$8sf_s$	$6sf_s$	$8sf_s$
Case #1	-68.38	-69.67	-65.65	-69.02
Case #2	-41.79	-32.67	-41.28	-30.65
Case #3	-33.47	-41.89	-32.37	-41.56
Case #4	-27.02	-31.91	-27.23	-31.58
Case #5	-51.73	-56.59	-54.75	-56.03

Moving on to the $S(t, f_{7,2})$ extraction, the amplitude levels of Case #1 are at $-65.65\ dB$ and $-69.02\ dB$ for the $6sf_s$ and $8sf_s$ signature respectively (Fig. 5.12). For Case #2 in Fig. 5.12a these signatures are erected at the height of $-41.28\ dB$ and $-30.65\ dB$ respectively, thus rising $24.37\ dB$ and $38.37\ dB$ compared to Case #1. Compared to Case #1, the double breakage at adjacency fault (Case #3) shown in Fig. 5.12b makes the signature of $6sf_s$ rise $33.28\ dB$ (spike at $-32.32\ dB$) and the $8sf_s$ signature rise $27.53\ dB$ (spike at $-41.56\ dB$). In addition, the same subcomponents for Case #4 mark themselves at $-27.23\ dB$ and $-31.58\ dB$ respectively, which indicates a rise of $38.42\ dB$ and $37.44\ dB$ respectively, when compared to Case #1 (Fig. 5.12c). The last breakage scenario depicted in Fig. 5.12d (Case #5) shows an amplitude of $-54.75\ dB$ for the $6sf_s$ signature (increase of $10.9\ dB$ over healthy) and an amplitude of $-56.03\ dB$ for the $8sf_s$ (increase $12.99\ dB$ over healthy). Considering the latter signatures' behaviour along with their amplitudes in the extracted $S(t, f_{7,1})$ trajectory above for Case #5, leads to the observation that the $6sf_s$ and $8sf_s$ subcomponents -although present and duly observable- do not show a very significant amplitude change compared to the potential they show in all the other cases and harmonics. Nonetheless, the method tracks for Case #5 a strong modulating frequency at the $2sf_s$ component carried in the $S(t, f_{7,1})$ and $S(t, f_{7,2})$ trajectories. This component is seen for Case #1- Case #5 in the latter trajectory at the amplitudes of: $-66.21\ dB$, $-23.47\ dB$, $-35.14\ dB$, $-31.18\ dB$ and $-23.01\ dB$ respectively (Table 5.7).

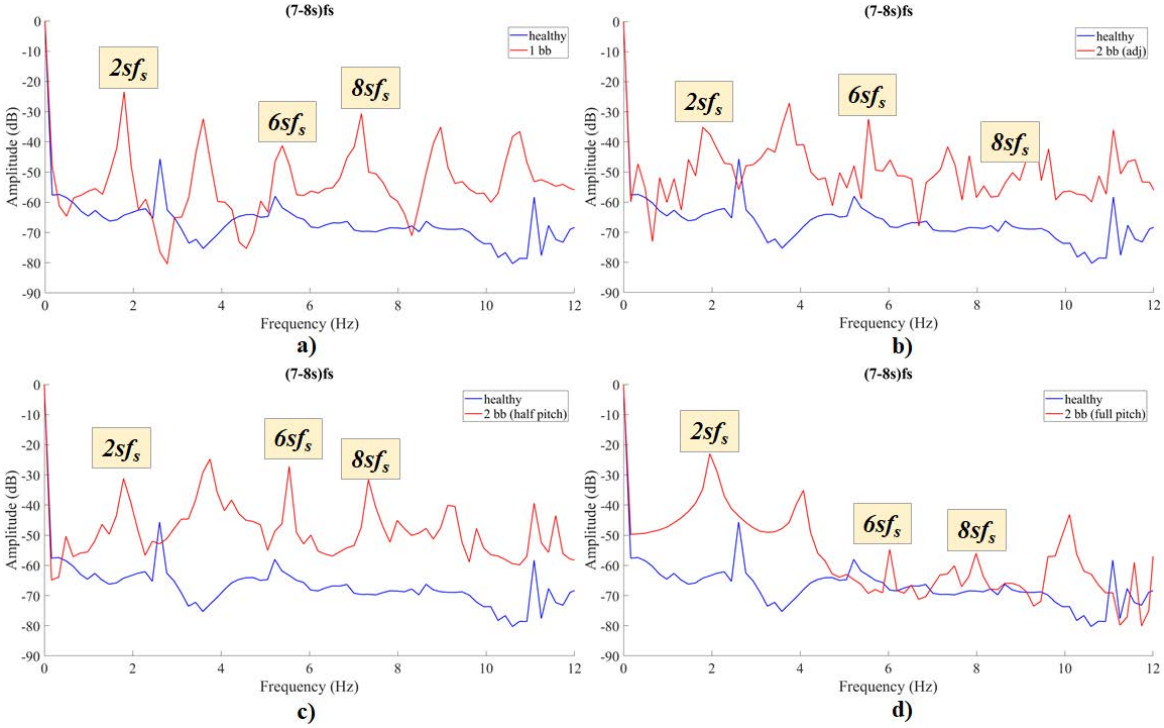

Fig. 5.12 Comparative spectra of extracted trajectories in the stator phase current for the $S(t, f_{7,2})$ spectral component: a) Case #1 vs Case #2 b) Case #1 vs Case #3 c) Case #1 vs Case #4 d) Case #1 vs Case #5

Table 5.7 Model # 1: Comparative table of the FFT amplitudes (dB) for the $2sf_s$ fault-related component in all examined harmonics for all cases - Extracted trajectories from the stator phase current spectral content

Case	$(5-4s)f_s$	$(5-6s)f_s$	$(7-6s)f_s$	$(7-8s)f_s$
Case #1	-70.58	-70.59	-64.18	-66.21
Case #2	-44.74	-44.48	-23.95	-23.47
Case #3	-36.02	-34.38	-35.58	-35.1
Case #4	-40.17	-43.23	-31.15	-31.18
Case #5	-34.52	-32.93	-22.51	-23.01

5.1.2 Stray Flux Analysis

Long-Term vs Short-Term Windows Analysis

Similarly with the stator current, the stray flux analysis starts with the discussed two-stage STFT spectrogram analysis before extraction. To aid a reader, in the all spectrograms regarding faulty cases, the bins created by the rolling windows are shown upon the area of interest as in previous section. As it was the case in the phase current signals, the stray flux signals of the healthy motor (Fig. 5.13) both stages of analysis show the non-existence of sidebands, as well as the non-existence of ripples over the whole steady-state regime. The spectral energy density is again characterised for enhancing only central frequencies of straight and flat morphology, which is evident in all the spectrograms of Fig. 5.13 and confirms a healthy rotor. Once again, these spectrograms are to be used as a baseline for the faulty ones. More importantly though, what one can derive from them is the fact that assumptions of stationarity or quasi-steady-state concepts are conveniently applicable only when a motor is healthy. In that case, the induction motor can be approached as a non-linear multiple input-multiple output system, which is approached linearly around points of operation - a concept demonstrated the past two decades and is combined with system modelling and application of control concepts.

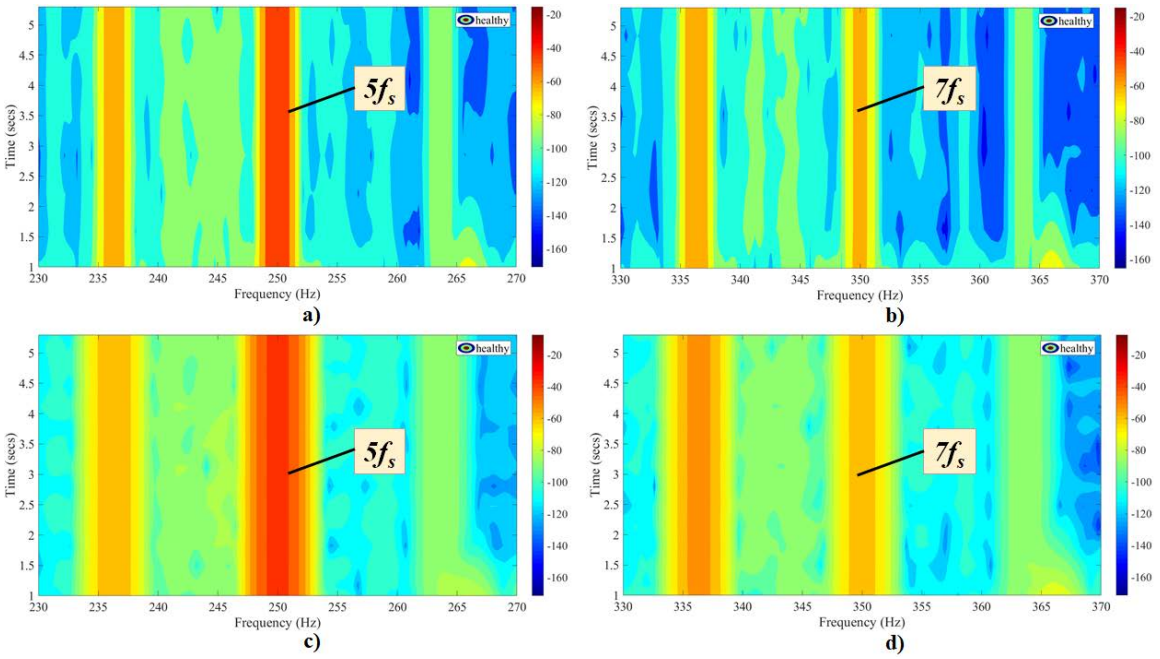

Fig. 5.13 Stages of analysis: localisation in frequency (a & b) & localisation in time (c & d) for Case #1

What is of interest in the research community however is the global monitoring and characterisation of electrical machine signals during fault conditions with a valuable perspective,

accounting for inherent system parameters like the slip and considering the non-linear distortions that are forced into the system like a fault's periodicity or the magnetic field distortions and asymmetry propagations. Such an approach for signal characterisation is attempted with the presented method. It is considered to have a major significance and contribution, as two aspects are covered, aiming for reliable and definitive diagnosis of rotor electrical faults: initially, with the two-stage approach the global characterisation is achieved and qualitatively analysed before proceeding to the post-processing; secondly, using only the stabilised part of the monitored system (steady-state regime) extraction of the frequency carrying components and evaluation of their own spectral content over time allows to track signatures forced into the varying amplitude signals during faults by fundamental mechanisms like the speed-ripple effect and the continuous $(1-s)f_s$ modulation during high-speed rotation and induction.

The single and double breakage scenarios (Case #2 and Case #3 respectively) are shown in Figures 5.14 and 5.15 respectively. Evidently, sidebands are detected by the long-term windows (Fig. 5.14a, b & Fig. 5.15a, b). In contrast with the stator current signals, the spectral density trajectories of the stray flux signals reveals more intense ripples in these cases. More specifically, oscillations of the period $1/2sf_s$ and $1/4sf_s$ are easily tracked in Figures 5.14c, d and 5.15c, d throughout the whole steady-state. Similar multicomponent signal profiles with tangible non-stationary characteristics are seen from the stray flux signals in the double breakage non-adjacent scenarios. More specifically, non-stationary multi-tone FM signals with carriers in the central frequencies of each graph and modulating sideband tones in their vicinity are admitted by the short-term windows. The modulating frequencies are dominant over the amplitude fluctuations as well, with a weakness of spectral components in the $S(t, f_{7,i})$ trajectory of Case #3 and the $S(t, f_{5,i})$ trajectory of Case #5.

The differences observed in the modulation patterns between stator current signals and stray flux signals relates with the differences observed also in the extracted components potency, as also explained in previous section. As stated in works of the latest years -and as also seen from the analysis here- it is sometimes essential to have diagnostic techniques like the stator current analysis and the stray flux analysis working complementary in a diagnostic process. Except for the prophylactic reasons, analysis provided on a machine through two measurements cross-validates the harmonic analysis for frequency tracking of fault-related components and subcomponents. At the same time, privileges of the one method cover drawbacks of the other and frequencies not detected or found at lower elevating amplitudes are tracked in the mutual cover of one to the other.

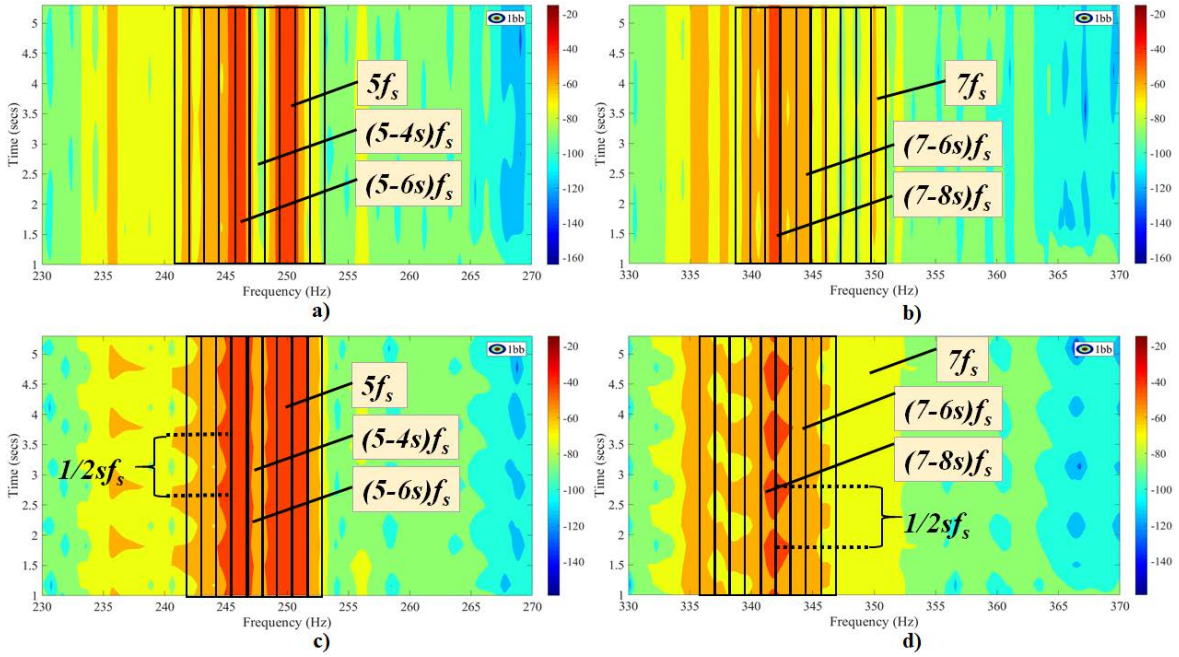

Fig. 5.14 Stages of analysis: localisation in frequency (a & b) & localisation in time (c & d) for Case #2

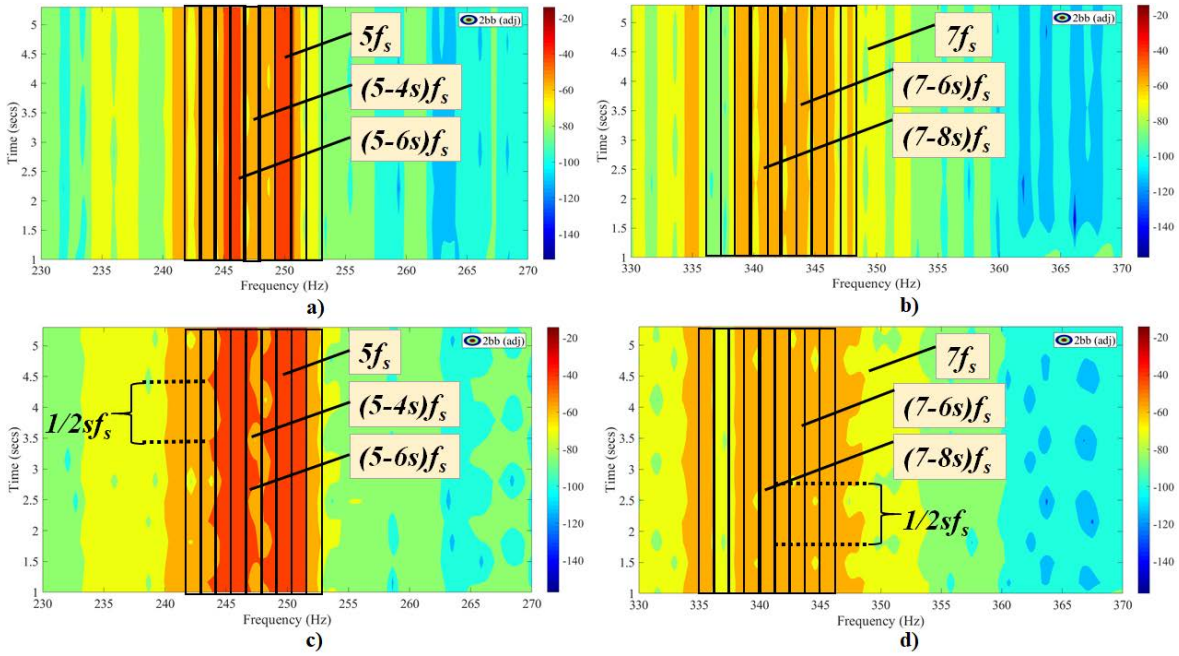

Fig. 5.15 Stages of analysis: localisation in frequency (a & b) & localisation in time (c & d) for Case #3

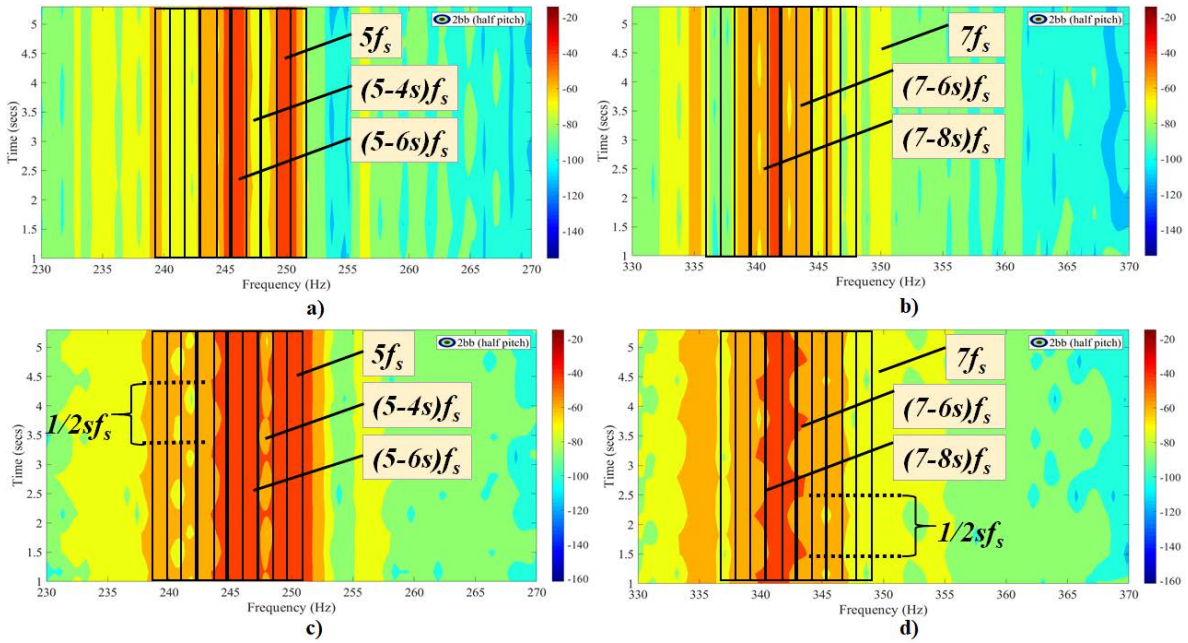

Fig. 5.16 Stages of analysis: localisation in frequency (a & b) & localisation in time (c & d) for Case #4

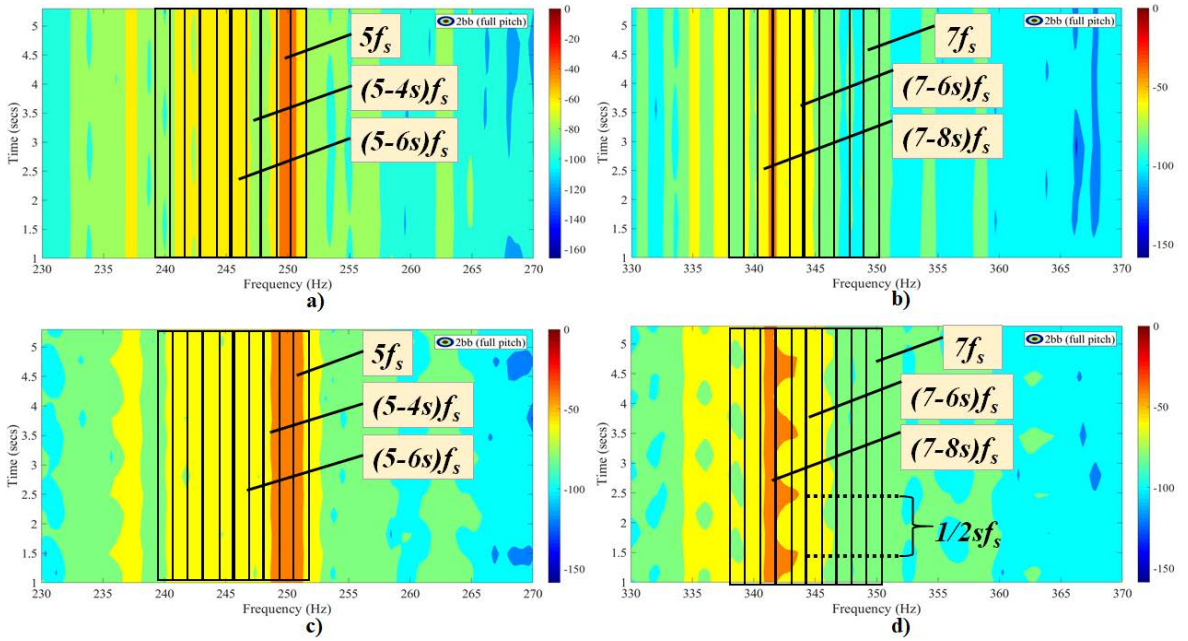

Fig. 5.17 Stages of analysis: localisation in frequency (a & b) & localisation in time (c & d) for Case #5

Frequency Extraction

5-th Harmonic

As done for the stator current measurements, after resolving the examined signals with the discussed two-stage analysis, the spectral content $S(t, f)$ is extracted. An example of stray flux extracted trajectories is shown in Fig. 5.18 & Fig. 5.19 for the upper and lower sideband components of the $5-th$ harmonic respectively. Some of the modulations equal to $2sf_s$ and $4sf_s$ in both figures, that can be easily located visually, are labelled on the depicted waveforms. The extracted trajectory is in turn handled as a periodical time-signal and their FFT's are computed. The waveforms admit signals that can be characterised as stationary and mono-component, as fixing them over a frequency frame will represent how they evolve in time, therefore the FFT is reliable to reveal their frequency content over the whole duration of the steady-state. The discussed signals represent the amplitude information changes and the information is extracted from the STFT ridges.

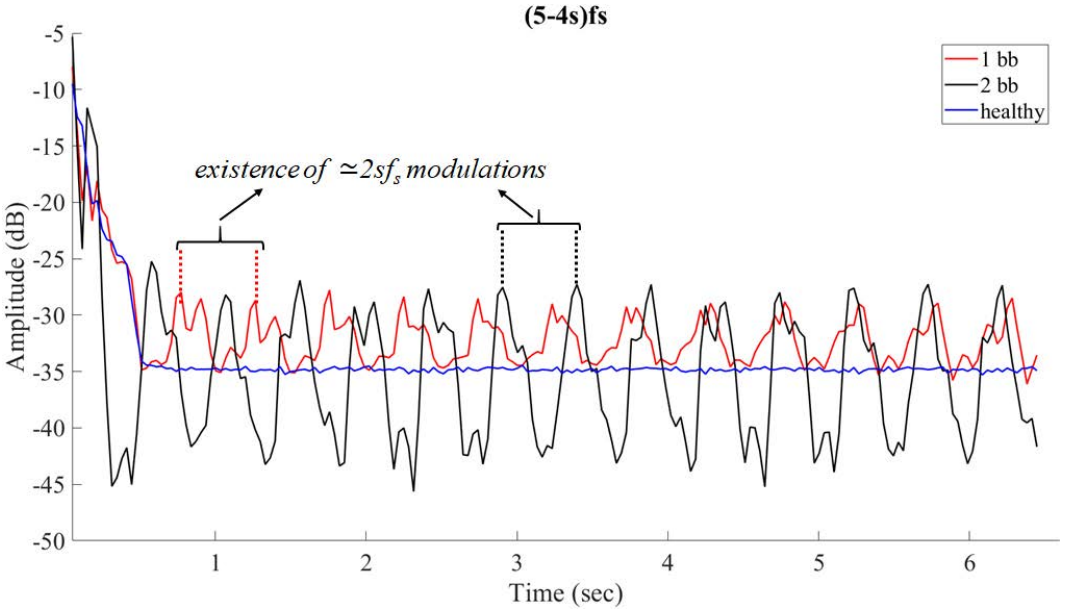

Fig. 5.18 Representation of the $S(t, f_{5,1})$ trajectories for Cases #1, #2 & #3

Regarding the area of the $5-th$ harmonic, the results provided by the frequency extraction are shown in Figures 5.20 & 5.21 and the amplitudes of the extracted frequency components in each harmonic are given in Table 5.8. In all FFT representations of these trajectories, even multiples of the sf_s are present. The same explanation as in the stator current applies, as data acquired from 2-D FEM regard a theoretically ideal model where the fault and its propagation will be tangible throughout the signals responses and transferred throughout the frequencies of stator current or stray flux during continuous induction.

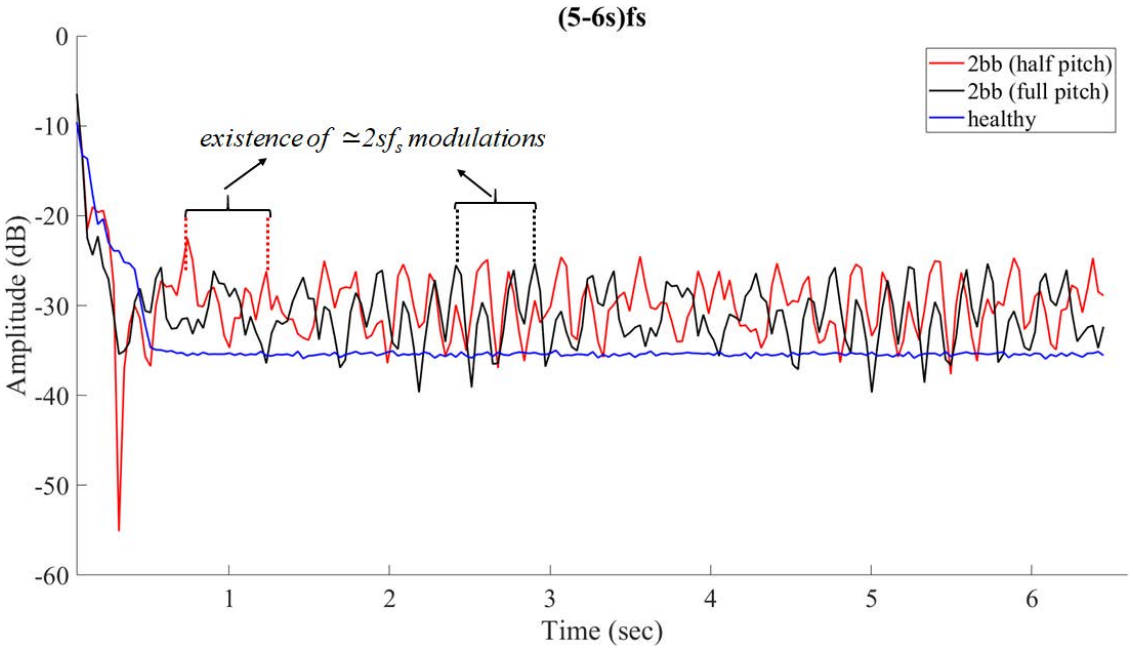

Fig. 5.19 Representation of the $S(t, f_{5,2})$ trajectories for Cases #1, #2 & #3

Considering the values presented in Table 5.8, it can be seen from Figure 5.20 that the same conclusion can be drawn about a healthy motor's extracted trajectory, thus being of a unique its own morphology than a faulty motor's, meaning that no spikes arise in any speed ripple related subcomponents and the value of the spectrum can be considered as almost a constant line. Localised within a frequency bin's length, Case #1 has a spectrum value at the $4sf_s$ and $6sf_s$ locations spiking at $-73.97\ dB$ and $-79.21\ dB$ respectively for the $S(t, f_{5,1})$ trajectory. During the single breakage (Fig. 5.20a), the same components spike at $-38.07\ dB$ and $-36.26\ dB$ respectively for Case #2. For Case #3 the discussed amplitudes are at the level of $-38.49\ dB$ and $-31.87\ dB$ respectively (Fig. 5.20b). For the two breakages at the half-pitch scenario (Case #4) the same components elevate at $-31.79\ dB$ and $-31.95\ dB$ (Fig. 5.20c). From Fig. 5.20d, Case #5 reveals the $4sf_s$ subcomponent at $-28.19\ dB$ and the $6sf_s$ at $-27.18\ dB$. The results provide validation of the method by FEM proving it as a reliable solution for the detection of non-adjacent broken bars. The $2sf_s$ component presents the values of $-67.63\ dB$, $-34.37\ dB$, $-25.95\ dB$, $-31.27\ dB$ and $-17.17\ dB$ from Case#1 - Case #5 respectively (Table 5.10).

Regarding the $S(t, f_{5,2})$ trajectory, Case #1 holds an amplitude of $-74.7\ dB$ and $-72.12\ dB$ at the points of $4sf_s$ and $6sf_s$ respectively, while the same observations apply for its spectrum morphology and distribution (Fig. 5.21). These components hold the amplitude values of -37.1 and -32.88 respectively for the one broken bar of Case #2 (Fig. 5.21a). The two adjacent broken bars fault of Case #3 (Fig. 5.21b) elevates the discussed components at

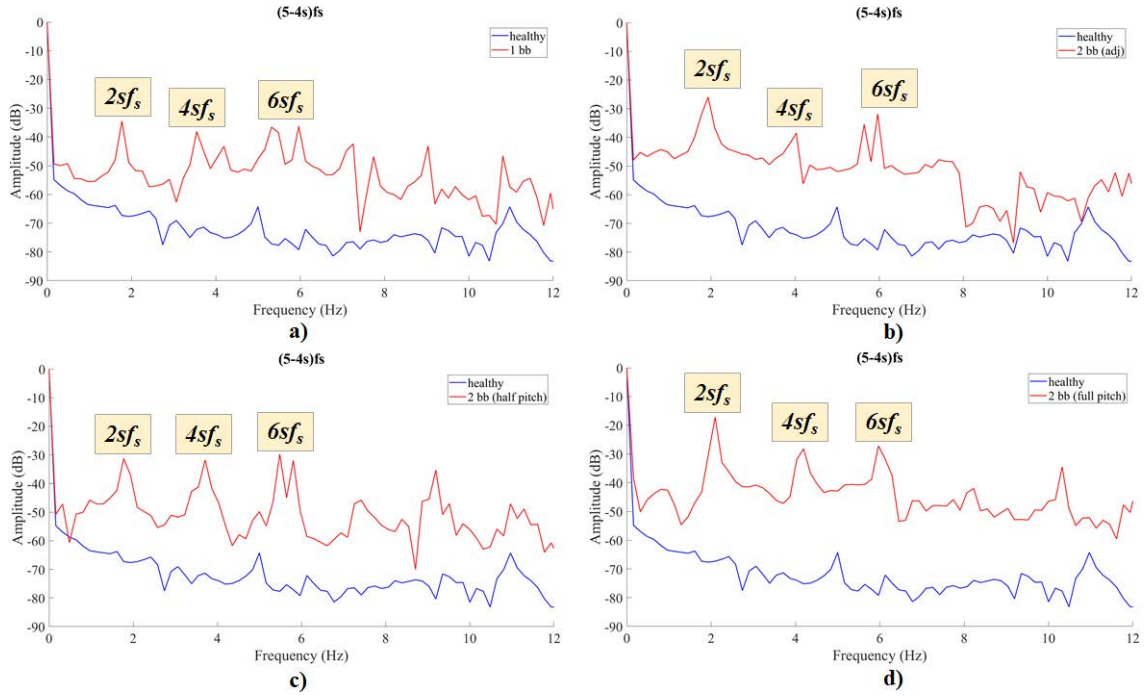

Fig. 5.20 Comparative spectra of extracted trajectories in the stray flux for the $S(t, f_{5,1})$ spectral component: a) Case #1 vs Case #2 b) Case #1 vs Case #3 c) Case #1 vs Case #4 d) Case #1 vs Case #5

-36.07 and -31.38 respectively, as expected to be due to the larger local asymmetry induced from the breakage part. For the half pitch scenario of Case #4 (Fig. 5.21c), the subcomponent at $4sf_s$ elevates at -31.11 dB and the $6sf_s$ one at -29.94 dB. Finally, from Fig. 5.21d, the examined components spike at -26.67 dB and -25.62 dB respectively for Case #5. Again, the latter two FEM cases are reliably diagnosed as rotor faults, both by the lower and upper sidebands's subcomponents at $4sf_s$ and $6sf_s$ and by the presence of the fault-related speed-ripple effect subcomponent at $2sf_s$. The latter one presents from Case #1 - Case #5 the values of -67.9 dB, -33.79 dB, -26.76 dB, -31.99 dB, -19.4 dB respectively (Table 5.10).

Table 5.8 FFT Amplitudes (dB) of $S(t, f_{5,i})$ for all cases of Model #1 (Stray Flux)

Case	$5f_s - 4sf_s$		$5f_s - 6sf_s$	
	$4sf_s$	$6sf_s$	$4sf_s$	$6sf_s$
Case #1	-73.97	-79.21	-74.7	-72.12
Case #2	-38.07	-36.26	-37.1	-32.88
Case #3	-38.49	-31.87	-36.07	-31.38
Case #4	-31.79	-31.95	-31.11	-29.94
Case #5	-28.19	-27.18	-26.67	-25.62

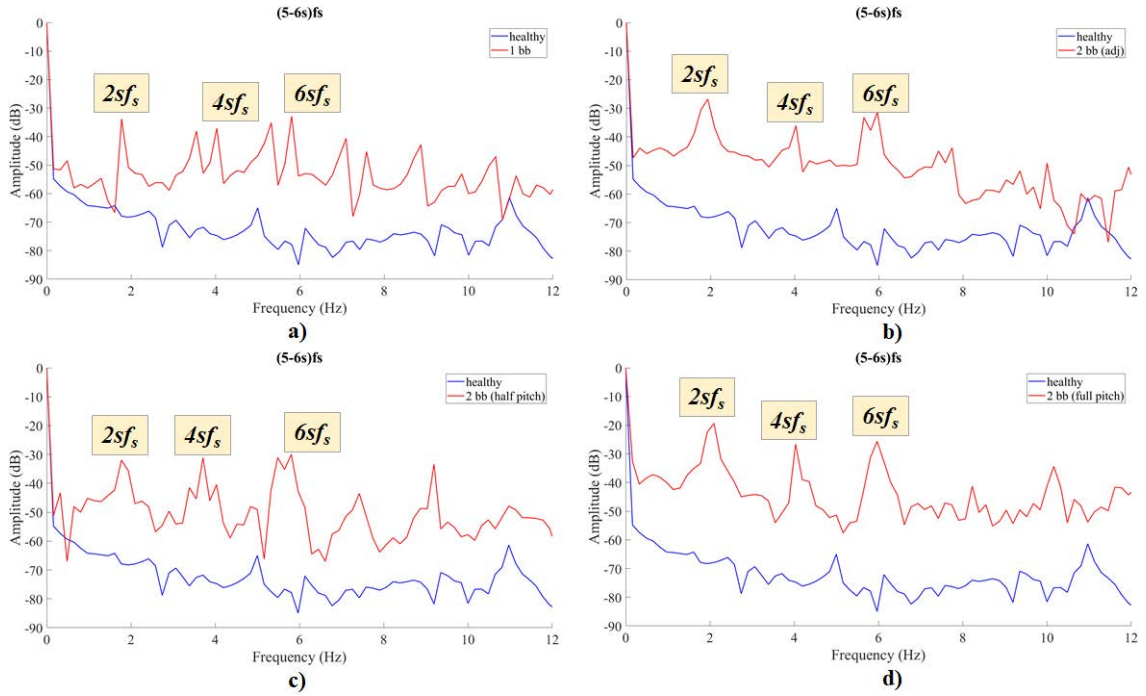

Fig. 5.21 Comparative spectra of extracted trajectories in the stray flux for the $S(t, f_{5,2})$ spectral component: a) Case #1 vs Case #2 b) Case #1 vs Case #3 c) Case #1 vs Case #4 d) Case #1 vs Case #5

7-th Harmonic

In the area of the $7-th$ harmonic, the results provided by the frequency extraction method are shown in Figures 5.22 & 5.23 and the investigated components' amplitudes are given in Tbale 5.9. The subcomponents examined in the $S(t, f_{7,i})$ carrier are the $6sf_s$ and $8sf_s$, along with the $2sf_s$ subcomponent. For the $S(t, f_{7,1})$, the healthy motor (Case #1) performs values of $-81.37\ dB$ at $6sf_s$ and $-80.77\ dB$ at $8sfs_s$. Comparing this as a baseline with Case #2, the $6sf_s$ signature rises with a difference of $45.68\ dB$ at $-35.69\ dB$, while the $8sf_s$ one performs an increase of $49.43\ dB$ reaching at $-31.38\ dB$ (5.22a). In a very similar manner with the $5-th$ harmonic, in the signatures of Case #3 the amplitudes spike at $-34.23\ dB$ and $-29.31\ dB$ for the $6sf_s$ and $8sf_s$ respectively, showing a corresponding increase of $47.14\ dB$ and $51.46\ dB$ with respect to the healthy motor (Fig. 5.22b). Compelling amplitude values to detect the fault are yielded for the challenging half-pitch breakage of Case #4, which present an increase of $49.87\ dB$ with respect to healthy motor at $6sf_s$ ($-31.5\ dB$), while the $8sf_S$ signature spikes $-46.45\ dB$ performing an increase of $34.32\ dB$ (Fig. 5.22c). In the full-pitch located breakages case (Case #5) the subcomponent of the $6sf_s$ and $8sf_s$ are quite competent compared to the same harmonic examined in the stator current; the first one ($6sf_s$) rises $57.7\ dB$ at $-23.67\ dB$, while the latter one rises $54.45\ dB$ at $-26.32\ dB$ with respect to Case #1 (Fig. 5.22d). The speed-ripple subcomponent signature at $2sf_s$ holds for

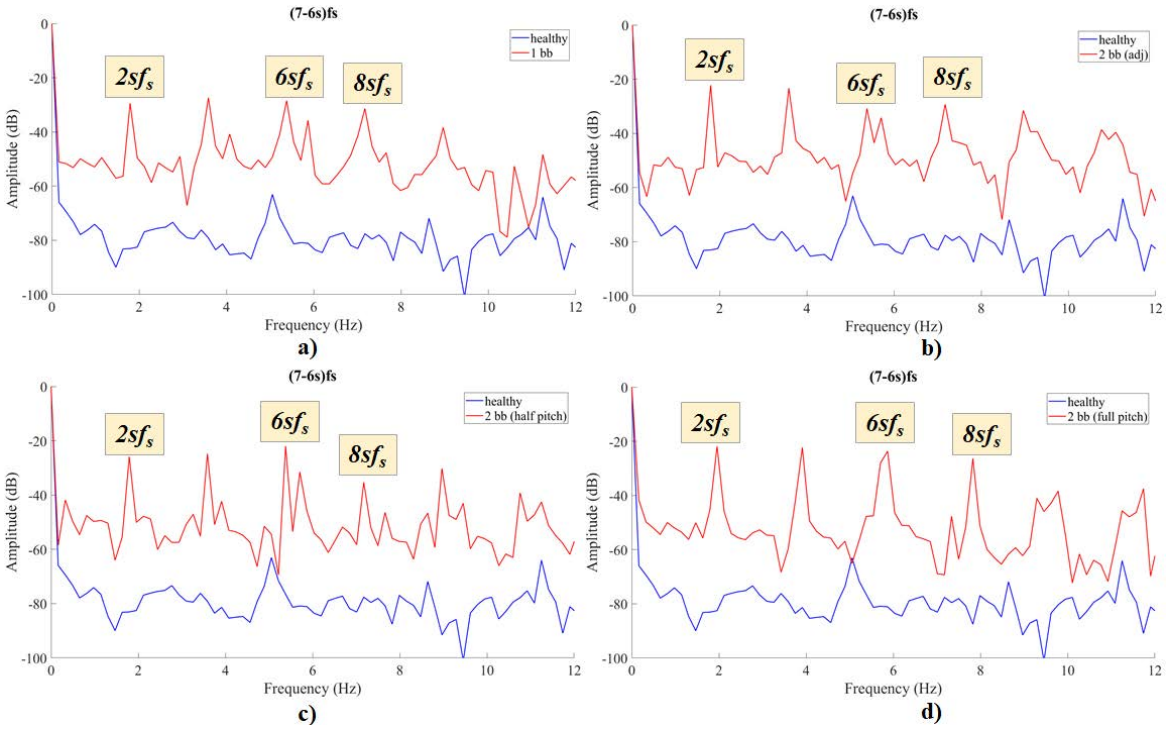

Fig. 5.22 Comparative spectra of extracted trajectories in the stray flux for the $S(t, f_{7,1})$ spectral component: a) Case #1 vs Case #2 b) Case #1 vs Case #3 c) Case #1 vs Case #4 d) Case #1 vs Case #5

thus specific trajectory the values of $-82.53\ dB$, $-29.34\ dB$, $-22.24\ dB$, $-25.89\ dB$ and $-21.91\ dB$ for Case #1 - Case #5 respectively (Table 5.10).

Moving on to the $S(t, f_{7,2})$ extraction, the amplitude levels of Case #1 are at $-81.79\ dB$ and $-83.34\ dB$ for the $6sf_s$ and $8sf_s$ signature respectively (Fig. 5.23). For Case #2 in Fig. 5.23a these signatures are erected at the height of $-33.24\ dB$ and $-37.25\ dB$ respectively, thus rising $48.55\ dB$ and $46.09\ dB$ compared to Case #1. Compared to Case #1, the double breakage at adjacency fault (Case #3) shown in Fig. 5.23b makes the signature of $6sf_s$ rise $49.93\ dB$ (spike at $-31.86\ dB$) and the $8sf_s$ signature rise $53.71\ dB$ (spike at $-29.63\ dB$). In addition, the same subcomponents for Case #4 mark themselves at $-28.41\ dB$ and $-35.34\ dB$ respectively, which indicates a rise of $53.38\ dB$ and $48\ dB$ respectively, when compared to Case #1 (Fig. 5.23c). The last breakage scenario depicted in Fig. 5.23d (Case #5) shows an amplitude of $-24.11\ dB$ for the $6sf_s$ signature (increase of $57.68\ dB$ over healthy) and an amplitude of $-27.24\ dB$ for the $8sf_s$ (increase $56.1\ dB$ over healthy). Considering the latter signatures' behaviour along with their amplitudes in the extracted $S(t, f_{7,1})$ trajectory above for Case #5, leads to the observation that the $6sf_s$ and $8sf_s$ subcomponents perform a much greater diagnostic potential than the corresponding harmonics in the stator current, something that marks again the conclusion that stray flux and stator current measurement should be working complementary. The tracking of the $2sf_s$ frequencies for Case #5 reveals a strong

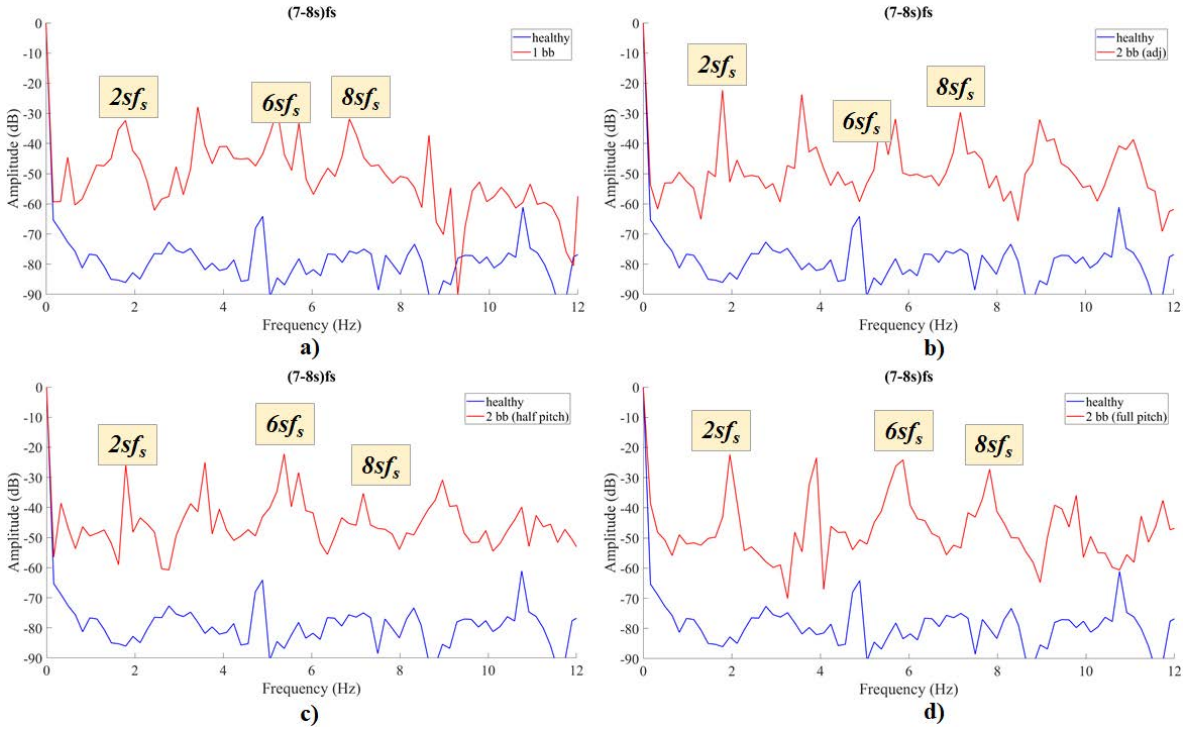

Fig. 5.23 Comparative spectra of extracted trajectories in the stray flux for the $S(t, f_{7,2})$ spectral component: a) Case #1 vs Case #2 b) Case #1 vs Case #3 c) Case #1 vs Case #4 d) Case #1 vs Case #5

modulating frequency at the $2sf_s$ component carried in the $S(t, f_{7,1})$ and $S(t, f_{7,2})$ trajectories. This component is seen for Case #1- Case #5 in the latter trajectory at the amplitudes of: $-66.21\ dB$, $-23.47\ dB$, $-35.14\ dB$, $-31.18\ dB$ and $-23.01\ dB$ respectively (Table 5.10).

Table 5.9 FFT Amplitudes (dB) of $S(t, f_{7,i})$ for all cases of Model #1 (Stray Flux)

Case	$7f_s - 6sf_s$		$7f_s - 8sf_s$	
	$6sf_s$	$8sf_s$	$6sf_s$	$8sf_s$
Case #1	-81.37	-80.77	-81.79	-83.34
Case #2	-35.69	-31.38	-33.24	-37.25
Case #3	-34.23	-29.31	-31.86	-29.63
Case #4	-31.5	-46.45	-28.41	-35.34
Case #5	-23.67	-26.32	-24.11	-27.24

Table 5.10 Model # 1: Comparative table of the FFT amplitudes (dB) for the $2sf_s$ fault-related component in all examined harmonics for all cases - Extracted trajectories from the radial stray flux spectral content

Case	$(5-4s)f_s$	$(5-6s)f_s$	$(7-6s)f_s$	$(7-8s)f_s$
Case #1	-67.63	-67.9	-82.53	-82.82
Case #2	-34.47	-33.79	-29.43	-32.34
Case #3	-25.95	-26.76	-22.24	-22.33
Case #4	-31.27	-31.99	-25.89	-25.85
Case #5	-17.17	-19.4	-21.91	-22.4

5.2 Model #2

Reliable Limit for Extraction

All components at twice the slip frequency ($\simeq 2ksf_s$ components) are calculated for each model's case and are given with the values of slip in Table 5.11. As it was for Model #1 (Table 5.3), the presented value expresses the distance of an examined component from the central harmonic and is accounted for when deriving the lower bound of the window sequence length. The FEM model for this motor is shown in Fig. 5.24.

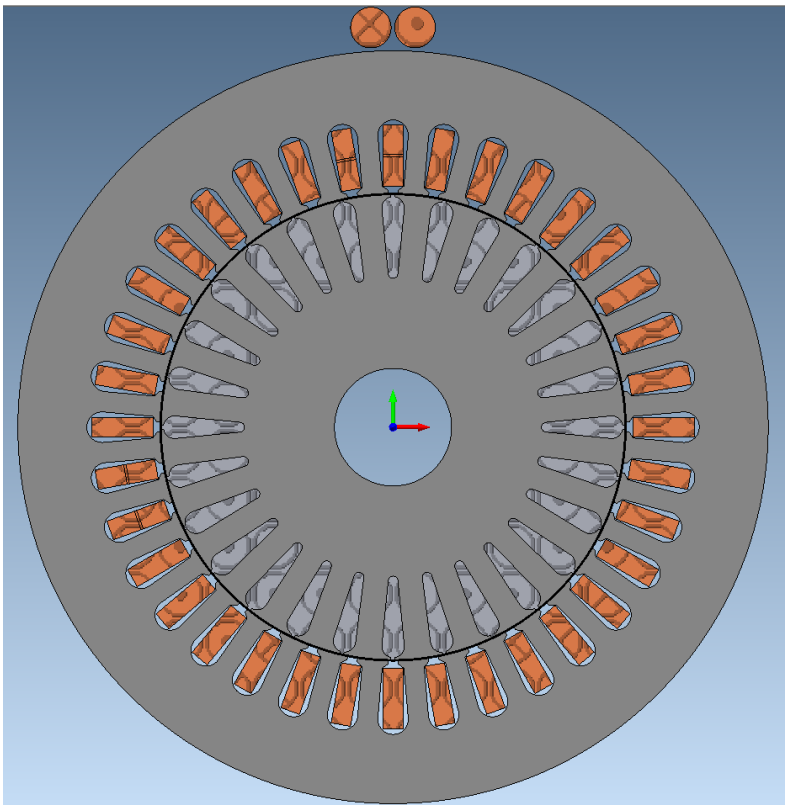

Fig. 5.24 FEM model of Model #2

Table 5.11 Slip values & distances of the $2ksf_s$ components in Hz for all cases of Model #2

Component	Case #1	Case #2	Case #3	Case #4	Case #5
	$s_1 \simeq 0.0195$	$s_2 \simeq 0.0204$	$s_3 \simeq 0.0215$	$s_4 \simeq 0.0213$	$s_5 \simeq 0.0212$
$2sf_s$	1.952	2.039	2.15	2.132	2.125
$4sf_s$	3.904	4.079	4.301	4.265	4.249
$6sf_s$	5.856	6.118	6.451	6.397	6.374
$8sf_s$	7.809	8.157	8.602	8.529	8.499

The minimum required window sequence lengths, calculated as described in Chapter4, are presented in Table 5.12 with the value used for the parameter ξ derived from exhaustive search. Each value in the table provides a window length capable to separate and capture the the sideband given in the first column. As done for Model #1, the largest of each column is chosen to assure seperability of frequencies distanced at least $2sf_s$ from each other and localisation in the next frequency chunk.

Table 5.12 Window sequence lower bounds for Model #2

$\xi = -0.14$	Case #1	Case #2	Case #3	Case #4	Case #5
$2sf_s$	4716	4515	4281	4317	4333
$4sf_s$	2358	2257	2141	2159	2166
$6sf_s$	1572	1504	1427	1439	1444
$8sf_s$	1179	1129	1071	1079	1083

5.2.1 Stator Phase Current Analysis

Frequency Extraction

5-th Harmonic

Regarding the area of the $5-th$ harmonic, the results provided by the frequency extraction are shown in Figures 5.25 & 5.26 and the amplitudes of the extracted frequency components in each harmonic are given in Table 5.13. In all FFT representations of these trajectories, even multiples of the sf_s are present. Considering the values presented in Table 5.13, it can be seen from Figure 5.25 that the same conclusion can be drawn about a healthy motor's extracted trajectory, thus being of a unique its own morphology than a faulty motor's, with no spikes arising in any speed ripple related subcomponents and the value of the spectrum can be considered as almost a constant line. Localised within a frequency bin's length, Case #1 has a spectrum value at the $4sf_s$ and $6sf_s$ locations spiking at $-76.19\ dB$ and $-70.23\ dB$ respectively for the $S(t, f_{5,1})$ trajectory. During the single breakage (Fig. 5.25a), the same

components spike at $-25.09\ dB$ and $-34.83\ dB$ respectively for Case #2. For Case #3 the discussed amplitudes are at the level of $-21.39\ dB$ and $-31.56\ dB$ respectively (Fig. 5.25b). For the two breakages at the half-pitch scenario (Case #4) the same components elevate at $-21.17\ dB$ and $-32.49\ dB$ (Fig. 5.25c). From Fig. 5.25d, Case #5 reveals the $4sf_s$ subcomponent at $-30.08\ dB$ and the $6sf_s$ at $-30.51\ dB$. The results provide validation of the method by FEM proving it as a reliable solution for the detection of non-adjacent broken bars. The $2sf_s$ component presents the values of $-67.39\ dB$, $-52.07\ dB$, $-33.56\ dB$, $-33.35\ dB$ and $-47.67\ dB$ from Case#1 - Case #5 respectively (Table 5.15).

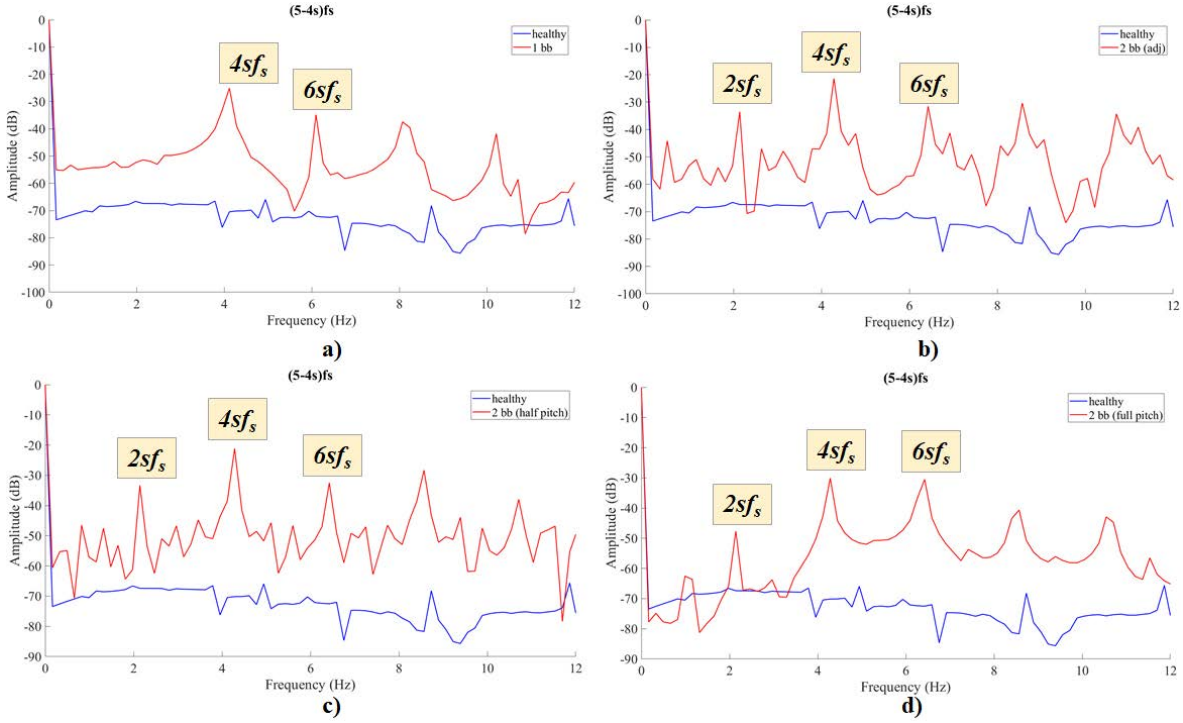

Fig. 5.25 Comparative spectra of extracted trajectories in the stator phase current for the $S(t, f_{5,1})$ spectral component: a) Case #1 vs Case #2 b) Case #1 vs Case #3 c) Case #1 vs Case #4 d) Case #1 vs Case #5

Regarding the $S(t, f_{5,2})$ trajectory, Case #1 holds an amplitude of $-75.63\ dB$ and $-70.1\ dB$ at the points of $4sf_s$ and $6sf_s$ respectively, while the same observations apply for its spectrum morphology and distribution (Fig. 5.26). These components hold the amplitude values of -24.841 and -34.49 respectively for the one broken bar of Case #2 (Fig. 5.26a). The two adjacent broken bars fault of Case #3 (Fig. 5.26b) elevates the discussed components at -21.39 and -31.74 respectively, as expected to be due to the larger local asymmetry induced from the breakage part. For the half pitch scenario of Case #4 (Fig. 5.26c), the subcomponent at $4sf_s$ elevates at $-21.52\ dB$ and the $6sf_s$ one at $-32.63\ dB$. Finally, from Fig. 5.26d, the examined components spike at $-29.84\ dB$ and $-30.16\ dB$ respectively for Case #5. Again, the latter two FEM cases are reliably diagnosed as rotor faults, both by

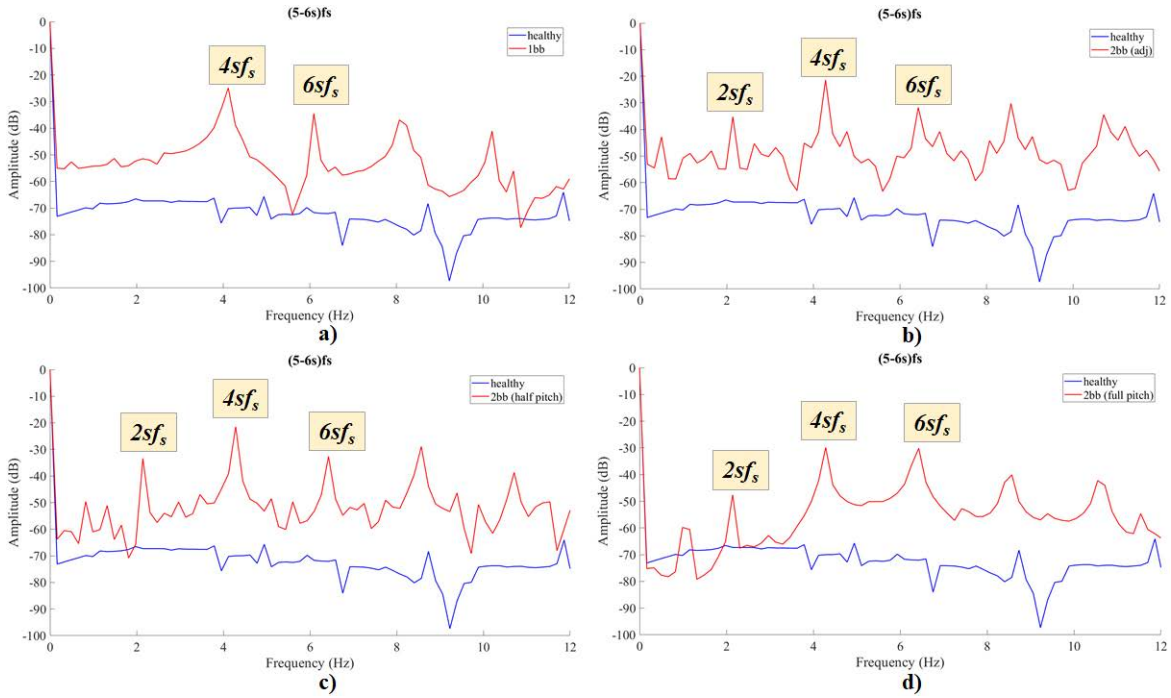

Fig. 5.26 Comparative spectra of extracted trajectories in the stator phase current for the $S(t, f_{5,2})$ spectral component: a) Case #1 vs Case #2 b) Case #1 vs Case #3 c) Case #1 vs Case #4 d) Case #1 vs Case #5

the lower and upper sidebands's subcomponents at $4sf_s$ and $6sf_s$ and by the presence of the fault-related speed-ripple effect subcomponent at $2sf_s$. The latter one presents from Case #1 - Case #5 the values of $-66.54\ dB$, $-51.36\ dB$, $-32.23\ dB$, $-33.39\ dB$, $-47.61\ dB$ respectively. It is observed that the $2sf_s$ subcomponent is not tangibly present in the single breakage case (Case #2) and the full-pitch breakage case (Case #5) (Table 5.15).

Table 5.13 FFT Amplitudes (dB) of $S(t, f_{5,i})$ for all cases of Model #2 (Stator Current)

Case	$5f_s - 4sf_s$		$5f_s - 6sf_s$	
	$4sf_s$	$6sf_s$	$4sf_s$	$6sf_s$
Case #1	-76.19	-70.23	-75.63	-70.1
Case #2	-25.09	-34.83	-24.84	-34.49
Case #3	-21.39	-31.56	-21.39	-31.74
Case #4	-21.17	-32.49	-21.52	-32.63
Case #5	-30.08	-30.51	-29.84	-30.16

7-th Harmonic

In the area of the $7-th$ harmonic, the results provided by the frequency extraction method are shown in Figures 5.27 & 5.28 and the investigated components' amplitudes are given

in Tbale 5.14. The subcomponents examined in the $S(t, f_{7,i})$ carrier are the $6sf_s$ and $8sf_s$, along with the $2sf_s$ subcomponent. For the $S(t, f_{7,1})$, the healthy motor (Case #1) performs values of $-59.83\ dB$ at $6sf_s$ and $-53.03\ dB$ at $8sfs_s$. Comparing this as a baseline with Case #2, the $6sf_s$ signature rises with a difference of $28.47\ dB$ at $-31.36\ dB$, while the $8sf_s$ one performs an increase of $9.54\ dB$ reaching at $-43.49\ dB$ (5.27a). In a very similar manner with the $5-th$ harmonic, in the signatures of Case #3 the amplitudes spike at $-29.33\ dB$ and $-45.93\ dB$ for the $6sf_s$ and $8sf_s$ respectively, showing a corresponding increase of $30.55\ dB$ and $7.1\ dB$ with respect to the healthy motor (Fig. 5.27b). Compelling amplitude values to detect the fault are yielded for the challenging half-pitch breakage of Case #4, which present an increase of $23.41\ dB$ with respect to healthy motor at $6sf_s$ ($-36.42\ dB$), while the $8sf_S$ signature spikes $-40.17\ dB$ performing an increase of $12.86\ dB$ (Fig. 5.27c). In the full-pitch located breakages case (Case #5) the subcomponent of the $6sf_s$ and $8sf_s$ rise $12.07\ dB$ at $-47.76\ dB$ and $9.95\ dB$ at $-43.08\ dB$ respectively compared to Case #1 (Fig. 5.27d). The speed-ripple subcomponent signature at $2sf_s$ holds for thus specific trajectory the values of $-64.59\ dB$, $-22.29\ dB$, $-27.12\ dB$, $-36.96\ dB$ and $-26.57\ dB$ for Case #1 - Case #5 respectively (Table 5.15).

Table 5.14 FFT Amplitudes (dB) of $S(t, f_{7,i})$ for all cases of Model #2 (Stator Current)

Case	$7f_s - 6sf_s$		$7f_s - 8sf_s$	
	$6sf_s$	$8sf_s$	$6sf_s$	$8sf_s$
Case #1	-59.83	-53.03	-63.01	-56.72
Case #2	-31.36	-43.49	-31.01	-43.01
Case #3	-29.33	-45.93	-28.68	-47.88
Case #4	-36.42	-40.17	-36.22	-39.95
Case #5	-47.76	-43.08	-48.49	-44.1

Moving on to the $S(t, f_{7,2})$ extraction, the amplitude levels of Case #1 are at $-63.01\ dB$ and $-56.72\ dB$ for the $6sf_s$ and $8sf_s$ signature respectively (Fig. 5.28). For Case #2 in Fig. 5.28a these signatures are erected at the height of $-31.01\ dB$ and $-43.01\ dB$ respectively, thus rising $32\ dB$ and $13.71\ dB$ compared to Case #1. Compared to Case #1, the double breakage at adjacency fault (Case #3) shown in Fig. 5.28b makes the signature of $6sf_s$ rise $34.33\ dB$ (spike at $-28.68\ dB$) and the $8sf_s$ signature rise $8.84\ dB$ (spike at $-47.88\ dB$). In addition, the same subcomponents for Case #4 mark themselves at $-36.22\ dB$ and $-39.95\ dB$ respectively, which indicates a rise of $26.79\ dB$ and $16.77\ dB$ respectively, when compared to Case #1 (Fig. 5.28c). The last breakage scenario depicted in Fig. 5.28d (Case #5) shows an amplitude of $-48.49\ dB$ for the $6sf_s$ signature (increase of $14.52\ dB$ over healthy) and an amplitude of $-44.1\ dB$ for the $8sf_s$ (increase $12.62\ dB$ over healthy). Considering the latter signatures' behaviour along with their amplitudes in the extracted $S(t, f_{7,1})$ trajectory

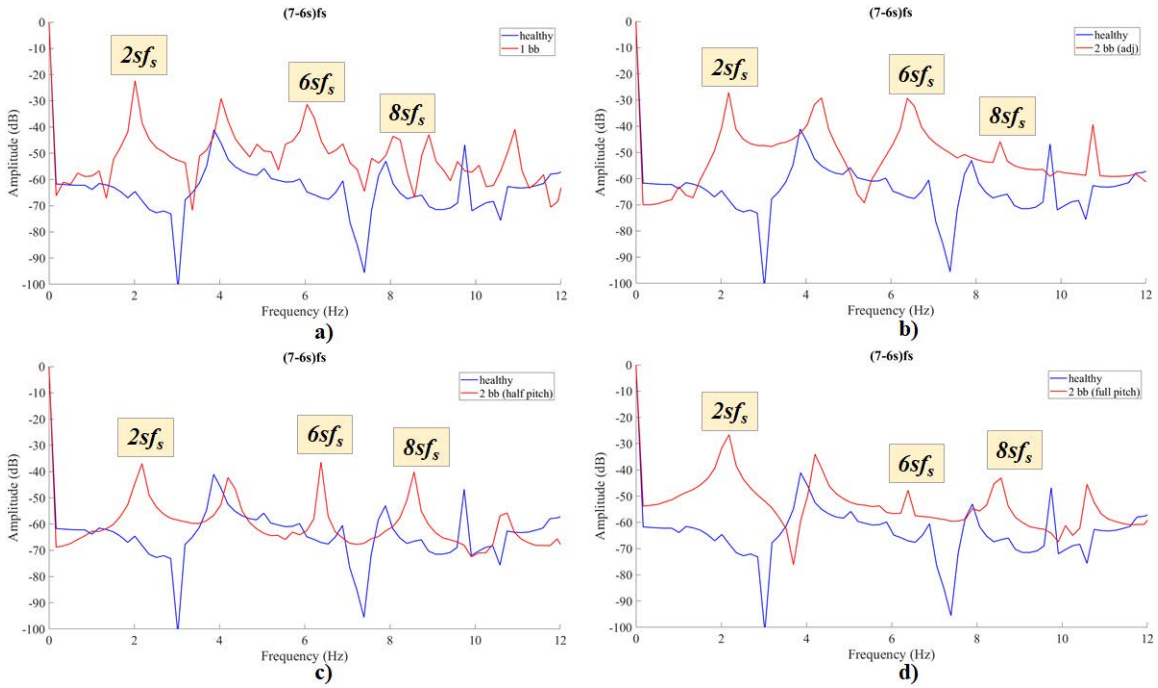

Fig. 5.27 Comparative spectra of extracted trajectories in the stator phase current for the $S(t, f_{7,1})$ spectral component: a) Case #1 vs Case #2 b) Case #1 vs Case #3 c) Case #1 vs Case #4 d) Case #1 vs Case #5

above for Case #5, leads to the observation that the $6sf_s$ and $8sf_s$ subcomponents -as it was with stator current measurement of Model #1- do not perform very well in the full-pitch breakage regarding increases, however still present and tangible enough to indicate a rotor fault condition; the same is observable for the $8sf_s$ extracted subcomponent in the single breakage and two adjacent broken bar cases (Case #2 & Case #3). The tracking of the $2sf_s$ frequencies for Case #5 reveals a strong modulating frequency at the $2sf_s$ component carried in the $S(t, f_{7,1})$ and $S(t, f_{7,2})$ trajectories. This component is seen for Case #1- Case #5 in the latter trajectory at the amplitudes of: $-68.36\ dB$, $-22.19\ dB$, $-27.31\ dB$, $-37.94\ dB$ and $-26.88\ dB$ respectively (Table 5.15).

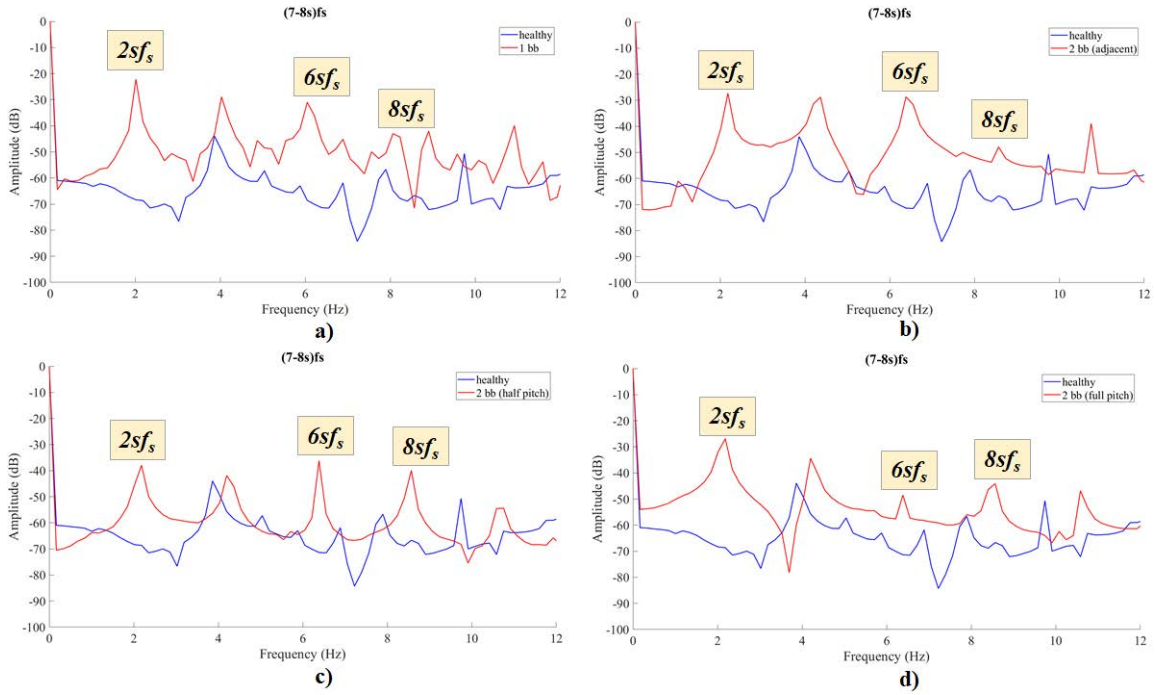

Fig. 5.28 Comparative spectra of extracted trajectories in the stator phase current for the $S(t, f_{7,2})$ spectral component: a) Case #1 vs Case #2 b) Case #1 vs Case #3 c) Case #1 vs Case #4 d) Case #1 vs Case #5

Table 5.15 Model # 2: Comparative table of the FFT amplitudes (dB) for the $2sf_s$ fault-related component in all examined harmonics for all cases - Extracted trajectories from the stator phase current spectral content

Case	$(5-4s)f_s$	$(5-6s)f_s$	$(7-6s)f_s$	$(7-8s)f_s$
Case #1	-67.39	-66.54	-64.59	-68.36
Case #2	-52.07	-51.36	-22.29	-22.19
Case #3	-33.56	-35.23	-27.12	-27.31
Case #4	-33.35	-33.39	-36.96	-37.94
Case #5	-47.67	-47.61	-26.57	-26.88

5.2.2 Stray Flux Analysis

Frequency Extraction

5-th Harmonic

Regarding the area of the $5-th$ harmonic, the results provided by the frequency extraction method are shown in Figures 5.29 & 5.30 and the amplitudes of the extracted frequency components in each harmonic are given in Table 5.16. The even multiples of the sf_s are present and tangible throughout the signals responses and being transferred throughout the frequencies of stator current or stray flux during continuous induction. Considering the

values presented in Table 5.16, it can be seen from Figure 5.29 that the extracted trajectory for Case #1 is as in all models so far free of fault related subcomponents in the FFT spectra. The healthy motor's (Case #1) spectrum at the $4sf_s$ and $6sf_s$ locations yields amplitudes at $-91.23\ dB$ and $-80.53\ dB$ respectively for the $S(t, f_{5,1})$ trajectory. During the single breakage (Fig. 5.29a), the same components spike at $-45.47\ dB$ and $-38.55\ dB$ respectively for Case #2. At the double breakage (Case #3), the discussed amplitudes are tangibly present at the level of $-37.82\ dB$ and $-31.74\ dB$ respectively (Fig. 5.29b). Interestingly, the analysed frequencies spike at a close level for the brekage at the half-pitch scenario (Case #4), thus being at $-36.58\ dB$ and $-30.09\ dB$ (Fig. 5.29c). From Fig. 5.29d, Case #5 reveals the $4sf_s$ subcomponent at $-37.82\ dB$ and the $6sf_s$ at $-29.44\ dB$. The $2sf_s$ component presents

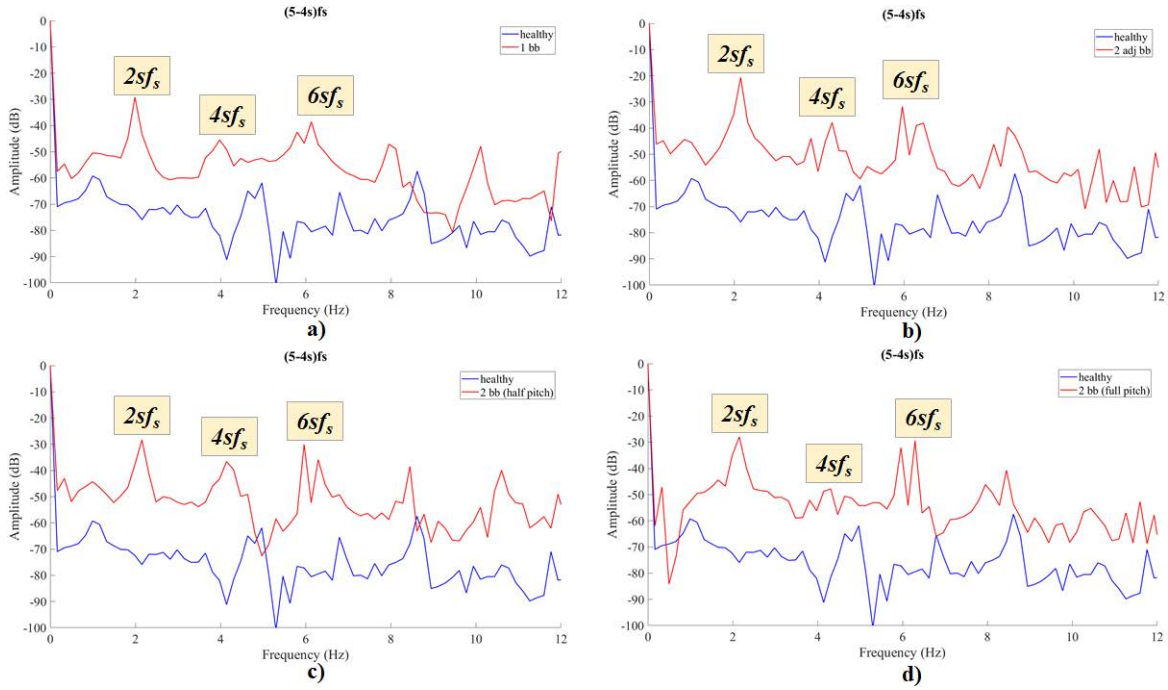

Fig. 5.29 Comparative spectra of extracted trajectories in the stray flux for the $S(t, f_{5,1})$ spectral component: a) Case #1 vs Case #2 b) Case #1 vs Case #3 c) Case #1 vs Case #4 d) Case #1 vs Case #5

the values of $-75.92\ dB$, $-29.19\ dB$, $-20.63\ dB$, $-28.34\ dB$ and $-27.95\ dB$ from Case#1 - Case #5 respectively (Table 5.18).

Regarding the $S(t, f_{5,2})$ trajectory, Case #1 holds an amplitude of $-91.22\ dB$ and $-76.11\ dB$ at the points of $4sf_s$ and $6sf_s$ respectively, while the same observations apply for its spectrum morphology and distribution (Fig. 5.30). These components hold the amplitude values of -41.97 and -37.75 respectively for the one broken bar of Case #2 (Fig. 5.30a). The two adjacent broken bars fault of Case #3 (Fig. 5.30b) elevates the discussed components at -37.57 and 28.93 respectively, as expected to be due to the larger asymmetry

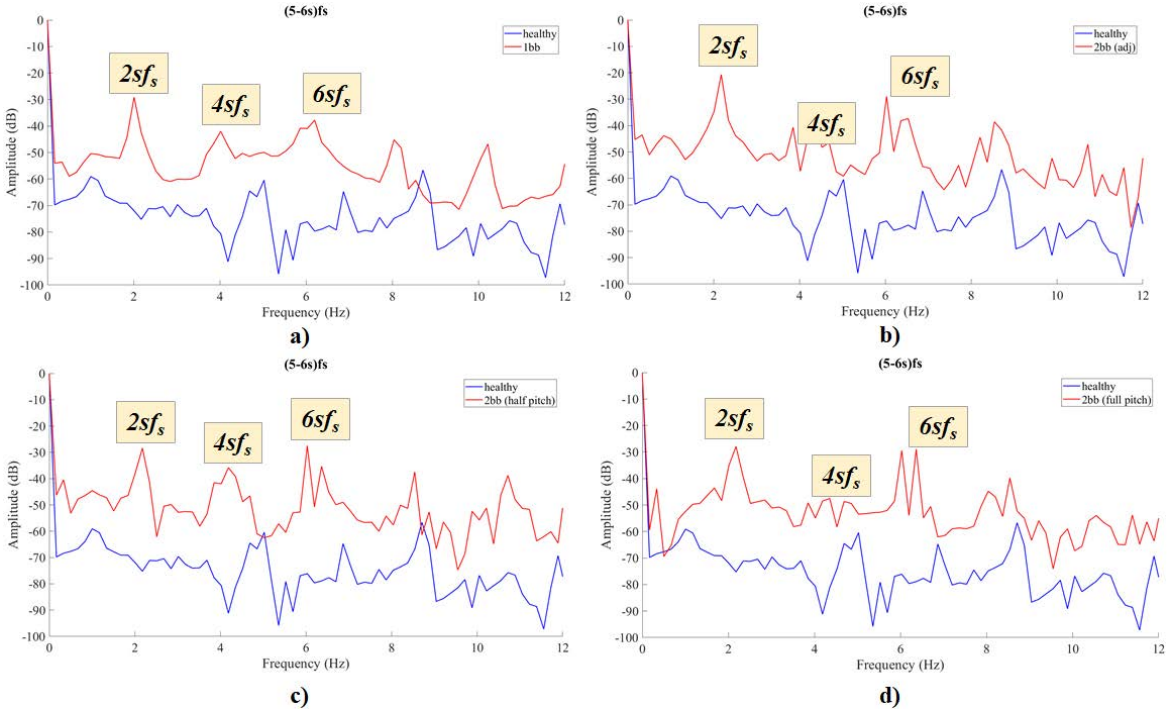

Fig. 5.30 Comparative spectra of extracted trajectories in the stray flux for the $S(t, f_{5,2})$ spectral component: a) Case #1 vs Case #2 b) Case #1 vs Case #3 c) Case #1 vs Case #4 d) Case #1 vs Case #5

caused in the rotating magnetic field by the extended broken bar area. For the half pitch scenario of Case #4 (Fig. 5.30c), the subcomponent at $4sf_s$ elevates at $-35.86\ dB$ and the $6sf_s$ one at $-27.48\ dB$. Finally, from Fig. 5.30d, the examined components spike at $-47.53\ dB$ and $-29.48\ dB$ respectively for Case #5. Again, the latter two FEM cases are identified as rotor faults, both by the lower and upper sidebands's subcomponents at $4sf_s$ and $6sf_s$ and by the presence of the fault-related speed-ripple effect subcomponent at $2sf_s$. The latter one presents from Case #1 - Case #5 the values of $-75.92\ dB$, $-29.19\ dB$, $-20.63\ dB$, $-28.34\ dB$, $-27.95\ dB$ respectively (Table 5.18).

Table 5.16 FFT Amplitudes (dB) of $S(t, f_{5,i})$ for all cases of Model #2 (Stray Flux)

Case	$5f_s - 4sf_s$		$5f_s - 6sf_s$	
	$4sf_s$	$6sf_s$	$4sf_s$	$6sf_s$
Case #1	-91.23	-80.53	-91.22	-76.11
Case #2	-45.47	-38.55	-41.97	-37.75
Case #3	-37.82	-31.74	-37.57	-28.93
Case #4	-36.58	-30.09	-35.86	-27.48
Case #5	-47.82	-29.44	-47.53	-29.48

7-th Harmonic

In the area of the $7-th$ harmonic, the results provided by the frequency extraction method are shown in Figures 5.31 & 5.32 and the investigated components' amplitudes are given in Tbale 5.17. The subcomponents examined in the $S(t, f_{7,i})$ carrier are the $6sf_s$ and $8sf_s$, along with the $2sf_s$ subcomponent. For the $S(t, f_{7,1})$, the healthy motor (Case #1) performs values of $-70.4\ dB$ at $6sf_s$ and $-65.39\ dB$ at $8sfs_s$. Comparing this as a baseline with Case #2, the $6sf_s$ signature rises with a difference of $42.65\ dB$ at $-27.75\ dB$, while the $8sf_s$ one performs an increase of $32.56\ dB$ reaching at $-32.83\ dB$. In a very similar manner with the $5-th$ harmonic, in the signatures of Case #3 the amplitudes spike at $-31.54\ dB$ and $-34.33\ dB$ for the $6sf_s$ and $8sf_s$ respectively, showing a corresponding increase of $38.86\ dB$ and $31.06\ dB$ with respect to the healthy motor (Fig. 5.31b). Compelling amplitude values to detect the fault are yielded for the challenging half-pitch breakage of Case #4, which present an increase of $46.34\ dB$ with respect to healthy motor at $6sf_s$ ($-24.06\ dB$), while the $8sf_S$ signature spikes $-28.04\ dB$ performing an increase of $37.35\ dB$ (Fig. 5.31c). In the full-pitch located breakages case (Case #5) the subcomponent of the $6sf_s$ and $8sf_s$ are competent in terms of increase,the first one rising $47.72\ dB$ at $-22.68\ dB$, while the latter one rises $35.33\ dB$ at $-30.06\ dB$ with respect to Case #1 (Fig. 5.31d). The speed-ripple subcomponent signature at $2sf_s$ holds for the specific trajectory the values of $-70.19\ dB$, $-30.34\ dB$, $-22.97\ dB$, $-28.02\ dB$ and $-31.32\ dB$ for Case #1 - Case #5 respectively (Table 5.18).

Moving on to the $S(t, f_{7,2})$ extraction, the amplitude levels of Case #1 are at $-76.88\ dB$ and $-65.15\ dB$ for the $6sf_s$ and $8sf_s$ signature respectively (Fig. 5.32). For Case #2 in Fig. 5.32a these signatures are erected at the height of $-26.7\ dB$ and $-31.58\ dB$ respectively, thus rising $50.18\ dB$ and $33.35\ dB$ compared to Case #1. Compared to Case #1, the double breakage at adjacency fault (Case #3) shown in Fig. 5.32b makes the signature of $6sf_s$ rise $47.42\ dB$ (spike at $-29.46\ dB$) and the $8sf_s$ signature rise $31.87\ dB$ (spike at $-33.28\ dB$). In addition, the same subcomponents for Case #4 mark themselves at $-24.41\ dB$ and $-28.59\ dB$ respectively, which indicates a rise of $52.47\ dB$ and $36.56\ dB$ respectively, when compared to Case #1 (Fig. 5.32c). The last breakage scenario depicted in Fig. 5.32d (Case #5) shows an amplitude of $-22.0\ dB$ for the $6sf_s$ signature (increase of $54.85\ dB$ over healthy) and an amplitude of $-28.26\ dB$ for the $8sf_s$ (increase $36.89\ dB$ over healthy). Again the stray flux analysis with the proposed method makes the fault related subcomponents duly observable and proves the stray flux analysis valuable in cases like the nbroken bar non-adjacency. This component is seen for Case #1- Case #5 in the latter trajectory at the amplitudes of: $-75.22\ dB$, $-29.14\ dB$, $-20.68\ dB$, $-28.41\ dB$ and $-27.92\ dB$ respectively (Table 5.18).

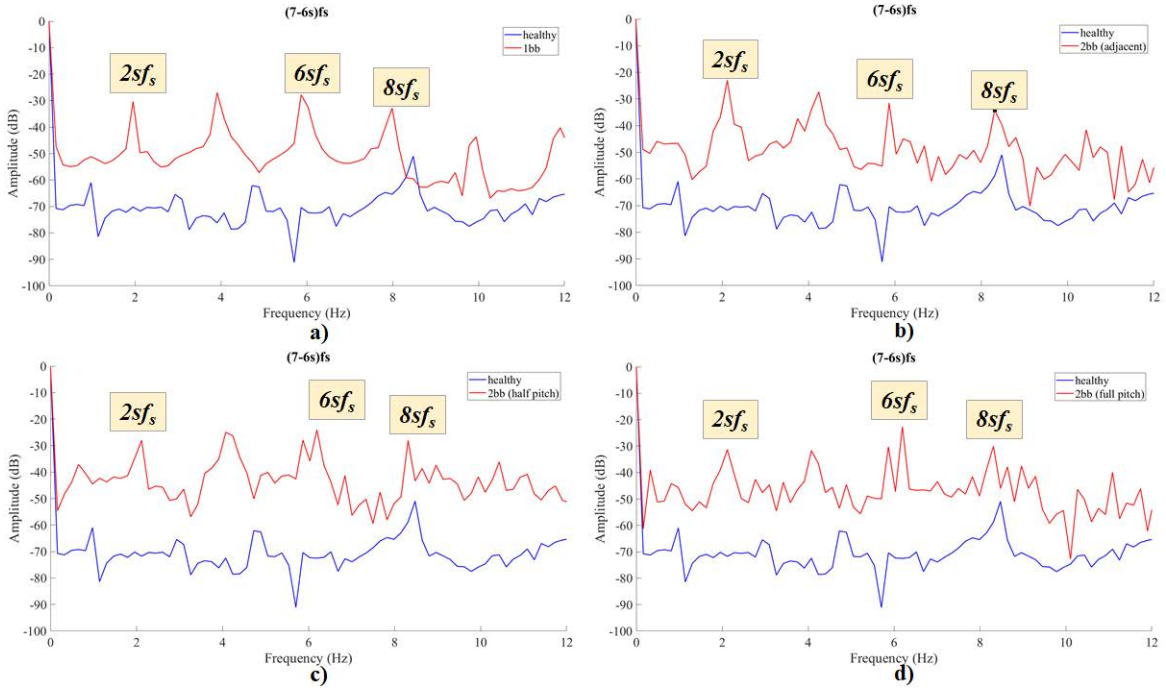

Fig. 5.31 Comparative spectra of extracted trajectories in the stray flux for the $S(t, f_{7,1})$ spectral component: a) Case #1 vs Case #2 b) Case #1 vs Case #3 c) Case #1 vs Case #4 d) Case #1 vs Case #5

Table 5.17 FFT Amplitudes (dB) of $S(t, f_{7,i})$ for all cases of Model #2 (Stray Flux)

Case	$7f_s - 6sf_s$		$7f_s - 8sf_s$	
	$6sf_s$	$8sf_s$	$6sf_s$	$8sf_s$
Case #1	-70.4	-65.39	-76.88	-65.15
Case #2	-27.75	-32.83	-26.7	-31.58
Case #3	-31.54	-34.33	-29.46	-33.28
Case #4	-24.06	-28.04	-24.41	-28.59
Case #5	-22.68	-30.06	-22.03	-28.26

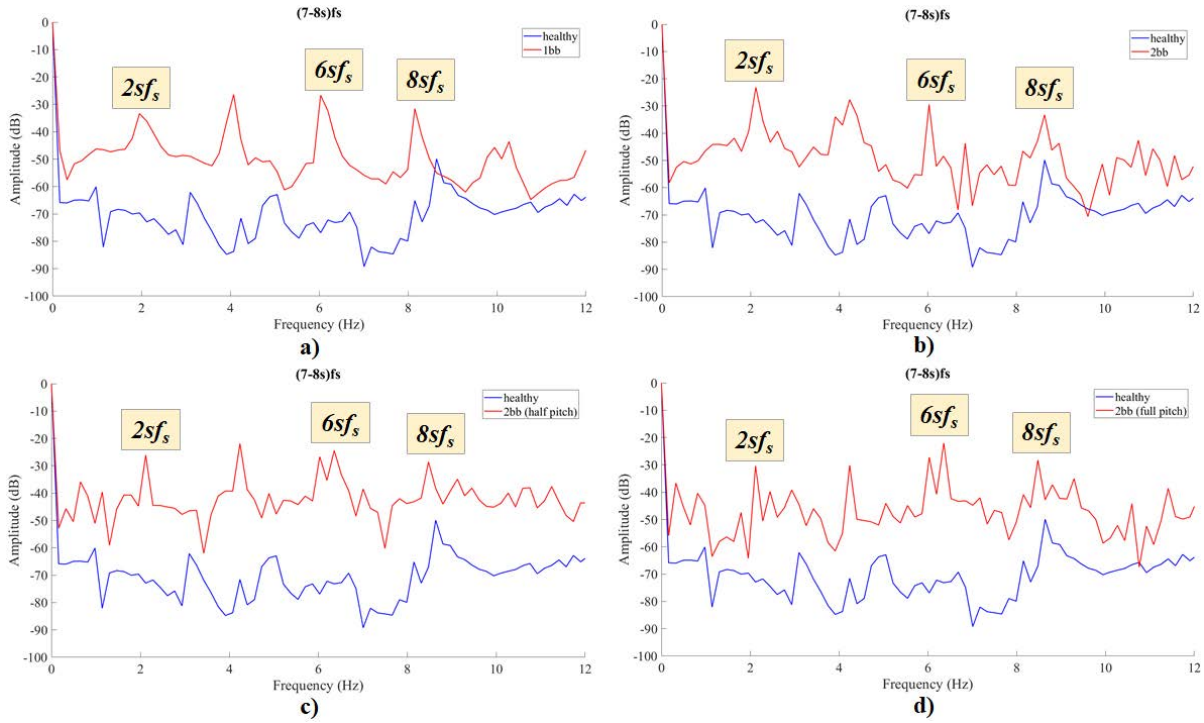

Fig. 5.32 Comparative spectra of extracted trajectories in the stray flux for the $S(t, f_{7,2})$ spectral component: a) Case #1 vs Case #2 b) Case #1 vs Case #3 c) Case #1 vs Case #4 d) Case #1 vs Case #5

Table 5.18 Model # 2: Comparative table of the FFT amplitudes (dB) for the $2sf_s$ fault-related component in all examined harmonics for all cases - Extracted trajectories from the radial stray flux spectral content

Case	$(5-4s)f_s$	$(5-6s)f_s$	$(7-6s)f_s$	$(7-8s)f_s$
Case #1	-75.92	-75.22	-70.19	-69.62
Case #2	-29.19	-29.14	-30.34	-33.37
Case #3	-20.63	-20.68	-22.97	-23.19
Case #4	-28.34	-28.41	-28.02	-26.11
Case #5	-27.95	-27.92	-31.32	-30.37

5.3 Model #3

Reliable Limit for Extraction

All components at twice the slip frequency ($\simeq 2ksf_s$ components) are calculated for each model's case and are given with the values of slip in Table 5.19. As it was for Models #1 & #2 (Table 5.3 & 5.11), the presented value expresses the distance of an examined component from the central harmonic and is accounted for when deriving the lower bound of the window sequence length. The FEM model for this motor is shown in Fig. 5.33.

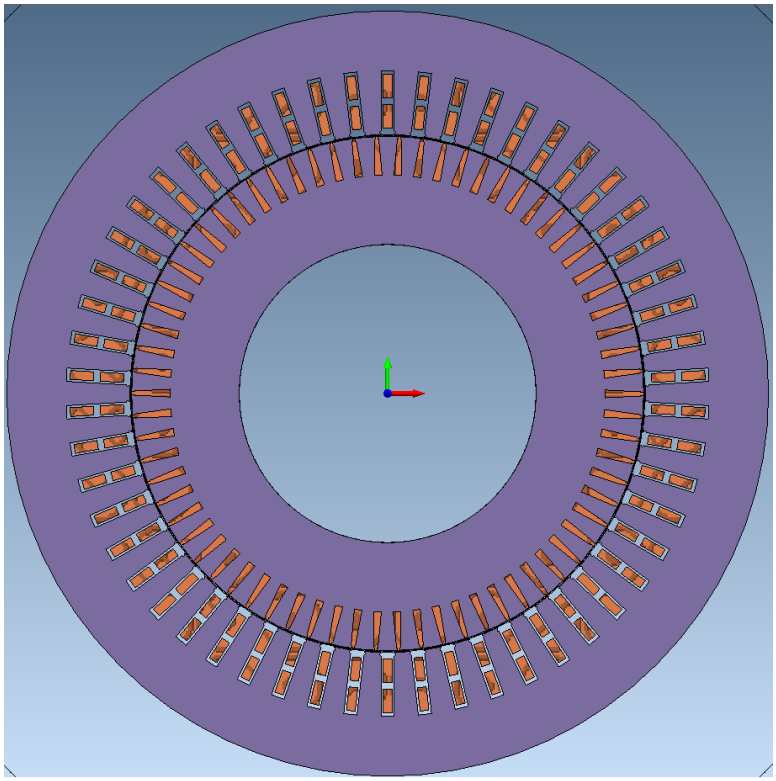

Fig. 5.33 FEM model of Model #3

Table 5.19 Slip values & distances of the $2ksf_s$ components in Hz for all cases of Model # 3

Component	Case #1	Case #2	Case #3	Case #4	Case #5
	$s_1 \simeq 0.009$	$s_2 \simeq 0.0091$	$s_3 \simeq 0.0.0095$	$s_4 \simeq 0.0.0095$	$s_5 \simeq 0.0094$
$2sf_s$	0.902	0.91	0.953	0.948	0.936
$4sf_s$	1.804	1.82	1.906	1.896	1.872
$6sf_s$	2.706	2.73	2.859	2.844	2.807
$8sf_s$	3.608	3.64	3.813	3.792	3.743

The minimum required window sequence lengths, calculated as described in Chapter4, are presented in Table 5.12 with the value used for the parameter ξ derived from exhaustive search. Each value in the table provides a window length capable to separate and capture the the sideband given in the first column. As done for Models #1 & #2, the largest of each column is chosen to assure seperability of frequencies distanced at least $2sf_s$ from each other and localisation in the next frequency chunk.

Table 5.20 Window sequence lower bounds for Model # 3

$\xi = -0.54$	Case #1	Case #2	Case #3	Case #4	Case #5
$2sf_s$	5459	5411	5166	5194	5261
$4sf_s$	2729	2705	2583	2597	2630
$6sf_s$	1819	1803	1722	1731	1753
$8sf_s$	1364	1352	1291	1298	1315

5.3.1 Stator Phase Current Analysis

Frequency Extraction

5-th Harmonic

With regards to the area of the $5-th$ harmonic, the results provided by the frequency extraction are shown in Figures 5.34 & 5.35 and the amplitudes of the extracted frequency components in each harmonic are given in Table 5.21. In all FFT representations of the trajectories, even multiples of the sf_s are present. Considering the values presented in Table 5.21, it can be seen from Figure 5.34 that the same conclusion can be drawn about a healthy motor's extracted trajectory, thus being of a unique its own morphology than a faulty motor's, meaning that no spikes arise in any speed ripple related subcomponents and the value of the spectrum can be considered as almost a constant line. Localised within a frequency bin's length, Case #1 has a spectrum value at the $4sf_s$ and $6sf_s$ locations spiking at $-74.91\ dB$ and $-80.83\ dB$ respectively for the $S(t, f_{5,1})$ trajectory. During the single breakage (Fig. 5.34a), the same components spike at $-35.23\ dB$ and $-54.39\ dB$ respectively for Case #2. For Case #3 the discussed amplitudes are at the level of $-45.64\ dB$ and $-61.55\ dB$ respectively (Fig. 5.34b). For the two breakages at the half-pitch scenario (Case #4) the same components elevate at $-42.8\ dB$ and $-54.79\ dB$ (Fig. 5.34c). From Fig. 5.34d, Case #5 reveals the $4sf_s$ subcomponent at $-40.22\ dB$ and the $6sf_s$ at $-57.98\ dB$. The results provide validation of the method by FEM proving it as a reliable solution for the detection of non-adjacent broken bars. The $2sf_s$ component presents the values of $-69.24\ dB$, $-34.16\ dB$, $-43.77\ dB$, $-34.01\ dB$ and $-47.8\ dB$ from Case#1 - Case #5 respectively (Table 5.23).

Table 5.21 FFT Amplitudes (dB) of $S(t, f_{5,i})$ for all cases of Model #3 (Stator Current)

Case	$5f_s - 4sf_s$		$5f_s - 6sf_s$	
	$4sf_s$	$6sf_s$	$4sf_s$	$6sf_s$
Case #1	-74.91	-80.83	-75.65	-82.32
Case #2	-35.23	-54.39	-35.31	-53.98
Case #3	-45.64	-61.55	-43.48	-62.74
Case #4	-42.8	-54.79	-43.01	-54.53
Case #5	-40.22	-57.98	-39.92	-54.66

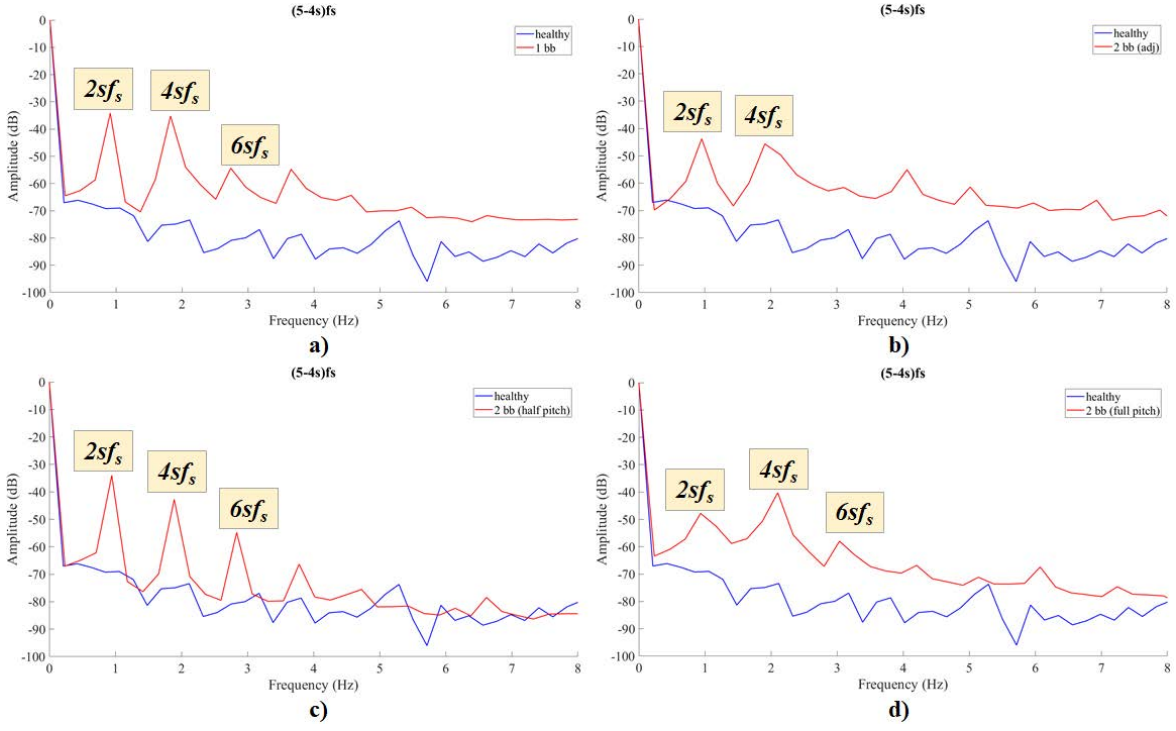

Fig. 5.34 Comparative spectra of extracted trajectories in the stator phase current for the $S(t, f_{5,1})$ spectral component: a) Case #1 vs Case #2 b) Case #1 vs Case #3 c) Case #1 vs Case #4 d) Case #1 vs Case #5

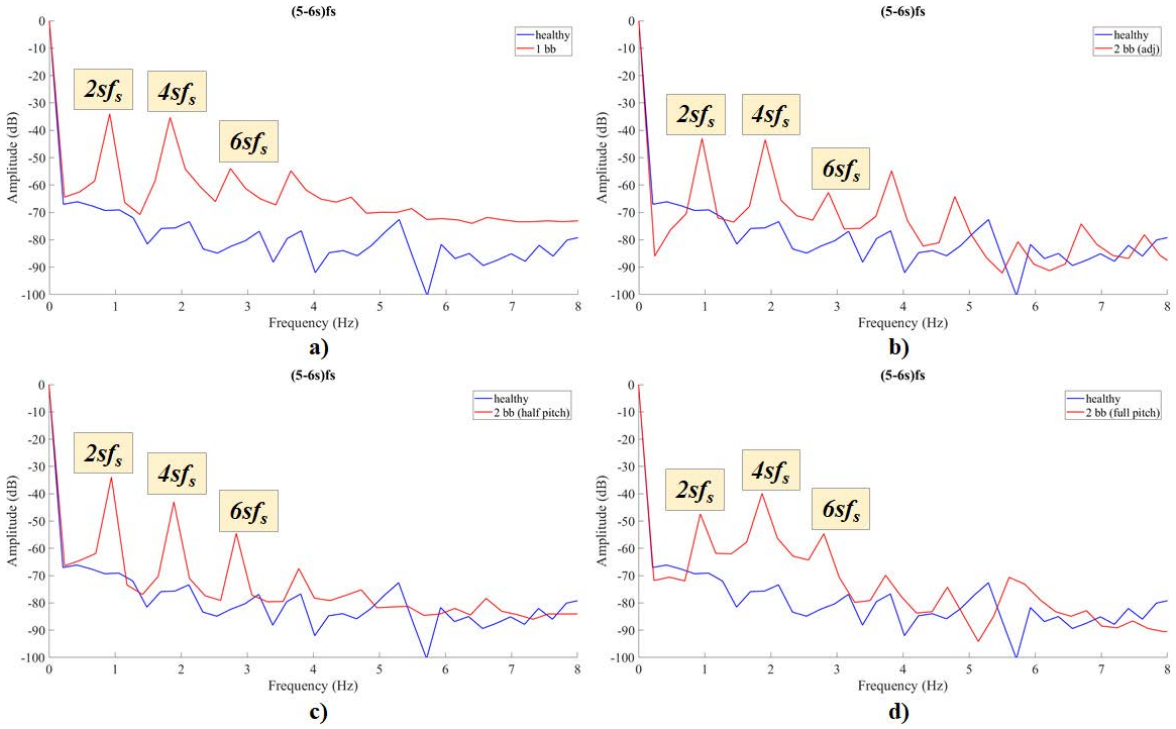

Fig. 5.35 Comparative spectra of extracted trajectories in the stator phase current for the $S(t, f_{5,2})$ spectral component: a) Case #1 vs Case #2 b) Case #1 vs Case #3 c) Case #1 vs Case #4 d) Case #1 vs Case #5

Referring to the $S(t, f_{5,2})$ trajectory, Case #1 holds an amplitude of $-75.65\ dB$ and $-82.32\ dB$ at the points of $4sf_s$ and $6sf_s$ respectively, while the same observations apply for its spectrum morphology and distribution (Fig. 5.35). These components hold the amplitude values of -35.31 and -53.98 respectively for the one broken bar of Case #2 (Fig. 5.35a). The two adjacent broken bars fault of Case #3 (Fig. 5.35b) elevates the discussed components at -43.48 and -62.74 respectively, as expected to be due to the larger local asymmetry induced from the breakage part. For the half pitch scenario of Case #4 (Fig. 5.35c), the subcomponent at $4sf_s$ elevates at $-43.01\ dB$ and the $6sf_s$ one at $-54.53\ dB$. Finally, from Fig. 5.35d, the examined components spike at $-39.92\ dB$ and $-54.66\ dB$ respectively for Case #5. Again, the latter two FEM cases are reliably diagnosed as rotor faults, both by the lower and upper sidebands's subcomponents at $4sf_s$ and $6sf_s$ and by the presence of the fault-related speed-ripple effect subcomponent at $2sf_s$. The latter one presents from Case #1 - Case #5 the values of $-69.31\ dB$, $-34\ dB$, $-42.98\ dB$, $-33.91\ dB$, $-47.39\ dB$ respectively (Table 5.23). The application of the method in the large induction motor ($1.1\ MW$) provides satisfactory results for the $5-th$ harmonic area. Such a case provides a more challenging problem: firstly, the problem of broken bars non-adjacency; secondly, as apart from the low value of slip and weak speed-ripple effect, the relative fault severity (2/70 bars) is lower than in Model #1 (2/32 bars) and Model #2 (2/28 bars) .

7-th Harmonic

In the area of the $7-th$ harmonic, the results provided by the frequency extraction method are shown in Figures 5.36 & 5.37 and the investigated components' amplitudes are given in Tbale 5.22. The subcomponents examined in the $S(t, f_{7,i})$ carrier are the $6sf_s$ and $8sf_s$, along with the $2sf_s$ subcomponent. For the $S(t, f_{7,1})$, the healthy motor (Case #1) performs values of $-68.66\ dB$ at $6sf_s$ and $-67.21\ dB$ at $8sfs_s$. Comparing this as a baseline with Case #2, the $6sf_s$ signature rises with a difference of $25.66\ dB$ at $-43\ dB$, while the $8sf_s$ one performs an increase of $19.39\ dB$ reaching at $-47.82\ dB$ (5.36a). In a very similar manner with the $5-th$ harmonic, in the signatures of Case #3 the amplitudes spike at $-36.03\ dB$ and $-36.33\ dB$ for the $6sf_s$ and $8sf_s$ respectively, showing a corresponding increase of $32.63\ dB$ and $30.88\ dB$ with respect to the healthy motor (Fig. 5.36b). Compelling amplitude values to detect the fault are yielded for the challenging half-pitch breakage of Case #4, which present an increase of $24.06\ dB$ with respect to healthy motor at $6sf_s$ ($-44.6\ dB$), while the $8sf_S$ signature spikes $-37.84\ dB$ performing an increase of $29.38\ dB$ (Fig. 5.36c). In the full-pitch located breakages case (Case #5) the subcomponent of the $6sf_s$ and $8sf_s$ are quite competent compared to the same harmonic examined in the stator current; the first one ($6sf_s$) rises $30\ dB$ at $-38.66\ dB$, while the latter one rises $30.74\ dB$ at $-36.47\ dB$ with respect to Case #1 (Fig. 5.36d). The speed-ripple subcomponent signature at $2sf_s$ holds for thus specific trajectory the values of $-56.65\ dB$, $-24.68\ dB$, $-21.3\ dB$, $-34.65\ dB$ and $-43.37\ dB$ for Case #1 - Case #5 respectively (Table 5.23).

Analysing the $S(t, f_{7,2})$ extraction, the amplitude levels of Case #1 are at $-68.62\ dB$ and $-67.29\ dB$ for the $6sf_s$ and $8sf_s$ signature respectively (Fig. 5.37). For Case #2 in Fig. 5.37a these signatures are erected at the height of $-43.76\ dB$ and $-47.25\ dB$ respectively, thus rising $24.68\ dB$ and $20.04\ dB$ compared to Case #1. Compared to Case #1, the double breakage at adjacency fault (Case #3) shown in Fig. 5.37b makes the signature of $6sf_s$ rise $32.93\ dB$ (spike at $-35.69\ dB$) and the $8sf_s$ signature rise $31.26\ dB$ (spike at $-31.26\ dB$). In addition, the same subcomponents for Case #4 mark themselves at $-45.41\ dB$ and $-38.27\ dB$ respectively, which indicates a rise of $23.21\ dB$ and $29.02\ dB$ respectively, when compared to Case #1 (Fig. 5.37c). The last breakage scenario depicted in Fig. 5.37d (Case #5) shows an amplitude of $-39.72\ dB$ for the $6sf_s$ signature (increase of $28.9\ dB$ over healthy) and an amplitude of $-36.4\ dB$ for the $8sf_s$ (increase $30.89\ dB$ over healthy). The tracking of the $2sf_s$ frequencies for Case #5 reveals a strong modulating frequency at the $2sf_s$ component carried in the $S(t, f_{7,2})$ trajectories at the amplitudes of: $-56.64\ dB$, $-24.72\ dB$, $-21.25\ dB$, $-35.11\ dB$ and $-43.48\ dB$ for Case #1- Case #5 respectively (Table 5.23).

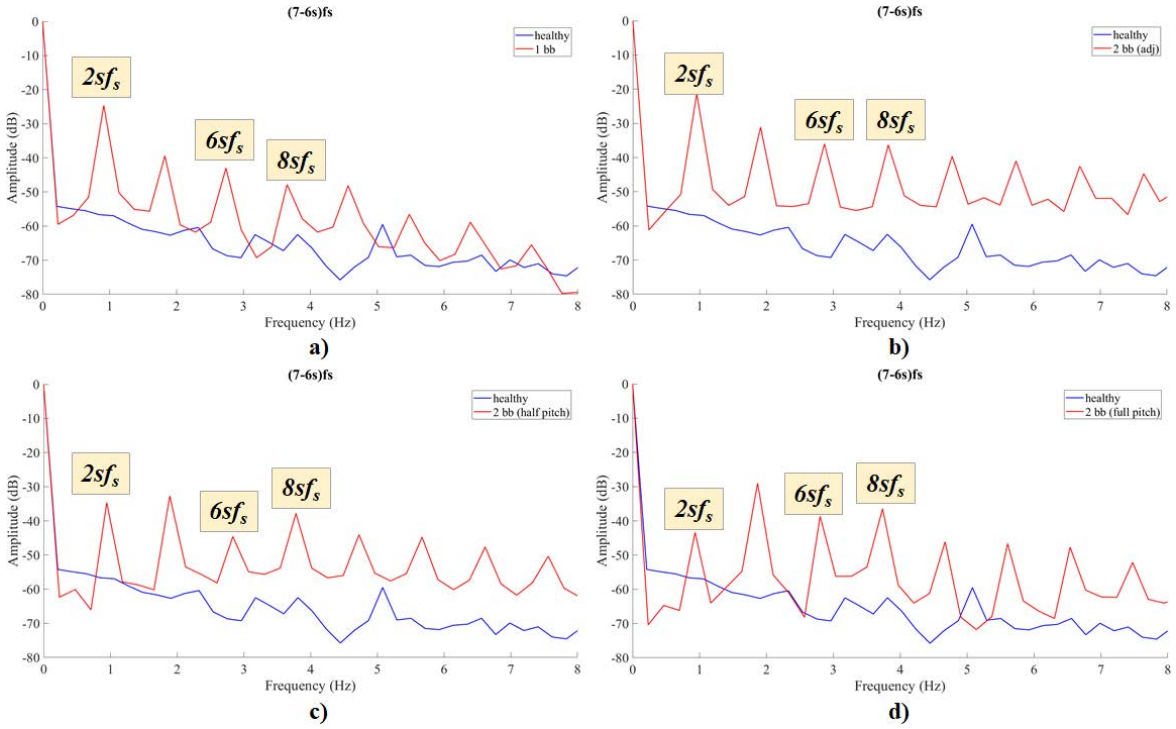

Fig. 5.36 Comparative spectra of extracted trajectories in the stator phase current for the $S(t, f_{7,1})$ spectral component: a) Case #1 vs Case #2 b) Case #1 vs Case #3 c) Case #1 vs Case #4 d) Case #1 vs Case #5

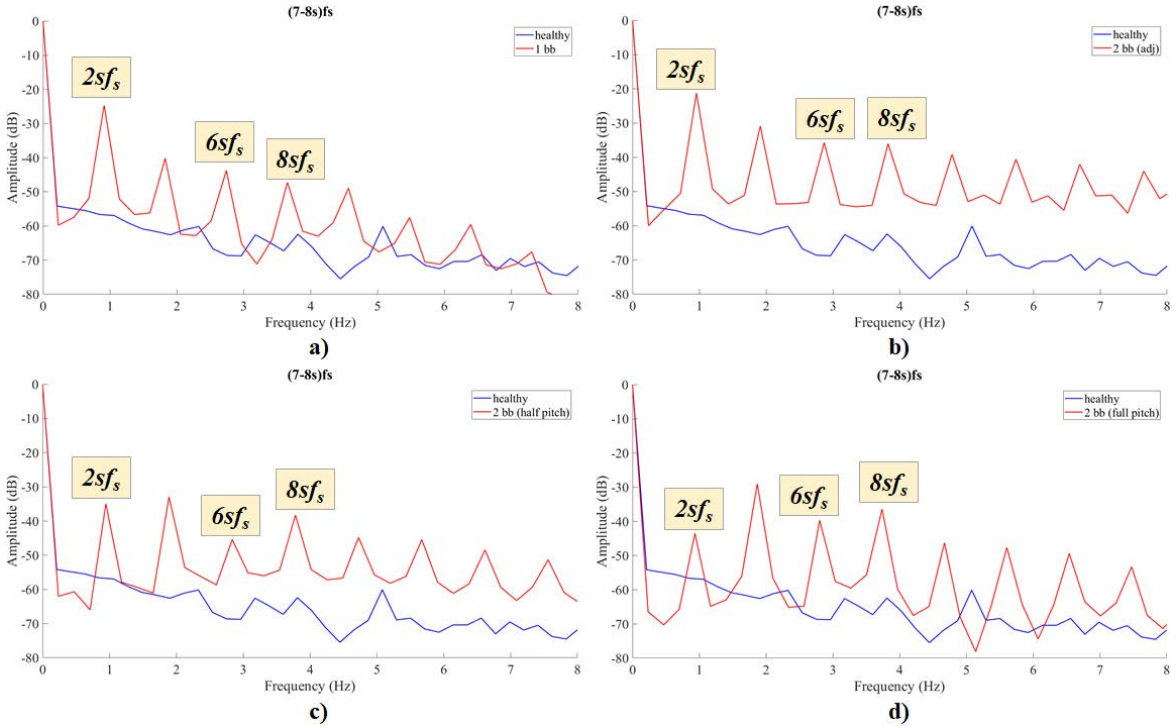

Fig. 5.37 Comparative spectra of extracted trajectories in the stator phase current for the $S(t, f_{7,2})$ spectral component: a) Case #1 vs Case #2 b) Case #1 vs Case #3 c) Case #1 vs Case #4 d) Case #1 vs Case #5

Table 5.22 FFT Amplitudes (dB) of $S(t, f_{7,i})$ for all cases of Model #3 (Stator Current)

Case	$7f_s - 6sf_s$		$7f_s - 8sf_s$	
	$6sf_s$	$8sf_s$	$6sf_s$	$8sf_s$
Case #1	-68.66	-67.21	-68.62	-67.29
Case #2	-43	-47.82	-43.76	-47.25
Case #3	-36.03	-36.33	-35.69	-36.03
Case #4	-44.6	-37.83	-45.41	-38.27
Case #5	-38.66	-36.47	-39.72	-36.4

Table 5.23 Model # 3: Comparative table of the FFT amplitudes (dB) for the $2sf_s$ fault-related component in all examined harmonics for all cases - Extracted trajectories from the stator phase current spectral content

Case	$(5-4s)f_s$	$(5-6s)f_s$	$(7-6s)f_s$	$(7-8s)f_s$
Case #1	-69.24	-69.31	-56.65	-56.64
Case #2	-34.16	-34	-24.68	-24.72
Case #3	-43.77	-42.98	-21.3	-21.25
Case #4	-34.01	-33.91	-34.65	-35
Case #5	-47.8	-47.39	-43.37	-43.48

5.3.2 Stray Flux Analysis

Frequency Extraction

5-th Harmonic

In the area of the $5-th$ harmonic, the results provided by the frequency extraction are shown in Figures 5.38 & 5.39 and the amplitudes of the extracted frequency components in each harmonic are given in Table 5.24. In all FFT representations of these trajectories, even multiples of the sf_s are present. Considering the values presented in Table 5.24, it can be seen from Figure 5.38 that the same conclusion can be drawn about a healthy motor's extracted trajectory, thus being of a unique its own morphology than a faulty motor's, meaning that no spikes arise in any speed ripple related subcomponents and the value of the spectrum can be considered as almost a constant line. Localised within a frequency bin's length, Case #1 has a spectrum value at the $4sf_s$ and $6sf_s$ locations spiking at $-53.4\ dB$ and $-51.37\ dB$ respectively for the $S(t, f_{5,1})$ trajectory. During the single breakage (Fig. 5.38a), the same components spike at $-24.72\ dB$ and $-28.75\ dB$ respectively for Case #2. This is a change of $28.68\ dB$ and $22.62\ dB$ with respect to Case #1. For Case #3 the discussed amplitudes are at the level of $-24.01\ dB$ and $-31.02\ dB$ respectively (Fig. 5.38b)s, which is respectively a change of $29.39\ dB$ and $22.62\ dB$ respectively compared to healthy motor. For the two breakages at the half-pitch scenario (Case #4) the same components elevate at $-21.69\ dB$

and $-31.35\ dB$, change in of $31.71\ dB$ and $20.02\ dB$ compared to the healthy points (Fig. 5.38c). From Fig. 5.38d, Case #5 reveals the $4sf_s$ subcomponent at $-26.86\ dB$ and the $6sf_s$ at $-34.03\ dB$, which is an elevation of $26.54\ dB$ and $17.34\ dB$ respectively versus Case #1. The theoretical $2sf_s$ component presents the values of $-51.22\ dB$, $-32.61\ dB$, $-19.57\ dB$, $-41.79\ dB$ and $-28.99\ dB$ from Case#1 - Case #5 respectively (Table 5.26).

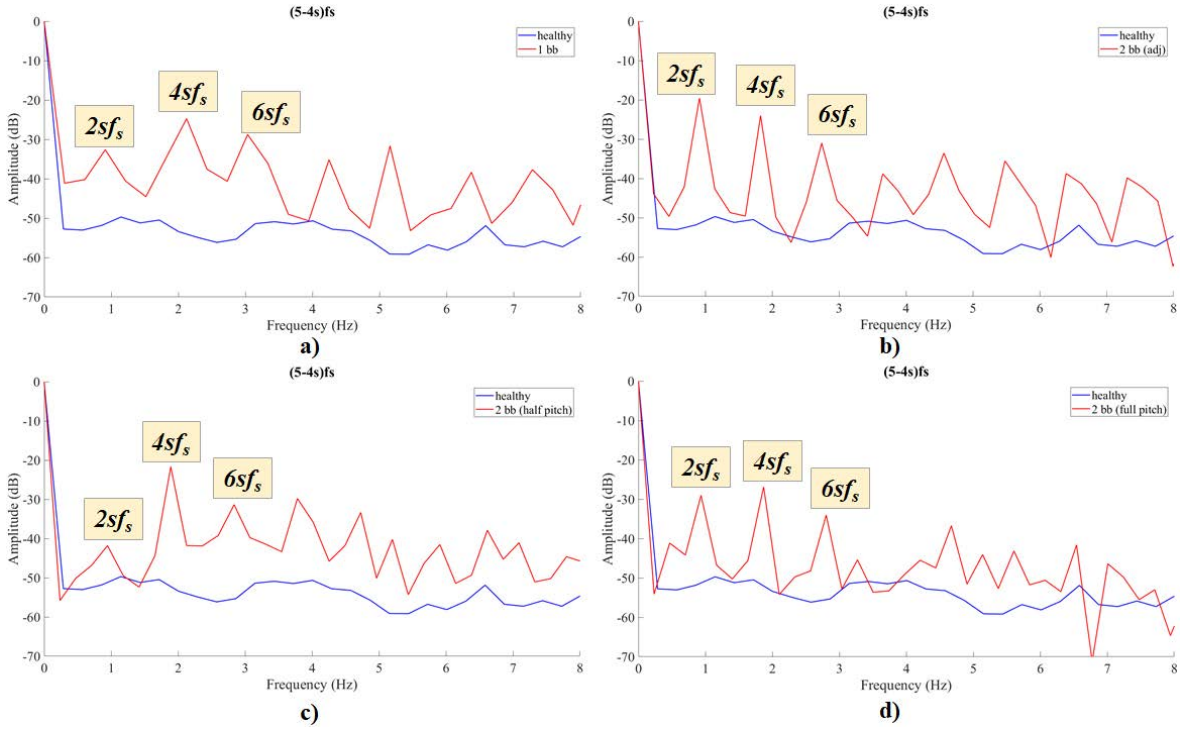

Fig. 5.38 Comparative spectra of extracted trajectories in the stray flux for the $S(t, f_{5,1})$ spectral component: a) Case #1 vs Case #2 b) Case #1 vs Case #3 c) Case #1 vs Case #4 d) Case #1 vs Case #5

Regarding the $S(t, f_{5,2})$ trajectory, Case #1 holds an amplitude of $-50.59\ dB$ and $-54.81\ dB$ at the points of $4sf_s$ and $6sf_s$ respectively, while the same observations apply for its spectrum morphology and distribution (Fig. 5.39). These components hold the amplitude values of -24.58 ($26.01\ dB$ increase) and -29.27 ($25.54\ dB$ increase) respectively for the one broken bar of Case #2 (Fig. 5.39a). The two adjacent broken bars fault of Case #3 (Fig. 5.39b) elevates the discussed components at -24.04 and -31.19 respectively, as expected to be due to the larger local asymmetry induced from the breakage part (increases of $26.55\ dB$ and $23.62\ dB$ respectively). For the half pitch scenario of Case #4 (Fig. 5.39c), the subcomponent at $4sf_s$ elevates at $-21.7\ dB$ and the $6sf_s$ one at $-32.47\ dB$, reporting increases of $28.89\ dB$ and $22.34\ dB$ respectively compared to the healthy Case #1. Finally, from Fig. 5.39d, the examined components spike at $-26.87\ dB$ and $-33.75\ dB$ respectively for Case #5, increasing from the healthy motor of Case #1 by $23.72\ dB$ and $21.06\ dB$ respectively. Regarding the $2sf_s$ subcomponent, the $S(t, f_{5,2})$ trajectory presents from Case #1 -

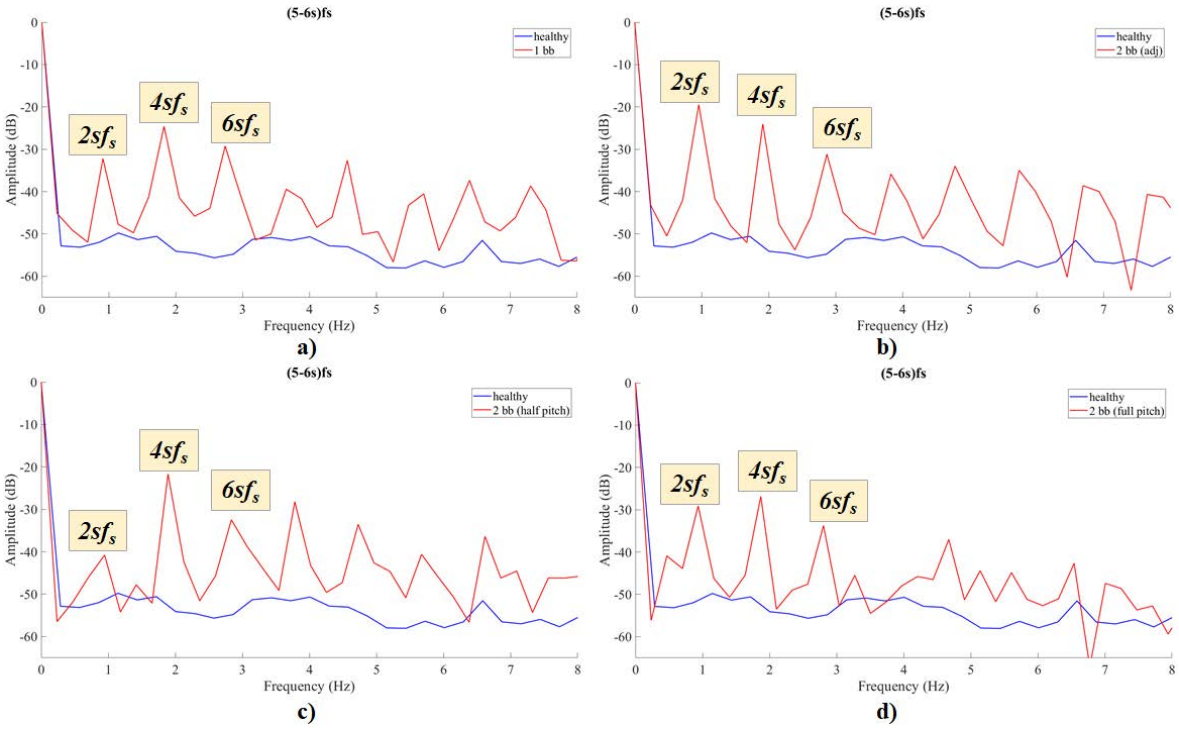

Fig. 5.39 Comparative spectra of extracted trajectories in the stray flux for the $S(t, f_{5,2})$ spectral component: a) Case #1 vs Case #2 b) Case #1 vs Case #3 c) Case #1 vs Case #4 d) Case #1 vs Case #5

Case #5 the values of $-51.99\ dB$, $-32.24\ dB$, $-19.48\ dB$, $-40.79\ dB$, $29.1\ dB$ respectively (Table 5.26).

Table 5.24 FFT Amplitudes (dB) of $S(t, f_{5,i})$ for all cases of Model #3 (Stray Flux)

Case	$5f_s - 4sf_s$		$5f_s - 6sf_s$	
	$4sf_s$	$6sf_s$	$4sf_s$	$6sf_s$
Case #1	-53.4	-51.37	-50.59	-54.81
Case #2	-24.72	-28.75	-24.58	-29.27
Case #3	-24.01	-31.02	-24.04	-31.19
Case #4	-21.69	-31.35	-21.7	-32.47
Case #5	-26.86	-34.03	-26.87	-33.75

7-th Harmonic

In the area of the $7-th$ harmonic, the results provided by the frequency extraction are shown in Figures 5.40 & 5.41 and the amplitudes of the extracted frequency components in each harmonic are given in Table 5.25. In all FFT representations of these trajectories, even multiples of the sf_s are present. Considering the values presented in Table 5.25, it can be seen

from Figure 5.40 that the same conclusion can be drawn about a healthy motor's extracted trajectory, thus being of a unique its own morphology than a faulty motor's, meaning that no spikes arise in any speed ripple related subcomponents and the value of the spectrum can be considered as almost a constant line. Localised within a frequency bin's length, Case #1 has a spectrum value at the $4sf_s$ and $6sf_s$ locations spiking at $-56.52\ dB$ and $-60.61\ dB$ respectively for the $S(t, f_{7,1})$ trajectory. During the single breakage (Fig. 5.40a), the same components spike at $-31.4\ dB$ and $-30.92\ dB$ respectively for Case #2. This is a change of $25.12\ dB$ and $29.69\ dB$ with respect to Case #1. For Case #3 the discussed amplitudes are at the level of $-26.53\ dB$ and $-33.06\ dB$ respectively (Fig. 5.40b)s, which is respectively a change of $29.99\ dB$ and $27.55\ dB$ respectively compared to healthy motor. For the two

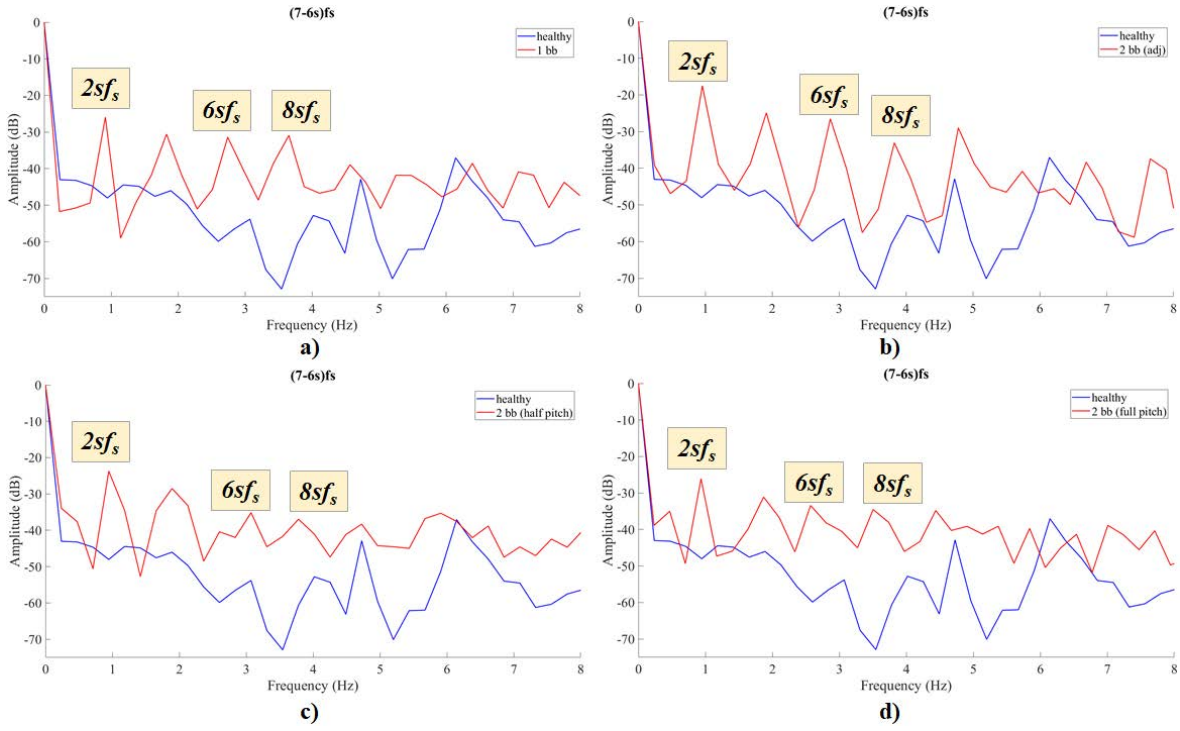

Fig. 5.40 Comparative spectra of extracted trajectories in the stray flux for the $S(t, f_{7,1})$ spectral component: a) Case #1 vs Case #2 b) Case #1 vs Case #3 c) Case #1 vs Case #4 d) Case #1 vs Case #5

breakages at the half-pitch scenario (Case #4) the same components elevate at $-35.15\ dB$ and $-36.95\ dB$, change in amplitude of $21.37\ dB$ and $23.66\ dB$ compared to the healthy points (Fig. 5.40c). From Fig. 5.40d, Case #5 reveals the $4sf_s$ subcomponent at $-33.43\ dB$ and the $6sf_s$ at $-35.54\ dB$, which is an elevation of $23.09\ dB$ and $26.07\ dB$ respectively versus Case #1. The theoretical $2sf_s$ component presents the values of $-48.01\ dB$, $-25.95\ dB$, $-17.52\ dB$, $-23.72\ dB$ and $-26.11\ dB$ from Case#1 - Case #5 respectively (Table 5.26).

Regarding the $S(t, f_{7,2})$ trajectory, Case #1 holds an amplitude of $-55.84\ dB$ and $-51.35\ dB$ at the points of $4sf_s$ and $6sf_s$ respectively, while the same observations ap-

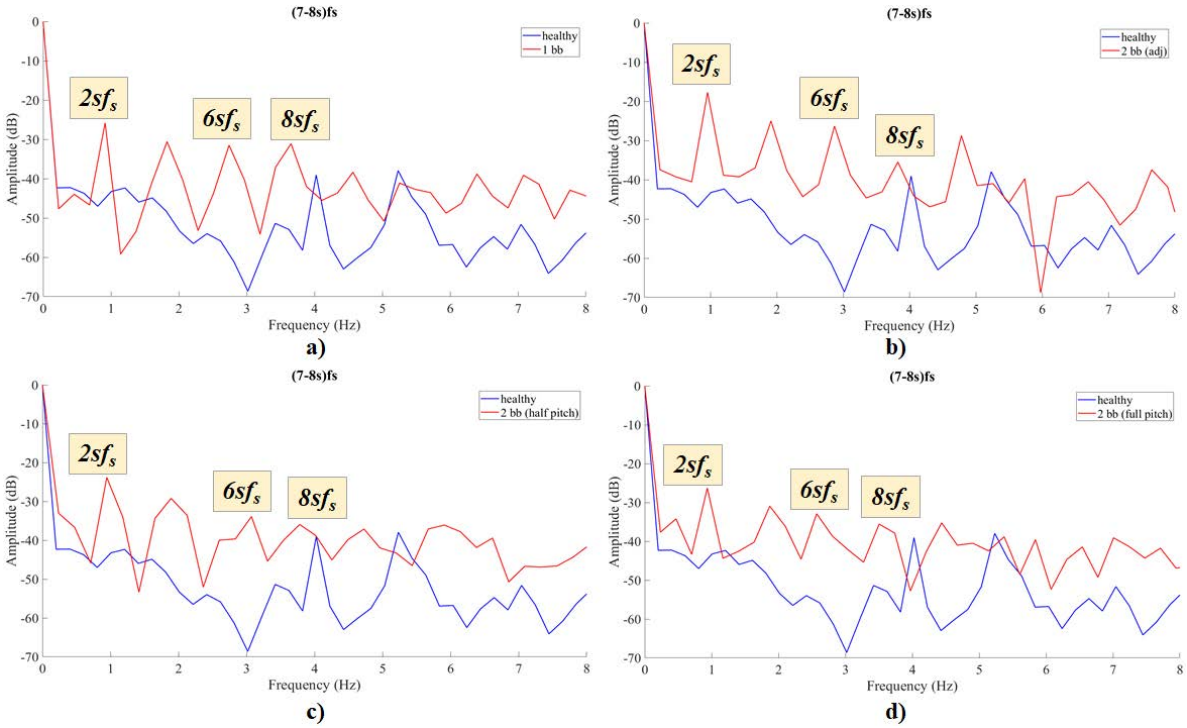

Fig. 5.41 Comparative spectra of extracted trajectories in the stray flux for the $S(t, f_{7,2})$ spectral component: a) Case #1 vs Case #2 b) Case #1 vs Case #3 c) Case #1 vs Case #4 d) Case #1 vs Case #5

Table 5.25 FFT Amplitudes (dB) of $S(t, f_{7,i})$ for all cases of Model #3 (Stray Flux)

Case	$7f_s - 6sf_s$		$7f_s - 8sf_s$	
	$6sf_s$	$8sf_s$	$6sf_s$	$8sf_s$
Case #1	-56.52	-60.61	-55.84	-51.35
Case #2	-31.4	-30.92	-31.47	-31.08
Case #3	-26.53	-33.06	-26.33	-35.46
Case #4	-35.15	-36.95	-33.89	-35.93
Case #5	-33.43	-34.54	-32.87	-35.54

ply for its spectrum morphology and distribution (Fig. 5.41). These components hold the amplitude values of -31.47 ($24.37\ dB$ increase) and -31.08 ($20.27\ dB$ increase) respectively for the one broken bar of Case #2 (Fig. 5.41a). The two adjacent broken bars fault of Case #3 (Fig. 5.41b) elevates the discussed components at -26.33 and -35.46 respectively, as expected to be due to the larger local asymmetry induced from the breakage part (increases of 29.51 dB and 15.89 dB respectively over healthy). For the half pitch scenario of Case #4 (Fig. 5.41c), the subcomponent at $4sf_s$ elevates at $-33.89\ dB$ and the $6sf_s$ one at $-35.93\ dB$, reporting increases of 21.95 dB and 15.42 dB respectively compared to the healthy Case #1. Finally, from Fig. 5.41d, the examined components spike at $-32.87\ dB$ and $-35.54\ dB$ respectively for Case #5, increasing from the healthy motor of Case #1 by 22.97 dB and 15.81 dB respectively. The $S(t, f_{7,2})$ trajectory presents the $2sf_s$ signature from Case #1 - Case #5 the values of $-46.99\ dB$, $-25.8\ dB$, $-17.73\ dB$, $-23.82\ dB$, $26.28\ dB$ respectively (Table 5.26).

Table 5.26 Model # 3: Comparative table of the FFT amplitudes (dB) for the $2sf_s$ fault-related component in all examined harmonics for all cases - Extracted trajectories from the radial stray flux spectral content

Case	$(5-4s)f_s$	$(5-6s)f_s$	$(7-6s)f_s$	$(7-8s)f_s$
Case #1	-51.82	-51.99	-48.01	-46.99
Case #2	-32.61	-32.24	-25.95	-25.8
Case #3	-19.57	-19.48	-17.52	-17.73
Case #4	-41.79	-40.79	-23.72	-23.82
Case #5	-28.99	-29.1	-26.11	-26.28

5.4 Discussion & Conclusive Remarks

From the analysis of the FEM datasets, the proposed method's application in stator current signals provided a reliable tool for identification whether a rotor is healthy or faulty. Initially the signals are evaluated on the time-frequency plane using the STFT spectrograms. This allows the monitoring of the spectral information from a time-varying prospect, as well as an initial frequency tracking around areas of interest ($5-th$ and $7-th$ harmonics) to examine if additional components are comprised in those areas. Further on, using the frequency extraction method, a set of harmonic signatures referred to as subcomponents are detected. A compelling evidence to proceed, is the major difference between the spectrum of trajectories from healthy motors (Case #1 in each model) and the spectrum of faulty cases. The subcomponents regard modulated carriers and sidebands in the examined harmonic zone and under faulty condition they will appear, regardless the fault severity or location.

These components make their presence only during a rotor fault, as they are enclosed in the carrier of the central harmonic, so their spectral information is withheld in the FFT of an extracted trajectory that will itself be present only during a fault. On the other hand, if a rotor is healthy the extracted spectrum does not provide the aforementioned signatures and a user can determine that the motor is healthy.

Regarding the data of Model #1, the stator current analysis provided satisfying results with the proposed method in all extracted sideband frequencies. An exception was detected in the $6sf_s$ and $8sf_s$ subcomponent signatures of the $S(t, f_{7,1})$ & $S(t, f_{7,2})$ trajectories for Case #5, which did not provide very satisfying alarm levels of amplitude change. Nevertheless, the result was enhanced by the analysis of the stray flux, which backed up the current analysis, as the discussed signatures were risen in detectable levels of amplitude. Furthermore, in all FEM cases a subcomponent signature at $2sf_s$ was revealed with the proposed method. This is a theoretical component and is existent due to the fault-modulated speed ripple effect by the $(1-2s)f_s$ fundamental field during breakage. Although this specific signature seems promising by the FEM datasets, it will be evident in next chapter that is more wise to rely in the other analysed subcomponents ($4sf_s$, $6sf_s$, $8sf_s$); this is because the $2sf_s$ one might be inherently present in real life machine problems and be risen due to manufacturing defects or environmental factors in a very similar level with the healthy one (if the latter one is present).

The stator current analysis of Model #2 provides compelling results as well, as the investigated set of frequencies reveal significant amplitude change in all cases. An exception is again spotted with regards to Case #5 (full-pitch breakage distance), where a weakness of the $6sf_s$ subcomponent to detect the fault was seen in the $S(t, f_{7,1})$ and the $S(t, f_{7,2})$ trajectories extraction. This weakness however is overcome with the complementary analysis of the stray flux, where no such deficiency was evident. On the contrary, the $6sf_s$ subcomponent signature in the stray flux performs strong increases in all extracted trajectories. In both stator phase current and stray flux, a diminishing effect of the $6sf_s$ and $8sf_s$ subcomponents is observed in Case #4 and Case #5. Nevertheless, all the other subcomponents examined with the method in the $5-th$ and $7-th$ harmonics perform a significant success in alarming for a rotor fault. This demonstrates not the significance of the two-stage analysis before the actual application of the frequency extraction method, but also the importance in the complementary analysis of stator current and stray flux measurements for definite diagnostic reliability.

The same observations regarding the extraction results apply for Model #3. In a very similar manner with the low voltage motors, the industrial motor model's signatures perform very well to indicate the rotor fault existence. The only exception is the $6sf_s$ component of the $5-$th harmonic in the stator current, which behaves the same for the single breakage

case and the adjacent breakages. This is expected since such a motor embeds a rotor with 70 bars, which is considered a quite large number of bars compared to the low voltage motors. In this case, when 1/70 or 2/70 bars break, the impact on subcomponents might be less tangible when examining a single or double adjacent breakage, compared to small motors. In other words, the spatial geometry of the motor and the larger number of bars make the asymmetry visible -and sometimes weak- to a very similar extent concerning the two discussed cases. Nevertheless, the fault is still detectable despite the lower asymmetry impact in the spatial field characteristics (and consequently in the harmonic content). This is a very important finding, as it is essential to map the harmonic behaviour in such industrial motors and compare them with laboratory level cases. As explained in the literature of Chapter 3, investigation of such cases is always vital as only a few historical case-studies from industry are available for machines of such sizes. Another significant observation for this model, like in Models #1 & #2, is that the $2sf_s$ component does not raise a very alarming amplitude for Case #4 (half pole pitch) compared to all other cases. However, this increase in amplitude is more than 11 dB, which is still promising. Nonetheless, the $2sf_S$ component is used for a cross-check and validation during this applications and is not chosen for the actual diagnosis part of the proposed method since all other extracted subcomponents prove more competent and promising.

Chapter 6

Results from Experiments

This chapter presents the results from the two induction motors used for experimental purposes, that were described in Chapter 4. Initially the frequency extraction method is applied on stator current signals of Motor #1, then on radial stray flux signals; the analysis in held under two different load profiles: the rated load condition and the half-rated load condition. The same spectral components of the $5-th$ and $7-th$ harmonics are examined with the proposed method. Regarding Motor #2, only stray flux measurements at the rated load condition will be analysed; however, for Motor #2, more rotors were tested than those of Motor #1, so more broken bar cases were available to examine.

6.1 Motor #1

As described in Chapter 4, Motor #1 is a $4-pole$ IM and embeds an aluminium die-cast rotor of 32 bars. As only two rotors were available, except for the healthy case which is referred to as Case #1, the rotor used to emulate the breakage fault was chosen to account for two breakage scenarios: one broken bar fault (Case #2) and two non-adjacent broken bars at half pole pitch distance (Case #3). The cases are summarised in Table 6.1 and will be used in the validation of the method during the rated and the half-rated load conditions.

Table 6.1
Summary of cases for Motor #1

Case	Breakage Location
Case #1	healthy
Case #2	single breakage
Case #3	2 bars at half pitch

6.1.1 Rated Load: Stator Phase Current Analysis

Reliable Limit for Extraction

All components at twice the slip frequency ($\simeq 2ksf_s$ components) are calculated for each model's case and are given with the values of slip in Table 6.2 for the rated load condition. Similarly with the Tables presented in the FEM models, the presented value expresses the distance of an examined component from the central harmonic and is accounted for when deriving the lower bound of the window sequence length.

Table 6.2 Slip values & $2ksf_s$ distances for all cases of Motor #1 - Rated Load Condition

Component	Case #1	Case #2	Case #3
	$s_1 \simeq 0.0268$	$s_2 \simeq 0.0252$	$s_3 \simeq 0.261$
$2sf_s$	2.68	2.52	2.61
$4sf_s$	5.36	5.04	5.22
$6sf_s$	8.04	7.56	7.83
$8sf_s$	10.72	10.08	10.44

The minimum required window sequence lengths, calculated as described in Chapter4, are presented in Table 6.3 with the value used for the parameter ξ derived from exhaustive search. Each value in the table provides a window length capable to separate and capture the the sideband given in the first column. As done for all motors in the FEM models, the largest of each column is chosen to assure seperability of frequencies distanced at least $2sf_s$ from each other and localisation in the next frequency chunk.

Table 6.3 Window sequence lower bounds for Motor #1 - Rated Load Condition

$\xi = -0.04$	Case #1	Case #2	Case #3
$2sf_s$	2455	2610	2520
$4sf_s$	1227	1305	1261
$6sf_s$	818	870	840
$8sf_s$	614	653	631

Frequency Extraction

5-th Harmonic

In the area of the $5-th$ harmonic, the results provided by the frequency extraction are shown in Figures 6.1 a-d and the amplitudes of the extracted frequency components in each harmonic are given in Table 6.4. As it was for data analysed from FEM simulations, the FFT spectra of these trajectories comprise even multiples of the sf_s for the faulty rotor cases. Localised within the $5-th$ harmonic area, Case #1 has a spectrum value at the $4sf_s$ and $6sf_s$ locations spiking at $-72.48\ dB$ and $-77.29\ dB$ respectively for the $S(t, f_{5,1})$ trajectory. During the single breakage (Fig. 6.1a), the same subcomponents spike at $-36.05\ dB$ and $-49.66\ dB$ respectively for Case #2, which is an increase o 36.43 dB and 27.63 dB with respect to Case #1. For the two breakages at the half-pitch scenario (Case #3) the same components elevate at $-39.27\ dB$ and $-44.11\ dB$, a difference in of 31.71 dB and 20.02 dB compared to the healthy points (Fig. 6.1b). Interestingly, the $2sf_s$ subcomponent is evidently present in the FFT of the $S(t, f_{5,1})$ extracted trajectory with an amplitude of $-60.03\ dB$ for Case #2, increased compared to the healthy Case #1 by 18.82 dB; the same signature rises more tangible in the case of the double breakage fault located at half-pitch distance (Case #3), showing an amplitude increase of 29.13 dB with its spike at $-49.72\ dB$ compared to Case #1. The $2sf_s$ signature's amplitudes are summarised for all cases in Table 6.6.

Table 6.4 FFT Amplitudes (dB) of $S(t, f_{5,i})$ for the cases of Motor #1 at Rated Load (Stator Current)

Case	$5f_s - 4sf_s$		$5f_s - 6sf_s$	
	$4sf_s$	$6sf_s$	$4sf_s$	$6sf_s$
Case #1	-72.48	-77.29	-66.77	-75.2
Case #2	-36.05	-49.66	-36.1	-47.41
Case #3	-39.27	-44.11	-38.42	-42.57

Similar is the behaviour of the $2sf_s$ signature in the spectra of the $S(t, f_{5,2})$ trajectory. The signature is insignificant for Case #1, where it holds an amplitude of $-75.03\ dB$; it rises by 14.48 dB compared to healthy for Case #2 ($-60.55\ dB$) and by 25.28 dB for Case #3 ($-49.75\ dB$). The values are presented in Table 6.6. Furthermore, the $4sf_s$ subcomponent's signature lies for Case #1 at $-66.77\ dB$ and the $6sf_s$ one's at $-75.2\ dB$, while the motor's spectra are relatively uniform and free from any modulations. The $4sf_s$ and $6sf_s$ subcomponents hold the amplitude values of $-36.1\ dB$ (30.67 dB increase from Case #1) and $-47.41\ dB$ (29.79 dB increase from Case #1) respectively for the one broken bar of Case #2 (Fig. 6.1c). For the half pitch scenario of Case #3 (Fig. 6.1d), the subcomponent at $4sf_s$ elevates at $-38.42\ dB$ and the $6sf_s$ one at $-42.57\ dB$, reporting increases of 28.35 dB and

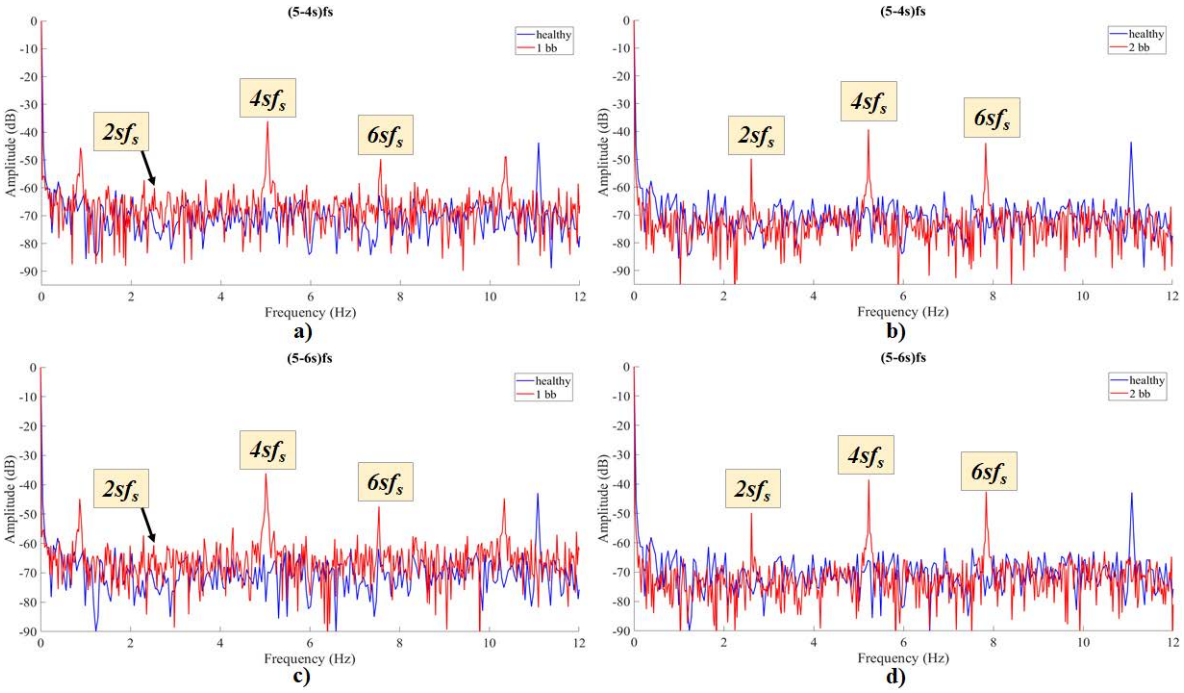

Fig. 6.1 Comparative spectra of extracted trajectories in the stator phase current for the spectral components of Motor #1 at the rated load condition: a) $S(t, f_{5,1})$ (Case #1 vs Case #2) b) $S(t, f_{5,1})$ (Case #1 vs Case #3) c)$S(t, f_{5,2})$ (Case #1 vs Case #2) and d) $S(t, f_{5,2})$ (Case #1 vs Case #3) spectral components of Motor #1

32.63 dB respectively compared to the healthy motor. In contrast with the FEM simulations, the theoretical speed-ripple component at $2sf_s$ is evidently weak in the experimental cases of the single breakage for the $5-th$ harmonic. As will be evident, this is the case for the other extracted trajectories as well. This comes in agreement with many works of the past handling rotor breakages; multiple reasons however of known and unknown origin might be the cause of this phenomenon. The first possible reasons are magnetic anisotropy, potential porosity (air-bubbles), lamination defects and other general manufacturing asymmetries which can never be known in a commercially available motor; these inherent asymmetries in the rotor will cause a $2sf_s$ oscillation at the fundamental frequency area, that will propagate further to the other higher harmonics like the ones examined in the proposed method. The direction of the vector representing this asymmetric oscillation is definitely random and unknown; so is the direction of the single breakage, running at the same time the possibility that these two might cancel out each other. Therefore, the speed-ripple effect will not be directly evident; however at the double breakage scenario (adjacent or non-adjacent), the secondly introduced broken bar will reinforce the damped speed-ripple of the initial single breakage. Furthermore, it is worth mentioning that when sensing signals with a static sensor -like the stator winding with regards to current or the stationary flux sensing coil in the case of stray flux- practically the speed-ripple manifests itself to the coil twice within a mechanical

rotation of the rotor (double breakage) instead of once per rotation (single breakage). Finally, a physical reason that plays an important role in every diagnostic method must be considered: the $2sf_s$ signatures in any type of analysis depend on the speed ripple effect; therefore, they also directly relate with the total inertia of the whole apparatus (rotor inertia and load inertia). Consequently, it is highly likely that the asymmetry caused by a single breakage will be creating a fault-related speed-ripple effect that is being subjected to a damping effect due to the total inertia of the rotor-load apparatus.

7-th Harmonic

The results of frequency extraction in the band of the $7-th$ harmonic are shown in Figures 6.2 a-d; the amplitudes of the extracted frequency components in each harmonic are given in Table 6.5. In all FFT representations of these trajectories, the even multiples of the sf_s ripple are present to examine their diagnostic potential. Considering the values presented in Table 6.5, it can be seen from Figure 6.2 that the same conclusion with the FEM motors can be drawn about a healthy motor's extracted trajectory, thus being of a unique morphology of its own and free from fault-related oscillations. Localised within the $7-th$ harmonic's frame, Case #1 has a spectrum value at the $6sf_s$ and $8sf_s$ locations spiking at $-51.58\ dB$ and $-50.58\ dB$ respectively for the $S(t, f_{7,1})$ trajectory. During the single breakage fault at Fig. 6.2a, the same subcomponents spike at $-39.39\ dB$ and $-38.66\ dB$ respectively for Case #2. This is a change of $12.19\ dB$ and $11.92\ dB$ respectively when compared with Case #1. For the two breakages at the half-pitch scenario (Case #3) the discussed signatures elevate at $-31.17\ dB$ and $-49.68\ dB$, which is an increase in amplitude of $20.41\ dB$ and $0.9\ dB$ respectively compared to the healthy points (Fig. 6.2b). The specific signature at $8sf_s$, seems to be rather incompetent in the extraction of stator current for detecting a faulty rotor regarding Case #3; this was also observed in the same case regarding the FEM models, however it was afterwards reliably extracted and used in the diagnostic decision with the stray flux measurements. The signature of the subcomponent at $2sf_s$ for Case #1 is stable at $-62.97\ dB$, while it rise by $11.8\ dB$ for Case #2 ($-51.17\ dB$) and by $14.32\ dB$ for Case #3 ($-48.65\ dB$). The latter signature's amplitudes are summarised in Table 6.6.

Regarding the $S(t, f_{7,2})$ trajectory, Case #1 holds an amplitude of $-64.09\ dB$ and $-57.23\ dB$ at the points of $6sf_s$ and $8sf_s$ respectively, while the same observations apply for its spectrum morphology and distribution (Fig. 6.2). These subcomponents reveal for Case #2 the amplitude values of $-38.05\ dB$ ($26.04\ dB$ increase versus healthy) and $-36.58\ dB$ ($20.65\ dB$ increase) respectively (Fig. 6.2a). For the half pitch scenario of Case #3 (Fig. 6.2b), the subcomponent at $6sf_s$ elevates at $-38.42\ dB$ and the $8sf_s$ one at $-42.57\ dB$, reporting increases of $28.35\ dB$ and $32.63\ dB$ respectively compared to the

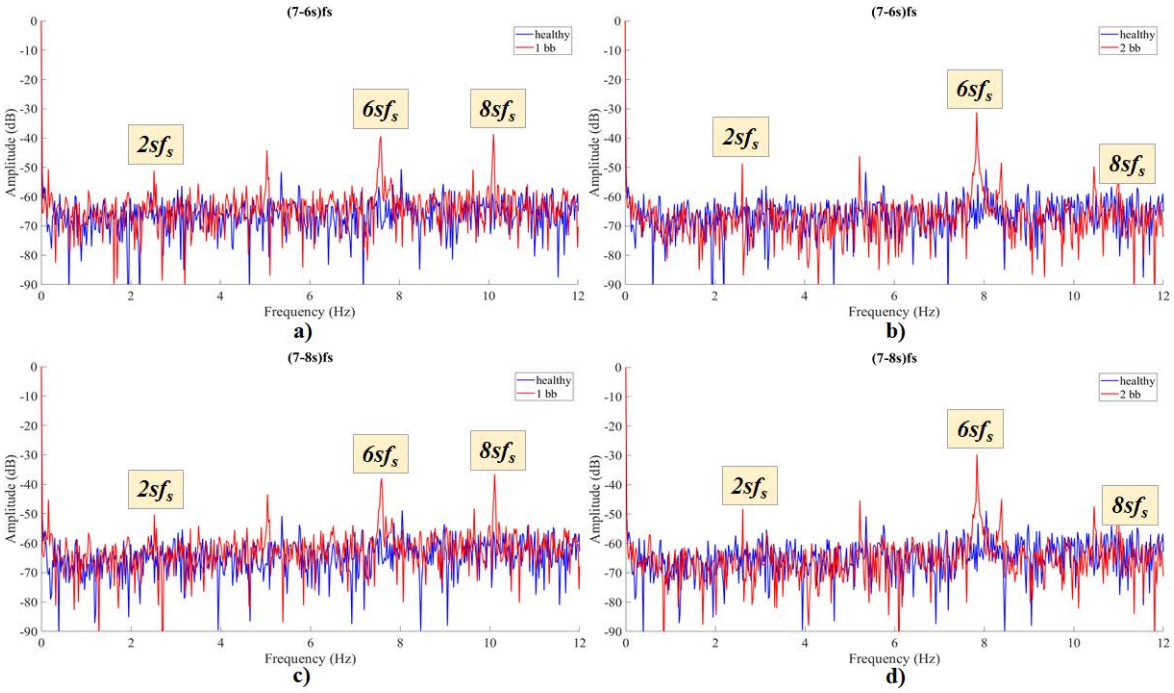

Fig. 6.2 Comparative spectra of extracted trajectories in the stator phase current for the spectral components of Motor #1 at the rated load condition: a) $S(t, f_{7,1})$ (Case #1 vs Case #2) b) $S(t, f_{7,1})$ (Case #1 vs Case #3) c)$S(t, f_{7,2})$ (Case #1 vs Case #2) and d) $S(t, f_{7,2})$ (Case #1 vs Case #3) spectral components of Motor #1

healthy Case #1. The fault-related speed-ripple subcomponent at $2sf_s$ (Table 6.6) lies at $-61.57\ dB$, while it spikes at $-50.35\ dB$ for Case #2 (increase $11.22\ dB$ over healthy) and at $-48.21\ dB$ for Case #3 (increase $13.36\ dB$).

Table 6.5 FFT Amplitudes (dB) of $S(t, f_{7,i})$ for the cases of Motor #1 at Rated Load (Stator Current)

Case	$7f_s - 6sf_s$		$7f_s - 8sf_s$	
	$6sf_s$	$8sf_s$	$6sf_s$	$8sf_s$
Case #1	-51.58	-50.58	-64.09	-57.23
Case #2	-39.39	-38.66	-38.05	-36.58
Case #3	-31.17	-49.68	-29.68	-47.37

Table 6.6 Motor # 1: Comparative table of the FFT amplitudes (dB) for the $2sf_s$ fault-related component in all examined harmonics for all cases - Extracted trajectories from the stator phase current spectral content at rated load

Case	$(5-4s)f_s$	$(5-6s)f_s$	$(7-6s)f_s$	$(7-8s)f_s$
Case #1	-78.85	-75.03	-62.97	-61.57
Case #2	-60.03	-60.55	-51.17	-50.35
Case #3	-49.72	-49.75	-48.65	-48.21

6.1.2 Rated Load: Stray Flux Analysis

Frequency Extraction

5-th Harmonic

In the area of the $5-th$ harmonic, the results provided by the frequency extraction are shown in Figures 6.3 a-d and the amplitudes of the extracted frequency components in each harmonic are given in Table 6.7. As it was for data analysed from FEM simulations and the extracted spectra from the stator phase current, the FFT spectra of these trajectories comprise even multiples of the sf_s for the faulty rotor cases. Localised within the $5-th$ harmonic area, Case #1 has a spectrum value at the $4sf_s$ and $6sf_s$ locations spiking at $-67.22\ dB$ and $-59.52\ dB$ respectively for the $S(t, f_{5,1})$ trajectory. During the single breakage (Fig. 6.3a), the same subcomponents spike at $-32.98\ dB$ and $-50.09\ dB$ respectively for Case #2, which is a compelling increase of 34.24 dB and 9.43 dB with respect to Case #1. For the two breakages at the half-pitch scenario (Case #3) the same components elevate at $-34.65\ dB$ and $-41.78\ dB$, a difference in of 32.57 dB and 17.74 dB compared to the healthy points (Fig. 6.3b). Interestingly, the $2sf_s$ subcomponent is evidently present in the FFT of the $S(t, f_{5,1})$ extracted trajectory with an amplitude of $-47.48\ dB$ for Case #2, having increased by 16.02 dB compared to the healthy Case #1 ($-63.5\ dB$); the same signature rises more tangible in the case of the double breakage fault located at half-pitch distance (Case #3), showing an amplitude increase of 21.31 dB with its spike at $-42.19\ dB$ compared to Case #1. The $2sf_s$ signature's amplitudes are summarised for all cases in Table 6.9.

Regarding the $S(t, f_{5,2})$ trajectory, Case #1 holds an amplitude of $-66.15\ dB$ and $-61.06\ dB$ at the points of $4sf_s$ and $6sf_s$ respectively, while the same observations apply for its spectrum morphology and distribution (Fig. 6.3). These subcomponents reveal for Case #2 the amplitude values of $-32.36\ dB$ (33.79 dB increase versus healthy) and $-49.47\ dB$ (11.59 dB increase) respectively (Fig. 6.3c). For the half pitch scenario of Case #3 (Fig. 6.3d), the subcomponent at $4sf_s$ elevates at $-34.14\ dB$ and the $6sf_s$ one at $-40.43\ dB$, reporting increases of 32.01 dB and 20.63 dB respectively compared to the healthy Case #1. The fault-related speed-ripple subcomponent at $2sf_s$ (Table 6.9) lies at $-61.34\ dB$, while it spikes at $-48.53\ dB$ for Case #2 (increase 12.81 dB over healthy) and at $-41.41\ dB$ for Case #3 (increase 19.93 dB).

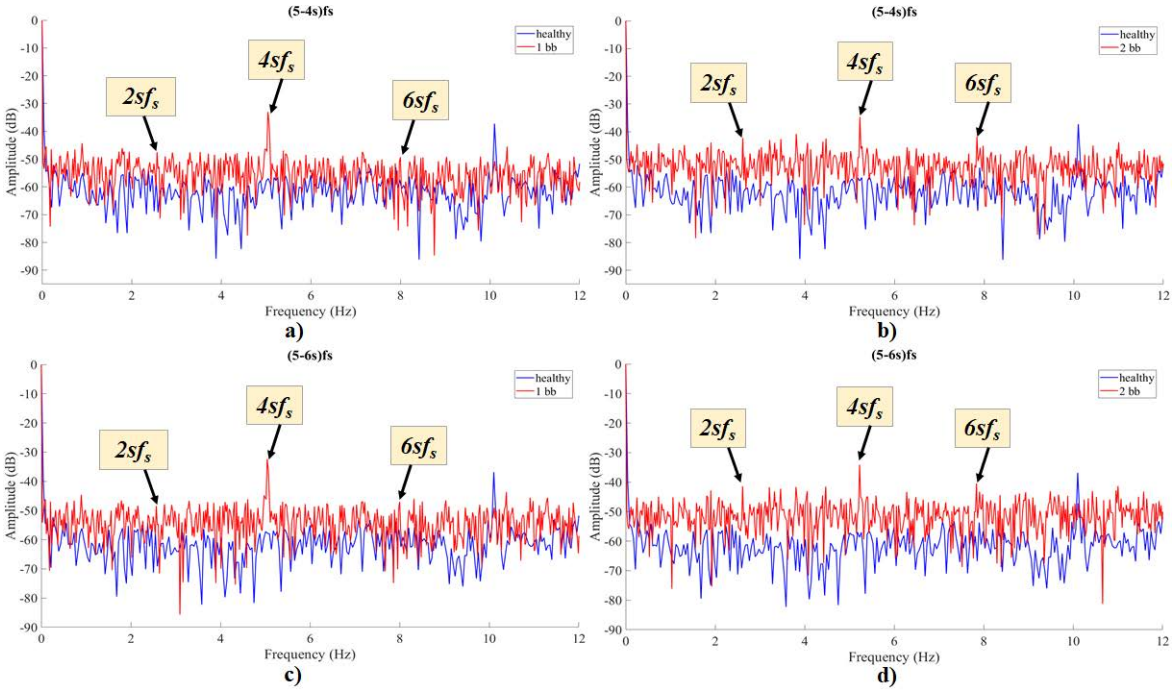

Fig. 6.3 Comparative spectra of extracted trajectories in the stray flux for the spectral components of Motor #1 at the rated load condition: a) $S(t, f_{5,1})$ (Case #1 vs Case #2) b) $S(t, f_{5,1})$ (Case #1 vs Case #3) c)$S(t, f_{5,2})$ (Case #1 vs Case #2) and d) $S(t, f_{5,2})$ (Case #1 vs Case #3) spectral components of Motor #1

Table 6.7 FFT Amplitudes (dB) of $S(t, f_{5,i})$ for the cases of Motor #1 at Rated Load (Stray Flux)

Case	$5f_s - 4sf_s$		$5f_s - 6sf_s$	
	$4sf_s$	$6sf_s$	$4sf_s$	$6sf_s$
Case #1	-67.22	-59.52	-66.15	-61.06
Case #2	-32.98	-50.09	-32.36	-49.47
Case #3	-34.65	-41.78	-34.14	-40.43

7-th Harmonic

In the area of the $7-th$ harmonic, the results provided by the frequency extraction are shown in Figures 6.4 a-d and the amplitudes of the extracted frequency components in each harmonic are given in Table 6.8. As it was for data analysed from FEM simulations and the extracted spectra from the stator phase current, the FFT spectra of these trajectories comprise even multiples of the sf_s for the faulty rotor cases. Localised within the $7-th$ harmonic area, Case #1 has a spectrum value at the $6sf_s$ and $8sf_s$ locations spiking at $-49.61\ dB$ and $-49.41\ dB$ respectively for the $S(t, f_{7,1})$ trajectory. During the single breakage (Fig. 6.4a), the same subcomponents spike at $-28.77\ dB$ and $-31.63\ dB$ respectively for Case #2, which is a compelling increase of 20.84 dB and 17.78 dB with respect to Case #1. For the two breakages at the half-pitch scenario (Case #3) the same components elevate at $-25.36\ dB$ and $-43.8\ dB$, a difference in of 24.25 dB and 5.61 dB compared to the healthy points (Fig. 6.4b). Interestingly, the $2sf_s$ subcomponent is evidently present in the FFT of the $S(t, f_{7,1})$ extracted trajectory with an amplitude of $-43.71\ dB$ for Case #2, having increased by 10.35 dB compared to the healthy Case #1 ($-54.06\ dB$); the same signature rises by a similar volume in the case of the double breakage fault located at half-pitch distance (Case #3), showing an amplitude increase of 10.49 dB with its spike at $-43.57\ dB$ compared to Case #1. The $2sf_s$ signature's amplitudes are summarised for all cases in Table 6.9.

Table 6.8 FFT Amplitudes (dB) of $S(t, f_{7,i})$ for the cases of Motor #1 at Rated Load (Stray Flux)

Case	$7f_s - 6sf_s$		$7f_s - 8sf_s$	
	$6sf_s$	$8sf_s$	$6sf_s$	$8sf_s$
Case #1	-49.61	-49.41	-48	-44.8
Case #2	-28.77	-31.63	-27.82	-27.42
Case #3	-25.36	-43.8	-24.63	-39.88

Regarding the $S(t, f_{7,2})$ trajectory, Case #1 holds an amplitude of $-48\ dB$ and $-44.8\ dB$ at the points of $6sf_s$ and $8sf_s$ respectively, while the same observations apply for its spectrum morphology and distribution (Fig. 6.4). These subcomponents reveal for Case #2 the amplitude values of $-27.82\ dB$ (20.18 dB increase versus healthy) and $-27.42\ dB$ (17.38 dB increase) respectively (Fig. 6.4c). For the half pitch scenario of Case #3 (Fig. 6.4d), the subcomponent at $6sf_s$ elevates at $-24.63\ dB$ and the $8sf_s$ one at $-39.88\ dB$, reporting increases of 23.37 dB and 4.92 dB respectively compared to the healthy Case #1. The fault-related speed-ripple subcomponent at $2sf_s$ (Table 6.9) lies at $-44.32\ dB$ for Case #1, while it spikes at $-42.57\ dB$ for Case #2 (increase 1.75 dB over healthy) and at $-41.29\ dB$ for Case #3 (increase 3.03 dB). The latter result confirms that the $2sf_s$ component is highly likely to be present in a considerable level even in healthy motors when it comes to real life

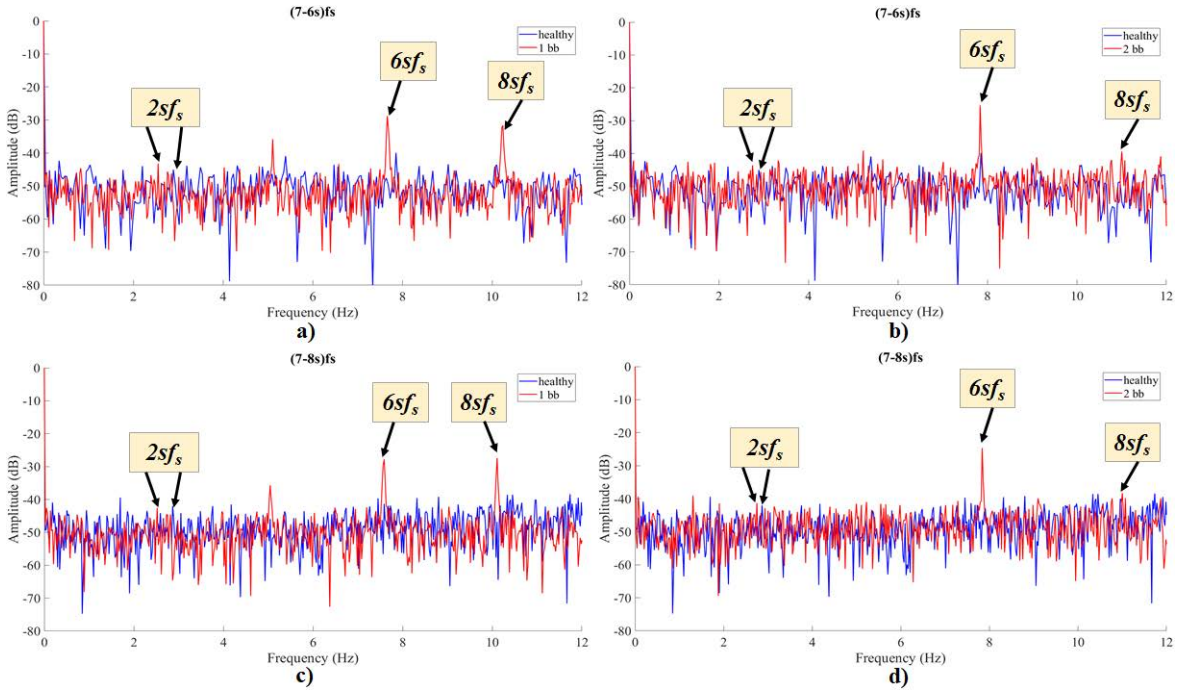

Fig. 6.4 Comparative spectra of extracted trajectories in the stray flux for the spectral components of Motor #1 at the rated load condition: a) $S(t, f_{7,1})$ (Case #1 vs Case #2) b) $S(t, f_{7,1})$ (Case #1 vs Case #3) c)$S(t, f_{7,2})$ (Case #1 vs Case #2) and d) $S(t, f_{7,2})$ (Case #1 vs Case #3) spectral components of Motor #1

applications; therefore, this subcomponent should be always evaluated but is not to be relied on for a definite diagnostic decision.

Table 6.9 Motor # 1: Comparative table of the FFT amplitudes (dB) for the $2sf_s$ fault-related component in all examined harmonics for all cases - Extracted trajectories from the stray flux spectral content at the rated load condition

Case	$(5-4s)f_s$	$(5-6s)f_s$	$(7-6s)f_s$	$(7-8s)f_s$
Case #1	-63.5	-61.34	-54.06	-44.32
Case #2	-47.48	-48.53	-43.71	-42.57
Case #3	-42.19	-41.41	-43.57	-41.29

6.1.3 Half-Rated Load: Stator Phase Current Analysis

Reliable Limit for Extraction

All components at twice the slip frequency ($\simeq 2ksf_s$ components) are calculated for each model's case and are given with the values of slip in Table 6.10 for the half-rated load condition. As before, the presented value expresses the distance of an examined component from the central harmonic and is accounted for when deriving the lower bound of the window sequence length. As expected, the half-rated load condition yields higher values for the lower bounds of the windowing sequence due to the slightly lower value of slip during this condition.

Table 6.10 Slip values & $2ksf_s$ distances for all cases of Motor #1 - Half Rated Load Condition

Component	Case #1	Case #2	Case #3
	$s_1 \simeq 0.0195$	$s_2 \simeq 0.0204$	$s_3 \simeq 0.0215$
$2sf_s$	1.8	1.81	1.68
$4sf_s$	3.6	3.62	3.36
$6sf_s$	5.4	5.43	5.04
$8sf_s$	7.2	7.24	6.72

The minimum required window sequence lengths, calculated as described in Chapter4, are presented in Table 6.11 with the value used for the parameter ξ derived from exhaustive search. Each value in the table provides a window length capable to separate and capture the the sideband given in the first column. As done for all FEM models and experimental cases, the largest of each column is chosen to assure seperability of frequencies distanced at least $2sf_s$ from each other and localisation in the next frequency chunk.

Table 6.11 Window sequence lower bounds for Motor #1 - Half Rated Load Condition

$\xi = -0.18$	Case #1	Case #2	Case #3
$2sf_s$	3121	3104	3344
$4sf_s$	1561	1552	1672
$6sf_s$	1040	1035	1115
$8sf_s$	780	776	836

Frequency Extraction

5-th Harmonic

The results of frequency extraction in the band of the $5-th$ harmonic are shown in Figures 6.5 a-d; the amplitudes of the extracted frequency components in each harmonic are given in Table 6.12. In all FFT representations of these trajectories, the even multiples of the sf_s ripple are present to examine their diagnostic potential. Considering the values presented in Table 6.12, it can be seen from Figure 6.5 that, as in all cases so far, the healthy motor's spectrum is free from any fault-related oscillations. Localised within the $5-th$ harmonic's frame, Case #1 has a spectrum value at the $4sf_s$ and $6sf_s$ locations spiking at $-68.02\ dB$ and $-65.01\ dB$ respectively for the $S(t, f_{5,1})$ trajectory. During the single breakage fault at Fig. 6.5a, the same subcomponents spike at $-40.14\ dB$ and $-53.7\ dB$ respectively for Case #2. This is a change of $27.88\ dB$ and $11.31\ dB$ respectively when compared with Case #1. For the two breakages at the half-pitch scenario (Case #3) the discussed signatures are erected at $-40.18\ dB$ and $-39.57\ dB$, which is an increase in amplitude of $27.84\ dB$ and $11.31\ dB$ respectively compared to the healthy points (Fig. 6.5b). The signature of the subcomponent at $2sf_s$ for Case #1 is at $-74.3\ dB$, while it rise by $11.58\ dB$ for Case #2 ($-62.72\ dB$) and by $26.35\ dB$ for Case #3 ($-47.95\ dB$). The latter signature's amplitudes are summarised in Table 6.14.

Table 6.12 FFT Amplitudes (dB) of $S(t, f_{5,i})$ for all cases of Motor #1 at Half-Rated Load (Stator Current)

Case	$5f_s - 4sf_s$		$5f_s - 6sf_s$	
	$4sf_s$	$6sf_s$	$4sf_s$	$6sf_s$
Case #1	-68.02	-65.01	-67.66	-67.4
Case #2	-40.14	-53.7	-39.72	-53.1
Case #3	-40.18	-39.27	-43.03	-44.73

Regarding the $S(t, f_{5,2})$ trajectory, Case #1 holds an amplitude of $-67.66\ dB$ and $-67.4\ dB$ at the points of $4sf_s$ and $6sf_s$ respectively, while the same observations apply for its spectrum morphology and distribution (Fig. 6.5). These subcomponents reveal for Case #2 the amplitude values of $-39.72\ dB$ ($27.94\ dB$ increase versus healthy) and $-53.1\ dB$ ($14.3\ dB$ increase) respectively (Fig. 6.5a). For the half pitch scenario of Case #3 (Fig. 6.5b), the subcomponent at $4sf_s$ elevates at $-43.03\ dB$ and the $6sf_s$ one at $-44.73\ dB$, reporting increases of $24.63\ dB$ and $22.67\ dB$ respectively compared to the healthy Case #1. The fault-related speed-ripple subcomponent at $2sf_s$ (Table 6.14) lies at $-67.3\ dB$, while it spikes at $-63.03\ dB$ for Case #2 (increase $4.27\ dB$ over healthy) and at $-53.29\ dB$ for Case #3 (increase $14.01\ dB$). The latter observation validates the inapplicability of the $2sf_s$

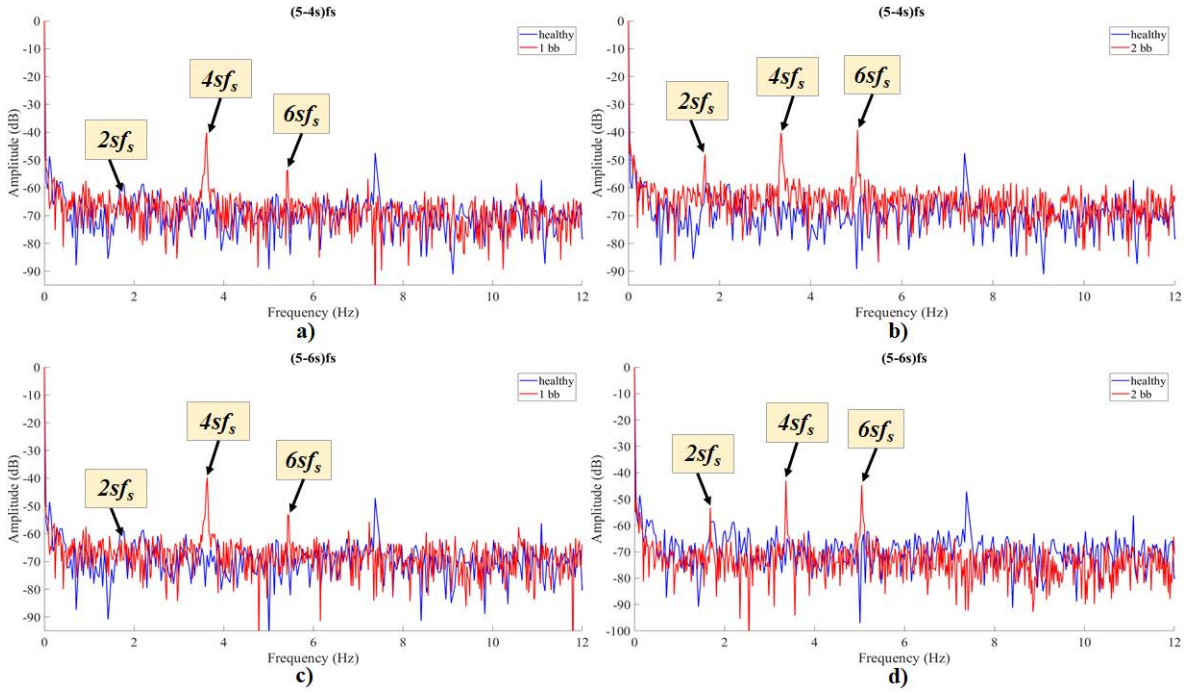

Fig. 6.5 Comparative spectra of extracted trajectories in the stator phase current for the spectral components of Motor #1 at the half-rated load condition: a) $S(t, f_{5,1})$ (Case #1 vs Case #2) b) $S(t, f_{5,1})$ (Case #1 vs Case #3) c)$S(t, f_{5,2})$ (Case #1 vs Case #2) and d) $S(t, f_{5,2})$ (Case #1 vs Case #3) spectral components of Motor #1

component to provide a diagnostic signature as it might be at same or similar level in healthy and faulty motors, while the other subcomponents in the investigated set of signatures prove more useful.

7-th Harmonic

In the area of the $7-th$ harmonic, the results provided by the frequency extraction are shown in Figures 6.6 a-d and the amplitudes of the extracted frequency components in each harmonic are given in Table 6.13. As it was for data analysed from FEM simulations and the extracted spectra from the stator phase current at rated load, the FFT spectra of these trajectories comprise even multiples of the sf_s for the faulty rotor cases. Localised within the $7-th$ harmonic area, Case #1 has a spectrum value at the $6sf_s$ and $8sf_s$ locations spiking at $-63.24\ dB$ and $-62.06\ dB$ respectively for the $S(t, f_{7,1})$ trajectory. During the single breakage (Fig. 6.6a), the same subcomponents spike at $-39.06\ dB$ and $-41.06\ dB$ respectively for Case #2, which is a compelling increase of 24.18 dB and 21 dB with respect to Case #1. For the two breakages at the half-pitch scenario (Case #3) the same components elevate at $-33.73\ dB$ and $-54.61\ dB$, which is a compelling difference in amplitude of 29.51 dB and 7.45 dB compared to the healthy points (Fig. 6.6b). Interestingly, the $2sf_s$

subcomponent is evidently present in the FFT of the $S(t, f_{7,1})$ extracted trajectory with an amplitude of $-51.43\ dB$ for Case #2, having increased by $15.72\ dB$ compared to the healthy Case #1 ($-67.15\ dB$); the same signature rises by a similar volume in the case of the double breakage fault located at half-pitch distance (Case #3), showing an amplitude increase of $17.55\ dB$ with its spike at $-49.6\ dB$ compared to Case #1. The $2sf_s$ signature's amplitudes are summarised for all cases in Table 6.14.

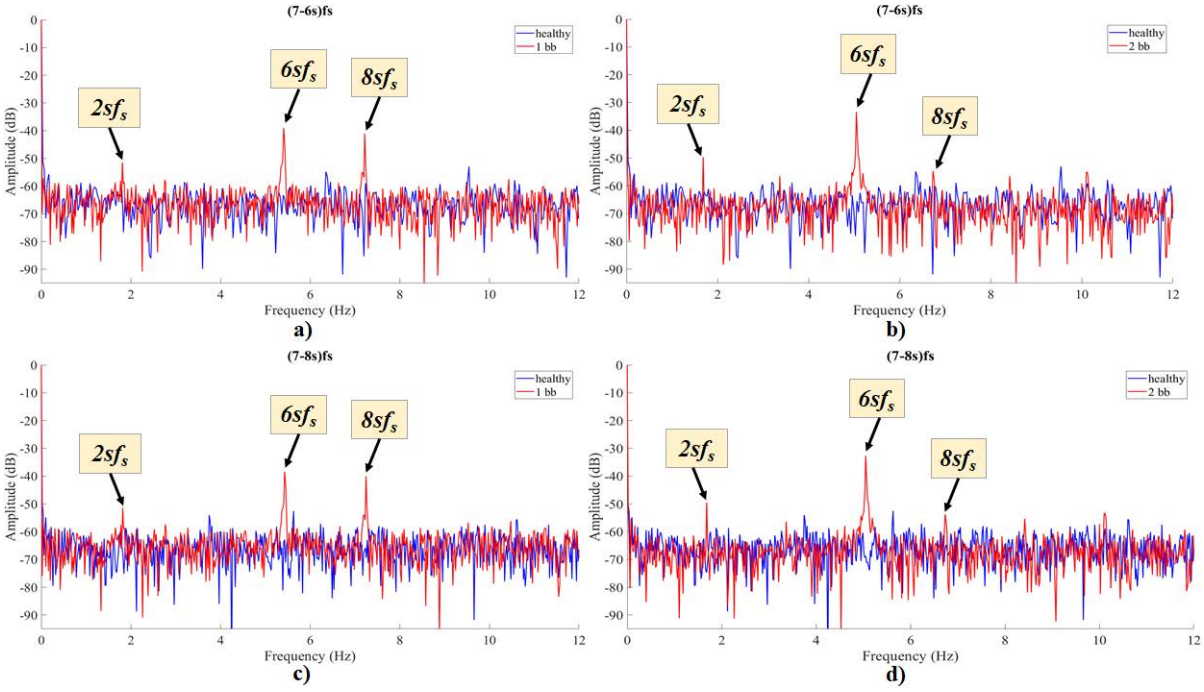

Fig. 6.6 Comparative spectra of extracted trajectories in the stator phase current for the spectral components of Motor #1 at the half-rated load condition: a) $S(t, f_{7,1})$ (Case #1 vs Case #2) b) $S(t, f_{7,1})$ (Case #1 vs Case #3) c)$S(t, f_{7,2})$ (Case #1 vs Case #2) and d) $S(t, f_{7,2})$ (Case #1 vs Case #3) spectral components of Motor #1

Regarding the $S(t, f_{7,2})$ trajectory, Case #1 holds an amplitude of $-65.69\ dB$ and $-66.82\ dB$ at the points of $6sf_s$ and $8sf_s$ respectively, while the same observations apply for its spectrum morphology and distribution (Fig. 6.6). These subcomponents reveal for Case #2 the amplitude values of $-38.43\ dB$ ($27.26\ dB$ increase versus healthy) and $-40\ dB$ ($26.82\ dB$ increase) respectively (Fig. 6.6c). For the half pitch scenario of Case #3 (Fig. 6.6d), the subcomponent at $6sf_s$ elevates at $-32.69\ dB$ and the $8sf_s$ one at $-53.78\ dB$, reporting increases of 33 dB and 13.04 dB respectively compared to the healthy Case #1. The fault-related speed-ripple subcomponent at $2sf_s$ (Table 6.14) lies at $-59.66\ dB$ for Case #1, while it spikes at $-51.43\ dB$ for Case #2 (increase 8.23 dB over healthy) and at $-49.53\ dB$ for Case #3 (increase 10.13 dB over healthy). The latter result confirms that the $2sf_s$ component is highly likely to be present in a considerable level even in healthy motors when it comes to real life applications; therefore, this subcomponent should be always evaluated but

is not to be relied on for a definite diagnostic decision. This observation is clear from most of the FEM cases as well, as it also was evident from the analysis at the rated load condition.

Table 6.13 FFT Amplitudes (dB) of $S(t, f_{7,i})$ for all cases of Motor #1 at Half-Rated Load (Stator Current)

Case	$7f_s - 6sf_s$		$7f_s - 8sf_s$	
	$6sf_s$	$8sf_s$	$6sf_s$	$8sf_s$
Case #1	-63.24	-62.06	-65.69	-66.82
Case #2	-39.06	-41.06	-38.43	-40
Case #3	-33.73	-54.61	-32.69	-53.78

Table 6.14 Motor # 1: Comparative table of the FFT amplitudes (dB) for the $2sf_s$ fault-related component in all examined harmonics for all cases - Extracted trajectories from the stator phase current spectral content at the half rated load condition

Case	$(5-4s)f_s$	$(5-6s)f_s$	$(7-6s)f_s$	$(7-8s)f_s$
Case #1	-74.3	-67.3	-67.15	-59.66
Case #2	-62.72	-63.03	-51.43	-51.43
Case #3	-47.95	-53.29	-49.6	-49.53

6.1.4 Half-Rated Load: Stray Flux Analysis

Frequency Extraction

5-th Harmonic

In the area of the $5-th$ harmonic, the results provided by the frequency extraction are shown in Figures 6.7 a-d and the amplitudes of the extracted frequency components in each harmonic are given in Table 6.15. As it was for data analysed from FEM simulations and the rated load experiment, the FFT spectra of these trajectories enclose components at the $2ksf_s$ frequencies for the faulty rotor cases. Within the $5-th$ harmonic area, Case #1 has a spectrum value at the $4sf_s$ and $6sf_s$ locations spiking at $-44.83\ dB$ and $-50.39\ dB$ respectively for the $S(t, f_{5,1})$ trajectory. During the single breakage (Fig. 6.7a), the same subcomponents spike at $-33.93\ dB$ and $-36.04\ dB$ respectively for Case #2, which is an increase o $10.9\ dB$ and $14.35\ dB$ with respect to Case #1. For the two breakages at the half-pitch scenario (Case #3) the same components elevate at $-38.56\ dB$ and $-43.59\ dB$, a difference in of $6.27\ dB$ and $6.8\ dB$ compared to the healthy points (Fig. 6.7b). The $S(t, f_{5,1})$ trajectory presents in the $2sf_s$ subcomponent from Case #1 - Case #3 the values of $-56.91\ dB$, $-47.1\ dB$ and $-45.16\ dB$ respectively (Table 6.17).

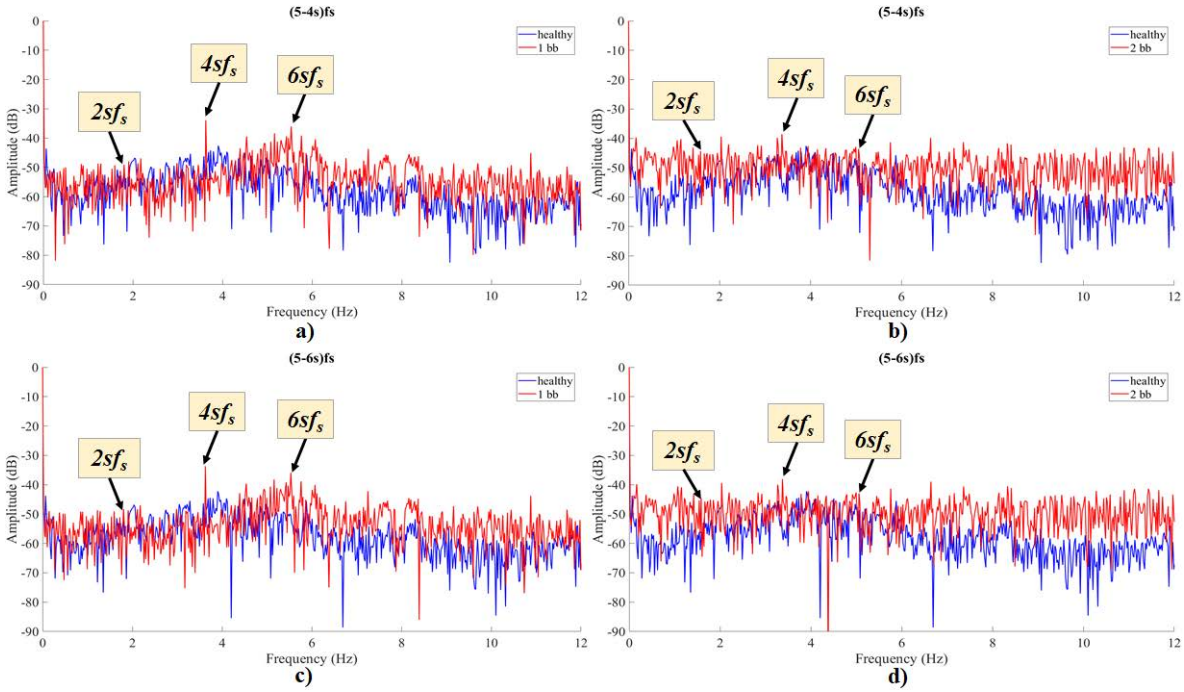

Fig. 6.7 Comparative spectra of extracted trajectories in the stray flux for the spectral components of Motor #1 at the half-rated load condition: a) $S(t, f_{5,1})$ (Case #1 vs Case #2) b) $S(t, f_{5,1})$ (Case #1 vs Case #3) c)$S(t, f_{5,2})$ (Case #1 vs Case #2) and d) $S(t, f_{5,2})$ (Case #1 vs Case #3) spectral components of Motor #1

Table 6.15 FFT Amplitudes (dB) of $S(t, f_{5,i})$ for all cases of Motor #1 at Half-Rated Load (Stray Flux)

Case	$5f_s - 4sf_s$		$5f_s - 6sf_s$	
	$4sf_s$	$6sf_s$	$4sf_s$	$6sf_s$
Case #1	-44.83	-50.39	-48.63	-50.02
Case #2	-33.93	-36.04	-33.71	-35.94
Case #3	-38.56	-43.59	-38.08	-42.65

Regarding the $S(t, f_{5,2})$ trajectory, Case #1 holds an amplitude of -48.63 dB and -50.02 dB at the points of $4sf_s$ and $6sf_s$ respectively (Fig. 6.7). These components hold the amplitude values of -33.71 dB (14.92 dB increase) and -35.94 dB (14.08 dB increase) respectively for the one broken bar of Case #2 (Fig. 6.7c). For the half pitch scenario of Case #3 (Fig. 5.39d), the subcomponent at $4sf_s$ elevates at -38.08 dB and the $6sf_s$ one at -42.65 dB, reporting increases of 10.55 dB and 7.37 dB respectively compared to the healthy Case #1. The $S(t, f_{5,2})$ trajectory presents in the $2sf_s$ subcomponent from Case #1 - Case #3 the values of -57.8 dB, -48.19 dB and -45.08 dB respectively (Table 6.17).

7-th Harmonic

The results of frequency extraction in the band of the $7-th$ harmonic are shown in Figures 6.8 a-d; the amplitudes of the extracted frequency components in each harmonic are given in Table 6.16. In all FFT representations of these trajectories, components of fault related $2ksf_s$ signatures are present to examine their diagnostic potential. Considering the values presented in Table 6.16, it can be seen from Figure 6.8 that the healthy motor's extracted trajectory is free from fault-related oscillations. Localised within the $7-th$ harmonic's frame, Case #1 has a spectrum value at the $6sf_s$ and $8sf_s$ locations spiking at -59.51 dB and -48.37 dB respectively for the $S(t, f_{7,1})$ trajectory. During the single breakage fault at Fig. 6.8a, the same subcomponents spike at -34.05 dB and -32.49 dB respectively for Case #2. This is a change of 25.46 dB and 15.88 dB respectively when compared with Case #1. For the two breakages at the half-pitch scenario (Case #3) the discussed signatures elevate at -29.11 dB and -40.17 dB, which is an increase in amplitude of 30.4 dB and 8.2 dB respectively compared to the healthy points (Fig. 6.8b). The small change in amplitude of this specific signature at $8sf_s$ was also observed in the same case regarding the FEM models, however it was afterwards reliably extracted and used in the diagnostic decision with the stray flux measurements. As seen here, this is not the case during the half-rated load condition since the component behaves the same way in stator current and stray flux extraction. The signature of the subcomponent at $2sf_s$ for Case #1 is stable at -59.41 dB, while it rise by

10.88 dB for Case #2 (-48.53 dB) and by 16.76 dB for Case #3 (-42.65 dB). The latter signature's amplitudes are summarised in Table 6.17.

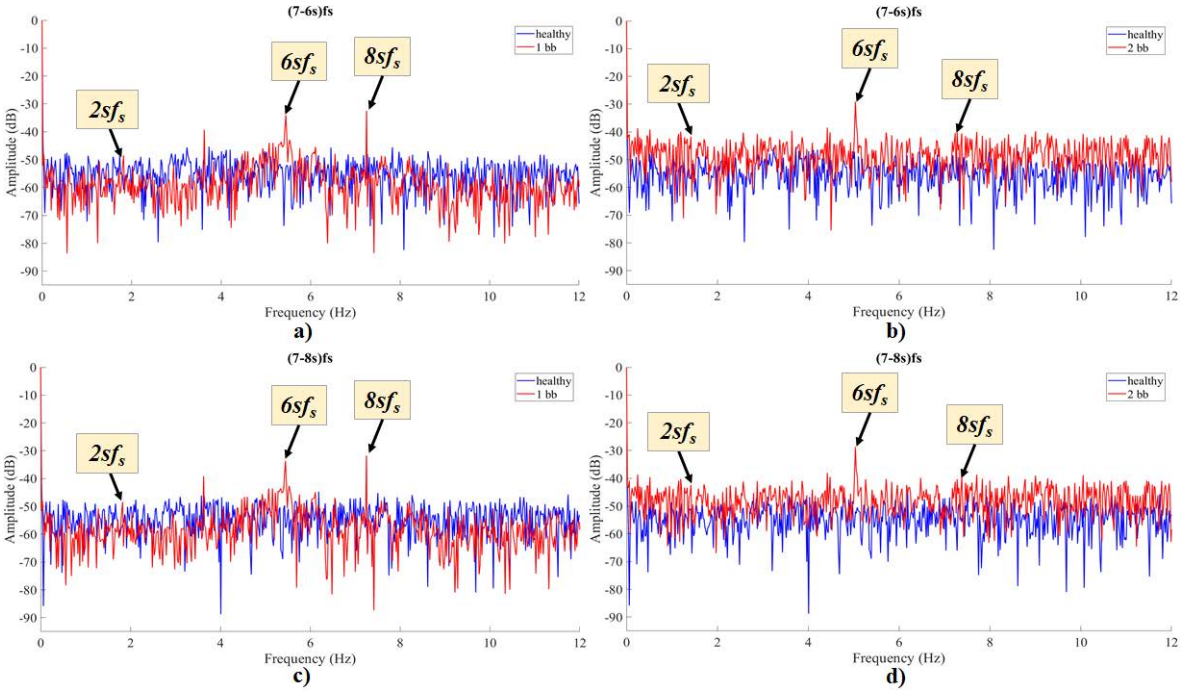

Fig. 6.8 Comparative spectra of extracted trajectories in the stray flux for the spectral components of Motor #1 at the half-rated load condition: a) $S(t, f_{7,1})$ (Case #1 vs Case #2) b) $S(t, f_{7,1})$ (Case #1 vs Case #3) c)$S(t, f_{7,2})$ (Case #1 vs Case #2) and d) $S(t, f_{7,2})$ (Case #1 vs Case #3) spectral components of Motor #1

Table 6.16 FFT Amplitudes (dB) of $S(t, f_{7,i})$ for all cases of Motor #1 at Half-Rated Load (Stray Flux)

Case	$7f_s - 6sf_s$		$7f_s - 8sf_s$	
	$6sf_s$	$8sf_s$	$6sf_s$	$8sf_s$
Case #1	-59.51	-48.37	-52.7	-57.77
Case #2	-34.05	-32.49	-33.66	-31.77
Case #3	-29.11	-40.17	-28.68	-42.38

Regarding the $S(t, f_{7,2})$ trajectory, Case #1 holds an amplitude of -52.7 dB and -57.77 dB at the points of $6sf_s$ and $8sf_s$ respectively, while the same observations apply for its spectrum morphology and distribution (Fig. 6.8). These subcomponents reveal for Case #2 the amplitude values of -33.66 dB (19.04 dB increase versus healthy) and -31.77 dB (26 dB increase) respectively (Fig. 6.8a). For the half pitch scenario of Case #3 (Fig. 6.8b), the subcomponent at $4sf_s$ elevates at -28.68 dB and the $6sf_s$ one at -42.38 dB, reporting increases of 24.02 dB and 15.39 dB respectively compared to the healthy Case #1. The fault-related speed-ripple subcomponent at $2sf_s$ (Table 6.17) lies at -60.53 dB, while it

spikes at $-48.24\ dB$ for Case #2 (increase 12.29 dB over healthy) and at $-42.2\ dB$ for Case #3 (increase 18.33 dB).

Table 6.17 Motor # 1: Comparative table of the FFT amplitudes (dB) for the $2sf_s$ fault-related component in all examined harmonics for all cases - Extracted trajectories from the stray flux spectral content at the half rated load condition

Case	$(5-4s)f_s$	$(5-6s)f_s$	$(7-6s)f_s$	$(7-8s)f_s$
Case #1	-56.91	-57.8	-59.41	-60.53
Case #2	-47.1	-48.19	-48.53	-48.24
Case #3	-45.16	-45.08	-42.65	-42.2

6.2 Motor #2: Stray Flux Analysis at Rated Load

The results presented in this section regard a 1.1 kW, 4-$pole$ IM. The experimental measurements were performed in University of Valencia under the rated load condition. The experiment handled several broken bar cases, which are summarised in Table 6.18.

Table 6.18
Summary of cases for Motor #2

Case	Breakage Location
Case #1	healthy
Case #2	2 adjacent bars
Case #3	2 bars at half pitch
Case #4	2 bars at full pitch

Reliable Limit for Extraction

All components at twice the slip frequency ($\simeq 2ksf_s$ components) are calculated for each case and are given with the values of slip in Table 6.19. As done so far, the presented value expresses the distance of an examined component from the central harmonic and is accounted for when deriving the lower bound of the window sequence length.

Table 6.19 Slip values & $2ksf_s$ distances for all cases of Motor #2 - Rated Load Condition

Component	Case #1	Case #2	Case #3	Case #4
	$s_1 \simeq 0.0132$	$s_2 \simeq 0.0132$	$s_3 \simeq 0.0088$	$s4 \simeq 0.0096$
$2sf_s$	1.32	1.32	0.88	0.96
$4sf_s$	2.64	2.64	1.76	1.92
$6sf_s$	3.96	3.96	2.64	2.88
$8sf_s$	5.28	5.28	3.52	3.84

The minimum required window sequence lengths, calculated as described in Chapter4, are presented in Table 6.20 with the value used for the parameter ξ derived from exhaustive search. As expected, the motors with equal value in slip (Case #1 & Case #2) yield equal lower bounds.

Table 6.20 Window sequence lower bounds for Motor #2 at Rated Load

$\xi = -0.36$	Case #1	Case #2	Case #3	Case #4
$2sf_s$	5190	5190	7785	7137
$4sf_s$	2595	2595	3893	3568
$6sf_s$	1730	1730	2595	2379
$8sf_s$	1298	1298	1946	1784

Frequency Extraction

5-th Harmonic

With regards to the $5-th$ harmonic, the results provided by the frequency extraction are shown in Figures 6.9 & 6.10 and the amplitudes of the extracted frequency components in each harmonic are given in Table 6.21. In all FFT representations of these trajectories, even multiples of the sf_s signature are present, as in the FEM models and previous experiments. Within the $5-th$ harmonic's frequency band, Case #1 (healthy) has a spectrum value at the $4sf_s$ and $6sf_s$ locations spiking at -52.05 dB and -56.6 dB respectively for the $S(t, f_{5,1})$ trajectory. During the two adjacent broken bar fault (Fig. 6.9b), the same components spike at -25.91 dB and -38.04 dB respectively for Case #2. This is a change of 26.14 dB and 18.56 dB with respect to Case #1. For Case #3 (breakages at half-pitch) the discussed amplitudes are at the level of -22.39 dB and -45.34 dB respectively (Fig. 6.9c)s, which is respectively a change of 29.66 dB and 11.26 dB respectively compared to the healthy motor. For the two breakages at the full-pitch distance (Case #4) the same components elevate at -22.55 dB and -32.52 dB, a change of 29.5 dB and 24.08 dB compared to the healthy points (Fig. 6.9d). The theoretical $2sf_s$ component presents the values of -44 dB, -28.09 dB, -37.75 dB and -37.45 dB from Case#1 - Case #4 respectively (Table 6.23), showing again that inherent imbalances are highly likely to make this specific component appear even in healthy motors.

Regarding the $S(t, f_{5,2})$ trajectory, Case #1 holds an amplitude of -50.91 dB and -55.62 dB at the points of $4sf_s$ and $6sf_s$ respectively, while the same observations apply for its spectrum morphology and distribution (Fig. 6.10). These components hold the amplitude values of -26.42 dB (24.49 dB increase) and -38.94 dB (16.68 dB increase) respectively for the two adjacent broken bars of Case #2 (Fig. 6.10b). The half pitch breakage distance scenario of Case #3 (Fig. 6.10c) elevates the discussed components at -22.77 dB and -45.43 dB respectively (increases of 28.14 dB and 10.19 dB respectively). For the full pitch scenario of Case #4 (Fig. 6.10d), the subcomponent at $4sf_s$ elevates at -25.45 dB and the $6sf_s$ one at -36.74 dB, reporting increases of 25.46 dB and 19.88 dB respectively compared to the healthy Case #1. The $S(t, f_{5,2})$ trajectory presents in the $2sf_s$ signature

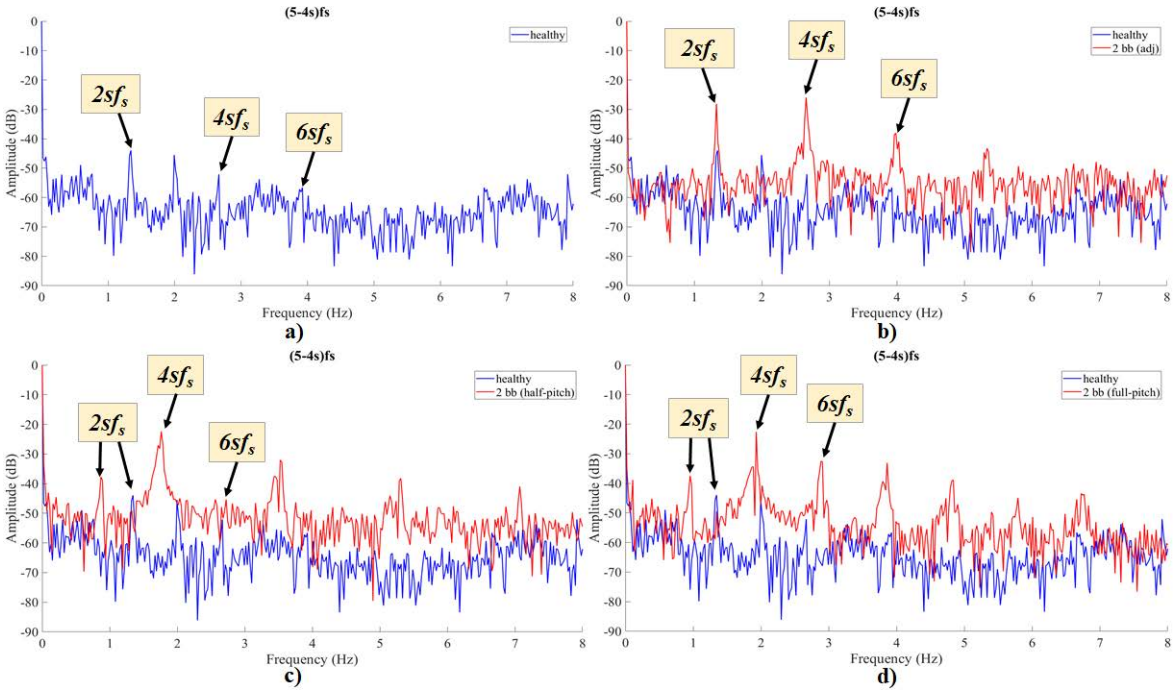

Fig. 6.9 Comparative spectra of extracted trajectories in the stray flux for the $S(t, f_{5,1})$ spectral component for Motor #2: a)Case #1 b)Case #2 c)Case #3 d)Case #4

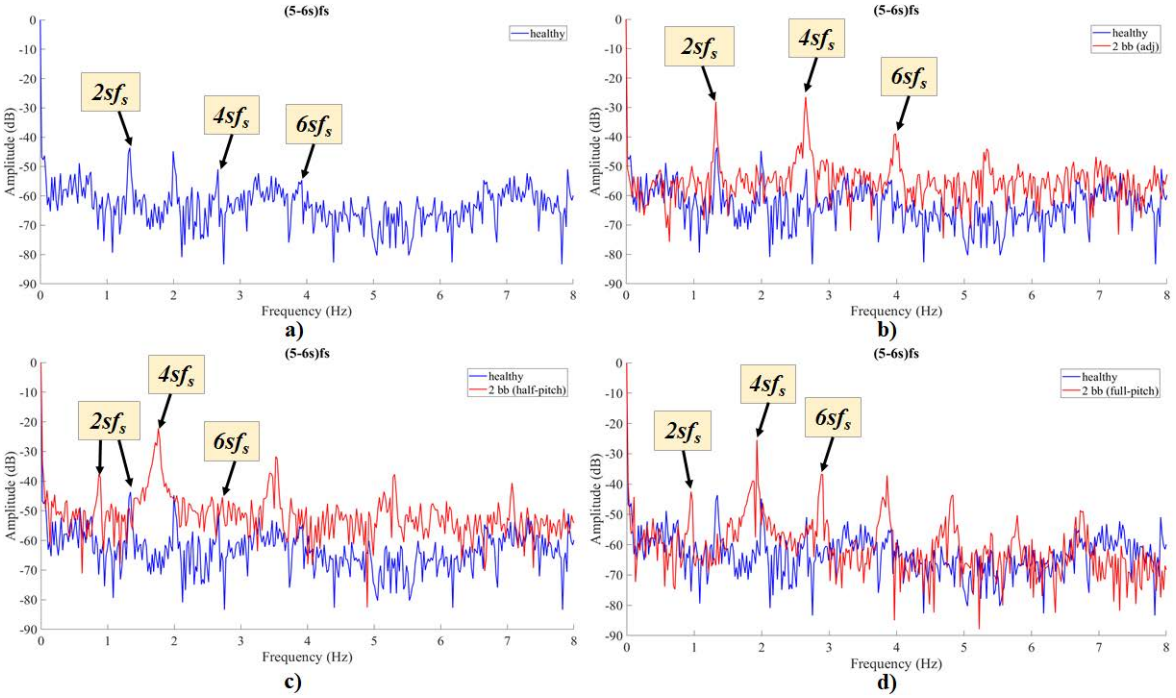

Fig. 6.10 Comparative spectra of extracted trajectories in the stray flux for the $S(t, f_{5,2})$ spectral component for Motor #2: a)Case #1 b)Case #2 c)Case #3 d)Case #4

from Case #1 - Case #4 the values of $-43.63\ dB$, $-28.07\ dB$, $-37.15\ dB$ and $-42.51\ dB$ respectively (Table 6.23).

Table 6.21 FFT Amplitudes (dB) of $S(t, f_{5,i})$ for all cases of Motor #2 (Stray Flux)

Case	$5f_s - 4sf_s$		$5f_s - 6sf_s$	
	$4sf_s$	$6sf_s$	$4sf_s$	$6sf_s$
Case #1	-52.05	-56.6	-50.91	-55.62
Case #2	-25.91	-38.04	-26.42	-38.94
Case #3	-22.39	-45.34	-22.77	-45.43
Case #4	-22.55	-32.52	-25.45	-36.74

7-th Harmonic

With regards to the $7-th$ harmonic, the results provided by the frequency extraction are shown in Figures 6.11 & 6.12 and the amplitudes of the extracted frequency components in each harmonic are given in Table 6.22. At this frequency zone, Case #1 has a spectrum value at the $6sf_s$ and $8sf_s$ locations spiking at $-57.36\ dB$ and $-70.15\ dB$ respectively for the $S(t, f_{7,1})$ trajectory. At two adjacent broken bars (Fig. 6.11b), the same components spike at $-30.22\ dB$ and $-50.68\ dB$ respectively for Case #2. This is a change of $27.14\ dB$ and $19.47\ dB$ with respect to Case #1. For Case #3 the discussed amplitudes are at the level of $-37.33\ dB$ and $-50.65\ dB$ respectively (Fig. 6.11c)s, which is respectively a change of $20.03\ dB$ and $19.5\ dB$ respectively compared to the healthy motor. For Case #4 the same components elevate at $-25.99\ dB$ for both signatures, a change of $31.37\ dB$ for the $6sf_s$ and $44.16\ dB$ for the $8sf_s$ compared to the healthy points (Fig. 6.11d). The $2sf_s$ signature presents the values of $-68.31\ dB$, $-47\ dB$, $-40.21\ dB$ and $-47.8\ dB$ from Case#1 - Case #4 respectively (Table 6.23).

Table 6.22 FFT Amplitudes (dB) of $S(t, f_{7,i})$ for all cases of Motor #2 (Stray Flux)

Case	$7f_s - 6sf_s$		$7f_s - 8sf_s$	
	$6sf_s$	$8sf_s$	$6sf_s$	$8sf_s$
Case #1	-57.36	-70.15	-71.44	-69.06
Case #2	-30.22	-50.68	-29.81	-50.05
Case #3	-37.33	-50.65	-27.04	-35.17
Case #4	-25.99	-25.99	-25.76	-30.45

Regarding the $S(t, f_{7,2})$ trajectory, Case #1 holds an amplitude of $-71.44\ dB$ and $-69.06\ dB$ at the points of $6sf_s$ and $8sf_s$ respectively (Fig. 6.12). These components hold the amplitude values of $-29.81\ dB$ ($41.63\ dB$ increase) and $-50.05\ dB$ ($19.01\ dB$

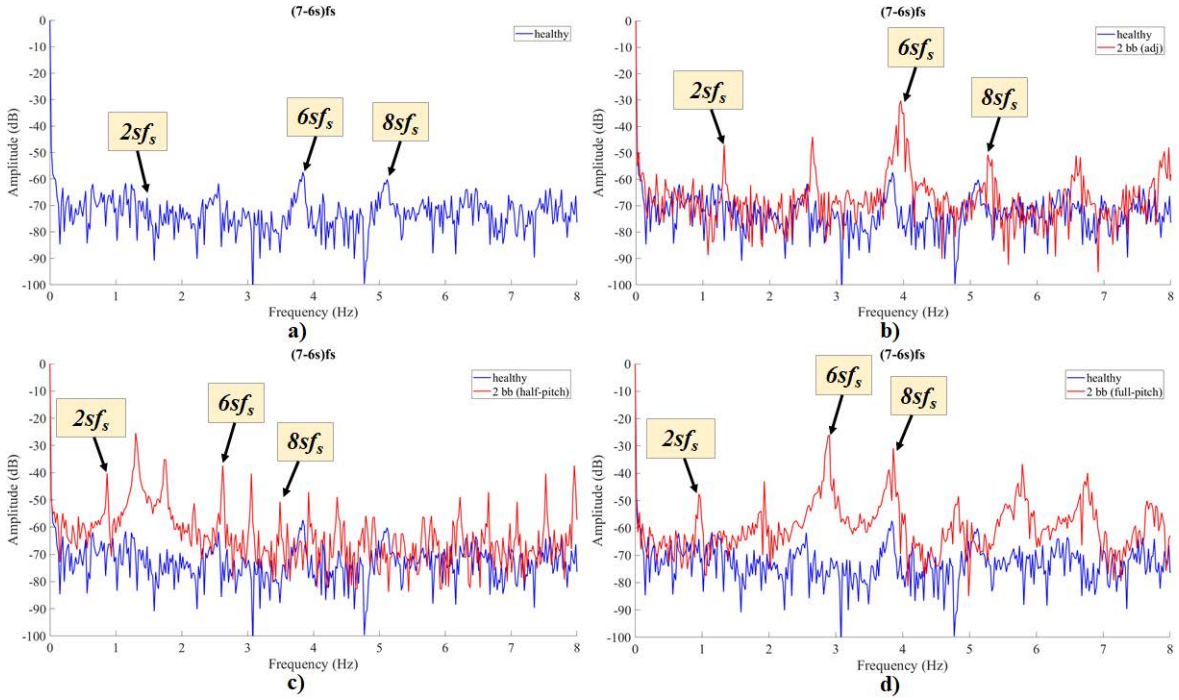

Fig. 6.11 Comparative spectra of extracted trajectories in the stray flux for the $S(t, f_{7,1})$ spectral component for Motor #2: a)Case #1 b)Case #2 c)Case #3 d)Case #4

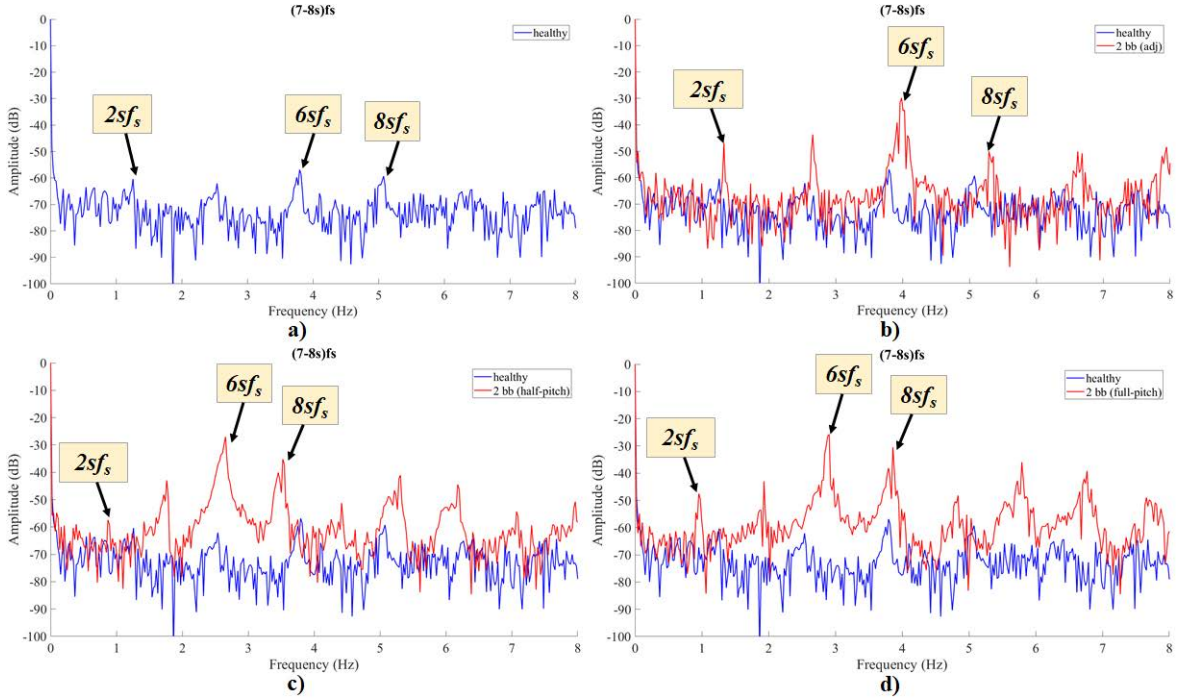

Fig. 6.12 Comparative spectra of extracted trajectories in the stray flux for the $S(t, f_{7,2})$ spectral component for Motor #2: a)Case #1 b)Case #2 c)Case #3 d)Case #4

increase) respectively for Case #2 (Fig. 6.12b). The half pitch breakage distance scenario of Case #3 (Fig. 6.12c) erects the discussed components at $-27.04\ dB$ and $-35.17\ dB$ respectively (increases of 44.4 dB and 33.89 dB respectively). For the full pitch scenario of Case #4 (Fig. 6.12d), the subcomponent at $6sf_s$ elevates at $-25.76\ dB$ and the $8sf_s$ one at $-30.45\ dB$, reporting increases of 45.68 dB and 38.61 dB respectively compared to Case #1. The $S(t, f_{7,2})$ trajectory presents in the $2sf_s$ signature from Case #1 - Case #4 the values of $-28.4\ dB$, $-40.08\ dB$, $-46.96\ dB$ and $-34.42\ dB$ respectively (Table 6.23). It is seen that the $2sf_s$ component of the $7-th$ harmonic appears stronger in the healthy motor than in all other cases, when extracted for the lower sideband; its behaviour is unpredicted regardless the motor condition, as it relates with the motor imperfections appearing randomly in unexpected amplitude levels and is therefore confirmed as unreliable for diagnostic purposes. Nevertheless, the signatures of the subcomponents at $6sf_S$ and $8sf_s$ perform very well and their amplitude variations are of good potential for a diagnostic decision.

Table 6.23 Motor # 2: Comparative table of the FFT amplitudes (dB) for the $2sf_s$ fault-related component in all examined harmonics for all cases - Extracted trajectories from the stray flux spectral content at rated load

Case	$(5-4s)f_s$	$(5-6s)f_s$	$(7-6s)f_s$	$(7-8s)f_s$
Case #1	-44.02	-43.63	-68.31	-67.87
Case #2	-28.09	-28.07	-47	-46.94
Case #3	-37.75	-37.15	-40.21	-57.42
Case #4	37.45	-41.51	-47.56	-47.52

6.3 Discussion & Conclusive Remarks

In the concluded chapter, the proposed method was applied on experimental measurements. The data originated from experiments on two induction motors with multiple faulty cases regarding the location of broken bars. The first motor (Motor #1) was tested at the healthy condition, the single breakage fault and at the double breakage within half pole pitch distance, corresponding to three scenarios of the examined FEM models in Chapter 5; in addition to the FEM validation, the method was successfully validated experimentally on stator phase current and stray magnetic flux signals at two different load levels, the rated load and the half-rated load condition. The second motor (Motor #2) was tested at the healthy condition, two adjacent breakages, two breakages at half pitch distance and two breakages at pole pitch distance; the method was successfully validated only on stray magnetic flux measurements at the rated load condition, thus corresponding to all the FEM models examined in Chapter 5.

The results from experiments fully agree with the FEM validation, as the method ushered the set of investigated signatures, therefore providing in all cases a reliable representation of the fault related harmonic subcomponents. The evaluation of these signatures rendered advantageous results regarding changes in their amplitudes that can alarm for a rotor fault existence; firstly, the discussed subcomponent signatures are manifesting themselves only under faulty rotor condition; secondly -even if they are prompt to appear in healthy motor cases due to unexpected inherent asymmetries or manufacturing imbalances- their level of amplitude is relatively low, whereas for a faulty case they spike at levels which are suitable to indicate and detect a rotor fault. More importantly though, the examined signatures arise and duly allow their amplitudes to raise a fault alarm regardless the location of the breakages. This was evidently clear through the analysis at both levels of load using stator current and stray flux measurements. Moreover, the method reliably detected the rotor fault condition in the stray flux measurements of Motor #2, confronting reliably the problem of non-adjacent breakages.

Finally, the concluded analysis performed an examination of the subcomponent frequency at $2sf_s$, as it has been and is still being used as a signature in many rotor fault detection methods. It was seen that this specific subcomponent is not always and necessarily fault-related, as it can be affected by manufacturing imperfections, inherent imbalances or rotor interchange during maintenance/replacement etc. Also, the mentioned signature might spike in a healthy motor at levels higher than a faulty one, hence running the risk of misleading a diagnostic process. This was evidently clear in Motor #2, where the component behaved in a very random pattern regardless of the motor's health condition. A similar outcome was observed in some experimental cases for the trajectories extracted, something that agrees with some case of the FEM models presented in Chapter 5 (especially Model #3). Nonetheless, the rest of the signatures ($4sf_s$, $6sf_s$, $8sf_s$) were able to determine a rotor fault condition and reliable enough in every set. The $5-th$ and $7-th$ harmonics are therefore chosen as the main suitable assets of the method to provide a reliable diagnostic tool for the detection of rotor faults.

Chapter 7

Conclusions & Future Research

The concluded dissertation addressed a diagnostic method for the reliable detection of rotor electrical faults using advanced digital signal processing. By means of frequency extraction, spectral information of the stator phase current and the stray magnetic flux was extracted and represented using a novel two-stage approach. The method was validated via extended FEM simulations and experimental measurements. The following two sections summarise the conclusions and the potential future research respectively, highlighting the presented outcomes and the contribution of this PhD thesis to the research community.

7.1 Conclusions & Novel Contribution

The problem of rotor electrical faults in induction motors is an issue frequently encountered in industry. In particular, the problem of adjacent and non-adjacent breakages on a rotor is continuously reported by researches for induction motors embedded in various industrial applications. The machine's rotating magnetic fields, the inherent speed ripple effect, the complex machine construction, complicated electromagnetic and thermal phenomena, the dynamic and time-varying nature of rotor faults, the fault-related speed ripple effect generation and its reaction chain, inherent manufacturing imbalances, coupled loads, and environmental conditions are only a few factors that can contribute to the masking of a rotor fault and let it evolve undetected. At the presence of each of these mechanisms, as well as at any combination of them, diagnostic engineers run the danger of misdiagnosing induction machines. The case of false-negative diagnosis has been frequently reported by published industrial case studies. This means that, while prior periodical maintenance had diagnosed these motors as healthy, partially broken or even damaged rotors were detected when the motors where disassembled and inspected. On the other hand, conventional diagnostic methods have alarmed for rotor faults due to load variations, shaft vibrations, or even due

to inherent machine geometries and special rotor constructions; however, inspection of the rotors during maintenance revealed no harm anywhere of the rotor body. The latter scenario makes up the cases of false-positive diagnosis.

The frequency extraction method proposed by this research presented reliable results to detect fault-related rotor frequencies in the measurements of stator phase current and stray magnetic flux. The first novelty of the method is a system-oriented limitation from the DSP and system perspective according to the system parameters, defining the boundaries within which the method can be applied using a $t-f$ spectral representation; thereupon, a $t-f$ method is used to reliably visualise and investigate the time-varying nature of the discussed frequency components. More specifically, utilising the STFT analysis for a $t-f$ representation of the monitored signals, the spectral information of targeted frequency bands was extracted for the trajectories enclosed in those areas. The two-stage $t-f$ analysis over the steady-state regime addresses whether a motor is free from sidebands or not, around the main frequencies of interest; at the indication of sidebands existence, the method proceeds with extraction of frequencies with the potential to carry fault-related information. Furthermore, the sidebands -which manifest themselves as trajectories- are handled as time-signals. Their examination in the time-domain is the initial evaluation, whereas their frequency-domain analysis detects specific subcomponents in the low-frequencies range that are definitive for diagnosing a rotor fault.

The discussed analysis is applied over the whole duration of the acquired measurements; however, focus is given on the steady-state regime in order to take advantage of the quasi-static nature of the fault. This allows for the first time to reliably detect the fault-related speed ripple effect and securely diagnose rotor electrical faults over the steady-state, which is the second novelty of the method. Therefore, the proposed signal analysis and characterisation provides a novel solution to the problems of false-negative/false-positive diagnostics of rotor faults, which have been a vice at the presence of non-adjacent breakages. The proposed method detects such faults, regardless the fault location; hence, it confronts reliably breakages of rotor bars and broken rotor rings for the first time in an abstract approach. The mentioned problem is well known in industry and academia, as proven by the amount of published works providing such cases; thus, the method proves its novelty and originality by the versatility in a variety of cases originating from theoretical cases (FEM simulations) as well as extended experiments.

The proposed diagnostic method is the first one that reliably tracks the rotationally propagated $2ksf_s$ rotor fault related components and exploits their nature during extraction of their harmonic content. Although such components have been examined in the stator current and stray flux so far, their analysis is performed over the steady-state regime using

classical approaches or during the transient regime using advanced approaches. The first approach assumes stationarity or a partial steady-state condition; therefore, it loses vital part of the signal's spectral characteristics during the dynamic behaviour that a rotor fault's implications have. The second approach is modern, advanced and promising; however, it requires fast and high resolution analysis for signals of a very short duration as the transient start-up is usually very quick. The proposed method uses the whole duration of a signal, the transient start-up and the steady-state. By using the advanced approach, the frequency tracking applied in the two-stage context allows the examination of the spectral content in a global and more appropriate way in terms of spectral analysis. Subsequently, the spectral analysis is handled within defined resolution (windowing) limits and optimal windowing selection for rotor faults. The above process yields a very important finding, which is the time-dependent extraction of a spectral component $S(t, f_a)$ for a specific frequency f_a and its neighbouring sidebands $S(t, f_{a,i})$. If sidebands are present in the examined frequency bands, their pattern over time will be evaluated during the steps of the method to apply in the final stage the classical approach of a frequency-domain analysis.

In all cases, the examined frequency bands provide rigorous results that allow the detection of non-adjacent broken rotor bars with the proposed method. Both the $5-th$ and the $7-th$ harmonics are versatile under the proposed analysis and the subcomponents carried in their spectral energy information are prompt candidates to reveal a faulty rotor. Therefore, due to the global approach and reliable spectral analysis of the method, the extracted components for the $S(t, f)$ trajectories form a vital tool for the detection of rotor faults. As most of the recent works dealing with advanced approaches in the literature lack the apt parameter setting or the generality of assumptions, the two-stage approach proposed in the current method is of major significance. On the one hand, it suggests a proper signal representation for spectral components accounting for dynamic aspects by the behaviour of the fault-related $2ksf_s$ components over time; consequently, it tracks the orbit of such components and their surrounding (sideband) harmonics. On the other hand, it further evaluates these extracted time-signals over their frequency-domain representation; therefore, it practically constitutes a safe preliminary step for a proper diagnostic approach aiming to use Machine Learning or pattern recognition tools.

Finally, the method was proven by the experimental results immune to manufacturing defects and general asymmetries (environmental or user-imposed). This also provides an added value in the area of induction motor diagnostics, since so far the issue of such deficiencies and the coherent confusion they cause at the presence of rotor faults remained unsolved. In a nutshell, from the DSP and system perspective, the identification of the frequencies' dynamic behaviour during fault detection proves that the symmetric nature

of the induction motor collapses during rotor fault conditions; however, the subsequent phenomena create a more advanced non-linear periodicity that has to be accounted for in system level. At the same time, inherent system parameters like the motor slip s or DSP setting parameters like the window sequence length and the local equivalent noise bandwidth are already of dynamic -or quasi dynamic- nature. Under the combination of these phenomena, the assumptions that a static frequency-domain representation like the FFT analysis will provide the necessary diagnostic information is no longer valid. Instead, the detection of fault related spectral signatures within the $t-f$ domain is required by a dynamic analysis which enables to use the advanced $t-f$ approach for the benefit of the apt post-processing by the classical approach. Such dynamic two-stage approaches can reliably extract the valuable diagnostic information that is usually encapsulated in the spectral characteristics, and that is usually lost during the application of approaches that have been utilised so far.

7.2 Future Work

There is a series of key points regarding the proposed method to form aspects of interest for future research in the academic community. One of them is the application of the method in different signals of more dynamic nature, like the electromagnetic torque or the motor speed. This will further validate the method and enhance its reliability by multi-variate measurements, as multiple measurements are already a state of the art in the field of electrical machines. Essentially, all diagnostic techniques ought to be put in trial with all available measurements to investigate all diagnostic possibilities. Also, from the DSP point of view, another aspect that might be investigated is the optimisation of the signal processing method and its steps prior to the frequency extraction. This means further research regarding the pre-setting of the STFT analysis and the boundary conditions, as well as the optimisation of the parameter ξ with other algorithms rather than the exhaustive search one. This will provide further insight to the windowing functions and their effect in diagnostic applications for rotor faults, as well as other types of faults, e.g. eccentricity or short-circuits. The last DSP future aspect is for the method to be put under trial with other advanced DSP approaches; such may include the initial $t-f$ representation by the use of transformations like the CWT & DWT, the Wigner-Ville distribution and any other transform that allows to expand a signal with improved time resolution within reliable extraction limits. Nevertheless, what should be targeted for is the apt monitoring by a $t-f$ analysis without expense on the complexity and the computational time of the application and the used algorithms.

Furthermore, some weak points of the presented research concern software and simulation issues. Expectedly, transient FEM simulations including motion components are extremely time consuming and come with huge computational burden. Therefore, the process of collecting extended datasets for several healthy and faulty models of a motor can sometimes last up to several months. Consequently, the FEM simulations of this research focused on motors at the full-load condition as this is the condition most frequently encountered in industry applications. Future research to this extent may include simulations at other load profiles, like the no-load, low-load and the medium-load conditions. Another possibility to expand this research is to run such models in 3D FEM simulations and compare the outcomes with 2D, especially if thermal aspects would be taken into account. Also, potential software developments of the near future could allow for FEM software like the one used in this research to connect via plug-ins with other useful software for modelling, signal analysis and monitoring. Such expansions could connect FEM software with environments like Matlab Simulink or LabView and allow the fast and accurate on-line monitoring.

As the demands in the industry of electric motors continuously grow, both in industrial power plants and in mobility applications, on-line condition monitoring is an aspect that is always considered to implement by diagnostic engineers. On this basis, another future aspect of this research is to implement the proposed approach using FPGA and hardware-in-the-loop tools for on-line condition monitoring and to test the method in such an expansion in industry. This can be done in combination with the aforementioned software plug-ins to achieve increased diagnostic reliability and accuracy. Considering this, another future point that this research could be expanded to is the use of FPGA tools and hardware-in-the-loop systems to develop a complete diagnostic instrumentation set-up for the decision of electrical machines' state while they operate.

To the same direction, another improvement of the presented research in the future could be the optimisation of the magnetic flux sensor. Although the search coils developed in this research have shown competent diagnostic potential in laboratory level and industrial applications, further development is possible. For example, an idea for future work is to embed filters within the sensor for measurements in extremely noisy environments, or in applications with magnetic interference. Furthermore, there is space for improvement regarding the discussed flux sensors to make them more user-friendly and commercially attractive. This can include the packaging of the sensor and enhancement of its material properties to make it more robust and resilient. Also, a configuration of multiple sensors can be used to examine how the method will perform on multi-variable measurements of stray magnetic fields and their analysis.

Moreover, the following are some weak points regarding the concluded research that can be looked into in the future. The rotor breakage scenarios of single breakage, double adjacent breakages, and double non-adjacent breakages can be expanded to further scenarios like triple breakages and multiple breakages on the rotor cage. Although the process of damaging a rotor is expensive and such studies will come with more cost, it is valuable to evaluate such cases of extreme faulty states regarding their diagnosis to assess the diagnostic potential of new methods. Also, such cases can be put under the microscope in combination with rotor end-ring breakages, bearing faults and eccentricity conditions. This will help to assess the method on the pipeline for diagnostic decisions regarding discrimination of faults, something that can be valuable for applications in industrial environments and mobility applications. Finally, the proposed methodology is expected to face some difficulties in extremely noisy applications or where extreme magnetic interference is present, as the sensors have been manufactured and tested for experiments of laboratory level and for stationary motors in industry. Other possible obstacles are submersible applications, motors used in drilling, crashers, and compressors as such applications constitute cases in environments with excessive noise and vibrations. These aspects ought to be investigated in parallel with the sensor optimisation, a point mentioned in the very beginning of possible future work and weak points improvement. Optimal packaging and embedded filters in the sensor are possible strategies to follow, in order to overcome such issues in the future and ensure diagnostic reliability and accuracy in any type of application.

References

[1] Chapman S. Electric machinery fundamentals. Tata McGraw-Hill Education; 2005.

[2] Adkins B. The general theory of electrical machines. Chapman & Hall; 1957.

[3] Safacas A. Electrical Machines II (in Greek). University of Patras; 2005.

[4] Xypteras I. Electrical Machines I: DC & Asynchronous Machines (in Greek). Ziti; 1997.

[5] Panagiotou P, Arvanitakis I, Lophitis N, Gyftakis KN. FEM Study of Induction Machines Suffering from Rotor Electrical Faults Using Stray Flux Signature Analysis. In: 2018 XIII International Conference on Electrical Machines (ICEM). IEEE; 2018. p. 1861–1867.

[6] Panagiotou PA, Arvanitakis I, Lophitis N, Antonino-Daviu JA, Gyftakis KN. FEM approach for diagnosis of induction machines' non-adjacent broken rotor bars by short-time Fourier transform spectrogram. The Journal of Engineering. 2019;2019(17):4566–4570.

[7] Toliyat HA, Nandi S, Choi S, Meshgin-Kelk H. Electric machines: modeling, condition monitoring, and fault diagnosis. CRC press; 2012.

[8] Faiz J, Joksimović G, Ghorbanian V. Fault diagnosis of induction motors. Institution of Engineering & Technology; 2017.

[9] Trigeassou JC. Electrical machines diagnosis. John Wiley & Sons; 2013.

[10] Thomson WT, Gilmore RJ, et al. Motor Current Signature Analysis To Detect Faults In Induction Motor Drives-Fundamentals, Data Interpretation, And Industrial Case Histories. In: Proceedings of the 32nd turbomachinery Symposium. Texas A&M University. Turbomachinery Laboratories; 2003. .

[11] Thomson WT, Fenger M. Case histories of current signature analysis to detect faults in induction motor drives. In: IEEE International Electric Machines and Drives Conference, 2003. IEMDC'03.. vol. 3. IEEE; 2003. p. 1459–1465.

[12] Bellini A, Filippetti F, Franceschini G, Tassoni C, Passaglia R, Saottini M, et al. Mechanical failures detection by means of induction machine current analysis: a case history. In: 4th IEEE International Symposium on Diagnostics for Electric Machines, Power Electronics and Drives, 2003. SDEMPED 2003. IEEE; 2003. p. 322–326.

[13] Bellini A, Filippetti F, Franceschini G, Tassoni C, Passaglia R, Saottini M, et al. On-field experience with online diagnosis of large induction motors cage failures using MCSA. IEEE Transactions on Industry Applications. 2002;38(4):1045–1053.

[14] Antonino-Daviu JA, Lee SB, Wiedenbrug E. Reliable detection of rotor bar failures in induction motors operating in petrochemical plants. In: 2014 Petroleum and Chemical Industry Conference Europe. IEEE; 2014. p. 1–9.

[15] Antonino-Daviu JA, Quijano-Lopez A, Fuster-Roig V, Nevot C. Case stories of induction motors fault diagnosis based on current analysis. In: 2016 Petroleum and Chemical Industry Conference Europe (PCIC Europe). IEEE; 2016. p. 1–9.

[16] Gyftakis K, Panagiotou N, PA, Spyrakis D. Recent Experiences with MCSA and Flux Condition Monitoring of Mechanical Faults in 6kV Induction Motors for Water Pumping Applications. In: 2019 IEEE 12th International Symposium on Diagnostics for Electrical Machines, Power Electronics and Drives (SDEMPED). IEEE; 2019. p. 214–219.

[17] Pyrhonen J, Jokinen T, Hrabovcova V. Design of rotating electrical machines. John Wiley & Sons; 2013.

[18] Bellini A, Concari C, Franceschini G, Tassoni C, Toscani A. Vibrations, currents and stray flux signals to asses induction motors rotor conditions. In: IECON 2006-32nd Annual Conference on IEEE Industrial Electronics. IEEE; 2006. p. 4963–4968.

[19] Concari C, Franceschini G, Tassoni C. Differential diagnosis based on multivariable monitoring to assess induction machine rotor conditions. IEEE Transactions on Industrial Electronics. 2008;55(12):4156–4166.

[20] Garcia-Ramirez A, Morales-Hernandez L, Osornio-Rios R, Garcia-Perez A, Romero-Troncoso R. Thermographic technique as a complement for MCSA in induction motor fault detection. In: 2014 International Conference on Electrical Machines (ICEM). IEEE; 2014. p. 1940–1945.

[21] Panagiotou PA, Arvanitakis I, Lophitis N, Antonino-Daviu JA, Gyftakis KN. On the broken rotor bar diagnosis using time–frequency analysis:'Is one spectral representation enough for the characterisation of monitored signals?'. IET Electric Power Applications. 2019;.

[22] Panagiotou P, Arvanitakis I, Lophitis N, Antonino-Daviu JA, Gyftakis KN. Analysis of stray flux spectral components in induction machines under rotor bar breakages at various locations. In: 2018 XIII International Conference on Electrical Machines (ICEM). IEEE; 2018. p. 2345–2351.

[23] Panagiotou PA, Arvanitakis I, Lophitis N, Antonino-Daviu J, Gyftakis KN. A New Approach for Broken Rotor Bar Detection in Induction Motors Using Frequency Extraction in Stray Flux Signals. IEEE Transactions on Industry Applications. 2019;.

[24] Panagiotou P, Arvanitakis I, Lophitis N, Gyftakis KN. Frequency Extraction of Stator Current Signals: A new Tool for Rotor Fault Detection. In: 2019 IEEE 12th International Symposium on Diagnostics for Electrical Machines, Power Electronics and Drives (SDEMPED). IEEE; 2019. p. 290–296.

[25] Gieras JF, Wang C, Lai JC. Noise of polyphase electric motors. CRC press; 2018.

[26] Boldea I, Nasar SA. The induction machines design handbook. CRC press; 2018.

[27] Nasar SA, Nasar S. Schaum's outline of theory and problems of electric machines and electromechanics. McGraw-Hill; 1998.

[28] Nasar SA. Electric Machines and Power Systems: Electric machines. vol. 1. Mcgraw-Hill College; 1995.

[29] Moallem M, Dawson G. An improved magnetic equivalent circuit method for predicting the characteristics of highly saturated electromagnetic devices. IEEE Transactions on magnetics. 1998;34(5):3632–3635.

[30] Boglietti A, Cavagnino A, Lazzari M. Algorithms for the computation of the induction motor equivalent circuit parameters-Part I. In: 2008 34th Annual Conference of IEEE Industrial Electronics. IEEE; 2008. p. 2020–2027.

[31] Boglietti A, Cavagnino A, Lazzari M. Algorithms for the computation of the induction motor equivalent circuit parameters-Part II. In: 2008 34th Annual Conference of IEEE Industrial Electronics. IEEE; 2008. p. 2028–2033.

[32] Daut I, Anayet K, Irwanto M, Gomesh N, Muzhar M, Syatirah MA. Parameters Calculation of 5 HP AC Induction Motor. In: Proceedings of International Conference on Applications and Design in Mechanical Engineering (ICADME), Batu Ferringhi, Penang, Malaysia; 2009. p. 1–5.

[33] Gyftakis KN. Electromagnetic analysis of faults in IM and development of new diagnostic methods (in Greek); 2015.

[34] Gyftakis KN, Kappatou J. The impact of the rotor slot number on the behaviour of the induction motor. Advances in Power Electronics. 2013;2013.

[35] Gyftakis KN, Panagiotou PA, Kappatou JC. Application of wedges for the reduction of the space and time-dependent harmonic content in squirrel-cage induction motors. Journal of Computational Engineering. 2013;2013.

[36] Landy C, Levy W, McCulloch M, Meyer A. The effect of deep-bar properties when assessing reswitching transients in squirrel cage induction motors. In: Conference Record of the 1991 IEEE Industry Applications Society Annual Meeting. IEEE; 1991. p. 35–39.

[37] Erlicki MS, Porat Y, Alexandrovitz A. Leakage field changes of an induction motor as indication of nonsymmetric supply. IEEE Transactions on Industry and General Applications. 1971;(6):713–717.

[38] Elkasabgy NM, Eastham AR, Dawson GE. Detection of broken bars in the cage rotor on an induction machine. IEEE transactions on industry applications. 1992;28(1):165–171.

[39] Toliyat HA, Lipo TA. Transient analysis of cage induction machines under stator, rotor bar and end ring faults. IEEE Transactions on Energy Conversion. 1995;10(2):241–247.

[40] Hsu JS. Monitoring of defects in induction motors through air-gap torque observation. IEEE Transactions on Industry Applications. 1995;31(5):1016–1021.

[41] Penman J, Stavrou A. Broken rotor bars: their effect on the transient performance of induction machines. IEE Proceedings-Electric Power Applications. 1996;143(6):449–457.

[42] Filippetti F, Franceschini G, Tassoni C, Vas P. AI techniques in induction machines diagnosis including the speed ripple effect. In: IAS'96. Conference Record of the 1996 IEEE Industry Applications Conference Thirty-First IAS Annual Meeting. vol. 1. IEEE; 1996. p. 655–662.

[43] Martin-Diaz I, Morinigo-Sotelo D, Duque-Perez O, Romero-Troncoso RJ. An experimental comparative evaluation of machine learning techniques for motor fault diagnosis under various operating conditions. IEEE Transactions on Industry Applications. 2018;54(3):2215–2224.

[44] Bessam B, Menacer A, Boumehraz M, Cherif H. Detection of broken rotor bar faults in induction motor at low load using neural network. ISA transactions. 2016;64:241–246.

[45] Cabal-Yepez E, Valtierra-Rodriguez M, Romero-Troncoso R, Garcia-Perez A, Osornio-Rios R, Miranda-Vidales H, et al. FPGA-based entropy neural processor for online detection of multiple combined faults on induction motors. Mechanical Systems and Signal Processing. 2012;30:123–130.

[46] Georgoulas G, Climente-Alarcon V, Antonino-Daviu JA, Stylios CD, Arkkio A, Nikolakopoulos G. A multi-label classification approach for the detection of broken bars and mixed eccentricity faults using the start-up transient. In: 2016 IEEE 14th International Conference on Industrial Informatics (INDIN). IEEE; 2016. p. 430–433.

[47] Mustafa MO, Varagnolo D, Nikolakopoulos G, Gustafsson T. Detecting broken rotor bars in induction motors with model-based support vector classifiers. Control Engineering Practice. 2016;52:15–23.

[48] Gangsar P, Tiwari R. Comparative investigation of vibration and current monitoring for prediction of mechanical and electrical faults in induction motor based on multiclass-support vector machine algorithms. Mechanical Systems and Signal Processing. 2017;94:464–481.

[49] Li C, Wang X, Tao Z, Wang Q, Du S. Extraction of time varying information from noisy signals: An approach based on the empirical mode decomposition. Mechanical Systems and Signal Processing. 2011;25(3):812–820.

[50] ;.

[51] Wang C, Gao RX, Yan R. Unified time–scale–frequency analysis for machine defect signature extraction: theoretical framework. Mechanical Systems and Signal Processing. 2009;23(1):226–235.

[52] Ebrahimi BM, Faiz J, Akin B. Pattern recognition for broken bars fault diagnosis in induction motors under various supply conditions. European Transactions on Electrical Power. 2012;22(8):1176–1190.

[53] Choqueuse V, Benbouzid MEH, et al. Current frequency spectral subtraction and its contribution to induction machines' bearings condition monitoring. IEEE Transactions on Energy Conversion. 2012;28(1):135–144.

[54] Iglesias-Martínez ME, de Córdoba PF, Antonino-Daviu JA, Conejero JA. Detection of Bar Breakages in Induction Motor via Spectral Subtraction of Stray Flux Signals. In: 2018 XIII International Conference on Electrical Machines (ICEM). IEEE; 2018. p. 1796–1802.

[55] Choqueuse V, Benbouzid M, et al. Induction machine faults detection using stator current parametric spectral estimation. Mechanical Systems and Signal Processing. 2015;52:447–464.

[56] Samanta AK, Naha A, Routray A, Deb AK. Fast and accurate spectral estimation for online detection of partial broken bar in induction motors. Mechanical Systems and Signal Processing. 2018;98:63–77.

[57] Stefani A, Filippetti F, Bellini A. Diagnosis of induction machines in time-varying conditions. In: 2007 IEEE International Symposium on Diagnostics for Electric Machines, Power Electronics and Drives. IEEE; 2007. p. 126–131.

[58] Gritli Y, Lee SB, Filippetti F, Zarri L. Advanced diagnosis of outer cage damage in double-squirrel-cage induction motors under time-varying conditions based on wavelet analysis. IEEE Transactions on industry applications. 2013;50(3):1791–1800.

[59] Guo Y, Kareem A. Non-stationary frequency domain system identification using time–frequency representations. Mechanical Systems and Signal Processing. 2016;72:712–726.

[60] Yuan X, Cai L. Variable amplitude Fourier series with its application in gearbox diagnosis—Part I: Principle and simulation. Mechanical systems and signal processing. 2005;19(5):1055–1066.

[61] Liu Y, Guo L, Wang Q, An G, Guo M, Lian H. Application to induction motor faults diagnosis of the amplitude recovery method combined with FFT. Mechanical Systems and Signal Processing. 2010;24(8):2961–2971.

[62] Elbouchikhi E, Choqueuse V, Trachi Y, Benbouzid M. Induction machine bearing faults detection based on Hilbert-Huang transform. In: 2015 IEEE 24th International Symposium on Industrial Electronics (ISIE). IEEE; 2015. p. 843–848.

[63] Sapena-Bano A, Pineda-Sanchez M, Puche-Panadero R, Martinez-Roman J, Kanović Ž. Low-cost diagnosis of rotor asymmetries in induction machines working at a very low slip using the reduced envelope of the stator current. IEEE Transactions on Energy Conversion. 2015;30(4):1409–1419.

[64] Walker JS. Fast fourier transforms. CRC press; 2017.

[65] Van de Vegte J, Xiaoli Y. Fundamentals of digital signal processing. Prentice Hall New Jersey, USA; 2002.

[66] Weisstein EW. Fast fourier transform. 2015;.

[67] Moustakides G. Basic Techniques of Digital Signal Processing (in Greek). Tziola pub lications. 2003;.

[68] Lohne M. The Computational Complexity of the Fast Fourier Transform. 2017;.

[69] Riera-Guasp M, Antonino-Daviu JA, Capolino GA. Advances in electrical machine, power electronic, and drive condition monitoring and fault detection: state of the art. IEEE Transactions on Industrial Electronics. 2014;62(3):1746–1759.

[70] Henao H, Capolino G, Martis C. On the stray flux analysis for the detection of the three-phase induction machine faults. In: 38th IAS Annual Meeting on Conference Record of the Industry Applications Conference, 2003.. vol. 2. IEEE; 2003. p. 1368–1373.

[71] Bouchikhi EH, Choqueuse V, Benbouzid M, Charpentier JF, Barakat G. A comparative study of time-frequency representations for fault detection in wind turbine. In: IECON 2011-37th Annual Conference of the IEEE Industrial Electronics Society. IEEE; 2011. p. 3584–3589.

[72] Lopez-Ramirez M, Romero-Troncoso RJ, Morinigo-Sotelo D, Duque-Perez O, Ledesma-Carrillo LM, Camarena-Martinez D, et al. Detection and diagnosis of lubrication and faults in bearing on induction motors through STFT. In: 2016 International Conference on Electronics, Communications and Computers (CONIELECOMP). IEEE; 2016. p. 13–18.

[73] Climente-Alarcón V, Antonino-Daviu J, Riera-Guasp M, Puche R, Escobar-Moreira L, Wiener N, et al. Diagnosis of stator short-circuits through Wigner-Ville transient-based analysis. In: 2009 35th Annual Conference of IEEE Industrial Electronics. IEEE; 2009. p. 1097–1102.

[74] Climente-Alarcon V, Riera-Guasp M, Antonino-Daviu J, Roger-Folch J, Vedreno-Santos F. Diagnosis of rotor asymmetries in wound rotor induction generators operating under varying load conditions via the Wigner-Ville Distribution. In: International Symposium on Power Electronics Power Electronics, Electrical Drives, Automation and Motion. IEEE; 2012. p. 1378–1383.

[75] Riera-Guasp M, Antonino-Daviu JA, Pineda-Sanchez M, Puche-Panadero R, Pérez-Cruz J. A general approach for the transient detection of slip-dependent fault components based on the discrete wavelet transform. IEEE transactions on Industrial electronics. 2008;55(12):4167–4180.

[76] Antonino-Daviu J, Riera-Guasp M, Roger-Folch J, Martínez-Giménez F, Peris A. Application and optimization of the discrete wavelet transform for the detection of broken rotor bars in induction machines. Applied and Computational Harmonic Analysis. 2006;21(2):268–279.

[77] Oumaamar MEK, Razik H, Rezzoug A, Khezzar A. Line current analysis for bearing fault detection in induction motors using Hilbert transform phase. In: International Aegean Conference on Electrical Machines and Power Electronics and Electromotion, Joint Conference. IEEE; 2011. p. 288–293.

[78] Puche-Panadero R, Pons-Llinares J, Roger-Folch J, Pineda-Sanchez M. Diagnosis of eccentricity based on the Hilbert transform of the startup transient current. In: 2009 IEEE International Symposium on Diagnostics for Electric Machines, Power Electronics and Drives. IEEE; 2009. p. 1–6.

[79] Youn YW, Yi SH, Hwang DH, Sun JH, Kang DS, Kim YH. MUSIC-based diagnosis algorithm for identifying broken rotor bar faults in induction motors using flux signal. Journal of Electrical Engineering and Technology. 2013;8(2):288–294.

[80] Sotelo DM, Troncoso RJR, Panagiotou P, Antonino-Daviu JA, Gyftakis KN. Reliable Detection of Rotor Bars Breakage in Induction Motors via MUSIC and ZSC Methods. IEEE Transactions on Industry Applications. 2017;p. in–press.

[81] Pons-Llinares J, Climente-Alarcón V, Vedreño-Santos F, Antonino-Daviu J, Riera-Guasp M. Electric machines diagnosis techniques via transient current analysis. In: IECON 2012-38th Annual Conference on IEEE Industrial Electronics Society. IEEE; 2012. p. 3893–3900.

[82] Pons-Llinares J, Antonino-Daviu JA, Riera-Guasp M, Pineda-Sanchez M, Climente-Alarcon V. Induction motor diagnosis based on a transient current analytic wavelet transform via frequency B-splines. IEEE Transactions on Industrial Electronics. 2010;58(5):1530–1544.

[83] Climente-Alarcon V, Antonino-Daviu JA, Vedreño-Santos F, Puche-Panadero R. Vibration transient detection of broken rotor bars by PSH sidebands. IEEE Transactions on Industry Applications. 2013;49(6):2576–2582.

[84] Prudhom A, Antonino-Daviu J, Razik H, Climente-Alarcon V. Time-frequency vibration analysis for the detection of motor damages caused by bearing currents. Mechanical Systems and Signal Processing. 2017;84:747–762.

[85] Antonino-Daviu J, Quijano-López A, Climente-Alarcon V, Razik H. Evaluation of the detectability of rotor faults and eccentricities in induction motors via transient analysis of the stray flux. In: 2017 IEEE Energy Conversion Congress and Exposition (ECCE). IEEE; 2017. p. 3559–3564.

[86] Ramirez-Nunez JA, Antonino-Daviu JA, Climente-Alarcón V, Quijano-López A, Razik H, Osornio-Rios RA, et al. Evaluation of the detectability of electromechanical faults in induction motors via transient analysis of the stray flux. IEEE Transactions on Industry Applications. 2018;54(5):4324–4332.

[87] Gao RX, Yan R. From Fourier transform to wavelet transform: a historical perspective. In: Wavelets. Springer; 2011. p. 17–32.

[88] Bellini A, Filippetti F, Tassoni C, Capolino GA. Advances in diagnostic techniques for induction machines. IEEE Transactions on industrial electronics. 2008;55(12):4109–4126.

[89] Alsaedi MA. Fault diagnosis of three-phase induction motor: a review. Appl Optics Signal Proc. 2015;4(1):1–8.

[90] Frosini L, Borin A, Girometta L, Venchi G. Development of a leakage flux measurement system for condition monitoring of electrical drives. In: 8th IEEE Symposium on Diagnostics for Electrical Machines, Power Electronics & Drives. IEEE; 2011. p. 356–363.

[91] Frosini L, Borin A, Albini A, Benzi F. New techniques to simulate and diagnose stator winding faults in low voltage induction motors. In: 2012 XXth International Conference on Electrical Machines. IEEE; 2012. p. 1783–1789.

[92] Penman J, Dey M, Tait A, Bryan W. Condition monitoring of electrical drives. In: IEE Proceedings B-Electric Power Applications. vol. 133. IET; 1986. p. 142–148.

[93] Penman J, Sedding H, Lloyd B, Fink W. Detection and location of interturn short circuits in the stator windings of operating motors. IEEE transactions on Energy conversion. 1994;9(4):652–658.

[94] Henao H, Demian C, Capolino GA. A frequency-domain detection of stator winding faults in induction machines using an external flux sensor. IEEE Transactions on Industry Applications. 2003;39(5):1272–1279.

[95] Stavrou A, Sedding HG, Penman J. Current monitoring for detecting inter-turn short circuits in induction motors. IEEE Transactions on energy conversion. 2001;16(1):32–37.

[96] Menacer A, Champenois G, Nait S, Mohamed S, Benakcha A, Moreau S, et al. Rotor failures diagnosis of squirrel cage induction motors with different supplying sources. Journal of Electrical Engineering and Technology. 2009;4(2):219–228.

[97] Lomax I. Assessment of induction motor cage fatigue life. In: 1991 Fifth International Conference on Electrical Machines and Drives (Conf. Publ. No. 341). IET; 1991. p. 281–284.

[98] Lee SB, Hyun D, Kang Tj, Yang C, Shin S, Kim H, et al. Identification of false rotor fault indications produced by online MCSA for medium-voltage induction machines. IEEE Transactions on Industry Applications. 2015;52(1):729–739.

[99] Shin S, Kim J, Lee SB, Lim C, Wiedenbrug EJ. Evaluation of the influence of rotor magnetic anisotropy on condition monitoring of two-pole induction motors. IEEE Transactions on Industry Applications. 2015;51(4):2896–2904.

[100] Sizov GY. Analysis, modeling, and diagnostics of adjacent and nonadjacent broken rotor bars in squirrel-cage induction machines. 2007;.

[101] Nandi S, Bharadwaj RM, Toliyat HA. Performance analysis of a three-phase induction motor under mixed eccentricity condition. IEEE Transactions on Energy Conversion. 2002;17(3):392–399.

[102] Mendes AM, Cardoso AM. Fault-tolerant operating strategies applied to three-phase induction-motor drives. IEEE Transactions on Industrial Electronics. 2006;53(6):1807–1817.

[103] Ying X. Characteristic performance analysis of squirrel cage induction motor with broken bars. IEEE Transactions on Magnetics. 2009;45(2):759–766.

[104] Garcia M, Panagiotou PA, Antonino-Daviu JA, Gyftakis KN. Efficiency assessment of induction motors operating under different faulty conditions. IEEE Transactions on Industrial Electronics. 2018;66(10):8072–8081.

[105] Antonino-Daviu J, Razik H, Quijano-Lopez A, Climente-Alarcon V. Detection of rotor faults via transient analysis of the external magnetic field. In: IECON 2017-43rd Annual Conference of the IEEE Industrial Electronics Society. IEEE; 2017. p. 3815–3821.

[106] Antonino-Daviu J, Riera-Guasp M, Roger-Folch J, Pérez R. An analytical comparison between DWT and Hilbert-Huang-based methods for the diagnosis of rotor asymmetries in induction machines. In: 2007 IEEE Industry Applications Annual Meeting. IEEE; 2007. p. 1932–1939.

[107] Stefani A, Bellini A, Filippetti F. Diagnosis of induction machines' rotor faults in time-varying conditions. IEEE Transactions on Industrial Electronics. 2009;56(11):4548–4556.

[108] Riera-Guasp M, Pineda-Sanchez M, Pérez-Cruz J, Puche-Panadero R, Roger-Folch J, Antonino-Daviu JA. Diagnosis of induction motor faults via gabor analysis of the current in transient regime. IEEE Transactions on Instrumentation and Measurement. 2012;61(6):1583–1596.

[109] Georgoulas G, Climente-Alarcon V, Dritsas L, Antonino-Daviu JA, Nikolakopoulos G. Start-up analysis methods for the diagnosis of rotor asymmetries in induction motors-seeing is believing. In: 2016 24th Mediterranean Conference on Control and Automation (MED). IEEE; 2016. p. 372–377.

[110] Schoen RR, Habetler TG, Kamran F, Bartheld RG. Motor bearing damage detection using stator current monitoring. In: Proceedings of 1994 IEEE Industry Applications Society Annual Meeting. vol. 1. IEEE; 1994. p. 110–116.

[111] Blodt M, Granjon P, Raison B, Rostaing G. Models for bearing damage detection in induction motors using stator current monitoring. IEEE transactions on industrial electronics. 2008;55(4):1813–1822.

[112] Immovilli F, Bellini A, Rubini R, Tassoni C. Diagnosis of bearing faults in induction machines by vibration or current signals: A critical comparison. IEEE Transactions on Industry Applications. 2010;46(4):1350–1359.

[113] Harlişca C, Szabó L, Frosini L, Albini A. Diagnosis of rolling bearings faults in electric machines through stray magnetic flux monitoring. In: 2013 8TH International Symposium on Advanced Topics in Electrical Engineering (Atee). IEEE; 2013. p. 1–6.

[114] Vitek O, Janda M, Hajek V, Bauer P. Detection of eccentricity and bearings fault using stray flux monitoring. In: 8th IEEE Symposium on Diagnostics for Electrical Machines, Power Electronics & Drives. IEEE; 2011. p. 456–461.

[115] Frosini L, Harlişca C, Szabó L. Induction machine bearing fault detection by means of statistical processing of the stray flux measurement. IEEE Transactions on Industrial Electronics. 2014;62(3):1846–1854.

[116] Yilmaz M, Krein PT. Capabilities of finite element analysis and magnetic equivalent circuits for electrical machine analysis and design. In: 2008 IEEE Power Electronics Specialists Conference. IEEE; 2008. p. 4027–4033.

[117] Mezani S, Laporte B, Takorabet N. Saturation and space harmonics in the complex finite element computation of induction motors. IEEE transactions on magnetics. 2005;41(5):1460–1463.

[118] Lv Y, Zhang W, Liu J. Analysis and diagnosis of broken rotor bars in induction motors based on maxwell. In: Proceedings of the 33rd Chinese Control Conference. IEEE; 2014. p. 3065–3069.

[119] Salon SJ. Finite element analysis of electrical machines. vol. 101. Kluwer academic publishers Boston; 1995.

[120] Ellison A, Yang S. Effects of rotor eccentricity on acoustic noise from induction machines. In: Proceedings of the Institution of Electrical Engineers. vol. 118. IET; 1971. p. 174–184.

[121] Vas P. Performance of three-phase squirrel-cage induction motors with rotor asymmetries. Periodica Polytechnica Electrical Engineering. 1975;19(4):309–315.

[122] Williamson S, Smith A. Steady-state analysis of 3-phase cage motors with rotor-bar and end-ring faults. In: IEE Proceedings B-Electric Power Applications. vol. 129. IET; 1982. p. 93.

[123] Kerszenbaum I, Landy C. The existence of large inter-bar currents in three phase squirrel cage motors with rotor-bar and/or end-ring faults. IEEE transactions on power apparatus and systems. 1984;(7):1854–1862.

[124] Walliser R, Landy C. Determination of interbar current effects in the detection of broken rotor bars in squirrel cage induction motors. IEEE Transactions on Energy conversion. 1994;9(1):152–158.

[125] Kliman GB, Koegl RA, Schulz Jr MW, Grabkowski SE. Rotor fault detector for induction motors. Google Patents; 1988. US Patent 4,761,703.

[126] Milimonfared J, Kelk HM, Nandi S, Minassians A, Toliyat HA. A novel approach for broken-rotor-bar detection in cage induction motors. IEEE Transactions on Industry Applications. 1999;35(5):1000–1006.

[127] Munoz AR, Lipo TA. Complex vector model of the squirrel-cage induction machine including instantaneous rotor bar currents. IEEE transactions on industry applications. 1999;35(6):1332–1340.

[128] Bellini A, Filippetti F, Franceschini G, Tassoni C, Kliman G. Quantitative evaluation of induction motor broken bars by means of electrical signature analysis. In: Conference Record of the 2000 IEEE Industry Applications Conference. Thirty-Fifth IAS Annual Meeting and World Conference on Industrial Applications of Electrical Energy (Cat. No. 00CH37129). vol. 1. IEEE; 2000. p. 484–491.

[129] Bangura JF, Demerdash NA. Effects of broken bars/end-ring connectors ad airgap eccentricities on ohmic and core losses of induction motors in ASD's using a coupled Finite Element-State Space Method. IEEE transactions on energy conversion. 2000;15(1):40–47.

[130] Bangura J, Demerdash N. Comparison between characterization and diagnosis of broken bars/end-ring connectors and airgap eccentricities of induction motors in ASDs using a coupled finite element-state space method. IEEE Transactions on Energy Conversion. 2000;15(1):48–56.

[131] Cardoso A, Saraiva E. The use of Park's vector in the detection of electrical failures on three-phase induction motors. In: Proc. Int. AMSE Conf. Modelling; 1987. .

[132] Cardoso AM, Saraiva E. On-line diagnostics of three-phase induction motors by Park's Vector. In: Proceedings of the International Conference on Electrical Machines. vol. 3. Pisa, Italy:[sn]; 1988. p. 231–234.

[133] Cardoso AM, Saraiva E. On-Line Diagnostics of Current Source Inverter Fed Induction Machines by Park's Vector Approach. In: Proceedings of the 1990 International Conference on Electrical Machines; 1990. p. 1000–1005.

[134] Cardoso AM, Saraiva E, Mateus MS, Ramalho A. On-line detection of airgap eccentricity in 3-phase induction motors, by Park's Vector approach. In: 1991 Fifth International Conference on Electrical Machines and Drives (Conf. Publ. No. 341). IET; 1991. p. 61–66.

[135] Cardoso AM, Cruz S, Carvalho J, Saraiva E. Rotor cage fault diagnosis in three-phase induction motors, by Park's vector approach. In: IAS'95. Conference Record of the 1995 IEEE Industry Applications Conference Thirtieth IAS Annual Meeting. vol. 1. IEEE; 1995. p. 642–646.

[136] Cardoso AM, Mendes A. Semi-converter fault diagnosis in DC motor drives, by Park's vector approach. 1996;.

[137] Cruz S, Cardoso AM. Rotor cage fault diagnosis in three-phase induction motors by the synchronous reference frame current Park's vector approach. In: Proc. Int. Conf. Elect. Mach.. vol. 2; 2000. p. 776–780.

[138] Cardoso AM. The Park's Vector Approach: a general tool for diagnostics of electrical machines, power electronics and adjustable speed drives. In: Record of the 1997 IEEE International Symposium on Diagnostics for Electrical Machines, Power Electronics and Drives; 1997. p. 261–269.

[139] MA Cruz S AJ Marques Cardoso. Rotor cage fault diagnosis in three-phase induction motors by extended Park's vector approach. Electric Machines &Power Systems. 2000;28(4):289–299.

[140] Cruz S, Cardoso AM. Rotor cage fault diagnosis in voltage source inverter-fed induction motors, by the Extended Park's Vector Approach. In: Proc. IEEE Int. Symp. Diagnostics for Electrical Machines, Power Electronics and Drives; 1999. p. 1–3.

[141] Estima JO, Freire NM, Cardoso AM. Recent advances in fault diagnosis by Park's vector approach. In: 2013 IEEE Workshop on Electrical Machines Design, Control and Diagnosis (WEMDCD). IEEE; 2013. p. 279–288.

[142] McCully P, Landy C. Evaluation of current and vibration signals for squirrel cage induction motor condition monitoring. 1997;.

[143] Benbouzid MEH. A review of induction motors signature analysis as a medium for faults detection. IEEE transactions on industrial electronics. 2000;47(5):984–993.

[144] Cruz S, Cardoso AM. Rotor cage fault diagnosis in three-phase induction motors by the total instantaneous power spectral analysis. In: Conference Record of the 1999 IEEE Industry Applications Conference. Thirty-Forth IAS Annual Meeting (Cat. No. 99CH36370). vol. 3. IEEE; 1999. p. 1929–1934.

[145] Drif M, Cardoso AM. Rotor cage fault diagnostics in three-phase induction motors, by the instantaneous non-active power signature analysis. In: 2007 IEEE International Symposium on Industrial Electronics. IEEE; 2007. p. 1050–1055.

[146] Drif M, Cardoso AM. The instantaneous reactive power approach for rotor cage fault diagnosis in induction motor drives. In: 2008 IEEE Power Electronics Specialists Conference. IEEE; 2008. p. 1548–1552.

[147] Drif M, Cardoso AM. Rotor cage fault diagnostics in three-phase induction motors, by the instantaneous phase-angle signature analysis. In: 2007 IEEE International Electric Machines & Drives Conference. vol. 2. IEEE; 2007. p. 1440–1445.

[148] Yahia K, Marques Cardoso AJ, Ghoggal A, Zouzou SE. Induction motors broken rotor bars diagnosis through the discrete wavelet transform of the instantaneous reactive power signal under time-varying load conditions. Electric Power Components and Systems. 2014;42(7):682–692.

[149] Drif M, Kim H, Kim J, Lee SB, Cardoso AJM. Active and Reactive Power Spectra-Based Detection and Separation of Rotor Faults and Low-Frequency Load Torque Oscillations. IEEE Transactions on Industry Applications. 2016;53(3):2702–2710.

[150] Bellini A, Filippetti F, Franceschini G, Tassoni C, Kliman GB. Quantitative evaluation of induction motor broken bars by means of electrical signature analysis. IEEE Transactions on industry applications. 2001;37(5):1248–1255.

[151] Williamson S, Gersh D. Representation of rotor spiders in reduced finite-element models for cage rotors. 1995;.

[152] Williamson S, Gersh D. Representation of rotor spiders and axial ventilation ducts in reduced finite-element models for cage rotors. IEE Proceedings-Electric Power Applications. 1996;143(6):423–428.

[153] Onuki T, Wakao S, Im J, Takahashi H, Miyokawa T. Design optimization of air-ducts in rotating machines with high power density. IEEE transactions on magnetics. 1998;34(5):2857–2860.

[154] Zhang Y, Ruan J, Huang T, Yang X, Zhu H, Yang G. Calculation of temperature rise in air-cooled induction motors through 3-D coupled electromagnetic fluid-dynamical and thermal finite-element analysis. IEEE Transactions on Magnetics. 2012;48(2):1047–1050.

[155] Lee S, Hong J, Lee SB, Wiedenbrug E, Teska M, Kim H. Evaluation of the Influence of Rotor Axial Air Ducts on Condition Monitoring of Induction Motors. In: IEEE Energy Conversion Congress and Exposition (ECCE). IEEE; 2012. p. 3016–3023.

[156] Yang C, Kang TJ, Hyun D, Lee SB, Antonino-Daviu J, Pons-Llinares J. Evaluation of the Influence of Rotor Axial Air Ducts on Condition Monitoring of Induction Motors. In: IEEE Energy Conversion Congress and Exposition (ECCE). IEEE; 2013. p. 2508–2515.

[157] Lee S, Hong J, Lee SB, Wiedenbrug EJ, Teska M, Kim H. Evaluation of the influence of rotor axial air ducts on condition monitoring of induction motors. IEEE Transactions on Industry Applications. 2013;49(5):2024–2033.

[158] Gyftakis K, Lee SB, Kappatou J, Antonino-Daviu J. Identification of the broken bar fault in induction motors with rotor air ducts through the torque spectrum. In: XXth International Conference on Electrical Machines (ICEM). IEEE; 2014. p. 1614–1620.

[159] Yang C, Kang TJ, Lee SB, Yoo JY, Bellini A, Zarri L, et al. Screening of false induction motor fault alarms produced by axial air ducts based on the space-harmonic-induced current components. IEEE Transactions on Industrial Electronics. 2014;62(3):1803–1813.

[160] Yang C, Kang TJ, Hyun D, Lee SB, Antonino-Daviu JA, Pons-Llinares J. Reliable detection of induction motor rotor faults under the rotor axial air duct influence. IEEE Transactions on Industry Applications. 2014;50(4):2493–2502.

[161] Park Y, Yang C, Kim J, Kim H, Lee SB, Gyftakis KN, et al. Stray Flux Monitoring for Reliable Detection of Rotor Faults under the Influence of Rotor Axial Air Ducts. IEEE Transactions on Industrial Electronics. 2018;66(10):7561–7570.

[162] Sobczyk T, Maciolek W. Diagnostics of rotor-cage faults supported by effects due to higher MMF harmonics. In: 2003 IEEE Bologna Power Tech Conference Proceedings,. vol. 2. IEEE; 2003. p. 5–pp.

[163] Sobczyk TJ, Maciolek W. Does the component (1- 2s) f 0 in stator currents is sufficient for detection of rotor cage faults? In: 2005 5th IEEE International Symposium on Diagnostics for Electric Machines, Power Electronics and Drives. IEEE; 2005. p. 1–5.

[164] Ceban A, Pusca R, Romary R. Eccentricity and broken rotor bars faults-Effects on the external axial field. In: The XIX International Conference on Electrical Machines-ICEM 2010. IEEE; 2010. p. 1–6.

[165] Meshgin-Kelk H, Milimonfared J, Toliyat HA. Interbar currents and axial fluxes in healthy and faulty induction motors. IEEE Transactions on Industry Applications. 2004;40(1):128–134.

[166] Ceban A, Pusca R, Romary R. Study of rotor faults in induction motors using external magnetic field analysis. IEEE Transactions on Industrial Electronics. 2011;59(5):2082–2093.

[167] Mirzaeva G, Saad KI, Jahromi MG. Comprehensive diagnostics of induction motor faults based on measurement of space and time dependencies of air gap flux. IEEE Transactions on Industry Applications. 2016;53(3):2657–2666.

[168] Concari C, Franceschini G, Tassoni C. Induction machine current space vector features to effectively discern and quantify rotor faults and external torque ripple. IET electric power applications. 2012;6(6):310–321.

[169] Mehala N, Dahiya R. Motor current signature analysis and its applications in induction motor fault diagnosis. International journal of systems applications, engineering & development. 2007;2(1):29–35.

[170] Mehrjou MR, Mariun N, Marhaban MH, Misron N. Rotor fault condition monitoring techniques for squirrel-cage induction machine—A review. Mechanical Systems and Signal Processing. 2011;25(8):2827–2848.

[171] Benbouzid MEH, Kliman GB. What stator current processing-based technique to use for induction motor rotor faults diagnosis? IEEE Transactions on Energy Conversion. 2003;18(2):238–244.

[172] Henao H, Razik H, Capolino GA. Analytical approach of the stator current frequency harmonics computation for detection of induction machine rotor faults. IEEE Transactions on Industry Applications. 2005;41(3):801–807.

[173] Bellini A, Concari C, Franceschini G, Lorenzani E, Tassoni C, Toscani A. Thorough understanding and experimental validation of current sideband components in induction machines rotor monitoring. In: IECON 2006-32nd Annual Conference on IEEE Industrial Electronics. IEEE; 2006. p. 4957–4962.

[174] Jung JH, Lee JJ, Kwon BH. Online diagnosis of induction motors using MCSA. IEEE Transactions on Industrial Electronics. 2006;53(6):1842–1852.

[175] Didier G, Ternisien E, Caspary O, Razik H. Fault detection of broken rotor bars in induction motor using a global fault index. IEEE Transactions on industry applications. 2006;42(1):79–88.

[176] Klein R, Ingman D, Braun S. Non-stationary signals: Phase-energy approach—Theory and simulations. Mechanical Systems and Signal Processing. 2001;15(6):1061–1089.

[177] Padovese L. Hybrid time–frequency methods for non-stationary mechanical signal analysis. Mechanical Systems and Signal Processing. 2004;18(5):1047–1064.

[178] Wang F, Mechefske CK. Adaptive modelling of transient vibration signals. Mechanical Systems and Signal Processing. 2006;20(4):825–842.

[179] ;.

[180] Rajagopalan S, Restrepo JA, Aller JM, Habetler T, Harley R. Wigner-Ville distributions for detection of rotor faults in brushless DC (BLDC) motors operating under non-stationary conditions. In: 2005 5th IEEE International Symposium on Diagnostics for Electric Machines, Power Electronics and Drives. IEEE; 2005. p. 1–7.

[181] Randall RB, Antoni J, Chobsaard S. The relationship between spectral correlation and envelope analysis in the diagnostics of bearing faults and other cyclostationary machine signals. Mechanical systems and signal processing. 2001;15(5):945–962.

[182] Jaksch I. Faults diagnosis of three-phase induction motors using envelope analysis. In: 4th IEEE International Symposium on Diagnostics for Electric Machines, Power Electronics and Drives, 2003. SDEMPED 2003. IEEE; 2003. p. 289–293.

[183] Didier G, Ternisien E, Caspary O, Razik H. A new approach to detect broken rotor bars in induction machines by current spectrum analysis. Mechanical Systems and Signal Processing. 2007;21(2):1127–1142.

[184] Cupertino F, De Vanna E, Salvatore L, Stasi S. Comparison of spectral estimation techniques applied to induction motor broken bars detection. In: 4th IEEE International Symposium on Diagnostics for Electric Machines, Power Electronics and Drives, 2003. SDEMPED 2003. IEEE; 2003. p. 129–134.

[185] Bellini A, Franceschini G, Tassoni C. Monitoring of induction machines by maximum covariance method for frequency tracking. IEEE Transactions on Industry Applications. 2006;42(1):69–78.

[186] Léonard F. Phase spectrogram and frequency spectrogram as new diagnostic tools. Mechanical Systems and Signal Processing. 2007;21(1):125–137.

[187] Bellini A, Filippetti F, Casadei D, Yazidi A, Capolino G. Monitoring of induction machines currents by high frequency resolution analysis. In: Conference Record of the 2006 IEEE Industry Applications Conference Forty-First IAS Annual Meeting. vol. 5. IEEE; 2006. p. 2320–2325.

[188] Supangat R, Ertugrul N, Soong W, Gray D, Hansen C, Grieger J. Detection of broken rotor bars in induction motor using starting-current analysis and effects of loading. IEE Proceedings-Electric Power Applications. 2006;153(6):848–855.

[189] Wang C, Zhou Z, Unsworth P, OFarrell T. Sensorless speed measurement of induction machines using short time Fourier transformation. In: 2008 International Symposium on Power Electronics, Electrical Drives, Automation and Motion. IEEE; 2008. p. 1114–1119.

[190] Juillerat N, Arisona SM, Schubiger-Banz S. Enhancing the quality of audio transformations using the multi-scale short-time Fourier transform. In: Proc. of the 10th IASTED conf. on Signal and Image Processing; 2008. .

[191] Aimer AF, Boudinar AH, Benouzza N, Bendiabdellah A. Simulation and experimental study of induction motor broken rotor bars fault diagnosis using stator current spectrogram. In: 2015 3rd International Conference on Control, Engineering & Information Technology (CEIT). IEEE; 2015. p. 1–7.

[192] Antonino-Daviu J, Popaleny P. Detection of induction motor coupling unbalanced and misalignment via advanced transient current signature analysis. In: 2018 XIII International Conference on Electrical Machines (ICEM). IEEE; 2018. p. 2359–2364.

[193] Bruzzese C, Santini E. On the frequency dependence of harmonic current side-band (HCSB) based rotor fault indicators for three-phase cage machines. In: 2007 IEEE International Symposium on Diagnostics for Electric Machines, Power Electronics and Drives. IEEE; 2007. p. 231–235.

[194] Jaksch I, Fuchs P. Rotor cage faults detection in induction motors by motor current demodulation analysis. In: 2007 IEEE International Symposium on Diagnostics for Electric Machines, Power Electronics and Drives. IEEE; 2007. p. 247–252.

[195] Jimenez GA, Munoz AO, Duarte-Mermoud MA. Fault detection in induction motors using Hilbert and Wavelet transforms. Electrical Engineering. 2007;89(3):205–220.

[196] Oumaamar M, Khezzar A, Boucherma M, Razik H, Andriamalala RN, Baghli L. Neutral voltage analysis for broken rotor bars detection in induction motors using Hilbert transform phase. In: 2007 IEEE Industry Applications Annual Meeting. IEEE; 2007. p. 1940–1947.

[197] Antonino-Daviu JA, Riera-Guasp M, Pineda-Sanchez M, Perez RB. A critical comparison between DWT and Hilbert–Huang-based methods for the diagnosis of rotor bar failures in induction machines. IEEE Transactions on Industry Applications. 2009;45(5):1794–1803.

[198] Antonino-Daviu J, Climente-Alarcón V, Pons-Llinares J, Pineda-Sánchez M, Jover-Rodriguez P, Arkkio A. Application of TFD tools for the tracing of eccentricity-related components in induction machines. In: 2009 35th Annual Conference of IEEE Industrial Electronics. IEEE; 2009. p. 1039–1044.

[199] Trajin B, Chabert M, Regnier J, Faucher J. Hilbert versus Concordia transform for three-phase machine stator current time-frequency monitoring. Mechanical Systems and Signal Processing. 2009;23(8):2648–2657.

[200] Puche-Panadero R, Pineda-Sanchez M, Riera-Guasp M, Roger-Folch J, Antonino-Daviu J, Perez-Cruz J. Diagnosis of rotor bar breakages based on the Hilbert transform of the current during the startup transient. In: 2009 IEEE International Electric Machines and Drives Conference. IEEE; 2009. p. 1434–1440.

[201] Tsoumas IP, Georgoulas G, Mitronikas ED, Safacas AN. Asynchronous machine rotor fault diagnosis technique using complex wavelets. IEEE Transactions on Energy Conversion. 2008;23(2):444–459.

[202] Kia SH, Henao H, Capolino GA. Diagnosis of broken-bar fault in induction machines using discrete wavelet transform without slip estimation. IEEE Transactions on Industry Applications. 2009;45(4):1395–1404.

[203] Hamdani S, Bouzida A, Touhami O, Ibtiouen R. Diagnosis of rotor fault in induction motor using the MUSIC analysis of the terminal voltage after switch-off. In: 2008 18th International Conference on Electrical Machines. IEEE; 2008. p. 1–5.

[204] Boudinar A, Bendiabdellah A, Benouzza N, Boughanmi N. Three phase induction motor incipient rotor's faults detection based on improved Root-MUSIC approach. International Review of Electrical Engineering. 2007;2(3):406–413.

[205] Blodt M, Regnier J, Faucher J. Distinguishing load torque oscillations and eccentricity faults in induction motors using stator current Wigner distributions. IEEE Transactions on Industry Applications. 2009;45(6):1991–2000.

[206] Rodriguez PJ, Belahcen A, Arkkio A. Signatures of electrical faults in the force distribution and vibration pattern of induction motors. IEE Proceedings-Electric Power Applications. 2006;153(4):523–529.

[207] Faiz J, Ebrahimi BM. A new pattern for detecting broken rotor bars in induction motors during start-up. IEEE Transactions on magnetics. 2008;44(12):4673–4683.

[208] Gritli Y, Bellini A, Rossi C, Casadei D, Filippetti F, Capolino G. Condition monitoring of mechanical faults in induction machines from electrical signatures: Review of different techniques. In: 2017 IEEE 11th International Symposium on Diagnostics for Electrical Machines, Power Electronics and Drives (SDEMPED). IEEE; 2017. p. 77–84.

[209] Henao H, Assaf T, Capolino G. Detection of voltage source dissymmetry in an induction motor using the measurement of axial leakage flux. In: Proc. ICEM; 2000. p. 1110–1114.

[210] Henao H, Capolino G, Demian C. Correlation between line current and leakage flux in an induction machine. In: Proceedings International Conference on Electrical Machines (ICEM'02); 2002. .

[211] Romary R, Corton R, Thailly D, Brudny J. Induction machine fault diagnosis using an external radial flux sensor. The European Physical Journal-Applied Physics. 2005;32(2):125–132.

[212] Kokko V. Condition monitoring of squirrel-cage motors by axial magnetic flux measurements. 2003;.

[213] Negrea MD, et al. Electromagnetic flux monitoring for detecting faults in electrical machines. 2006;.

[214] Assaf T, Henao H, Capolino GA. Simplified axial flux spectrum method to detect incipient stator inter-turn short-circuits in induction machine. In: 2004 IEEE International Symposium on Industrial Electronics. vol. 2. IEEE; 2004. p. 815–819.

[215] Yazidi A, Henao H, Capolino G, Artioli M, Filippetti F, Casadei D. Flux signature analysis: An alternative method for the fault diagnosis of induction machines. In: 2005 IEEE Russia Power Tech. IEEE; 2005. p. 1–6.

[216] Lamim Filho P, Pederiva R, Brito J. Detection of stator winding faults in induction machines using an internal flux sensor. In: 2007 IEEE International Symposium on Diagnostics for Electric Machines, Power Electronics and Drives. IEEE; 2007. p. 432–437.

[217] Yazidi A, Henao H, Capolino GA. Broken rotor bars fault detection in squirrel cage induction machines. In: IEEE International Conference on Electric Machines and Drives, 2005. IEEE; 2005. p. 741–747.

[218] Kia SH, Henao H, Capolino GA, Martis C. Induction machine broken bars fault detection using stray flux after supply disconnection. In: IECON 2006-32nd Annual Conference on IEEE Industrial Electronics. IEEE; 2006. p. 1498–1503.

[219] Fatemi SR, Henao H, Capolino G. Gearbox monitoring by using the stray flux in an induction machine based electromechanical system. In: MELECON 2008-The 14th IEEE Mediterranean Electrotechnical Conference. IEEE; 2008. p. 484–489.

[220] Ahmed I, Ahmed M. Comparison of stator current, axial leakage flux and instantaneous power to detect broken rotor bar faults in induction machines. In: 2008 Australasian Universities Power Engineering Conference. IEEE; 2008. p. 1–6.

[221] Pusca R, Romary R, Ceban A, Brudny JF. An online universal diagnosis procedure using two external flux sensors applied to the ac electrical rotating machines. Sensors. 2010;10(11):10448–10466.

[222] Vitek O, Janda M, Hajek V. Effects of eccentricity on external magnetic field of induction machine. In: Melecon 2010-2010 15th IEEE Mediterranean Electrotechnical Conference. IEEE; 2010. p. 939–943.

[223] Ishkova I, Vítek O. Analysis of induction motor faults by means of monitoring the current and magnetic flux density spectrums. In: 2016 International Symposium on Power Electronics, Electrical Drives, Automation and Motion (SPEEDAM). IEEE; 2016. p. 611–616.

[224] Harlişca C, Szabó L, Frosini L, Albini A. Bearing faults detection in induction machines based on statistical processing of the stray fluxes measurements. In: 2013 9th IEEE International Symposium on Diagnostics for Electric Machines, Power Electronics and Drives (SDEMPED). IEEE; 2013. p. 371–376.

[225] Frosini L, Borin A, Girometta L, Venchi G. A novel approach to detect short circuits in low voltage induction motor by stray flux measurement. In: 2012 XXth International Conference on Electrical Machines. IEEE; 2012. p. 1538–1544.

[226] Mirzaeva G, Saad K. Ac motor instrumentation and main air gap flux measurement for fault diagnostics. In: 2013 Australasian Universities Power Engineering Conference (AUPEC). IEEE; 2013. p. 1–6.

[227] Cabanas MF, Pedrayes F, Melero MG, García CHR, Cano JM, Orcajo GA, et al. Unambiguous detection of broken bars in asynchronous motors by means of a flux measurement-based procedure. IEEE Transactions on Instrumentation and Measurement. 2010;60(3):891–899.

[228] Romary R, Pusca R, Lecointe J, Brudny J. Electrical machines fault diagnosis by stray flux analysis. In: 2013 IEEE Workshop on Electrical Machines Design, Control and Diagnosis (WEMDCD). IEEE; 2013. p. 247–256.

[229] Dias CG, Chabu IE. Spectral analysis using a Hall effect sensor for diagnosing broken bars in large induction motors. IEEE Transactions on Instrumentation and Measurement. 2014;63(12):2890–2902.

[230] Saad K, Mirzaeva G. Space harmonics analysis of the main air gap flux of an induction motor and its applicability to detect faults. In: 2014 Australasian Universities Power Engineering Conference (AUPEC). IEEE; 2014. p. 1–6.

[231] Saad K, Mirzaeva G. Fault diagnosis of induction motors by space harmonics analysis of the main air gap flux. In: 2014 International Conference on Electrical Machines (ICEM). IEEE; 2014. p. 1608–1613.

[232] Faiz J, Ebrahimi BM, Toliyat H, Abu-Elhaija W. Mixed-fault diagnosis in induction motors considering varying load and broken bars location. Energy Conversion and Management. 2010;51(7):1432–1441.

[233] Garcia-Perez A, Romero-Troncoso RJ, Cabal-Yepez E, Osornio-Rios RA, de Jesus Rangel-Magdaleno J, Miranda H. Startup current analysis of incipient broken rotor bar in induction motors using high-resolution spectral analysis. In: 8th IEEE Symposium on Diagnostics for Electrical Machines, Power Electronics & Drives. IEEE; 2011. p. 657–663.

[234] Antonino-Daviu J, Riera-Guasp M, Pineda-Sanchez M, Puche-Panadero R, Pérez R, Jover-Rodriguez P, et al. Fault diagnosis in induction motors using the Hilbert-Huang Transform. Nuclear Technology. 2011;173(1):26–34.

[235] Faiz J, Ghorbanian V, Ebrahimi BM. A new criterion for rotor broken bar fault diagnosis in line-start and inverter-fed induction motors using Hilbert-Huang transform. In: 2012 IEEE International Conference on Power Electronics, Drives and Energy Systems (PEDES). IEEE; 2012. p. 1–6.

[236] Oumaamar MEK, Razik H, Rezzoug A, Khezzar A. Line current analysis for bearing fault detection in induction motors using Hilbert transform phase. In: International Aegean Conference on Electrical Machines and Power Electronics and Electromotion, Joint Conference. IEEE; 2011. p. 288–293.

[237] Bensalem S, Bacha K, Benbouzid M, Chaari A. Induction Motor Fault Diagnosis Using a Hilbert-Park Lissajou's Curve Analysis and Neural Network-Based Decision. 2013;.

[238] Pons-Llinares J, Morinigo-Sotelo D, Duque-Perez O, Antonino-Daviu J, Perez-Alonso M. Transient detection of close components through the chirplet transform: Rotor faults in inverter-fed induction motors. In: IECON 2014-40th Annual Conference of the IEEE Industrial Electronics Society. IEEE; 2014. p. 3386–3392.

[239] Pons-Llinares J, Antonino-Daviu J, Roger-Folch J, Moríñigo-Sotelo D, Duque-Pérez O. Mixed eccentricity diagnosis in inverter-fed induction motors via the adaptive slope transform of transient stator currents. Mechanical Systems and Signal Processing. 2014;48(1-2):423–435.

[240] Cabal-Yepez E, Garcia-Ramirez AG, Romero-Troncoso RJ, Garcia-Perez A, Osornio-Rios RA. Reconfigurable monitoring system for time-frequency analysis on industrial equipment through STFT and DWT. IEEE Transactions on Industrial Informatics. 2012;9(2):760–771.

[241] Su YC, Lian KL, Chang HH. Feature selection of non-intrusive load monitoring system using STFT and wavelet transform. In: 2011 IEEE 8th International Conference on e-Business Engineering. IEEE; 2011. p. 293–298.

[242] Corral-Hernandez JA, Antonino-Daviu J, Pons-Llinares J, Climente-Alarcon V, Frances-Galiana V. Transient-based rotor cage assessment in induction motors operating with soft starters. IEEE Transactions on Industry Applications. 2015;51(5):3734–3742.

[243] Granda D, Aguilar WG, Arcos-Aviles D, Sotomayor D. Broken bar diagnosis for squirrel cage induction motors using frequency analysis based on MCSA and continuous wavelet transform. Mathematical and Computational Applications. 2017;22(2):30.

[244] Gyftakis KN, Kappatou JC. The zero-sequence current as a generalized diagnostic mean in Δ-connected three-phase induction motors. IEEE Transactions on Energy conversion. 2013;29(1):138–148.

[245] Gyftakis KN, Antonino-Daviu JA, Garcia-Hernandez R, McCulloch MD, Howey DA, Cardoso AJM. Comparative experimental investigation of broken bar fault detectability in induction motors. IEEE Transactions on Industry Applications. 2015;52(2):1452–1459.

[246] Antonino-Daviu JA, Gyftakis KN, Garcia-Hernandez R, Razik H, Cardoso AJM. Comparative influence of adjacent and non-adjacent broken rotor bars on the induction motor diagnosis through MCSA and ZSC methods. In: IECON 2015-41st Annual Conference of the IEEE Industrial Electronics Society. IEEE; 2015. p. 001680–001685.

[247] Popaleny P, Antonino-Daviu J. Electric Motors Condition Monitoring Using Currents and Vibrations Analyses. In: 2018 XIII International Conference on Electrical Machines (ICEM). IEEE; 2018. p. 1834–1840.

[248] Gritli Y, Rossi C, Casadei D, Filippetti F, Capolino GA. A diagnostic space vector-based index for rotor electrical fault detection in wound-rotor induction machines under speed transient. IEEE Transactions on Industrial Electronics. 2017;64(5):3892–3902.

[249] Concari C, Pietrini G, Soldati A, Tassoni C, Toscani A, Franceschini G. Induction Machines with Rotor Faults: Analysis of the Physical Quantities for Different Operating Conditions and Machine Sizes for Improved Diagnostics. In: 2018 International Symposium on Power Electronics, Electrical Drives, Automation and Motion (SPEEDAM). IEEE; 2018. p. 208–215.

[250] Antonino-Daviu J, Aviyente S, Strangas EG, Riera-Guasp M. Scale invariant feature extraction algorithm for the automatic diagnosis of rotor asymmetries in induction motors. IEEE Transactions on Industrial Informatics. 2012;9(1):100–108.

[251] Georgoulas G, Karvelis P, Stylios CD, Tsoumas IP, Antonino-Daviu JA, Climente-Alarcon V. Automatizing the broken bar detection process via short time Fourier transform and two-dimensional piecewise aggregate approximation representation. In: 2014 IEEE Energy Conversion Congress and Exposition (ECCE). IEEE; 2014. p. 3104–3110.

[252] Georgoulas G, Tsoumas IP, Antonino-Daviu JA, Climente-Alarcón V, Stylios CD, Mitronikas ED, et al. Automatic pattern identification based on the complex empirical mode decomposition of the startup current for the diagnosis of rotor asymmetries in asynchronous machines. IEEE Transactions on Industrial Electronics. 2013;61(9):4937–4946.

[253] Karvelis P, Georgoulas G, Tsoumas IP, Antonino-Daviu JA, Climente-Alarcón V, Stylios CD. A symbolic representation approach for the diagnosis of broken rotor bars in induction motors. IEEE Transactions on Industrial Informatics. 2015;11(5):1028–1037.

[254] Godoy WF, da Silva IN, Goedtel A, Palácios RHC, Lopes TD. Application of intelligent tools to detect and classify broken rotor bars in three-phase induction motors fed by an inverter. IET Electric Power Applications. 2016;10(5):430–439.

[255] Martin-Diaz I, Romero-Troncoso RJ, Morinigo-Sotelo D, Duque-Perez O. Evaluation of intelligent approaches for motor diagnosis under changing operational conditions. In: 2017 IEEE 11th International Symposium on Diagnostics for Electrical Machines, Power Electronics and Drives (SDEMPED). IEEE; 2017. p. 65–71.

[256] García-Escudero LA, Duque-Perez O, Fernandez-Temprano M, Morinigo-Sotelo D. Robust detection of incipient faults in VSI-fed induction motors using quality control charts. IEEE Transactions on Industry Applications. 2016;53(3):3076–3085.

[257] Filippetti F, Bellini A, Capolino GA. Condition monitoring and diagnosis of rotor faults in induction machines: State of art and future perspectives. In: 2013 IEEE Workshop on Electrical Machines Design, Control and Diagnosis (WEMDCD). IEEE; 2013. p. 196–209.

[258] Miljković D. Brief review of motor current signature analysis. HDKBR Info magazin. 2015;5(1):14–26.

[259] Jiang C, Li S, Habetler TG. A review of condition monitoring of induction motors based on stray flux. In: 2017 IEEE Energy Conversion Congress and Exposition (ECCE). IEEE; 2017. p. 5424–5430.

[260] Lamim Filho P, Pederiva R, Brito J. Detection of stator winding faults in induction machines using flux and vibration analysis. Mechanical Systems and Signal Processing. 2014;42(1-2):377–387.

[261] Frosini L, Magnaghi M, Albini A. An improved diagnostic system to detect inter-turns short circuits in low voltage stator windings. In: 2015 IEEE Workshop on Electrical Machines Design, Control and Diagnosis (WEMDCD). IEEE; 2015. p. 220–225.

[262] Ewert P. Use of axial flux in the detection of electrical faults in induction motors. In: 2017 International Symposium on Electrical Machines (SME). IEEE; 2017. p. 1–6.

[263] Surya G, Khan Z, Ballal M. Radial flux signature analysis for identifying source unbalance and stator turn fault in cage motors using radial flux sensing coil. In: 2016 IEEE 1st International Conference on Power Electronics, Intelligent Control and Energy Systems (ICPEICES). IEEE; 2016. p. 1–6.

[264] Frosini L, Zanazzo S, Albini A. A wavelet-based technique to detect stator faults in inverter-fed induction motors. In: 2016 XXII International Conference on Electrical Machines (ICEM). IEEE; 2016. p. 2917–2923.

[265] Saad K, Mirzaeva G. Advanced diagnosis of rotor faults in large induction motors based on internal flux measurement. In: 2016 IEEE Industry Applications Society Annual Meeting. IEEE; 2016. p. 1–8.

[266] Irhoumah M, Pusca R, Lefevre E, Mercier D, Romary R. Detection of the Stator Winding Inter-Turn Faults in Asynchronous and Synchronous Machines Through the Correlation Between Harmonics of the Voltage of Two Magnetic Flux Sensors. IEEE Transactions on Industry Applications. 2019;55(3):2682–2689.

[267] Frosini L, Magnaghi M, Albini A, Magrotti G. A new diagnostic instrument to detect generalized roughness in rolling bearings for induction motors. In: 2015 IEEE 10th International Symposium on Diagnostics for Electrical Machines, Power Electronics and Drives (SDEMPED). IEEE; 2015. p. 239–245.

[268] Saad K, Mirzaeva G. Space-time representation of the main air gap flux of a three phase squirrel cage induction motor and its application to detect eccentricity. In: 2015 IEEE International Electric Machines & Drives Conference (IEMDC). IEEE; 2015. p. 1466–1472.

[269] Chernyavska I, Vítek O. Analysis of air-gap eccentricity in inverter fed induction motor by means of motor current signature analysis and stray flux of motor. In: 2017 IEEE 11th International Symposium on Diagnostics for Electrical Machines, Power Electronics and Drives (SDEMPED). IEEE; 2017. p. 72–76.

[270] Salem SB, Salah M, Touti W, Bacha K, Chaari A. Stray Flux analysis for monitoring eccentricity faults in induction motors: Experimental study. In: 2017 International Conference on Control, Automation and Diagnosis (ICCAD). IEEE; 2017. p. 292–297.

[271] Liu Z, Tian G, Cao W, Dai X, Shaw B, Lambert R. Non-invasive load monitoring of induction motor drives using magnetic flux sensors. IET Power Electronics. 2017;10(2):189–195.

[272] Jaksch I, Schreiber R, Fuchs P. The analysis of induction motor electromagnetic field and shaft revolution oscillations at dynamic rotor faults. In: 2015 IEEE International Workshop of Electronics, Control, Measurement, Signals and their Application to Mechatronics (ECMSM). IEEE; 2015. p. 1–6.

[273] Clark SW, Stevens D. Induction motor rotor bar damage evaluation with magnetic field analysis. IEEE Transactions on Industry Applications. 2015;52(2):1469–1476.

[274] Mirzaeva G, Saad KI. Advanced diagnosis of rotor faults and eccentricity in induction motors based on internal flux measurement. IEEE Transactions on Industry Applications. 2018;54(3):2981–2991.

[275] Chernyavska I, Vítek O. Analysis of broken rotor bar fault in a squirrel-cage induction motor by means of stator current and stray flux measurement. In: 2016 IEEE International Power Electronics and Motion Control Conference (PEMC). IEEE; 2016. p. 532–537.

[276] Goktas T, Arkan M, Mamis MS, Akin B. Broken rotor bar fault monitoring based on fluxgate sensor measurement of leakage flux. In: 2017 IEEE International Electric Machines and Drives Conference (IEMDC). IEEE; 2017. p. 1–6.

[277] Goktas T, Arkan M, Mamis MS, Akin B. Separation of induction motor rotor faults and low frequency load oscillations through the radial leakage flux. In: 2017 IEEE Energy Conversion Congress and Exposition (ECCE). IEEE; 2017. p. 3165–3170.

[278] Gyftakis KN, Panagiotou PA, Lee SB. Introduction of the Zero-Sequence Stray Flux as a Reliable Diagnostic Method of Rotor Electrical Faults in Induction Motors. In: IECON 2019-45th Annual Conference of the IEEE Industrial Electronics Society. IEEE; 2019. p. 0000–0001.

[279] Riera-Guasp M, Cabanas MF, Antonino-Daviu JA, Pineda-Sánchez M, García CHR. Influence of nonconsecutive bar breakages in motor current signature analysis for the diagnosis of rotor faults in induction motors. IEEE Transactions on Energy Conversion. 2009;25(1):80–89.

[280] Martinez J, Belahcen A, Arkkio A. Broken bar indicators for cage induction motors and their relationship with the number of consecutive broken bars. IET Electric Power Applications. 2013;7(8):633–642.

[281] Faiz J, Ebrahimi BM. Locating rotor broken bars in induction motors using finite element method. Energy conversion and Management. 2009;50(1):125–131.

[282] Sahraoui M, Cardoso AJM, Ghoggal A. The use of a modified prony method to track the broken rotor bar characteristic frequencies and amplitudes in three-phase induction motors. IEEE Transactions on Industry Applications. 2014;51(3):2136–2147.

[283] Sizov GY, Sayed-Ahmed A, Yeh CC, Demerdash NA. Analysis and diagnostics of adjacent and nonadjacent broken-rotor-bar faults in squirrel-cage induction machines. IEEE Transactions on Industrial Electronics. 2009;56(11):4627–4641.

[284] Menacer A, Moreau S, Benakcha A, Said MSN. Effect of the position and the number of broken bars on asynchronous motor stator current spectrum. In: 2006 12th International Power Electronics and Motion Control Conference. IEEE; 2006. p. 973–978.

[285] Menacer A, Moreau S, Champenois G, Saïd MSN, Benakcha A. Experimental detection of rotor failures of induction machines by stator current spectrum analysis in function of the broken rotor bars position and the load. In: EUROCON 2007-The International Conference on" Computer as a Tool". IEEE; 2007. p. 1752–1758.

[286] Gyftakis KN, Antonino-Daviu JA, Cardoso AM. A reliable indicator to detect non-adjacent broken rotor bars severity in induction motors. In: 2016 XXII International Conference on Electrical Machines (ICEM). IEEE; 2016. p. 2910–2916.

[287] Kral C, Pirker F, Schagginger M, Wieser RS. Sequences of field oriented control for the detection of faulty rotor bars in induction machines. The Vienna monitoring method. In: AMC'98-Coimbra. 1998 5th International Workshop on Advanced Motion Control. Proceedings (Cat. No. 98TH8354). IEEE; 1998. p. 463–468.

[288] Mirafzal B, Demerdash NA. Effects of load on diagnosing broken bar faults in induction motors using the pendulous oscillation of the rotor magnetic field orientation. In: Conference Record of the 2004 IEEE Industry Applications Conference, 2004. 39th IAS Annual Meeting.. vol. 2. IEEE; 2004. p. 699–707.

[289] Mirafzal B, Demerdash NA. Effects of load magnitude on diagnosing broken bar faults in induction motors using the pendulous oscillation of the rotor magnetic field orientation. IEEE Transactions on Industry Applications. 2005;41(3):771–783.

[290] Mirafzal B, Demerdash NA. On innovative methods of induction motor inter-turn and broken-bar fault diagnostics. IEEE Transactions on Industry applications. 2006;42(2):405–414.

[291] Halem N, Zouzou S, Srairi K, Guedidi S. Influence of broken rotor bars location in the squirrel cage induction motor using finite element method. Journal of Fundamental and Applied Sciences. 2013;5(1):110–119.

[292] Gyftakis KN, Cardoso AJM, Antonino-Daviu JA. Introducing the Filtered Park's and Filtered Extended Park's Vector Approach to detect broken rotor bars in induction motors independently from the rotor slots number. Mechanical Systems and Signal Processing. 2017;93:30–50.

[293] Miceli R, Gritli Y, Di Tommaso A, Filippetti F, Rossi C. Vibration signature analysis for monitoring rotor broken bar in double squirrel cage induction motors based on wavelet analysis. COMPEL: The International Journal for Computation and Mathematics in Electrical and Electronic Engineering. 2014;33(5):1625–1641.

[294] Turoň V. A Study of Parameters Setting of the STADZT. Acta Polytechnica. 2012;52(5).

[295] Harris F. Windows, harmonic analysis, and the discrete Fourier transform, Rep. NUC TP532, Nay Undersea Center, San Diego, Calif. 1969;.

[296] Harris FJ. On the use of windows for harmonic analysis with the discrete Fourier transform. Proceedings of the IEEE. 1978;66(1):51–83.

[297] Cohen L, Lee C. Local bandwidth and optimal windows for the short time Fourier transform. In: Advanced algorithms and architectures for signal processing IV. vol. 1152. International Society for Optics and Photonics; 1989. p. 401–425.

[298] Trethewey MW. Window and overlap processing effects on power estimates from spectra. Mechanical Systems and Signal Processing. 2000;14(2):267–278.

[299] Mateo C, Talavera JA. Short-time Fourier transform with the window size fixed in the frequency domain. Digital Signal Processing. 2018;77:13–21.

[300] Mateo C, Talavera JA. Short-time Fourier transform with the window size fixed in the frequency domain (STFT-FD): Implementation. SoftwareX. 2018;8:5–8.

[301] Wang LH, Zhang QD, Zhang YH, Zhang K. The time-frequency resolution of short time Fourier transform based on multi-window functions. In: Advanced Materials Research. vol. 214. Trans Tech Publ; 2011. p. 122–127.

[302] Qaisar SM, Fesquet L, Renaudin M. An adaptive resolution computationally efficient short-time Fourier transform. Journal of Electrical and Computer Engineering. 2008;2008.

[303] Villegas-Ortega A, Asiaín-Olivares TI, Ruiz-Vega D. Program for the detection and diagnosis of broken rotor bars in squirrel-cage motors. In: 2016 IEEE International Autumn Meeting on Power, Electronics and Computing (ROPEC). IEEE; 2016. p. 1–6.

[304] Jaganathan K, Eldar YC, Hassibi B. Recovering signals from the short-time Fourier transform magnitude. In: 2015 IEEE International Conference on Acoustics, Speech and Signal Processing (ICASSP). IEEE; 2015. p. 3277–3281.

[305] Wang C, Zhou Z, Unsworth PJ, Igic P. Current space vector amplitude fluctuation based sensorless speed measurement of induction machines using short time Fourier transformation. In: 2008 34th Annual Conference of IEEE Industrial Electronics. IEEE; 2008. p. 1869–1874.

[306] Gröchenig K. Foundations of time-frequency analysis. Springer Science & Business Media; 2013.

[307] Shokrollahi E, Zargar G, Riahi M. Using continuous wavelet transform and short time Fourier transform as spectral decomposition methods to detect of stratigraphic channel in one of the Iranian south-west oil fields. International Journal of Science and Emerging Technologies. 2013;5(5):291–299.

[308] Brown RA, Lauzon ML, Frayne R. Developments in time-frequency analysis of biomedical signals and images using a generalized Fourier synthesis. In: Recent Advances in Biomedical Engineering. IntechOpen; 2009. .

[309] Sheikhani A, Behnam H, Mohammadi MR, Noroozian M, Golabi P. Analysis of quantitative Electroencephalogram background activity in Autism disease patients with Lempel-Ziv complexity and Short Time Fourier Transform measure. In: 2007 4th IEEE/EMBS International Summer School and Symposium on Medical Devices and Biosensors. IEEE; 2007. p. 111–114.

[310] Riviere CN, Reich SG, Thakor NV. Adaptive Fourier modeling for quantification of tremor. Journal of neuroscience methods. 1997;74(1):77–87.

[311] Ferreira FJ, Baoming G, de Almeida AT. Reliability and operation of high-efficiency induction motors. In: 2015 IEEE/IAS 51st Industrial & Commercial Power Systems Technical Conference (I&CPS). IEEE; 2015. p. 1–13.

[312] Ferreira FJ, Baoming G, de Almeida AT. Reliability and Operation of High-Efficiency Induction Motors. IEEE transactions on industry applications. 2016;52(6):4628–4637.

[313] Georgoulas G, Karvelis P, Stylios C, Frosini L, Tsoumas I. Exploring the detectability of short-circuit faults in inverter-fed induction motors. In: IECON 2018-44th Annual Conference of the IEEE Industrial Electronics Society. IEEE; 2018. p. 5930–5935.

[314] Georgoulas G, Frosini L, Tsoumas I, Loutas T, Albini A. An Automatic Method for Condition Monitoring of Inverter Fed Induction Motors. In: 2018 XIII International Conference on Electrical Machines (ICEM). IEEE; 2018. p. 1754–1760.

[315] Yuan X, Cai L. Variable amplitude Fourier series with its application in gearbox diagnosis—Part II: Experiment and application. Mechanical systems and signal processing. 2005;19(5):1067–1081.

[316] Liu Z, Jin Y, Zuo MJ, Feng Z. Time-frequency representation based on robust local mean decomposition for multicomponent AM-FM signal analysis. Mechanical Systems and Signal Processing. 2017;95:468–487.

[317] Hon TK. Time-frequency analysis and filtering based on the short-time Fourier transform. King's College London (University of London); 2013.

[318] Cohen L. Time-frequency analysis. vol. 778. Prentice hall; 1995.

[319] Boashash B. Time frequency signal analysis and processing: A comprehensive reference. 2003;.

[320] Putland GR, Boashash B. Can a signal be both monocomponent and multicomponent? In: Third Australasian Workshop on Signal Processing Applications (WoSPA 2000); 2000. p. 14–15.

[321] Papadimitriou CH, Steiglitz K. Combinatorial optimization. vol. 24;.

[322] Ltd IC. Magnet CAD package: User manual. Infolytica Montreal,, Canada; 2007.

[323] Manual MU. Infolytica Corporation. Quebec, Canada. 2008;.

[324] Gyftakis KN, Panagiotou PA, Lee SB. The Role of the Mechanical Speed Frequency on the Induction Motor Fault Detection via the Stray Flux. In: 2019 IEEE 12th International Symposium on Diagnostics for Electrical Machines, Power Electronics and Drives (SDEMPED). IEEE; 2019. p. 201–207.